

**ASSESSMENT OF THE SPATIOTEMPORAL VARIABILITY OF OPTICAL  
AND BIOGEOCHEMICAL PARAMETERS IN THE LOWER AMAZON  
REGION AND OF THE CARBON CONTENT IN THE AMAZON RIVER  
CONTINUUM USING IN SITU AND REMOTE SENSING DATA**

Aline de Matos Valerio

Doctorate Thesis Course Graduate in  
Remote Sensing, guided by Drs. Milton  
Kampel and Vincent Vantrepotte.

URL do documento original:  
<<http://urlib.net/xx/yy>>

INPE  
São José dos Campos  
2018

## Cataloging in Publication Data

---

Cutter Valerio, Aline de Matos  
Assessment of the spatiotemporal variability of optical and biogeochemical parameters in the Lower Amazon region and of the carbon content at the Amazon River continuum using in situ and Remote Sensing data/ Aline de Matos Valerio. - São José dos Campos: INPE, 2017.

Thesis (Doctorate in Remote Sensing) - Instituto Nacional de Pesquisas Espaciais, São José dos Campos, 2017.  
Guiding: Drs. Milton Kampel and Vincent Vantrepotte

1. Amazon River Continuum. 2. Biogeochemical parameters. 3. Bio-optical properties. 4. CDOM. 5. Carbon budget. 6. Water colour remote sensing.  
Título

---



Esta obra foi licenciada sob uma Licença Creative Commons Atribuição-NãoComercial 3.0 Não Adaptada.

This work is licensed under a Creative Commons Attribution-NonCommercial 3.0 Unported License.

[Informar aqui sobre marca registrada](#)



## AMAZONAS

*Por la selva serpentea  
dejando imborrable marca  
de los ríos el monarca  
y el paraíso recrea.  
Dios por allí se pasea  
y contempla embelesado  
cómo el sol por Él creado  
antes de ir al caserío  
le pide permiso al río  
que está en su curso atrapado.*

*En su caudal que se ahonda  
con dirección al Atlántico  
de las aves bajo el cántico  
se desliza la anaconda.  
El río deja la fronda  
lleno de temeridad  
y en un duelo de verdad  
como una cuenta a saldar  
muere enfrentando al mar  
¡y el mar es inmensidad!"*

*Luis Bárcena Giménez, 2004*

*Este trabalho é dedicado a todas as aguerridas fortalezas de minha vida, Ivan, minhas famílias Matos, Valerio e Gil e, sobretudo, a minha mãe.*



## AGRADECIMENTOS

Agradeço primeiramente a Deus, minha força e meu escudo. Agradeço a Ele pelas oportunidades que me foram dadas e por Seu amor por mim. Nestas oportunidades, conheci pessoas maravilhosas a quem também sou muito grata. Sendo assim, agradeço ao meu orientador de longa jornada, Dr. Milton Kampel que sempre me apoiou. Agradeço ao meu co-orientador Dr. Vincent Vantrepotte por me auxiliar nesta jornada, fazendo também significantes contribuições a este documento. Mais que passar conhecimento, se tornaram também amigos.

Em especial agradeço ao Dr. Jeffrey Richey por me oferecer a oportunidade de trabalhar no projeto TROCAS e fazer parte desta família. Cada participante do grupo deu a sua contribuição a este documento também, sendo pesquisadores ou tripulação. Sendo assim agradeço ao time TROCAS e amigos: Jeff, Nick, Henrique, Vania, Diani, Victor, Alan, Rodrigo, Alex, Joel, Daimio, Gilvan, Cica, Leno, Jeremias, Adriano, Daniel e Borboleta. Este projeto foi um marco em minha vida da qual serei eternamente grata. Agradeço também a oportunidade de ter participado do projeto ANACONDAS e de ter conhecido a Dr. Patricia Yager.

Agradeço aos meus amigos e colegas do INPE que seja por importantes conversas triviais ou discutindo o meu trabalho, sempre se fizeram presentes: Gabriel, Nati, Lauri, Fran, Lari, João Felipe, Gustavo, Lino, Felipe, Daniel, Carlos. Do mesmo modo gostaria de agradecer a todos dos grupos MOceanS e Antares.

À Coordenação de Aperfeiçoamento de Pessoal de Nível Superior (CAPES) pela bolsa de estudos. Ao Programa de Pós-Graduação em Sensoriamento Remoto pelo suporte financeiro a minha ida ao evento International Ocean Colour Science Meeting e a publicação fruto da tese. À Fundação de Amparo à Pesquisa do Estado de São Paulo (FAPESP) e National Science Foundation (NSF) pelo auxílio financeiro aos trabalhos de campo no Rio Amazonas. À Gordon and Betty Moore Foundation pelo apoio financeiro aos trabalhos de campo na pluma do Rio Amazonas.

Tenho uma inefável gratidão aos amigos e família, que mesmo não fazendo parte deste mundo acadêmico, sempre me incentivaram a continuar e acreditaram no meu potencial, com uma paciência acolhedora.

Por fim, minha maior gratidão é ao meu marido, meu melhor amigo e meu maior encorajador para superar qualquer dificuldade da vida. Ivan, obrigada por estar sempre ao meu lado e me fazer ser melhor.





## ABSTRACT

The Amazon River continuum plays a crucial role to the global carbon budget but its geographic extension challenges in situ observations. Due to its high temporal and synoptic coverage, the water colour remote sensing (WCRS) represents a relevant observation tool to monitor the distribution and variability of carbon content and other biogeochemical parameters on the Amazon waters. However, the optimal exploitation of the information provided by WCRS for investigating biogeochemical dynamics of a water system relies on accurate retrieval of bio-optical properties of the area investigated. This work focused on the Lower Amazon River continuum where a comprehensive description of the spatiotemporal variability of radiometric, bio-optical and biogeochemical parameters was performed with the aim of mapping carbon content from remote sensing observation. In the Lower Amazon River region (LAR), in situ sampling of remote sensing reflectance, bio-optical parameters (absorption properties of the coloured dissolved organic matter ( $a_{\text{CDOM}}$ ), total particulate matter, phytoplankton and non-algal particles ( $a_{\text{nap}}$ )) and biogeochemical parameters (suspended particulate matter (SPM), chlorophyll-*a*, dissolved organic carbon (DOC) concentration, and partial pressure of dioxide carbon ( $p\text{CO}_2$ )) were acquired for all regional hydrological seasons (i.e. rising water (RW), high water (HW), falling water (FW) and low water (LW)), over the 2014-2017 time period. In the Amazon River plume (ARP), in situ  $p\text{CO}_2$ , sea surface salinity (SSS) and water surface temperature (SST) were acquired during HW, FW and LW seasons during 2010-2012. The general description of the bio-optical characteristics of the Lower Amazon River performed from this original data set has allowed a clear optical distinction between waters from the Amazon mainstream (NAP and CDOM dominated) and those corresponding to the Amazon tributaries (clear waters and CDOM dominated). The analysis of the spatiotemporal variability of the Lower Amazon bio-optical properties emphasized: 1) the predominant impact of Amazon tributaries dilution on biogeochemical parameters and degradation processes of the DOM along the Amazon course; 2) the homogeneity in the Amazon bio-optical characteristics during the HW, FW, LW seasons the latter contrasting with the RW season (SPM major characteristics); 3) the sensitivity of the Amazon water to exceptional hydrological conditions; 4) the restricted influence of small scale processes (e.g. tidal effects) on the regional bio-optical characteristics. Regional CDOM ( $a_{\text{CDOM}}(412)$ ) and CDOM spectral slope in the UV,  $S_{275-295}$ ), DOC and  $p\text{CO}_2$  inversion algorithms were developed.  $a_{\text{CDOM}}(412)$  and  $S_{275-295}$  empirical formulations based on a multiband linear relationship ( $N = 100$ ,  $R^2 = 0.67$ ,  $p < 0.05$ ) and a nonlinear relationship ( $N = 100$ ,  $R^2 = 0.83$ ,  $p < 0.05$ ), respectively, were first developed. The DOC retrieval from  $a_{\text{CDOM}}(412)$  in the LAR has been shown to be relatively complex relying on the specific consideration of the seasonal pattern in the algorithm definition (distinction between RW and the other seasons).  $p\text{CO}_2$  was satisfactorily retrieved from a unique algorithm using CDOM and temperature as input parameters ( $N = 69$ ,  $R^2 = 0.80$ ,  $p < 0.05$ ). The models developed here for estimating  $a_{\text{CDOM}}(412)$ ,  $S_{275-295}$ , DOC and  $p\text{CO}_2$  were applied on Medium Resolution Imaging

Spectrometer (MERIS) seasonal composite images for the years of 2010-2011 to illustrate the spatiotemporal dynamics of the carbon contents in the Amazon waters. Amazon River was found to represent a source of carbon during all seasons, with the highest (lowest) carbon export during the RW (LW). The intra-seasonal variability underlines the strong dynamics of the transition areas between the river and oceanic waters. In the ARP,  $p\text{CO}_2$  was satisfactorily retrieved using SSS and SST as proxies ( $N = 76$ ,  $R^2 = 0.74$ ,  $p < 0.05$ ) and the model was applied on Soil Moisture and Ocean Salinity (SMOS) images for the years of 2010-2014. The analysis of SMOS-based  $p\text{CO}_2$  maps has illustrated the impact of the hydrological pattern on inter and intra-annual  $p\text{CO}_2$  variability. The ARP during the RW and HW seasons was generally representing a net source of  $\text{CO}_2$ . Conversely, during the FW and LW seasons, the ARP was a net sink of  $\text{CO}_2$ . The latter results restricted carbon sink area when compared to previous observations and net source of  $\text{CO}_2$  (during some periods of the year) are particularly original. This study emphasized the crucial need of additional in situ information (especially in the river to ocean transition area) for refining and better validating the models developed in this study and thus obtain a better insight into the understanding of the role of the Amazon River Continuum on the global carbon budget. The methods here proposed to assess the carbon content in the Amazon River continuum might be potentially applied to other large river systems, especially over tropical areas.

Keywords: Amazon River continuum. Biogeochemical parameters. Bio-optical properties. CDOM. Carbon budget. Water colour remote sensing.

**AVALIAÇÃO DA VARIABILIDADE ESPAÇO-TEMPORAL DOS PARÂMETROS ÓPTICOS E  
BIOGEOQUÍMICOS NA REGIÃO DO BAIXO AMAZONAS E DAS FRAÇÕES DE CARBONO  
NO CONTINUUM DO RIO AMAZONAS UTILIZANDO DADOS IN SITU E DE  
SENSORIAMENTO REMOTO**

**RESUMO**

O continuum do Rio Amazonas é uma região determinante no balanço de carbono global, mas sua extensão geográfica dificulta sua observação in situ. Considerando as características de alta resolução temporal e cobertura sinóptica, o sensoriamento remoto da cor da água (SRCA) representa uma ferramenta importante para monitorar a distribuição e variabilidade das frações de carbono e outros parâmetros biogeoquímicos nas águas amazônicas. Entretanto, a eficácia dos produtos gerados por SRCA para estudar a dinâmica biogeoquímica de um sistema aquático, depende da acurácia e precisão para representar as propriedades bio-ópticas da área investigada. Este trabalho foi desenvolvido no continuum do Baixo Rio Amazonas, onde uma descrição abrangente da variabilidade espaço-temporal de dados radiométricos, bio-ópticos e biogeoquímicos foi realizada com o objetivo de mapear as frações de carbono por SRCA. Na região do Baixo Amazonas (RBA), foram feitas amostragens in situ de reflectância de sensoriamento remoto, parâmetros bio-ópticos como os coeficientes de absorção pela matéria orgânica colorida dissolvida ( $a_{CDOM}$ ), material particulado total, fitoplâncton e partículas não-algais ( $a_{nap}$ ), e parâmetros biogeoquímicos como o material particulado em suspensão (SPM), concentração de clorofila-*a*, concentração de carbono orgânico dissolvido (DOC), e pressão parcial do dióxido de carbono ( $pCO_2$ ) para todas as estações hidrológicas - enchente, cheia, vazante e baixa, durante o período de 2014-2017. Na pluma do Rio Amazonas (PRA), dados in situ de  $pCO_2$ , salinidade da superfície do mar (SSS) e temperatura da superfície do mar (SST) foram adquiridos durante as estações de cheia, vazante e baixa durante os anos de 2010-2012. As características bio-ópticas descritas neste trabalho permitiram uma clara distinção entre o corpo de água principal do Rio Amazonas, dominado por NAP e CDOM, e os tributários de águas claras e dominados por CDOM. A análise da variabilidade espaço-temporal das propriedades bio-ópticas evidenciou: 1) o impacto da diluição dos parâmetros biogeoquímicos causados pela contribuição dos tributários assim como os processos de degradação do DOM no curso do Rio Amazonas; 2) a homogeneidade das características bio-ópticas durante as estações hidrológicas de cheia, vazante e baixa, em contraste com a estação da enchente (característica predominante do SPM); 3) a vulnerabilidade das águas amazônicas às condições hidrológicas excepcionais; 4) a pouca influência de processos de menor escala (por exemplo,

efeito de maré) nas características bio-ópticas regionais. Foram desenvolvidos algoritmos de inversão regionais de CDOM, ( $a_{\text{CDOM}}(412)$  e da inclinação da curva no intervalo do UV,  $S_{275-295}$ ), DOC e  $p\text{CO}_2$ . Primeiro foram desenvolvidas formulações empíricas de  $a_{\text{CDOM}}(412)$  ( $N = 100$ ,  $R^2 = 0.67$ ,  $p < 0.05$ ) e  $S_{275-295}$  ( $N = 100$ ,  $R^2 = 0.83$ ,  $p < 0.05$ ), baseados em modelo linear multivariado e não linear, respectivamente. Devido a diferentes padrões sazonais de DOC (clara distinção da enchente em relação às demais), sua estimativa foi particularmente complexa. A  $p\text{CO}_2$  foi estimada satisfatoriamente a partir de uma relação multivariada usando CDOM e temperatura ( $N = 69$ ,  $R^2 = 0.80$ ,  $p < 0.05$ ). Os modelos desenvolvidos para estimar  $a_{\text{CDOM}}(412)$ ,  $S_{275-295}$ , DOC e  $p\text{CO}_2$ , foram aplicados em imagens sazonais do sensor orbital *Medium Resolution Imaging Spectrometer* (MERIS) para os anos de 2010-2011 para demonstrar a dinâmica das frações de carbono nas águas amazônicas. O Rio Amazonas foi fonte de carbono durante todas as estações com a maior (menor) emissão de carbono durante a cheia (baixa). A variabilidade intra-sazonal destaca a forte dinâmica em áreas de transição entre águas de rio e oceano. Na PRA, a  $p\text{CO}_2$  foi satisfatoriamente estimada a partir de uma relação multivariada usando SSS e SST ( $N = 76$ ,  $R^2 = 0.74$ ,  $p < 0.05$ ) e o modelo foi aplicado em dados do sensor *Soil Moisture and Ocean Salinity* (SMOS) para os anos de 2010-2014. A análise dos mapas da  $p\text{CO}_2$ -SMOS evidenciou o impacto do padrão hidrológico na variabilidade inter e intra-anual na  $p\text{CO}_2$ . Em geral, a PRA durante as estações de enchente e cheia atuou como uma fonte de  $\text{CO}_2$ , enquanto que durante as estações de vazante e baixa se comportou como um sumidouro de  $\text{CO}_2$ . Os resultados aqui apresentados demonstram que a PRA sequestra menos carbono do que se presume atualmente e que inclusive, pode também agir como emissor de  $\text{CO}_2$  durante alguns períodos do ano. Este estudo enfatiza a necessidade de se obter informações adicionais in situ (principalmente na área de transição entre o rio e o oceano) para refinar e melhorar a validação dos modelos aqui desenvolvidos e assim obter uma melhor compreensão do papel do continuum do Rio Amazonas no balanço global de carbono. Os métodos propostos por este estudo para estimar as frações de carbono no continuum do Rio Amazonas tem potencial para aplicação em outros grandes rios globais, especialmente em regiões tropicais.

Palavras-chave: Continuum do Rio Amazonas. Parâmetros biogeoquímicos. Propriedades bio-ópticas. CDOM. Balanço de carbono. Sensoriamento remoto da cor da água.

## LIST OF FIGURES

Figure 2.1 - Fractions of aquatic dissolved organic matter. ....	10
Figure 2.2 - A) Absorption spectra ( $a_{CDOM}$ ) of coloured dissolved organic matter (CDOM) for different types of water. B) Estimates of the exponential slope parameter for different types of water using nonlinear fitting over the wavelength interval 320-400. ....	13
Figure 2.3 - DOM composition as a relative percentage bar of humic organic matter (yellow), iDOM (blue), and other minor compounds (green). ....	25
Figure 3.1 - Flowchart of the main activities: remote sensing and in situ data collection, processing and analysis. ....	32
Figure 3.2 - TROCAS campaigns (T1-T6) during the study period (2014-2017). ....	35
Figure 3.3 - Study area showing the in situ sampling oceanographic routes and the sampling stations during 2010-2012. ....	37
Figure 3.4 - Average of the seasonal water discharge for TROCAS period (2014-2017). ....	38
Figure 3.5 - B/M Mirage used during all TROCAS cruises (2014-2017). ....	39
Figure 3.6 - Discharge of the years covered in this study (2010-2014) of the Amazon River. ....	42
Figure 3.7 - Sun and sensor geometry used in field measurements. ....	44
Figure 3.8 - Field measurements during TROCAS campaigns. ....	49
Figure 4.1 - Average $a_{phy}$ and standard deviation spectrum for: A) Amazon River and, B) CW rivers. ....	65
Figure 4.2 - Correlation between chl <sub>a</sub> and: A) $a_{phy}(443)$ ; B) $a_{phy}(680)$ , for the Lower Amazon. ....	66
Figure 4.3 - Scatterplot of $a_p(443)$ as a function of SPM. ....	68
Figure 4.4 - Measured $R_{rs}$ (A) not normalized and (B) normalized for the Lower Amazon region. ....	71
Figure 4.5 - Average normalized spectra resultant from the K-means clustering analysis of the Lower Amazon region. ....	72
Figure 4.6 - Spatial distribution of bio-optical variability along the Amazon mainstream. ....	76
Figure 4.7 - Bathymetry and velocity profile of the Amazon River at Óbidos, Almeirim, Macapá South and Macapá North channels. ....	79
Figure 4.8 - Spatial distribution of bio-optical variability across the Amazon River channel at three sampling stations. ....	80
Figure 4.9 - River discharge and tidal variability of radiometric and bio-optical properties. ....	83

Figure 5.1 - Spatial distribution of biogeochemical parameters along the Amazon mainstream.....	97
Figure 5.2 - Direct relationship between $a_{\text{CDOM}}(412)$ and [DOC].....	99
Figure 5.3 - Relationship between $S_{275-295}$ and $a^*_{\text{CDOM}}(412)$ for the Lower Amazon region.....	101
Figure 5.4 - Relationship between $a_{\text{CDOM}}(412)$ and $S_{275-295}$ for all sampling campaigns (N = 80, $R^2 = 0.85$ , $p < 0.05$ ).....	104
Figure 5.5 - Estimative of $p\text{CO}_2$ in the Lower Amazon region. ....	105
Figure 5.6 - Estimative of $p\text{CO}_2$ for different sampling seasons, clearwater and Amazon River. ....	107
Figure 6.1 - Estimative of $a_{\text{CDOM}}$ in the Lower Amazon region. ....	118
Figure 6.2 - Estimative of $S_{275-295}$ in the Lower Amazon region.....	120
Figure 6.3 - Lower Amazon transitional water seasonal MERIS composites illustrating the distribution of: A) $a_{\text{CDOM}}(412)$ ( $\text{m}^{-1}$ ); B) $S_{275-295}$ ( $\text{nm}^{-1}$ ); C) DOC concentration ( $\mu\text{mol L}^{-1}$ ); D) $p\text{CO}_2$ ( $\mu\text{atm}$ ) in 2010 and 2011. ....	122
Figure 6.4 - Average and standard deviation of $a_{\text{CDOM}}(412)$ ( $\text{m}^{-1}$ ), $S_{275-295}$ ( $\text{nm}^{-1}$ ), DOC concentration ( $\mu\text{mol L}^{-1}$ ) and $p\text{CO}_2$ ( $\mu\text{atm}$ ) for the extracted area of the Macapá south (MSC) and Macapá north (MNC) channel of the Amazon River and Tocantins River (TO). ....	125
Figure 6.5 - Coefficient of variation (%) for $a_{\text{CDOM}}(412)$ , $S_{275-295}$ , DOC and $p\text{CO}_2$ by hydrological season: A) 2010 and; B) 2011. ....	129
Figure 7.1 - SMOS 3 months composite products of: A) Sea Surface Salinity and B) Sea Surface Temperature for the Western Tropical North Atlantic, according to the discharge season for the years of 2010-2014. ....	139
Figure 7.2 - Computed area for the Amazon River Plume by discharge season during 2010-2014.....	142
Figure 7.3 - Relationships of in situ $p\text{CO}_2$ , SSS and SST in the Amazon River plume. ..	143
Figure 7.4 - Linear relationship between in situ and SMOS parameters in the Amazon River plume.....	146
Figure 7.5 - Estimative of $p\text{CO}_2$ using SMOS in the Amazon River plume and Western Tropical North Atlantic. ....	148
Figure 7.6 - Estimated- $p\text{CO}_2$ for the Western Tropical North Atlantic area using SMOS products according to the discharge season for the years of 2010-2014.....	149
Figure 7.7 - Sea-air $\text{CO}_2$ flux ( $\mu\text{mol m}^2 \text{s}^{-1}$ ) estimated for the Western Tropical North Atlantic area with SMOS products according to the discharge season for the years of 2010-2014.....	157
Figure 7.8 - Average of all sea-air $\text{CO}_2$ flux for the Amazon River Plume area with SMOS resolution of $0.5^\circ$ according to the discharge season for the years of 2010-2014.....	158

Figure A.1 - Coefficients of determination for the nonlinear relationship between selected wavelengths from in situ $R_{rs}$ and SPM. ....	207
Figure A.2 - Estimated suspended particle matter as a function of $p_w(761)$ for Amazon and clearwater rivers using Lower Amazon coefficients and Nechad et al. (2010) – N10 coefficients. ....	209

## LIST OF TABLES

Table 2.1 - Collection of band ratios from empirical algorithms proposed on the literature for retrieve CDOM in ocean, coastal and inland waters. ....	19
Table 3.1 - In situ and remote sensing data used to assess the carbon content at the Lower Amazon River (TROCAS campaign, 2014-2017) and at the Amazon River plume (ANACONDAS campaign, 2010-2012).....	30
Table 3.2 - Dates of TROCAS campaigns during the years of 2014-2017 and the respective discharge river season. ....	41
Table 3.3 - Dates of the ANACONDAS oceanographic cruises at the Amazon River plume during the years of 2010-2012 and the respective discharge season. ....	41
Table 4.1 - Total number of in situ data gathered during the years of 2014-2017.....	59
Table 4.2 - Bio-optical characteristics of Amazon River and Clearwater rivers. ....	62
Table 4.3 - Absorption budget of the Amazon River (Am) and clearwater rivers (CW) for the seasons: Rising water (RW), High water (HW), Falling water (FW) and Low water (LW). SD – Standard Deviation; CV - Coefficient of Variation. ....	70
Table 4.4 - Bio-optical characteristics of the four optical water types for Lower Amazon. ....	73
Table 4.5 - Coefficients of variation of $a_{CDOM}(443)$ , SPM, chl <i>a</i> and $R_{rs}(761)$ along the Amazon River mainstream, during the different seasons: High Water (HW), Low water (LW), Falling water (FW) and Rising Water (RW). ....	77
Table 4.6 - Coefficients of variation of $a_{CDOM}(443)$ , $S_{275-295}$ , $a_p(443)$ , $S_{p400-800}$ , SPM, chl <i>a</i> and $R_{rs}(761)$ along the Amazon River mainstream (considering all hydrological seasons together).....	78
Table 4.7 - Coefficients of variation of chl <i>a</i> , $a_{CDOM}(443)$ and SPM for the margins along the mainstream Amazon River during different discharge seasons. ....	81
Table 4.8 - Coefficients of variation of $a_{CDOM}(443)$ , SPM and $R_{rs}(671)$ according to tidal cycle. ....	84
Table 5.1 - Total of in situ data for the campaigns during the years of 2014-2017.....	90
Table 5.2 - General statistics for clearwater (CW) and Amazon River stations considering all sampling periods (2014-2017). ....	91
Table 5.3 - Average of parameters for each sampling campaign for the clearwaters (CW) and Amazon River (Am) samples.....	93
Table 5.4 - Expressions and coefficients for the relationship $a^*_{CDOM}(412)$ vs $S_{275-295}$ , $S_{275-295}$ vs $a_{CDOM}(412)$ and $a_{CDOM}(412)$ vs DOC. ....	103
Table 5.5 - Simple regression models describing the relationship of $pCO_2$ and CDOM, temperature (T) and chl <i>a</i> at the Lower Amazon. ....	106



Table 6.1 - Empirical algorithms for estimating CDOM with the coefficients calibrated for the Lower Amazon region.....	116
Table 6.2 - Average and standard deviation ( $\pm$ ) of $a_{\text{CDOM}}(412)$ ( $\text{m}^{-1}$ ), $S_{275-295}$ ( $\text{nm}^{-1}$ ), DOC concentration ( $\mu\text{mol L}^{-1}$ ) and $p\text{CO}_2$ ( $\mu\text{atm}$ ) measured at the Amazon's River mouth by in situ sampling and MERIS images extracted samples, for comparison.....	127
Table 7.1 - Statistics for the SSS (psu) at the Amazon River Plume. ....	140
Table 7.2 - Statistics for the SST ( $^{\circ}\text{C}$ ) at the Amazon River Plume.....	141
Table 7.3 - General statistics of in situ $p\text{CO}_2$ sampled during the three oceanographic cruises (2010-2012). ....	144
Table 7.4 - General statistics of the variables used to develop the model for the Amazon River Plume, before and after averaging to match the SMOS spatial resolution of $0.5^{\circ}$ . ....	145
Table 7.5 - Statistics for the estimated $p\text{CO}_2$ ( $\mu\text{atm}$ ) for the Amazon River Plume. ....	151
Table 7.6 - Sensitivity index for each coefficient of the model, in the interval of $26-30^{\circ}\text{C}$ .....	152
Table 7.7 - Standard values relative to the higher sensitivity index (%) for each coefficient of the model, in the interval of $26-30^{\circ}\text{C}$ .....	153
Table 7.8 - Statistics for the Sea-air $\text{CO}_2$ flux ( $\mu\text{mol m}^2 \text{s}^{-1}$ ) for the Amazon River Plume. ....	155
Table 7.9 - Statistics for the $\text{CO}_2$ flux ( $\text{Tg C y}^{-1}$ ) for the Amazon River Plume. ....	160

## LIST OF ABBREVIATIONS

ALI	Advanced Land Imager
ANA	Brazilian National Water Agency
ANACONDAS	Amazon Influence on the Atlantic: Carbon export from Nitrogen fixation by Diatom Symbiosis
ANN	Artificial Neural Network
AOP	Apparent Optical Properties
ARP	Amazon River Plume
ASTER	Advanced Spaceborne Thermal Emission and Reflection Radiometer
B95	Bricaud et al., 1995 model
Bias	Mean Relative Difference
CDM	Coloured Detrital Matter
CDOM	Coloured Dissolved Organic Matter
chl <sub>a</sub>	Chlorophyll-a concentration
CMDL	Climate Monitoring and Diagnostics Laboratory
CO <sub>2</sub>	Carbon Dioxide
CV	Coefficient of Variation
CW	Clearwater
DMSO	Dimethyl Sulfoxide
DOC	Dissolved Organic Carbon
DOM	Dissolved Organic Matter
ENSO	El Niño Southern Oscillation
ESRL	Earth System Research Laboratory
ETM+	Landsat 7 Enhanced Thematic Mapper Plus
FW	Falling Water Season
GSM	Garver-Siegel-Maritorena Model
HW	High Water Season
iDOM	Invisible Dissolved Organic Matter
IOP	Inherent Optical Properties
LI-COR	Non-Dispersive Infrared CO <sub>2</sub> Gas Analyzer
LOAC	Land-to-Ocean Aquatic Continuum
LUT	Spectral Matching Look-Up-Table
LW	Low Water Season
M15	Martinez et al., 2015 model
MERIS	Medium Resolution Imaging Spectrometer
MIM	Matrix Inversion Method
MNC	Macapá North Channel
MODIS	Moderate Resolution Imaging Spectroradiometer
MRAD	Mean Relative Absolute Difference

MSC	Macapá South Channel
MSI	Sentinel 2 Multi-Spectral Instrument
N10	Nechad et al., 2010 model
NAP	Non-Algal Particles
NASA	National Aeronautics and Space Administration
NIR	Near-Infrared
NOAA	National Oceanic and Atmospheric Administration
OCTS	Ocean Color Temperature Sensor
OCW	Optically Complex Waters
OLCI	Sentinel 3 Ocean and Land Colour Instrument
OLI	Landsat 8 Operational Land Imager
OM	Organic Matter
OSC	Optically Significant Constituents
OWT	Optical Water Types
$p\text{CO}_2$	Partial Pressure of Carbon Dioxide
QAA	Quasi-Analytical Algorithm
RMSE	Root Mean Square Error
RTE	Radiative Transfer Equation
RW	Rising Water Season
SA	Sensitivity Analysis
SD	Standard Deviation
SeaDAS	SeaWiFS Data Analysis System Software
SeaWiFS	Sea-Viewing Wide Field-of-View Sensor
SIOPs	Specific Inherent Optical Properties
SMOS	Soil Moisture and Ocean Salinity
SPM	Suspendend Particulate Matter
SSS	Sea Surface Salinity
SST	Sea Surface Temperature
TM	Landsat Thematic Mapper 5
TO	Tocantins River
T-R	Transmittance-Reflectance quantitative Method
TROCAS	Net Ecosystem Exchange of the Lower Amazon River – from Land to the Ocean and Atmosphere
UV	Ultraviolet
VIIRS	Visible Infrared Imaging Radiometer Suite
WTNA	Western Tropical North Atlantic

## LIST OF SYMBOLS

$\lambda$	wavelength
$a$	total absorption
$a^*_{\text{CDOM}}$	DOC specific coefficient absorption
$a_{\text{CDOM}}$	absorption coefficient of CDOM
$a_{\text{nap}}$	absorption coefficient of NAP
$a_{\text{p}}$	absorption coefficient of total particles
$a_{\text{phy}}$	absorption coefficient of phytoplankton
$a_{\text{w}}$	absorption coefficient of pure water
$b$	scattering coefficient
$b_b$	backscattering coefficient
$b_{\text{CDOM}}$	scattering coefficient of CDOM
$b_{\text{nap}}$	scattering coefficient of NAP
$b_{\text{phy}}$	scattering coefficient of phytoplankton
$E_d$	downwelling irradiance
$E_u$	upwelling irradiance
$fc$	laboratory correction factor
$K_d$	downwelling attenuation coefficient
$L_g$	radiance from a reference panel
$L_{\text{sky}}$	water surface reflected sky radiance
$L_u$	upwelling radiance
$L_w(\lambda)$	water leaving radiance
$Q$	ratio of upwelling irradiance and upwelling radiance
$R$	irradiance reflectance
$R^2$	coefficient of determination
$R_{\text{rs}}$	Remote Sensing Reflectance
$S_{\text{CDOM}}$	slope of $a_{\text{CDOM}}$
$S_{\text{nap}}$	slope of $a_{\text{nap}}$
$S_{\text{p}}$	slope of $a_{\text{p}}$
$S_{\text{R}}$	slope ratio
$\rho_{\text{air-river}}$	sky glint correction coefficient at the air-sea interface



## CONTENTS

1	INTRODUCTION .....	1
1.2	Objectives .....	5
1.2.1	General .....	5
1.2.2	Specific.....	5
1.3	Document structure .....	6
2	THEORETICAL BACKGROUND .....	9
2.1	Dissolved organic matter .....	9
2.2	Dissolved organic carbon .....	10
2.3	Coloured dissolved organic matter .....	11
2.4	Partial pressure of carbon dioxide .....	14
2.5	Optical significant constituents.....	15
2.6	Inherent and apparent optical properties .....	16
2.7	Water colour models to assess CDOM.....	18
2.8	Remote sensing of carbon content .....	23
2.8.1	DOC.....	23
2.8.2	$p\text{CO}_2$ .....	25
3	MATERIALS AND METHODS .....	29
3.1	Overview .....	29
3.2	Study area.....	32
3.2.1	Lower Amazon.....	32
3.2.2	Amazon River Plume .....	35
3.3	Extreme climate events during the campaigns.....	37
3.3.1	TROCAS.....	37
3.3.2	ANACONDAS.....	38
3.4	Cruise description.....	39
3.4.1	TROCAS.....	39
3.4.2	ANACONDAS.....	41
3.5	In situ data.....	43
3.5.1	TROCAS.....	43

3.5.2	ANACONDAS.....	49
3.6	Quality control.....	50
3.7	Remote sensing data .....	50
3.7.1	Medium Resolution Imaging Spectrometer .....	50
3.7.2	Soil Moisture and Ocean Salinity .....	51
3.8	Statistics .....	52
4	BIO-OPTICAL VARIABILITY OF THE LOWER AMAZON WATERS.....	55
4.1	Introduction.....	55
4.2	Materials and methods .....	58
4.2.1	In situ data.....	58
4.2.2	Classification of the in situ $R_{rs}$ spectra .....	60
4.3	Results and discussion.....	61
4.3.1	Bio-optical general characteristics of the Lower Amazon .....	61
4.3.2	Optical classification of the Lower Amazon waters .....	70
4.3.3	Bio-optical spatial-seasonal variability along the river .....	75
4.3.4	River transversal bio-optical variability.....	78
4.3.5	Tidal impact on the Amazon bio-optical variability .....	81
4.4	Final considerations .....	84
5	USING CDOM OPTICAL PROPERTIES FOR ESTIMATING DOC CONCENTRATIONS AND $pCO_2$ IN THE LOWER AMAZON RIVER .....	87
5.1	Introduction.....	87
5.2	Materials and methods .....	90
5.3	Results and discussion.....	90
5.3.1	Optical and biogeochemical variability of the Lower Amazon River and tributary waters.....	90
5.3.2	$a_{CDOM}(412)$ to DOC relationships.....	98
5.3.3	$a_{CDOM}(412)$ and $pCO_2$ relationships .....	104
5.4	Final considerations .....	109
6	EVALUATION OF CDOM EMPIRICAL ALGORITHMS AND CARBON CONTENT MAPPING USING MERIS IMAGES .....	111
6.1	Introduction.....	111

6.2	Material and methods.....	113
6.2.1	Empirical algorithms.....	113
6.2.2	Satellite-based carbon content maps .....	115
6.3	Results and discussion.....	115
6.3.1	CDOM optical properties empirical inversion algorithms performance.	115
6.3.2	Satellite-based carbon content maps .....	121
6.4	Final considerations .....	130
7	SEASONAL AND INTER-ANNUAL VARIABILITY OF CARBON DIOXIDE FLUXES IN THE AMAZON RIVER PLUME BASED ON SOIL MOISTURE AND OCEAN SALINITY SATELLITE DATA.....	133
7.1	Introduction.....	133
7.2	Materials and methods .....	135
7.2.1	$p\text{CO}_2$ predictive algorithm .....	135
7.2.2	Sea-air $\text{CO}_2$ flux.....	136
7.2.3	Sensitivity analysis.....	137
7.2.4	Amazon River Plume area .....	138
7.3	Results and discussion.....	138
7.3.1	Remote sensing SST and SSS variability .....	138
7.3.2	Correlation among measured parameters in the ARP and validation of modeled $p\text{CO}_2$ .....	142
7.3.3	Sensitivity analysis.....	152
7.3.4	Spatiotemporal distribution of $\text{CO}_2$ fluxes in the WTNA.....	154
7.3.5	Study limitations and future suggestions.....	162
7.4	Final considerations .....	164
8	CONCLUDING REMARKS AND RECOMMENDATIONS .....	167
	REFERENCES .....	171
	Appendix A .....	205
A.1	SPM regional algorithm.....	205



## 1 INTRODUCTION

Inland (e.g. rivers, estuaries and lakes) and marine waters (coastal and oceanic) are all components of an integrated system. The flow of the water, starting with rainfall and headwaters, carries particulate and dissolved materials from land to oceans driving the biogeochemical cycle of a suite of components including carbon (WARD et al., 2017; XENOPOULOUS et al., 2017; BILLEN et al., 1991). The understanding of the biogeochemical dynamics induced by the land-ocean exchanges is therefore crucial. However, despite this connectivity between inland and oceanic waters, most of biogeochemical studies focus on specific components, locations, where limnologists and oceanographers have still a limited (although increasing willing) exchange of information (XENOPOULOUS et al., 2017).

The importance of aquatic ecosystems in the land-to-ocean continuum has been first brought up by Vannote et al. (1980) with the River Continuum Concept. Since then, many conceptual models have been derived as the Flood-Pulse Concept (JUNK et al., 1989), Pulse Shunt Concept (RAYMOND et al., 2016), Land-Ocean Aquatic Continuum (LOAC) (BILLEN et al., 1991), Submarine Groundwater Discharge (MOORE et al., 2010), among others (XENOPOULOS et al., 2017). In summary, all concept models stand for the water physical-biogeochemical properties to be in constant change as transiting downstream further into the ocean, by the interaction with the landscape around, the processes related to the water itself, as well as due to the impact of weather and climate forcing.

Outside the limits of the river basin, the river plume is a major component that integrates distinct water masses. Freshwater river plumes have a substantial impact on the salinity, sea surface temperature, nutrients and carbon availability and primary production (MEDEIROS et al., 2016, 2015; WEBER et al., 2016; GOES et al., 2014; GRODSKY et al., 2014; COLES et al., 2013; MOLLERI et al., 2010; SUBRAMANIAM et al., 2008; COOLEY et al., 2007). The variability on those parameters has a direct influence

on the regional biota and an evident socio-economic relevance, as for example, for fishery (JOHNS et al., 2014). Furthermore, the river plume can also play a significant role on sea-air interaction as for example, acting at the intensification of hurricanes (GRODSKY et al., 2012; FIELD, 2007).

The water inland-ocean connectivity is even more evident when using remotely sensed observations such as satellite images, which has the advantage to capture the dynamic and heterogeneous nature of the surface waters. In situ sampling on the other hand, represents a considerable challenge for an effective and representative monitoring scheme considering the large distance among sampling stations and the usual punctual feature of the sampling (TYLER et al., 2016; PALMER et al., 2015). Nevertheless, in situ sampling obviously remains crucial being a required step for future validation and robust analysis of remote sensing observations.

The water bodies across the LOAC are usually optically complex waters (OCW), where optically significant constituents (OSC) covariate independently (SATHYENDRANATH, 2000). An increasing number of studies, dedicated to LOAC applications, has focused on the development of inversion algorithms needed to retrieve biogeochemical information from remote sensing data (e.g. HAN et al., 2016; MARTINEZ, et al., 2015). In inland waters, most of the current studies are focused on lakes, reservoirs and floodplains (SCHAFFER et al., 2017; ALCÂNTARA et al., 2016; WATANABE et al., 2016; BREZONIK et al., 2015; NOVO et al., 2006), while when moving toward the ocean, studies are mainly concentrated on coastal waters usually including estuarine and river plume data (e.g. HAN et al., 2016; LOISEL et al., 2014; RUDORFF et al., 2018; DOGLIOTTI et al., 2015). Relatively few studies specifically aim their attention on rivers (SANTOS et al., 2018; MARTINEZ et al., 2015; MONTANHER et al., 2014). This fact may be tied to some circumstances: i) the intrinsic transience of the river, with short-term changes of water properties; ii) the difficulty to capture the medium time-scale variability related to seasonality, often questioning the representativeness of the

samples; iii) the difficulty to access the river for sampling in some specific geographic areas.

A large part of remote sensing studies dealing with inland OCW are dedicated to the assessment of suspended particulate matter concentration (SPM) particularly in the perspective of further applications related to the study of sediment transport and geomorphological processes related to river/estuarine systems. Such SPM inversion algorithms are usually based on straightforward models using a single red or near infrared (NIR) reflectance wavelength (MARTINEZ et al., 2015; NECHAD et al., 2010). On the other hand, in coastal, river plume or even eutrophic inland waters, chlorophyll-*a* (chl*a*) retrieval is a common subject of interest considering that the characterization of phytoplankton dynamics is of high importance for studying aquatic ecosystem structure and functioning (LINS et al., 2017; LOISEL et al., 2017; WATANABE et al., 2015). Additionally, chl*a* is commonly used as an index of phytoplankton biomass in many studies (LOISEL et al., 2017; ZHOU et al., 2016; LI et al., 2013).

Compared to SPM and chl-*a*, retrieving coloured dissolved organic matter absorption properties (CDOM) of a water body from satellite observation can be very challenging (NELSON; SIEGEL et al., 2013; BRICAUD et al., 1981) in particular due to the similar absorption spectrum of CDOM and non-algal particles (NAP) (LEE et al., 2002; MARITORENA et al., 2002; GARVER; SIEGEL, 1997). An increase in CDOM loads within the water body increases the absorption and therefore decreases the signal of the water-leaving radiance. In the presence of high CDOM-low radiometric signal the increased impact of signal-to-noise issues also imply in the requirement of a high precision (e.g. high spectral resolution) remotely sensed radiometric signal for allowing an accurate retrieval of CDOM absorption (AURIN et al., 2012; MATTHEWS et al., 2011). This also induces the necessity to use effective atmospheric correction schemes, especially for radiometric measurements in the blue spectral domain, which is usually more indicated for CDOM retrieval (MANNINO et al., 2014). The estimation of the water radiometric information on these wavelengths is however, particularly

challenging, being more affected by the scattering of atmospheric aerosols (MOUW, 2015; ZHU et al., 2014; MATTHEWS et al., 2011).

Despite the interest of studying CDOM distribution per se (e.g. light availability in the water column and monitoring of the freshwater dispersion in coastal waters), another major interest of estimating CDOM from remote sensing observation stands in the strong link, especially in coastal and inland waters (e.g. KUTSER et al., 2016; VANTREPOTTE et al., 2015), between CDOM optical properties and bulk dissolved organic carbon (DOC) concentration. Among the numerous studies documenting the CDOM to DOC dependency from in situ observations, only a few deals with tropical areas especially in the southern hemisphere. Besides that, existing studies in the tropical areas are usually not representative of the natural variability of these ecosystems, being quite limited in terms of temporal and spatial coverage (MASSICOTE et al., 2017; WARD et al., 2017). However, the understanding of DOC dynamics in the LOAC represents a key issue for better constraining the actual role of these ecosystems in the global carbon budget.

The degradation of DOC and the subsequent release of carbon dioxide (CO<sub>2</sub>) to the atmosphere represent a major process driving the carbon cycle dynamics (WARD et al., 2013). Recent studies have emphasized the importance of this carbon source to the atmosphere in the lower reaches of the Amazon River, showing that the inclusion of the latter area in the global carbon budget increases in several fold the CO<sub>2</sub> emissions previously estimated (SAWAKUCHI et al., 2017; RICHEY et al., 2002). The Amazon River plume (ARP) is usually recognized as an area of net sink of carbon, associated with its high primary productivity rates occurring especially at the river plume border (SUBRAMANIAM et al., 2008; COOLEY et al., 2007). This apparent contrast between the Amazon River and the Amazon River plume, rises a major scientific question: where the transition between CO<sub>2</sub> supersaturated to undersaturated waters within the Amazon river system occurs?

The answer to this question suffers from current observation gaps between the fresh and saline waters. This lack of information, which represents a main issue for studying the carbon flux along the Amazon River continuum, is also noted for other large rivers worldwide. The current scarcity of information tends to induce an omission of these transition areas in the existing global carbon budget (WARD et al., 2017; XENOPOULOS et al., 2017). However, when including the inner waters as part of the ARP carbon fluxes estimates, CO<sub>2</sub> budgets changed from undersaturated to near equilibrium in the Western Tropical North Atlantic (WTNA) region (COOLEY et al., 2007; SUBRAMANIAN et al., 2008; IBANHEZ et al., 2016), emphasizing the importance of considering the carbon fluxes occurring in these transition systems.

In this general scientific context, two main statements can be raised: i) regional accurate remote sensing products can contribute to the understanding of the Amazon River's role on the CO<sub>2</sub> budget and; ii) regional accurate remote sensing products can provide wide spatiotemporal observations of the current gap to support future studies that will contribute to better answer questions about the CO<sub>2</sub> turnover.

## **1.2 Objectives**

### **1.2.1 General**

The general objective of the present work is to evaluate the potential use of remote sensing observations to retrieve the carbon content along the Lower Amazon continuum, considering the variability occurring over the different hydrological seasons.

### **1.2.2 Specific**

The specific objectives of the current study were to:

- Characterize the spatiotemporal variability of the optically significant constituents in the Lower Amazon.

- Assess the potential of CDOM for estimating DOC and partial pressure of CO<sub>2</sub> ( $p\text{CO}_2$ ) in the Lower Amazon region.
- Evaluate the performance of empirical algorithms to retrieve carbon contents from an original regional in situ data set and apply the best performing algorithms to map the spatial distribution of CDOM, DOC and  $p\text{CO}_2$  using MEduM Resolution Imaging Spectrometer data.

Estimate  $p\text{CO}_2$  and carbon fluxes at the Amazon River plume and generate maps of  $p\text{CO}_2$  and carbon fluxes distribution at the Amazon River plume, using Soil Moisture and Ocean Salinity data.

### **1.3 Document structure**

In the Introduction chapter, the core of the thesis is presented, including what was the motivation and what are the objectives that guided the development of this study.

The second chapter presents a theoretical background of concepts and basic foundations considered relevant for the analysis of the studies developed in the next chapters.

The third chapter presents the dataset used in the frame of this work, and describes the methodology performed in common to all development chapters, as data processing and analysis. Is worthy to note that, more specific methodologies are however, presented and discussed in each respective chapter, when required.

In the fourth chapter, the variability of the optical and biogeochemical parameters is discussed, regarding different spatiotemporal scales.

In the fifth chapter, the in situ carbon content is focused, and relationships between CDOM-DOC and CDOM- $p\text{CO}_2$  are proposed.

The sixth chapter consists on the retrieval of CDOM by remote sensing reflectance, testing different empirical formulations. The selected CDOM model (based on the best performance) and carbon content models developed on the previous fifth chapter, are applied on MEduM Resolution Imaging

Spectrometer images to assess the spatiotemporal variability on the Lower Amazon River.

The seventh chapter is focused on the Amazon River plume and a relationship between sea surface salinity in conjunction with sea surface temperature are proposed to estimate  $p\text{CO}_2$ . The proposed  $p\text{CO}_2$  model is applied on Soil Moisture and Ocean Salinity data to assess the spatiotemporal variability of  $p\text{CO}_2$  and carbon flux in the study region.

Finally, the eight chapter presents the main conclusions of this study and suggestions for future work.





## **2 THEORETICAL BACKGROUND**

### **2.1 Dissolved organic matter**

Terrestrial humic substances are the dominant contributor to the dissolved organic matter (DOM) pool in freshwaters. In addition to humic substances, a minor portion of DOM at non eutrophicated inland waters is leached from phytoplankton. The DOM derived from the phytoplankton is highly labile and promptly consumed by bacterial processes and usually doesn't persist in the environment for a long time compared with humic DOM (HANSEN et al., 2016).

Humic substances differ in size and complexity, varying between soluble and insoluble compounds. These compounds are divided into three main groups that are chemically similar but has different molecular weight: humin fractions (insoluble and black in colour), humic acids (alkaline soluble and dark brown to gray-black colour) and fulvic acid (alkaline and acid soluble, light yellow to yellow-brown in colour) (KIRK, 2011; STEVENSON, 1982) (Figure 2.1).

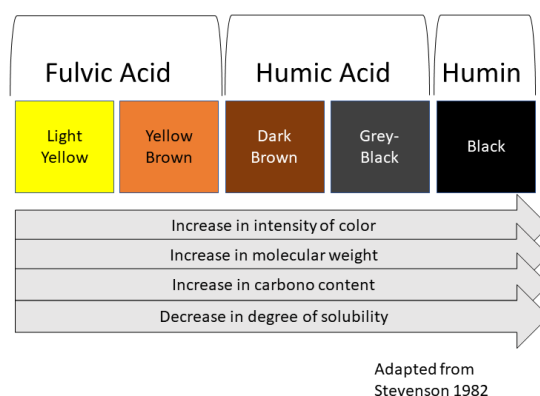
Humic and fulvic acids travel with river water to the ocean, while the humin fraction has higher molecular weight and it is usually adsorbed to mineral particles. Thus, large part of this fraction is settled below surface water by gravitational force and it is susceptible to hydrodynamic lift and drag, similar to what happens to the particulate organic matter (KIRK, 2011; BATTIN et al., 2008; LIBES, 2009).

In the Amazon basin, fulvic acids are the dominant fraction and has a meaningful signature of vascular plants called lignin. In general, its amount remains globally stable in time while the humic acids are more dependent of the River Negro discharge seasonality, the main source of DOM to the Amazon River (RODRÍGUEZ-ZUÑIGA et al., 2008; ERTEL et al., 1986; RICHEY et al., 1986). In the Lower Amazon, the Amazon River also receives DOM from clearwater rivers as Tapajós and Xingu as well as from floodplains (MOREIRA-TURCQ et al., 2003) increasing significantly the total of DOM in

the Amazon mainstream (increase of about 8% according to RAYMOND; SPENCER, 2015).

Microbial degradation and photochemical oxidation are the main processes responsible for the transformation of DOM into carbon dioxide (CO<sub>2</sub>) within inland waters (RAYMOND; SPENCER, 2015; WARD et al., 2013; RODRÍGUEZ-ZUÑIGA et al., 2008). In the Amazon River, the sediment rich water restrains the light penetration resulting in a restricted DOM photooxidation rate while the major DOM remineralization process is due to the bacterial respiration (WARD et al., 2016; WARD et al., 2013). Conversely, in clearwater rivers the lower velocity flow may allow a greater impact of photochemical reactions on DOM degradation (SPENCER et al., 2009; RODRÍGUEZ-ZUÑIGA et al., 2008).

Figure 2.1 - Fractions of aquatic dissolved organic matter.



Source: Author's production, adapted from Stevenson 1982.

## 2.2 Dissolved organic carbon

In rivers, dissolved organic carbon (DOC) is the major fraction of DOM (KLAVINS, 1997) and is formed by humic and fulvic acids among which the recalcitrant humic substances are responsible for the major part of DOC (60-90%) (RAYMOND; SPENCER et al., 2015; LEENHEER; CROUÉ, 2003; KLAVINS, 1997). Within the Amazon basin, autochthonous DOC released by phytoplankton exudation/degradation represents a

minor part of the DOC pool due to the presence of sediment-rich water and/or to a very acid water as the Negro River and other small tributaries, that limits phytoplankton growth. Conversely the relative contribution of this autochthonous source to the total DOC content is more significant in clearwater rivers (MOREIRA-TURCQ et al., 2003). The concentration of DOC in streams and rivers ranges from about 5 to 500  $\mu\text{mol L}^{-1}$  in most inland waters, being modulated by precipitation, drainage basin characteristics, as well as by anthropogenic activity (SACHSE et al., 2005; MULHOLLAND, 2003).

The final aim of assessing watershed DOC is to quantify the flux of reduced carbon to the ocean and understand the role of terrestrial inputs on the global carbon budget. Current studies estimate that the global fluvial export of DOC to the ocean ranges between 0.17 and 0.25  $\text{Pg C y}^{-1}$  (MAYORGA et al., 2010; BATTIN et al. 2008; CAUWET, 2002). In the Amazon basin, DOC accounted for 50% of total organic matter transported by the river and was the predominant organic matter (OM) type in most of the investigated tributaries. Furthermore, floodplain areas are also relevant sources of DOC to the Amazon River (RICHEY et al., 1990). In total, the Amazon River is assumed to account for about 12% of the global DOC flux (MOREIRA-TURCQ et al., 2003).

In spite of the clear scientific interest of assessing precisely the DOC flux from land to the ocean in order to better understand the global carbon cycle, current estimates are based on only restricted observations. This limitation due to a low temporal and spatial coverage are generally extrapolated over large scales being thus potentially affected by quite large uncertainties (RAYMOND; SPENCER et al., 2015).

### **2.3 Coloured dissolved organic matter**

Coloured dissolved organic matter (CDOM) represents the pigmented fraction of DOM that has a direct impact on light and nutrient availability in aquatic environments. CDOM is a complex combination of humic and fulvic acids (CARDER et al. 1989) that is quantified in practice by its absorption coefficient ( $a_{\text{CDOM}} \text{ m}^{-1}$ ). Particularly high in the

ultraviolet (UV) spectral domain, the CDOM absorption spectrum described as  $(\lambda)$  increases exponentially with decreasing wavelength (BRICAUD et al., 1981) (Figure 2.2.A). The latter absorption characteristics induce that the major impact of the CDOM on the water leaving radiance is observed at lower wavelengths of the visible spectrum.

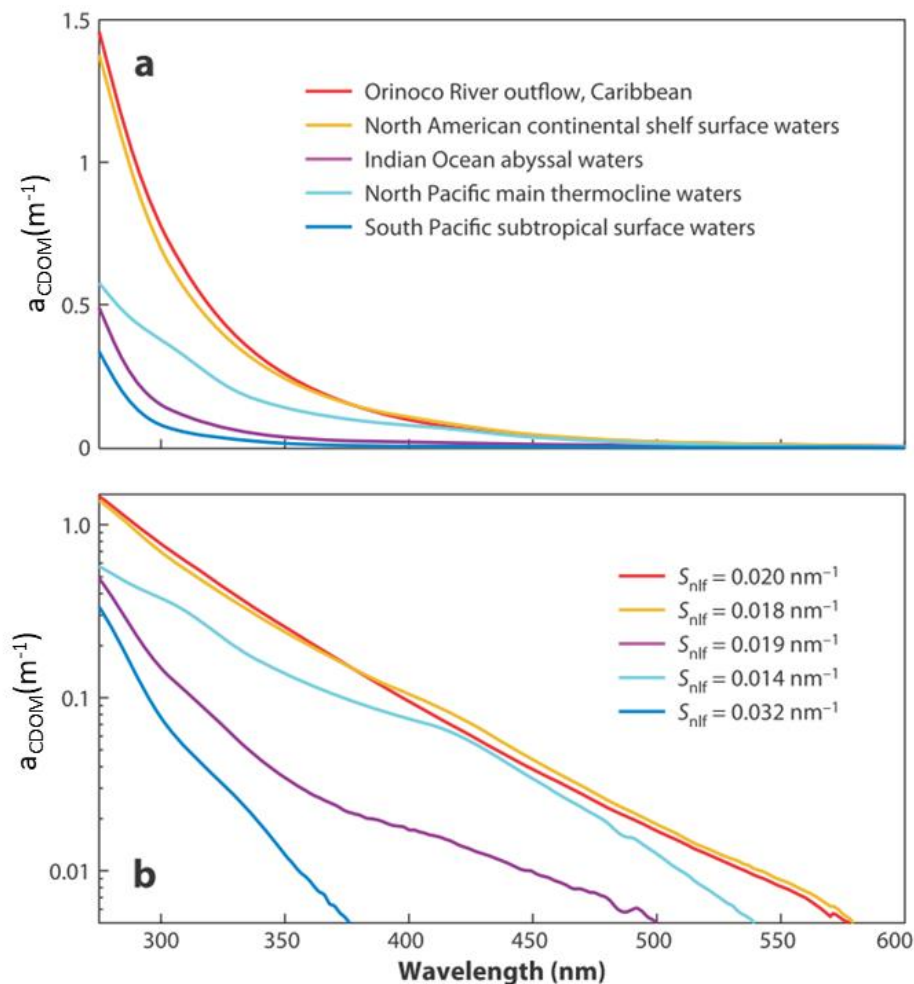
In addition to the CDOM quantitative assessment through its absorption coefficient at a discrete wavelength (usually in the UV or blue), the exponential slope -  $S$  ( $\text{nm}^{-1}$ ) of the CDOM absorption spectrum, provides insights into CDOM inner characteristics (e.g. chemistry, source and diagenesis) (Figure 2.2.B). Variation in CDOM spectral slope has been for instance related to the proportion of fulvic and humic acids (CARDER et al., 1989) while this optical parameter has been more recently also documented to represent a potential tracer of the terrestrial DOC in coastal waters (FICHOT; BENNER, 2012).

Nevertheless, the slope interval chosen for computing  $S$  has been subject of a variety of wavelengths choices according to the authors (NELSON; SIEGEL, 2013; HELMS et al., 2008; BRICAUD, 1981; CARDER et al., 1989), making difficult comparison among studies especially for studies dealing with UV-visible spectral slopes computed over a broad spectral window (TWARDOWSKI et al., 2004).

The use of a narrow wavelength range to calculate  $S$  has the advantage of minimizing the variation caused by dilution (BROWN 1977) and, currently, this approach has been preferred to those considering a broader wavelength range (VANTREPOTTE et al., 2015; FICHOT; BENNER, 2012; 2011). Furthermore, recent studies have showed that variation in the slope of the CDOM spectra in the UV domain namely between 275-295 nm ( $S_{275-295}$ ) can be related to the presence of dissolved lignin in coastal waters (FICHOT; BENNER, 2012) while the ratio of the CDOM spectral slopes ( $S_R$ ) computed over the spectral ranges 275-295 and 350-400 nm was found to be a good proxy for describing DOM molecular weight (MW) and photochemically induced shifts in the

molecular weight (HELMS et al., 2008). High values of  $S_{275-295}$  and  $S_R$  indicate a CDOM of lower MW. The great advantage of assessing CDOM variability, besides its potential link with DOC, is also to examine DOM composition. For example, the DOC flux may not vary in a watershed during a deforestation process, but the quality of DOM transported by the river may indicate land use and land cover changes (BERNARDES et al., 2004).

Figure 2.2 - A) Absorption spectra ( $a_{CDOM}$ ) of coloured dissolved organic matter (CDOM) for different types of water. B) Estimates of the exponential slope parameter for different types of water using nonlinear fitting over the wavelength interval 320-400.



Source: NELSON; SIEGEL et al., 2013.

## 2.4 Partial pressure of carbon dioxide

The continuous degradation of DOM through biological or photochemical processes contributes to an increase in the partial pressure of carbon dioxide ( $p\text{CO}_2$ ) above the equilibrium with the atmosphere. The supersaturation of  $\text{CO}_2$  leads to a gas evasion flux from freshwater to atmosphere (KOEHLER et al., 2014). A huge global dataset over lakes was analyzed and showed that the supersaturation of  $\text{CO}_2$  was related to the presence of DOC and independent of the temperature (SOBEK et al., 2005). Further studies have corroborated this analysis for boreal and temperate inland waters (LAPIERRE; DEL GIORGIO, 2012; LARSEN et al., 2011).

Nevertheless, when this analysis is performed over tropical regions, including Brazilian lakes at the Amazon Basin, the same  $p\text{CO}_2$ -DOC relationship could not be verified (PINHO et al., 2015; MAROTTA et al., 2010). The prior global analysis by Sobek et al., 2005 was considering a data set where tropical lakes were largely underrepresented ( $\leq 2\%$ ) due to the sparsity of such data in the literature, probably misleading the actual global validity of the corresponding results. In fact,  $p\text{CO}_2$  within Brazilian lakes did not show any correlation with DOC, while significant relationships were found between  $p\text{CO}_2$  and rainfall (FONTES et al., 2015; MAROTTA et al., 2010) or temperature data (MAROTTA et al. 2009a). In addition to rainfall and temperature, Kosten et al. (2010) used the ratio of chl $a$  to CDOM to estimate  $p\text{CO}_2$  for many Brazilian lakes.

Brazilian lakes and Amazonian rivers present an overall persistence of daily and annual  $\text{CO}_2$  outgassing (PINHO et al., 2015; MAROTTA et al., 2009b; RICHEY et al., 2002), although seasonal and spatial variability can be evidenced (RUDORFF et al., 2011). The  $\text{CO}_2$  outgassing is supported by an intense bacterial respiration (RICHEY et al., 2002) that can be driven by the effect of the temperature on the aquatic metabolism (MAROTTA et al., 2009) and enhanced by the organic matter and  $\text{CO}_2$  contribution of surrounding forest and floodplains (ABRIL et al., 2014; SAWAKUCHI et al., 2017; RAYMOND et al., 2013).

## 2.5 Optical significant constituents

The measured upwelling radiance from a water body is resultant of the inherent optical properties (IOPs) of its optically significant constituents (OSC), hence the bio-optical properties. Phytoplankton, non-algal particles (NAP) and CDOM are OSC that modulate the colour of the water through their inherent properties of absorption or scattering the light penetrating into the water body (PRIEUR; SATHYENDRANATH, 1981). Pristine studies aiming to retrieve bio-optical properties of the water from remote sensing observation were focused on oceanic waters, where phytoplankton and their related products are the dominant OSC (CARDER et al., 1991). Since then, sophisticated inverse models were developed for assessing with a satisfying accuracy a variety of bio-optical and biogeochemical products from radiometric measurements in oceanic waters showing a dominant impact of phytoplankton and phytoplankton derived products (MOREL; GENTILI, 2009; MARITORENA et al., 2002; LEE et al., 2002; CARDER et al., 1999; GARVER; SIEGEL, 1997).

Phytoplankton and non-algal particle absorption ( $a_{\text{phy}}$  and  $a_{\text{nap}}$ ) in ocean and coastal water were subject of diverse studies and are currently well or reasonably well understood (BRICAUD et al., 1995; BABIN et al., 2003; CIOTTI et al., 2006). Likewise,  $a_{\text{phy}}$  and  $a_{\text{nap}}$  relationships with chl $a$  (CHASE et al., 2013; CIOTTI et al., 2006; BRICAUD et al., 2004; 1998; 1995; BABIN et al., 2003) and SPM (BABIN et al., 2003) have been largely documented. In waters with higher sediment concentration, more effort has been made to relate  $a_{\text{nap}}$  and SPM, with inverse models to retrieve SPM from reflectance being the aim of many studies (HAN et al., 2016; MARTINEZ et al., 2015; SISWANTO et al., 2011). On the other hand, less is known about the relationship of  $a_{\text{phy}}$  and chl $a$  in highly turbid waters and further studies are required.

Many studies also aimed to retrieve and monitoring CDOM in optically complex waters by remote sensing, as well as using CDOM as a proxy to assess carbon content on those waters (e.g. KUTSER et al., 2015; VANTREPOTTE et al., 2015; ZHU et al., 2014).

The state of the art of these studies are more discussed on the following sections (see sections 2.2.7 and 2.2.8).

## 2.6 Inherent and apparent optical properties

The water colour is determined by the combined influence of scattering and absorption of the incident light by OSC as well as by pure water itself. One way of obtaining information of the OSC concentration in the water is to measure the ascending radiance ( $L_u$ ) which is subject to variations in the geometry of the incident light (solar zenith angle) as well as environmental conditions (e.g., cloud cover and surface wind speed) (MOBLEY, 1999). Considering its dependency on the geometry, the latter radiometric variable is referred as an apparent optical property (AOP) (LEE et al., 2005; LEE; DU, 2005; MOREL; MARITORENA, 2001) in opposition to absorption and scattering properties, which are referred as inherent optical properties (IOP) of the water. The absorption  $a(\lambda)$  and scattering  $b(\lambda)$  coefficients, determine the exponential rate of the radiant energy flux decay, by a defined optical path and by the incident radiant flux unit, during the processes of absorption and scattering, respectively (KIRK, 2011).

Among the scattered photons, those that are backscattered provides information about OSC present in the water column. The backscattering coefficient ( $b_b$ ) can be used as an index of particle bulk and is dependent of the particle size distribution, shape and composition (ULLOA et al., 1994).

Both scattering and absorption processes are additive and can be described as Equations 2.1 and 2.2:

$$a(\lambda) = a_w(\lambda) + a_{phy}(\lambda) + a_{CDOM}(\lambda) + a_{nap}(\lambda) \quad (2.1)$$

$$b(\lambda) = b_w(\lambda) + b_{phy}(\lambda) + b_{CDOM}(\lambda) + b_{nap}(\lambda) \quad (2.2)$$



where  $w$ ,  $phy$ ,  $CDOM$  and  $nap$  are pure water, phytoplankton, CDOM and non-algal particles, respectively.

The relationship between IOPs and AOPs can be established by the means of the Radiative Transfer Equation (RTE), which defines the water radiance distribution ( $L_w$ ) as a function of absorption and scattering. The irradiance reflectance is defined ( $R(\lambda)$ ) as the upwelling irradiance ( $E_u$ ) normalized by the downwelling irradiance ( $E_d$ ) just below the water surface, and it is related to the absorption and backscattering coefficients as defined by PREISONDORFER (1976) in Equation 2.3:

$$R(\lambda) = \frac{E_u(\lambda)}{E_d(\lambda)} = f(\lambda) \frac{b_b(\lambda)}{a(\lambda)} \quad (2.3)$$

where  $f$  is the parameter that relates the reflectance irradiance with the coefficient ratio of backscattering  $b_b(\lambda)$  and absorption  $a(\lambda)$  and is dependent of the sun geometry.

This relationship between IOP and AOP is important because it allows the development of algorithms that estimate the bio-optical properties from remote sensing observation of the water colour. The orbital remote sensing focused on the colour of the water measure the upwelling radiance and, therefore, the Equation 2.3 was modified to the ratio between the upwelling radiance ( $L_u$ ) and the downwelling irradiance ( $E_d$ ). This ratio is known as Remote Sensing Reflectance ( $R_{rs}$ ) (GORDON et al., 1988) and is defined as (Equation 2.4):

$$R_{rs}(\lambda) \equiv \frac{R(\lambda)}{Q(\lambda)} = \frac{L_u(\lambda)}{E_d(\lambda)} \cong \frac{f(\lambda)}{Q(\lambda)} \frac{b_b(\lambda)}{a(\lambda)} \quad (2.4)$$

where  $Q$  is the ratio of upwelling irradiance and the upwelling radiance ( $Q \equiv \frac{E_u}{L_u}$ ) and it is dependent of the sun geometry.

## **2.7 Water colour models to assess CDOM**

Most of the models that derive products from water colour can be divided into empirical or semi-analytical formulations. Empirical algorithms are simple or multiple regressions between the OSC of interest and the remote sensing reflectance (or reflectance ratios) at selected wavelengths. These algorithms can be linear or non-linear and requires less knowledge on the relationship of AOP and IOP. Because of the nature of the regression, empirical algorithms are only appropriate for water with similar characteristics to those for which it was created.

Several empirical algorithms have been developed to estimate CDOM from reflectance band ratios considering various levels of water turbidity and remote sensing sensors: Ocean Color Temperature Sensor (OCTS), Sea-Viewing Wide Field-of-View Sensor (SeaWiFS), Moderate Resolution Imaging Spectroradiometer (MODIS), Medium Resolution Imaging Spectrometer (MERIS), Landsat Thematic Mapper 5 (TM), Landsat 7 Enhanced Thematic Mapper Plus (ETM+), Landsat 8 Operational Land Imager (OLI), Advanced Land Imager (ALI), Visible Infrared Imaging Radiometer Suite (VIIRS), Sentinel 2 Multi-Spectral Instrument (MSI), Sentinel 3 Ocean and Land Colour Instrument (OLCI), are some of the orbital sensors used on the water colour studies. The band ratio is generally adjusted to the chosen sensor and can be separated in eight groups using the following radiometric bands: blue, green, red and NIR (Table 2.1).

Table 2.1 - Collection of band ratios from empirical algorithms proposed on the literature for retrieve CDOM in ocean, coastal and inland waters.

Band Ratio	R <sub>rs</sub> band (nm)	Sensor	Datasets/ Study sites	Reference
Blue/Green	443/510 (or 520)	SeaWiFS, OCTS	California Current	Kahru and Mitchell, 2001
	490/555	SeaWiFS, MODIS-Aqua	Coastal water	Tassan 1994; Mannino et al., 2008; Siswanto et al., 2011; Mannino et al., 2014
	412/555, 443/555	MODIS	Ocean waters	Carder et al., 2003
	443/555, 488/555, 667/555	MODIS	Coastal water	Carder et al., 2004
Green/Blue	565/483	Landsat TM and ETM+	Kolyma River, Siberia	Griffin et al., 2011
Red/Blue	670/490	SeaWiFS	NOMAD dataset, coastal and ocean waters	Tiwari et al., 2011
	667/488	MODIS	Northern Gulf of Mexico, influenced by Mississippi River	Schaeffer et al., 2015
	665/489	MERIS	New England, Middle Atlantic and Gulf Coast Estuaries USA	Keith et al., 2016
Blue/Red	412/670	SeaWiFS, MODIS-Aqua	Continental margin of the northeastern of U.S.	Mannino et al., 2014
Blue/NIR	483/830	Landsat TM	Minnesota Lakes, U.S.	Brezonik et al., 2005
	490/740	Sentinel 2 MSI	Inland waters	Brezonik et al., 2015

Green/Green	510/555 (or 560)	SeaWiFS; MERIS	Northern Gulf of Mexico, influenced by Mississippi River	D'Sa et al., 2006; Tehrani et al., 2013
Green/Red	560 /655	Landsat-8 OLI	Barataria Bay, Louisiana; Inland waters	Brezonik et al., 2015; Joshi et al., 2015
	565/660	ALI	Lakes in Sweden and Finland	Kutser et al., 2005
	510/670	---	Mississippi River Plume	Del Castillo; Miller, 2008
	570/655	---	Pomeranian lakes and Baltic sea	Ficek et al., 2011
	560/665	MERIS	Swedish lakes	Kutser et al., 2015
	551/671	VIIRS	Apalachicola Bay	Joshi et al., 2017
Green/NIR	510/753	Sentinel 3 OLCI	Inland waters	Brezonik et al., 2015

Source: Author's production

The semi-analytical algorithms are partly based on the radiative transfer equation, relating the  $R_{rs}$  to the IOP. It is expected that, since these algorithms are based on an optical closure, should outperform empirical algorithms when applied on different optical water types and are suitable for applications in a broader geographic area. However, semi-analytical algorithms still depend on empirical relationships (WANG et al., 2017; LOISEL et al., 2013; ODERMATT et al., 2012; CARDER et al., 1999; MOREL; GORDON, 1980) and they are susceptible to failure when not calibrated for specific optical characteristics. Likewise, the Matrix Inversion Method (MIM) uses semi-analytical approach but additionally needs the knowledge about the specific inherent optical properties (SIOPs). Because these parameters are site-specific, MIM are generally not effective for different optical water classes without in situ measurements

(BRANDO et al., 2012; CAMPBELL et al., 2010; ZHU et al., 2014). Other methods as spectral matching look-up-table (LUT) (MOBLEY et al., 2005) and artificial neural network (ANN) (JAMET et al., 2012; SCHILLER; DOERFFER, 1999) usually are time-consuming because they require a large set of training data to relate with the measured parameter (ZHU et al., 2014). Moreover, Kishino et al. (2005) had discussed the difficulty to retrieve CDOM by ANN using Advanced Spaceborne Thermal Emission and Reflection Radiometer (ASTER) data.

At oceanic waters, CDOM is responsible for 40-85% of total absorption at 440 nm and particulate matter contributes to 5-20% (NELSON et al., 1998). For this reason, they are measured as a single parameter called coloured detrital matter (CDM) where CDOM is determinant (LEE et al., 2002; MARITORENA et al., 2002; GARVER; SIEGEL, 1997). At optically complex waters, there is usually a greater contribution of CDOM and particulate matter, requiring a more precise estimative of the two optically significant constituents (LOISEL et al., 2014; MATSUOKA et al., 2013; ZHU et al., 2011).

The semi-analytical algorithms developed to retrieve the CDM and  $chl a$  products in oceanic regions such as the Garver-Siegel-Maritorena model (GSM) (MARITORENA et al., 2002; GARVER; SIEGEL, 1997) and the Quasi-Analytical Algorithm (QAA) (LEE et al., 2002) are reliable in the presence of the phytoplankton dominated with CDOM considered as phytoplankton sub product and low NAP levels. The application of these algorithms is however not directly adapted to optically complex waters. When these algorithms are used to estimate  $chl a$ , for example, on waters with high concentration of CDOM and/or SPM, they usually fail. To retrieve  $chl a$ , GSM and QAA uses the blue and green wavelengths where other OSC dominates. The higher absorption of CDOM at lower wavelengths, for example, may overestimate  $chl a$  (LE et al., 2013).

Further, the use of such semi analytical formulations also requires an additional step aiming to split CDM into CDOM and NAP which is in practice difficult to achieve (LEE et al., 2002; MARITORENA et al., 2002; GARVER; SIEGEL, 1997). Some works endeavored

to modify the QAA and GSM algorithms to retrieve the products  $a_{\text{phy}}$ ,  $a_{\text{CDOM}}$ , and  $a_p$  separately using satellite data acquired over rivers, reservoirs, estuaries and coastal regions (WATANABE et al., 2018; LI et al., 2017; WANG et al., 2017; DONG et al., 2013; MATSUOKA et al., 2013; ZHU; YU, 2013; ZHU et al., 2011). The success of these adaptation of QAA and GSM semi-analytical algorithms are based on the removal of  $a_p$  contribution from the CDM absorption using the backscattering coefficient. The backscattering coefficient is usually obtained for specific water conditions making the semi-analytical algorithms dependent upon empirical relationships to tune the algorithm.

Despite the reasonable performance of the adapted GSM algorithm, the algorithm worked better for oceanic than coastal waters where more data are available (MATSUOKA et al., 2013). Although the performance of the adapted QAA algorithm was satisfactory for a variety of rivers and estuaries waters, the amount of in situ data for these areas is still modest in face of ocean dataset and more data are required to strength the performance of such semi-analytical methods (ZHU et al., 2013).

Loisel et al. (2014) proposed a new semi-analytical algorithm to retrieve  $a_{\text{CDOM}}$  in contrasted coastal waters by relating  $a_{\text{CDOM}}$  with the vertical attenuation coefficient ( $K_d$ ) at 412 and 555 nm.  $K_d$  can be estimated from in situ downwelling irradiance vertical profile as well as from the inversion of water colour remote sensing measurements. Despite the good performance, the algorithm was developed for a certain range of  $a_{\text{CDOM}}$  and more data are required to calibrate the algorithm for new applications.

When comparing the performance of different algorithms applied in optically complex inland water, a global comprehension indicates an overestimation for low-CDOM water and underestimation for CDOM rich water. The QAA adapted version outperformed the other semi-analytical algorithms assessed by Zhu et al. (2014) and even the empirical algorithms when all the dataset is considered independent of the

$a_{CDOM}$  range. Nevertheless, the empirical algorithms had an indubitably better performance for considered CDOM rich water ( $a_{CDOM}(440) > 3.4 \text{ m}^{-1}$ ) (ZHU et al., 2014).

## **2.8 Remote sensing of carbon content**

### **2.8.1 DOC**

The water colour remote sensing can provide quantitative estimates of carbon content specifically when a relationship between CDOM and DOC, and/or CDOM and  $p\text{CO}_2$  is established. Numerous studies use CDOM as a proxy to assess the spatial distribution of DOC at coastal waters and then quantify the transport of terrestrial organic carbon to the sea (VANTREPOTTE et al., 2015; MATSUOKA et al., 2014; 2013; 2012; TEHRANI et al., 2013; DEL CASTILLO; MILLER, 2008; VODACEK et al., 1997) or to assess the DOM autochthonous production following a phytoplankton bloom (DANHIEZ et al., 2017). More recently, the interest of water colour community is turning toward inland waters and empirical algorithms has been developed to retrieve DOC with satisfying accuracy (BREZONIK et al., 2015; KUTSER et al., 2015; ZHU et al., 2014; GRIFFIN et al., 2011).

The CDOM-DOC relationship has been described as highly variable spatially and seasonally (VECCHIO et al., 2002) which is a drawback to predict DOC from a simple linear relationship. To overcome this limitation, alternative approaches to retrieve DOC concentrations have been proposed in coastal waters using relationships relating the CDOM spectral slope in the UV domain  $S_{275-295}$  to the CDOM to DOC ratio (VANTREPOTTE et al., 2015; FICHOT; BENNER, 2012; 2011).

At freshwaters and coastal dominated by riverine waters the possible assessment of DOC from CDOM is challenging, considering the numerous processes (e.g. different source of DOM, photodegradation, flocculation, microbial respiration) possibly acting on the relation between the optical and carbon content of DOM (BREZONIK et al., 2015; WARD et al., 2013; JIANG et al., 2012; LOISELLE et al., 2010; CHEN et al., 2004).

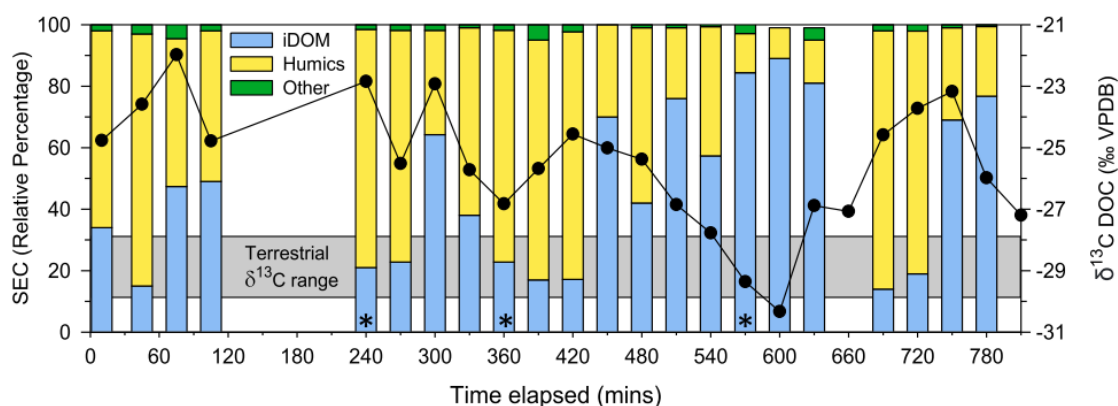
Nevertheless, on coastal waters, the dilution gradient observed supports the CDOM-DOC relationship (VANTREPOTTE et al., 2015) while on inland waters this dilution gradient is not observed.

Some possible causes of the CDOM-DOC decoupling have been discussed on the literature. One possible cause is the association of available iron on the water with DOM. The iron binds with DOM and can interfere on the biodegradation of the carbon bind (XIAO et al., 2016) as well as can affect the colour intensity of CDOM (BREZONIK et al., 2015; KOHLER et al., 2013; XIAO et al., 2013). Iron is also related to the photochemical flocculation of DOM (HELMS et al., 2013) that can lead to a non-conservative behavior of CDOM and DOC at coastal waters. In waters with high primary productivity, CDOM-DOC relationship can also collapse by the autochthonous production of DOM (DANHIEZ et al., 2017).

Another reason is that a fraction of DOC is uncoloured and therefore invisible (iDOM) from CDOM measurements. The proportion of iDOM to DOC can be variable (Figure 2.3) and have been related as a cause of the CDOM-DOC relationship failure in some coastal waters, highly polluted rivers and tropical rivers at specific seasons (COOK et al., 2017; LI et al., 2016; PEREIRA et al., 2014; CHEN et al., 2004; VODACEK et al., 1997). Therefore, when CDOM and DOC covary, or iDOM is constant in DOC, a good correlation CDOM-DOC can be established. However, this relationship can be weakened if an external factor influences this ratio (CHEN et al., 2004).



Figure 2.3 - DOM composition as a relative percentage bar of humic organic matter (yellow), iDOM (blue), and other minor compounds (green).



Source: PEREIRA et al., 2014.

Over the Amazon region, the seasonality (Dry-Wet) changes the carbon dynamics (JOHNSON et al., 2006a), and after a rainfall storm, a young and unprocessed DOC is transported from landscape to the water rapidly and in great amount (JOHNSON et al., 2006b). Recent studies have reported that the increase of iDOM as a response to rainfall events in tropical river is likely responsible for the decoupling between CDOM and DOC (PEREIRA et al., 2014).

## 2.8.2 $p\text{CO}_2$

Satellite based approaches to estimate  $p\text{CO}_2$  in oceanic and coastal waters have been increasingly used, while such studies are still very scarce for inland water applications (KUTSER et al., 2015). Estimates of  $p\text{CO}_2$  based on orbital sensor observation can provide a synoptic view of spatial scale  $p\text{CO}_2$  as well as innovative information about its temporal variation, complementing in situ observations and helping the understanding of  $\text{CO}_2$  flux dynamics. In this way, remote sensing can point out which areas are source or net sink of  $\text{CO}_2$ , and monitor impacts of climate and anthropogenic changes on the global carbon budget.

In coastal waters,  $p\text{CO}_2$  has been estimated using different approaches (LOHRENZ et al., 2018; IBÁÑHEZ et al., 2016; SONG et al., 2016; XU et al., 2016; BAI et al., 2015;

HALES et al., 2012; BORGES et al., 2010; TELSZEWSKI et al., 2009; ZHU et al., 2009; LOHRENZ; CAI, 2006; SARMA et al., 2006). Most of the studies found in the literature, estimate  $p\text{CO}_2$  from empirical relationships (LOHRENZ et al., 2018; XU et al., 2016; BORGES et al., 2010; ZHU et al., 2009; LOHRENZ; CAI, 2006; SARMA et al., 2006), but other approaches such as machine learning methods (HALES et al., 2012; TELSZEWSKI et al., 2009) and a mechanistic semi-analytical algorithm (SONG et al., 2016; BAI et al., 2015) were also recently proposed. Except for Kutser et al. (2015) that made a direct linear relationship between  $p\text{CO}_2$  and MERIS turbidity index, other authors used a combination of remote sensing products to develop the aforementioned algorithms. The most frequently used products are  $\text{chl}a$  (LOHRENZ et al., 2018; SONG et al., 2016; XU et al., 2016; BAI et al., 2015; HALES et al., 2012; BORGES et al., 2010; TELSZEWSKI et al., 2009; ZHU et al., 2009; LOHRENZ; CAI, 2006; SARMA et al., 2006), temperature (IBÁÑHEZ et al., 2016; SONG et al., 2016; XU et al., 2016; BAI et al., 2015; HALES et al., 2012; TELSZEWSKI et al., 2009; ZHU et al., 2009; LOHRENZ; CAI, 2006; SARMA et al., 2006) and salinity that can be diversely derived from CDOM (BAI et al., 2015; LOHRENZ; CAI, 2006), from a hydrodynamical model (BORGES et al., 2010) or estimated using microwave sensors such as Soil Moisture and Ocean Salinity (SMOS) (IBÁÑHEZ et al., 2016). Other products as wind (LOHRENZ et al., 2018; HALES et al., 2012), rain (IBÁÑHEZ et al., 2016), mixed layer depth (TELSZEWSKI et al., 2009), normalized fluorescence line height (LOHRENZ et al., 2018), detrital and dissolved absorption at 443 nm (LOHRENZ et al., 2018), diffuse attenuation coefficient at 531 nm (LOHRENZ et al., 2018) and  $R_{rs}$  at certain wavelengths (BAI et al., 2015) were also used in the frame of various studies.

The retrieval of water colour products in optically complex waters are a challenge as mentioned previously. The Amazon River and Amazon River plume can add an extra complexity due to the high turbidity of the water when compared to other coastal waters. A first issue is related in this case to the performance of the atmospheric correction (WANG et al., 2012; SHI; WANG, 2007). Further, high concentrations of suspended sediments have a high signal response in the NIR which could lead to an

erroneously classification of water pixels as clouds (leading to a great loss of information) when satellite data are processed using standard software, using open ocean colour as a default setting (LOISEL et al., 2013).

Finally, while the estimation from satellite observation of variables (such as  $chl\alpha$ ) used as a proxy for estimating  $pCO_2$  is now reliable for oceanic waters (MOREL; GENTILI, 2009; CARDER et al., 1999; GORDON; MOREL, 1983; MOREL; PRIEUR, 1977), the assessment of such biogeochemical products over very turbid waters is still challenging (GITELSON et al., 2008; DALL'OMO et al., 2005). Therefore, the use of a proxy such as  $chl\alpha$  or CDOM as part of a  $pCO_2$  algorithm can be a source of error in the  $pCO_2$  estimates if this optical complexity is not taken in account. This difficulty of using remote sensing products to estimate  $pCO_2$  in complex optical environment like river-influenced region, especially closer to the shore was for instance recently illustrated by Lohrenz et al. (2018).



### **3 MATERIALS AND METHODS**

This chapter provides a general characterization of the study area, in situ and remote sensing data used to develop this study as well as the data processing and analysis. More detailed information regarding specific methodologies is provided in the corresponding chapters.

#### **3.1 Overview**

This thesis was developed in the context of two projects. Both projects are multidisciplinary and had induced an effort of several institutions with the common objective to study the carbon flux over the Amazon continuum (<http://amazoncontinuum.org/>). The projects are complementary with one project focusing on the Lower Amazon River and the other one on the Amazon River Plume.

The project “Net Ecosystem Exchange of the Lower Amazon River – from Land to the Ocean and Atmosphere”, TROCAS, (FAPESP Proc. 12/51187-0) has as a goal of unravelling the sequences of processes and sources of terrestrially-derived organic matter driving the CO<sub>2</sub> outgassing to the atmosphere from the Lower Amazon. The TROCAS campaigns were realized in 2014-2017.

The project “Amazon Influence on the Atlantic: Carbon export from Nitrogen fixation by Diatom Symbiosis”, ANACONDAS, (NSF-OCE-0934095 and NSF-OCE-0934036) was aiming to understand the role of diatom-diazotroph assemblages on carbon export and/or sequestration at the Amazon River Plume. The ANACONDAS campaigns were realized in 2010-2012.

The present study attempts to tie river and ocean in the concept of a river continuum (SEDELL et al., 1989), bringing together both projects. Although TROCAS and ANACONDAS has different datasets, the carbon dynamics can be represented and assessed by remote sensing. To retrieve the carbon content over the Amazon

continuum, this study used different approaches considering the availability of the different data gathered within the latter projects (Table 3.1).

Table 3.1 - In situ and remote sensing data used to assess the carbon content at the Lower Amazon River (TROCAS campaign, 2014-2017) and at the Amazon River plume (ANACONDAS campaign, 2010-2012).

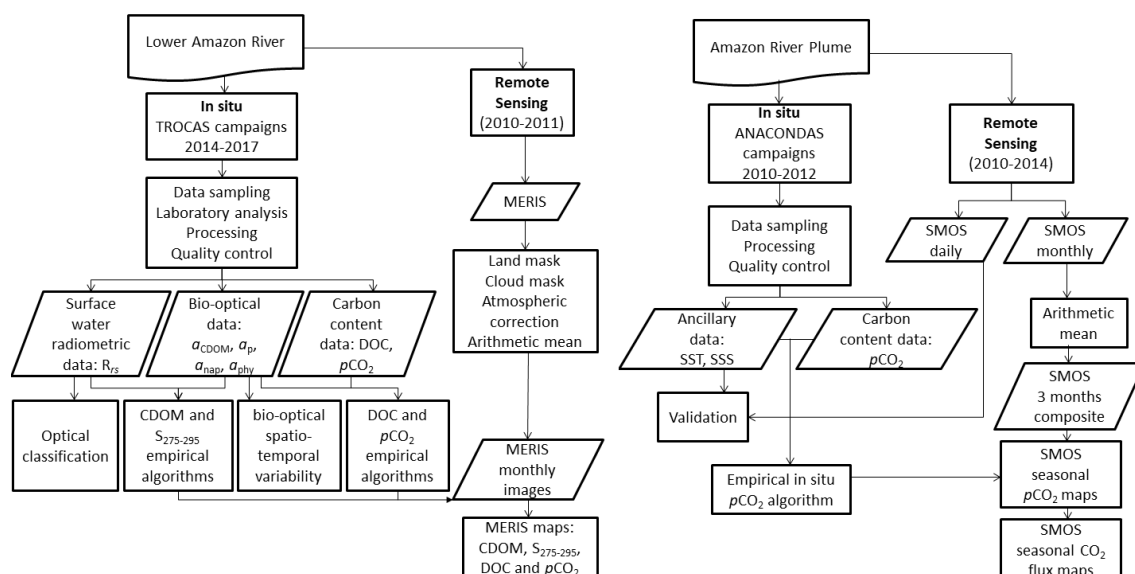
	TROCAS	ANACONDAS
$R_{rs}$ ( $sr^{-1}$ )	x	--
SPM ( $mg\ L^{-1}$ )	x	--
chl $a$ ( $mg\ L^{-1}$ )	x	--
$a_{CDOM}(\lambda)$ ( $m^{-1}$ )	x	--
$a_p(\lambda)$ ( $m^{-1}$ )	x	--
$a_{nap}(\lambda)$ ( $m^{-1}$ )	x	--
$a_{phy}(\lambda)$ ( $m^{-1}$ )	x	--
DOC ( $\mu mol\ L^{-1}$ )	x	--
$pCO_2$ ( $\mu atm$ )	x	x
water temperature ( $^{\circ}C$ )	x	x
Salinity (psu)	--	x
MERIS	x	--
SMOS	--	x

Source: Author's production.

For the Lower Amazon River, TROCAS six cruises were performed during the years of 2014-2017, along a transect between Óbidos and Macapá, covering all discharge seasons. Radiometric, bio-optical and carbon content samples were collected. A characterization of optical characteristics of the region investigated was performed through the definition of an optical typology of the water masses sampled ( $R_{rs}$  based optical classification) and a description of the regional spatial and temporal bio-optical variability. In situ  $R_{rs}$  were used to develop a regional CDOM and  $S_{275-295}$  inversion algorithms, while CDOM was used as a proxy to estimate DOC and  $pCO_2$  by empirical algorithms. Finally, these empirical algorithms were applied to a time-series of MERIS monthly average images to generate seasonal CDOM,  $S_{275-295}$ , DOC and  $pCO_2$  maps for the years of 2010-2011.

For the Amazon River Plume, three cruises were held during 2010-2012, during different discharge seasons (more detailed on the section 3.2.2). From the ANACONDAS cruises, sea surface temperature (SST), sea surface salinity (SSS) and  $p\text{CO}_2$  in situ data were specifically assessed for this study. The relationship between the latter three variables was explored in order to develop an inversion algorithm of  $p\text{CO}_2$  in the Amazon River plume. In situ SSS and SST data were further used to validate SMOS L3 daily SSS and SST products. The study period was extended from 2010 to 2014 taking advantage of the availability of SMOS products in this period. SMOS L3 monthly averages images were used to calculate trimestral seasonal means (Jan-Feb-Mar, Apr-May-Jun, Jul-Aug-Sep, Oct-Nov-Dec), according to the discharge seasonality (more detailed on section 3.2.1). The developed  $p\text{CO}_2$  empirical algorithm was applied to the SMOS seasonal composites time series, for deriving  $p\text{CO}_2$  distribution within the Amazon River Plume. The use of the  $p\text{CO}_2$  maps in addition to SST and wind information also available from the SMOS L3 data, would allow the computation of  $\text{CO}_2$  fluxes at regional scale (more detailed in section Chapter 7). The data used, and methodology performed to develop this study are represented on the following flowchart (Figure 3.1).

Figure 3.1 - Flowchart of the main activities: remote sensing and in situ data collection, processing and analysis.



Source: Author's production.

During TROCAS campaigns (2014-2017) and ANACONDAS study years (2010-2014), extreme climate events affected rainfall regime in the study area (JIMÉNEZ-MUÑOZ et al., 2016; MARENGO; ESPINOZA, 2016; ESPINOZA et al., 2014; SATYAMURTY et al., 2013) and consequently, the river discharge delivered to the ocean. The impact of such extreme climate events on the dynamics of the optical and biogeochemical parameters investigated in the frame of this study is described in the course of the following chapters.

## 3.2 Study area

### 3.2.1 Lower Amazon

The Lower Amazon River comprehends here the area along a 900 km transect between the upstream boundary at Óbidos (01°55.141' S, 55°31.543' W) and the Amazon river mouth (Figure 3.2) at Macapá. The downstream boundary was the north and south channels near Macapá, which are the last two well-constrained channels near the



Amazon River mouth (00°05.400' S, 51°03.200' W and 00°09.415' S, 50°37.353' W, respectively). At Óbidos, the width of the Amazon River is 2.3 km and at Macapá, each channel has a width of 11 km. The width of the mainstream at the Lower Amazon is stable and has little variation along the seasonal discharge (BIRKETT et al., 1998).

The annual precipitation in this region varies around 2000 mm. The rising water starts at the end of December and reaches the high-water level peak in May. In June, the water level starts to fall and the minimum is observed in November (MERTES; MAGADZIRE, 2008; MARTINEZ et al., 2003). According to previous studies in this region (SAWAKUCHI et al., 2017; WARD et al., 2015), the seasonal discharge months are defined as: Rising water (RW) (Jan, Feb, Mar), High water (HW) (Apr, May, Jun), Falling water (FW) (Jul, Aug, Sep) and Low water (LW) (Oct, Nov, Dec).

During the low water season, the physical influence of sea tides at the Lower Amazon can be observed to up to 1000 km upstream from the sea (KOSUTH et al., 2009). At the river's mouth, Macapá is highly influenced by sea-tide and experiences semi-diurnal flow reversals (WARD et al., 2015) but no saline intrusion is observed (NIKIEMA et al., 2007) and thus the upstream region is considered only as riverine waters.

The location of Óbidos is crucial for monitoring the dynamics of the Amazon basin. It is the last monitoring gauge of the Brazilian National Water Agency of Brazil (ANA) downstream the Amazon River where the main river has already received the contribution of large rivers such as the Solimões, Negro and Madeira, additionally to the one of small tributaries. Downstream Óbidos, the Amazon River also receives the inputs from two large rivers: Tapajós and Xingu. The annual average discharge at Óbidos was  $183,787 \pm 63,305 \text{ m}^3\text{-s}^{-1}$  from 2010 to 2017. Considering the discharge measured at ANA stations at Tapajós and Xingu rivers (Itaituba and Altamira, respectively), their contributions increase by 11% the final discharge of the Amazon to the ocean.

In addition to the Amazon River, samples were also collected in Tapajós, Xingu, Paru, Jari and Jaraçu rivers as well as at the Lago Grande de Curuai floodplain lake (Figure 3.2). These latter rivers are classified as clearwater (CW) rivers (SIOLI, 1984), generally presenting high levels of primary production when compared with turbid Amazon River waters (WARD et al., 2015). The sampling at CW was always performed at the outfall portion of the river, and therefore under the Amazon River influence. The magnitude of the Amazon River influence over the CW river is varying according to the CW river size and its proximity to the Amazon river mouth due to a semi-diurnal flow reversal (FERRAZ, 1975; WARD et al., 2015). The seasonality of the water discharge is also decisive on the influence of the mainstream upon the tributaries. The sampling at Tapajós and Xingu was performed at a “lake-like” portion of these rivers, where the water flow is almost lentic.

The Lower Amazon region between Óbidos and Macapá represents ~13% of the Amazon basin’s surface (WARD et al., 2015) and although recent findings showed that it is a crucial area for the global carbon budget assessments (SAWAKUCHI et al., 2017), this region remained until now relatively unstudied. The tidal effects plus the large width of the river, hampering in situ studies in the latter region.

Figure 3.2 - TROCAS campaigns (T1-T6) during the study period (2014-2017).



The map indicates the assessed rivers from the Lower Amazon region and on which campaign it were sampled.

Source: Author's production.

### 3.2.2 Amazon River Plume

The Amazon River Plume (ARP) is located at the Western Tropical North Atlantic (WTNA), defined in this study as 15°N-5°S; 60°W-45°W. The limits of WTNA were chosen in order to compare with previous studies in the same area (GOES et al., 2014; YEUNG et al., 2012; SUBRAMANIAM et al., 2008; COOLEY et al., 2007).

Draining an area of approximately 6.5 million km<sup>2</sup>, the Amazon basin represents roughly 20% of all freshwater discharge to the global ocean (RAYMOND et al., 2013; RICHEY et al., 2002; 1990). When flowing into the WTNA, the dispersal of the ARP can

extend offshore to an area of 106 km<sup>2</sup> (MOLLERI et al., 2010). The salinity is highly variable and dependent on the seasonality; surface water of the plume can be fresher (less saline) than the water beneath the barrier layer on the ocean (LENTZ; LIMEBURNER, 1995). The seasonal extent of the plume is a result of several processes including the Amazon River discharge, current advection, ocean rainfall and turbulent mixing by seasonal winds (GRODSKY et al., 2014; COLES et al., 2013; NIKIEMA et al., 2007; HU et al., 2004).

When the Amazon River reaches the ocean, it meets the North Brazil Current and its waters are transported northwestward along the Brazilian Shelf in the direction of the Guyana Current. During the FW to LW seasons, a fraction of the ARP is retroflected and carried eastward by the North Equatorial Counter Current. During the RW the water is trapped in the river mouth (recirculation current), due to the onshore trade winds against the coast (LENTZ; LIMEBURNER, 1995) (Figure 3.3).

Figure 3.3 - Study area showing the in situ sampling oceanographic routes and the sampling stations during 2010-2012.



Different colours are corresponding to the performed cruises. The North Brazil Current and the North Equatorial Counter Current are shown in dark blue.

Source: Author's production.

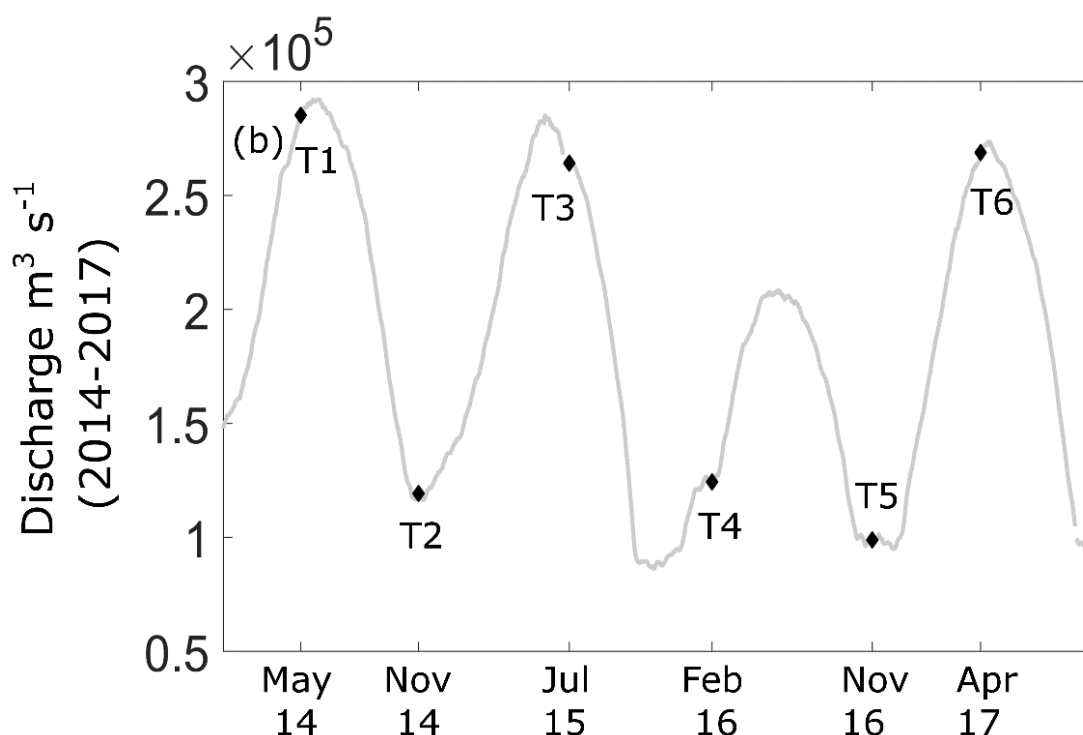
### 3.3 Extreme climate events during the campaigns

#### 3.3.1 TROCAS

The sampling period of 2014-2017 was marked by exceptional climate events. The year of 2014 was characterized by a record flood in the Amazon Basin that started with a La Niña event in 2012 increasing the rainfall regime and followed with an SST positive anomaly in the tropical Atlantic south of the Equator and western tropical Pacific (MARENGO; ESPINOZA, 2016; ESPINOZA et al., 2014; SATYAMURTY et al., 2013). During the rising water season of 2014, the rainfall within the south-western Amazon was 80-100% above usual records (ESPINOZA et al., 2014).

Conversely, the year of 2015-2016 was marked by a severe drought caused by El Niño, especially at the eastern Amazon (JIMÉNEZ-MUÑOZ et al., 2016). The low level of the river caused a disconnection of the Amazon River from some streams and floodplains (MARENGO et al., 2011) potentially resulting in lower inputs of organic matter at the river's mainstream. The flood of 2014 and the drought of 2016 can be clearly observed from the hydrographic data (Figure 3.4).

Figure 3.4 - Average of the seasonal water discharge for TROCAS period (2014-2017).



The campaigns are showed on the hydrological curve.

Source: Author's production.

### 3.3.2 ANACONDAS

The year of 2010 was also marked by a strong El Niño that caused severe drought (MARENGO et al., 2011). The 2 years beyond the sampling period (2012-2014) included in our analysis, were characterized by a record flood in the Amazon Basin that started with a La Niña event in 2012 and continued with an anomalous SST in the tropical

Atlantic south of the Equator and western tropical Pacific (MARENGO; ESPINOZA, 2016; ESPINOZA et al., 2014; SATYAMURTY et al., 2013).

### **3.4 Cruise description**

#### **3.4.1 TROCAS**

During the years 2014-2017, six cruises were performed onboard of B/M Mirage, a classical Amazonian wood boat adapted with laboratories for scientific missions (Figure 3.5). The cruises allowed a description of the optical and biogeochemical spatiotemporal variability of the Amazon considering all the seasonal discharge situations. The CW rivers were sampled during the TROCAS 1-4 campaigns while during the TROCAS 5-6, only waters from Amazon River mouth were sampled (Table 3.2).

Figure 3.5 - B/M Mirage used during all TROCAS cruises (2014-2017).



Source: Author's production.

The general objective of TROCAS 1-4 cruises (T1-T4) was to study the organic matter fate within the Amazon. Therefore, all campaigns started at Óbidos going downstream to Macapá, to go along with the river flowing into the Atlantic Ocean. This journey usually takes three to five days (WARD et al., 2015).

For consistency, during T1-T4 the same four locations were sampled and considered as main stations: Óbidos at 900 km upstream, Almeirim in the middle of the transect (~450 km upstream), Macapá North Channel (MNC) and Macapá South Channel (MSC), downstream (Figure 3.2). For each of these locations the sampling was performed at three sub-stations distributed equidistantly across the channel (e.g., center and left/right margin). In addition to these four locations, Tapajós and Xingu rivers were also sampled during all T1-T4 campaigns (single station only). Furthermore, new stations were added along the cruises to increment the sampling. The new stations were: Grande Lago de Curuai floodplain lake, CW rivers Paru, Jari and Jaraçu; and Santarem at the meeting of Tapajós and Amazonas rivers. Additionally, water samples were also taken underway.

The last two campaigns, T5 and T6, turned the focus to assess the tidal influence and the semi-diurnal flow reverses over the biogeochemical parameters. Therefore, only the channels of MCN and MCS were sampled. At these stations, the sampling was performed similarly than during the previous campaigns, over margins and center of the river. Further, the boat was also anchored in the center of the river in both channels and the samples were performed each 1:30h for 13 hours in order to monitor tidal effects. TROCAS 5 and 6 also differentiated from the previous campaigns by having stations closer to the ocean (Figure 3.2).



Table 3.2 - Dates of TROCAS campaigns during the years of 2014-2017 and the respective discharge river season.

Campaign	Discharge season	Date	Amazon River samples	clear water river samples
TROCAS 1	High	May-14	yes	yes
TROCAS 2	Low	Nov-14	yes	yes
TROCAS 3	Falling	Jul-15	yes	yes
TROCAS 4	Rising	Feb-16	yes	yes
TROCAS 5	Low	Nov-16	yes	no
TROCAS 6	High	April-17	yes	no

Source: Author's production.

At the main stations the sampling consisted of: above-water radiometry, water surface collection for bio-optical properties and biogeochemical characterization.

### 3.4.2 ANACONDAS

Three oceanographic cruises offshore of the Amazon River mouth and along its plume into the WTNA were performed during 2010-2012 (Table 3.3).

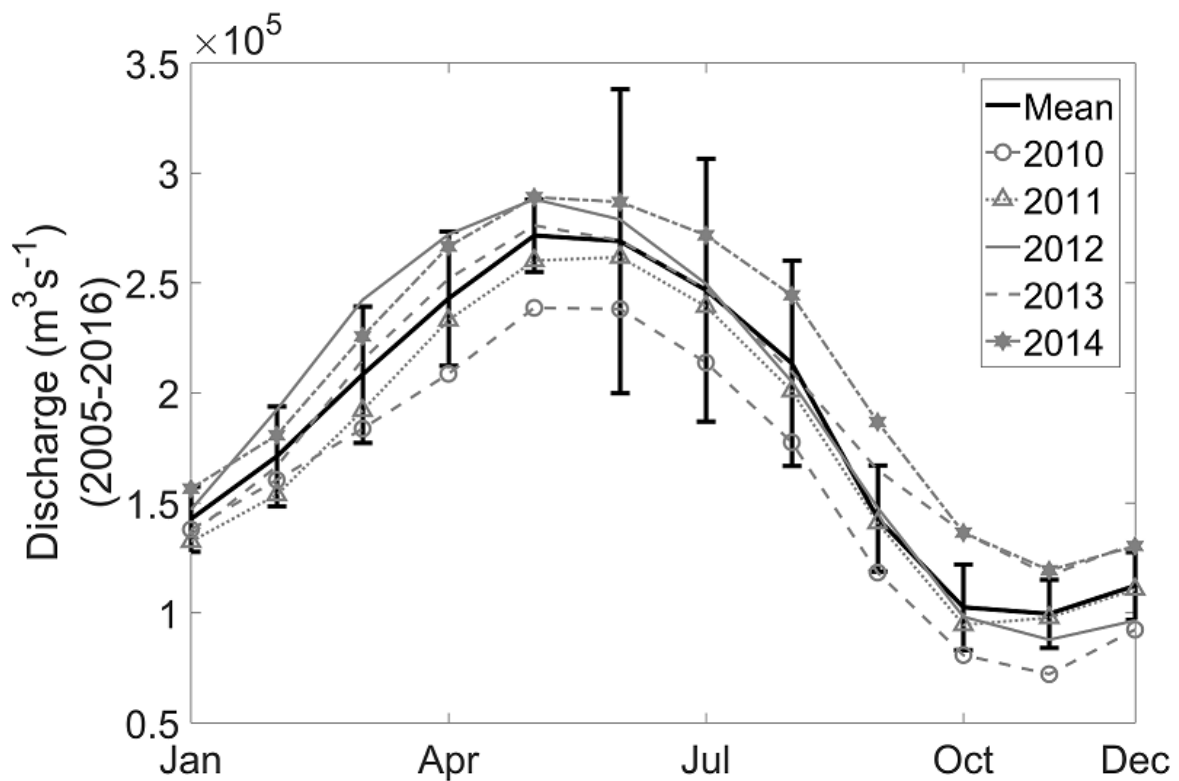
Table 3.3 - Dates of the ANACONDAS oceanographic cruises at the Amazon River plume during the years of 2010-2012 and the respective discharge season.

Campaign	Discharge season	Date
ANACONDAS 1	High	05-23 Jun 2010
ANACONDAS 2	Falling-Low	02 Sep - 06 Oct 2011
ANACONDAS 3	Falling	13 - 29 Jul 2012

Source: Author's production.

The set of months when data were collected represents the main hydrologic periods covering the years of 2010 to 2012 (Figure 3.6). This study considers the river plume as the area covered by surface waters with SSS < 35 for consistency with prior studies that established this threshold for the ARP (IBÁNHEZ et al., 2015; 2016; GRODSKY et al., 2014; COLES et al., 2013).

Figure 3.6 - Discharge of the years covered in this study (2010-2014) of the Amazon River.



The mean and standard deviation monthly historical discharge (2005-2016) are shown. Discharge data acquired from Óbidos station, from the Brazilian National Agency of Waters (ANA, <http://hidroweb.ana.gov.br>).

Source: Author's production.

### 3.5 In situ data

#### 3.5.1 TROCAS

##### 3.5.1.1 Above-water radiometry

Above water radiometry was measured with a portable hyperspectral radiometer FieldSpec® (ASD Inc.) which collects radiance ( $L$ ,  $\mu\text{W m}^{-2}\text{sr}^{-1}$ ) in the range of 350 to 1100 nm (bandwidth 1nm) and a field-of-view of 25°. The acquisition geometry followed Mobley (1999) recommendations to avoid shadows and sunglint contamination in the measurements (Figure 3.7). The radiance measurements were conducted between 09:00 am to 04:00 pm local time (Figure 3.8.A).

Total water leaving radiance ( $L_w$ ), sky radiance ( $L_{sky}$ ) and the radiance from a white panel Spectralon reference ( $L_g$ ) were consecutively measured 6 to 10 times. The later parameter was used to estimate the downwelling irradiance ( $E_d$ ) (Equation 3.1):

$$E_d(\lambda) = L_g(\lambda)f_c\pi \quad (3.1)$$

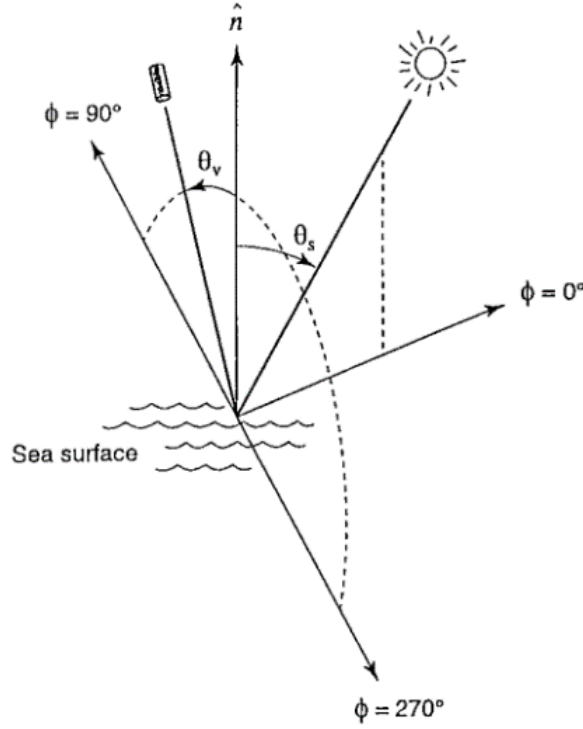
where  $f_c$  is a correction factor estimated in laboratory by the ratio of a standard Spectralon reference that remains in the laboratory by the Spectralon panel used at the fieldwork.

The remote sensing reflectance ( $R_{rs}$ ) can be computed according to Equation 3.2:

$$R_{rs} = \frac{L_w}{E_d} = \frac{L_u - \rho_{air-river} * L_{sky}}{E_d} \quad (3.2)$$

where  $L_u$  is the upwelling radiance that reaches the sensor and  $\rho_{air-river}$  is a sky glint correction coefficient at the air-sea interface.

Figure 3.7 - Sun and sensor geometry used in field measurements.



Source: MOBLEY, 1999.

There are several methods in the literature to correct the optical signal from sun glint interference. In the present study we used the approach of Ruddick et al. (2006), here called R06 which is indicated for turbid to highly turbid waters. The  $\rho_{air-river}$  is a function of wind and cloud cover (Equation 3.3 and 3.4).

$$\frac{L_{sky}(\lambda=750)}{E_D(\lambda=750)} \geq 0.05 \rightarrow \rho_{air-river} = 0.0256 \quad (3.3)$$

or

$$\frac{L_{sky}(\lambda=750)}{E_D(\lambda=750)} < 0.05 \rightarrow \rho_{air-river} = 0.0256 + 0.00039W + 0.000034W^2 \quad (3.4)$$

where W is the wind measured concomitantly with the radiometric measurements.

The residual glint or white offset correction was corrected by using the bands of  $R_{rs}(780)$  and  $R_{rs}(720)$  (RUDDICK et al., 2005) (Equation 3.5).

$$\frac{\alpha * R_{rs}(\lambda=780) - R_{rs}(\lambda=720)}{\alpha - 1} \quad (3.5)$$

where  $\alpha = 2.35$ , according to the average similarity reflectance spectrum.

### 3.5.1.2 Bio-optical measurements

Surface water sample collection for bio-optical measurements was made using a bucket at all stations and aliquots of water were filtrated onboard (Figure 3.8.B). Sub-samples were collected for absorption coefficients of total particle matter ( $a_p(\lambda) \text{ m}^{-1}$ ), non-algal particle ( $a_{nap}(\lambda) \text{ m}^{-1}$ ), phytoplankton ( $a_{phy}(\lambda) \text{ m}^{-1}$ ) and CDOM ( $a_{CDOM}(\lambda) \text{ m}^{-1}$ ). Aliquots of surface water were also used for chl $a$  concentration and suspended particulate matter concentration (SPM). Water was filtered onboard up to one hour after collection (except for the SPM) under gentle vacuum ( $< 5 \text{ mm Hg}$ ), according to the NASA protocol (MITCHELL et al., 2002). The filters for particulate matter absorption and chl $a$  were stored in a portable ultrafreezer during the cruise and stored in liquid nitrogen until posterior analysis using a spectrophotometer and fluorimeter, respectively. The laboratory analysis for SPM, chl $a$ ,  $a_p$ ,  $a_{nap}$  and  $a_{phy}$  was performed in a time period lower than three months after collection. For CDOM, the laboratory analysis was performed with a maximum of three weeks after the first sample collection.

The absorption coefficients of CDOM and particulate matter were analyzed using a Shimadzu UV-2450 spectrophotometer, within the interval of 250-850 nm.

### 3.5.1.3 Absorption of particulate matter, non-algal particles and phytoplankton

Duplicate surface water samples were filtered through 25 mm Whatman GF/F glass fiber filters (0.7  $\mu\text{m}$  nominal pore size). The filtration water was performed in order to

obtain a sufficient coloration of the filter pad, varying the volume between 10-125 ml depending on the river water quality.

The  $a_p$  spectra were calculated using the method of transmittance-reflectance (T-R) (TASSAN; FERRARI, 2002). The T-R method is more recommended for particle-rich water by correcting the light backscattering by the particle sample with an integrating sphere.

After  $a_p$  measurement, the sample filters were soaked with Sodium Hypochlorite for 20 minutes and washed with drops of Milli-q water to remove pigments from the particles retained. The T-R method is performed once again using the de-pigmented filters, obtaining  $a_{nap}$ .  $a_{phy}$  is obtained by  $a_{phy} = a_p - a_{nap}$ .

#### **3.5.1.4 Absorption of coloured dissolved organic matter**

After removing larger part of the suspended particles used to estimate  $a_p$ , the remained filtered surface water samples were filtered again using 0.2  $\mu$ m polycarbonate membranes (Whatman Nuclepore, 25 mm). Samples were stored in pre-combusted glass bottles (450°C, 6 hours) wrapped with aluminum foil and kept under refrigeration (4°C) until further laboratory analysis. CDOM samples were exposed to room temperature before spectrophotometric analysis in order to avoid any bias due to the thermal difference between the samples and the reference water (Milli-Q water).  $a_{CDOM}(\lambda)$  is calculated from absorbance measurements as followed (Equation 3.6):

$$a_{CDOM}(\lambda) = 2.303 \cdot \frac{A(\lambda)}{L} \quad (3.6)$$

where  $A(\lambda)$  is the absorbance of the filtered water sample at the specific wavelength  $\lambda$  and  $L$  is the optical pathway of the quartz cell in meter (here 0.1 m).

As recommended by Babin et al. (2003), a baseline correction was applied to each spectrum by subtracting the mean absorbance in the range of 680-690 nm from the

whole spectrum. The absorption spectral shape of CDOM is estimated using a linear least-squares regression of the logarithm of  $a_{CDOM}(\lambda)$  and reported with units of  $\text{nm}^{-1}$  (BRICAUD et al., 1981) (Equation 3.7):

$$a_{CDOM}(\lambda) = a_{CDOM}(\lambda_0)e^{-s(\lambda-\lambda_0)} \quad (3.7)$$

where  $a_{CDOM}(\lambda)$  is the absorption coefficient at wavelength  $\lambda$ ,  $a_{CDOM}(\lambda_0)$  is the absorption coefficient at a reference wavelength  $\lambda_0$  and  $S$  is the spectral slope in the spectral range from  $\lambda_0$  to  $\lambda$  with  $\lambda_0 < \lambda$ .

Recent publications have demonstrated the importance of the slope in the range of 275-295 nm ( $S_{275-295}$ ) for better constraining the natural variability in the DOC specific coefficient absorption ( $a^*_{CDOM}$ ) (VANTREPOTTE et al., 2015; FICHOT; BENNER, 2012; 2011; HELMS et al., 2008). Furthermore, Helms et al., (2008) have highlighted the importance of the slope ratio  $S_{275-295}/S_{350-400}$  as a potential proxy for assessing DOM molecular weight. Consequently,  $S_{275-295}$ ,  $S_{350-400}$  and the slope ratio  $S_R$  were specifically computed in this study.

#### **3.5.1.5 Chlorophyll-*a* concentration**

Chlorophyll-*a* (chl*a*,  $\mu\text{g L}^{-1}$ ) concentration was measured from 25 to 100 ml of water samples filtered using 25 mm Whatman GF/F glass fiber filters (0.7  $\mu\text{m}$  nominal pore size). At the laboratory, triplicates samples of pigments were extracted from the filters after immersion in 10ml of 90% acetone/Dimethyl sulfoxide (DMSO) solution (60/40 by volume, SHOAF; LIUM 1976) for 24h, in the dark at  $-10^\circ\text{C}$ . The resultant extraction was analyzed using a calibrated bench Turner Designs 10-AU fluorimeter.

#### **3.5.1.6 Suspended particulate matter concentration**

Suspended particulate matter concentration (SPM,  $\text{mg L}^{-1}$ ) was determined gravimetrically following the method of Van der Linde (1998). Before field work, 0.45  $\mu\text{m}$  (nominal pore size) cellulose acetate filters (Millipore) were dried for 24h at the

laboratory, weighed ( $W_1$ ) and placed in petri plates for transportation. At field, a volume ( $V$ ) of 150 to 400 ml of surface water was filtered and filters for SPM were stored for further laboratory analysis (Figure 3.8.C). At the laboratory, SPM filters were dried for 72h at 50°C and weighed ( $W_2$ ) to determine the SPM according to Equation 3.8:

$$\frac{W_1 - W_2}{V} \quad (3.8)$$

### 3.5.1.7 Carbon content

Surface water samples collected for carbon content measurements were obtained using a submersible pump. Sub-samples were collected for DOC and  $p\text{CO}_2$ . Both laboratory analyses were performed less than three weeks after the first collection.

#### 3.5.1.7.1 Dissolved organic carbon

Surface water samples were filtered through pre-combusted (500°C, 5h) GF/F glass fiber filters 0.7  $\mu\text{m}$  nominal pore size (Whatman) using a 60 mL syringe (Figure 3.8.D). The samples were stored in 25 mL pre-combusted glass vials washed with acid, closed with Teflon lids and preserved in the field with 25  $\mu\text{L}$  of 50% HCl at 0-4°C. At the laboratory, DOC concentration ( $[\text{DOC}]$ ,  $\mu\text{mol L}^{-1}$ ) was measured using a Shimadzu Total Organic Carbon Analyzer (Model TOCVCPH).

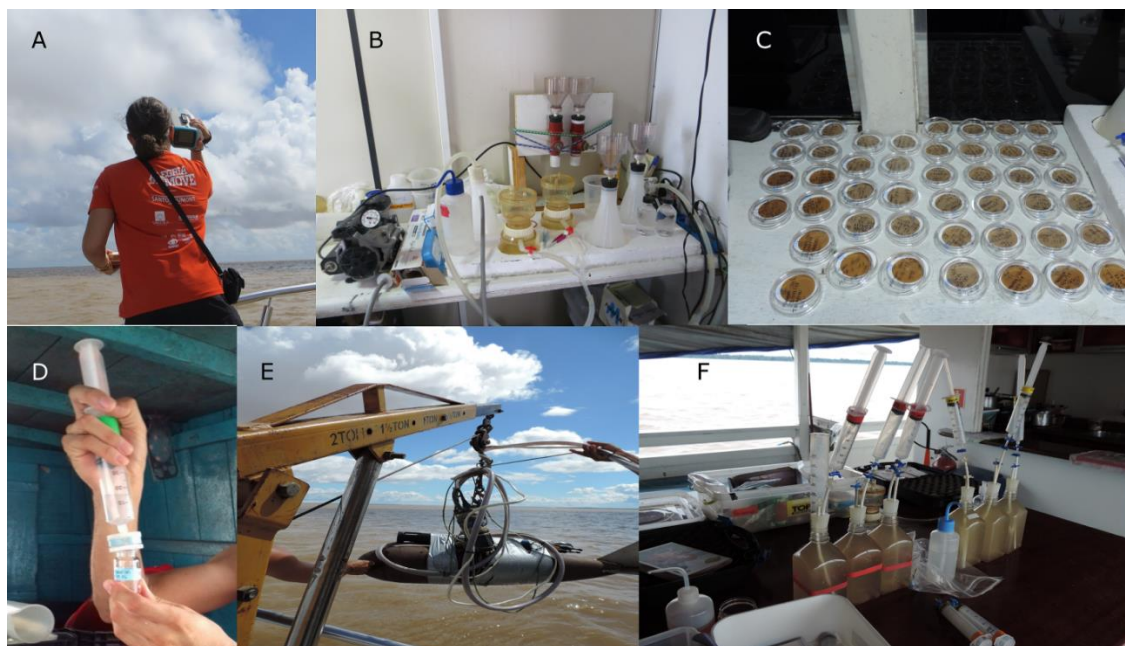
#### 3.5.1.7.2 Partial pressure of carbon dioxide

$p\text{CO}_2$  was measured after extraction from water samples by headspace equilibration. A 1L polycarbonate bottle was overflowed three times with water pumped from the surface (Figure 3.8.E) before being closed with a stopper equipped with two stop-cocks and short/long straws to allow creation of a headspace (Figure 3.8.F). After injecting 60 mL of  $\text{N}_2$  and removing 60 mL of water the bottle was sealed and shaken vigorously for 2 min (RASERA et al., 2013). The headspace was then removed with a 60 mL syringe and samples (three replicates of each) were stored in vials pre-evacuated with a hand



pump. At the laboratory, the samples were injected into a Picarro G2201-i Cavity Ring-Down Spectrometer (CRDS).  $p\text{CO}_2$  values were corrected based on the common gas law (LISS, 1973).

Figure 3.8 - Field measurements during TROCAS campaigns.



A) Radiometric measurement with the FieldSpec HH above-water radiometer; B) Bio-optical properties filtration kit for absorption measurements ( $a_{\text{CDOM}}$ ,  $a_p$ ,  $chl a$ ); C) Cellulose acetate filters (0.45  $\mu\text{m}$  pore) after suspended particulate matter filtration in the Amazon River; D) Dissolved organic carbon filtering apparatus; E) Pump chained to a weight for collecting surface waters; F) Headspace method for  $p\text{CO}_2$  analysis.

Source: Author's production.

### 3.5.2 ANACONDAS

Sea surface temperature (SST) and sea surface salinity (SSS) were measured continuously during the three oceanographic cruises (R/V Knorr KN197 – June of 2010; R/V Melville MV1110 - September to October 2011; R/V Atlantis AT21-04 July of 2012) (Figure 3.3), using the shipboard underway seawater system.

Surface  $p\text{CO}_2$  during the oceanographic cruises was measured using an underway  $p\text{CO}_2$  system with a non-dispersive infrared  $\text{CO}_2$  gas analyzer (LI-COR 6252) and standardized

using CO<sub>2</sub>-air reference gas mixtures from National Oceanic and Atmospheric Administration (NOAA) Climate Monitoring and Diagnostics Laboratory (CMDL). The in situ oceanographic data consists of 15,392 data points, taken every 10 minutes during the three cruises.

According to the Earth System Research Laboratory from the National Oceanic and Atmospheric Administration (NOAA), the atmospheric carbon dioxide is ~400 µatm. When the  $p\text{CO}_2$  of the water exceeds this threshold, the water body is considered a source of CO<sub>2</sub>, when it is below this threshold the water body uptakes the CO<sub>2</sub> from the atmosphere.

### **3.6 Quality control**

The coefficient of variation ( $cv = (\sigma/\mu) \cdot 100$ ) (Equation 3.9) of chl $a$ , SPM, DOC and  $R_{rs}$  was computed for each station. For chl $a$ , SPM, DOC and  $p\text{CO}_2$ , only samples with CV close or lower than 10% between the triplicates was kept and averaged to get the final value representative for each station. For  $R_{rs}$  the same procedure was adopted considering the interval of 400-840 nm.

### **3.7 Remote sensing data**

#### **3.7.1 Medium Resolution Imaging Spectrometer**

Reduced spatial resolution (1x1 km<sup>2</sup>) of daily  $R_{rs}(\lambda)$  derived from MERIS sensor were downloaded from the NASA Goddard Space Flight Center, Ocean Ecology Laboratory, Ocean Biology Processing group for the 2010-2011 period. Subsequently to land masking, a cloud mask adapted for turbid waters was applied (L2ESA) prior to atmospheric correction (BANKS; MÉLIN, 2015).

Atmospheric correction was performed in the presence of sun-glint, using POLYMER method that consists in a technique for spectral matching that depends of two models: polynomial atmospheric model representing the scattering of the atmosphere and sun-

glint, and the bio-optical ocean water reflectance model (STEINMETZ et al., 2011). The main advantage of the combined method of cloud mask and atmospheric correction for turbid water is the gain of spatial coverage. Seasonal images have been processed from arithmetic mean. The final images were cropped for the coordinates (00°00.000' S, 02°00.000' N, 51°00.000' W, 48°00.000' W) referent to the Amazon River mouth. Seasonal maps of  $a_{CDOM}(412)$ ,  $S_{275-295}$ , DOC and  $pCO_2$  were generated using MERIS seasonal composites by math band function. The arithmetic mean and math band performed using MERIS images were processed using SeaWiFS Data Analysis System (SeaDAS) software version 7.4 (URL: <http://seadas.gsfc.nasa.gov>) freely provided by NASA.

### **3.7.2 Soil Moisture and Ocean Salinity**

SMOS mission measures microwave radiation emitted from the Earth's surface at 1.4 to 1.427 GHz, using an interferometric radiometer. SMOS was launched on November 2009 and in May 2010 started to provide data to the scientific community (MECKLENBURG et al., 2012; REUL et al., 2012). In this study, daily level three product (L3) with 0.5° of spatial resolution delivered by the Centre National d' Etudes Spatiales - Institut Français de Recherche pour l' Exploitation de la Mer (CNES- IFREMER) was used. The selected product is only available for the years of 2010-2014 and provides SSS, SST and Wind Speed (WS) data. SMOS products were acquired concomitantly to the oceanographic cruises (Table 3.3) also including  $\pm 1$  day around in situ sampling dates during the cruises of 2010-2012. This approach is justified to avoid missing data due to the 3 days revisit time of SMOS.

SMOS products were further processed using the SeaDAS v. 7.4 software. All images were cropped for the WTNA area, and the math band function was used to calculate the  $pCO_2$  and the sea-air CO<sub>2</sub> net flux for the entire study area. The mosaic function was used for the three-month composite images according to the Amazon River discharge season.

The choice to work with SMOS instead of a visible sensor for the Amazon River plume was here performed considering the dataset currently available. For the present investigation no sufficient information on the bio-optical properties for the Amazon River plume was available, and therefore, the use of an ocean colour sensor was not possible. Conversely, the possibility to assess  $p\text{CO}_2$  from water optical properties (CDOM) was investigated in the Lower Amazon River through dedicated measurements. Even though SMOS is more suitable for our data set, it has a drawback due to a higher microwave brightness temperature of the land, which contaminates the ocean signal leading to inaccurate near-shore SSS values (TALONE et al., 2008). Thus, we restricted its use for applications to water masses beyond 100 km offshore.

### 3.8 Statistics

The accuracy of estimates was evaluated using statistical indicators including the coefficient of determination ( $R^2$ ), root mean square error (RMSE), the mean relative absolute difference (MRAD) and the mean relative difference (Bias) expressed respectively as:

$$R^2 = \frac{SS_{res}}{SS_{tot}} \quad (3.10)$$

$$RMSE = \sqrt{\frac{\sum_{i=1}^N (y_i - x_i)^2}{N}} \quad (3.11)$$

$$MRAD = 100 \cdot \frac{1}{N} \sum_{i=1}^N \frac{|y_i - x_i|}{x_i} \quad (3.12)$$

$$Bias = 100 \cdot \frac{1}{N} \sum_{i=1}^N \frac{y_i - x_i}{x_i} \quad (3.13)$$

where  $SS_{res}$  is the sum of squares of residuals,  $SS_{tot}$  is the total sum of squares,  $x_i$  is the in situ data for a define parameter and  $y_i$  its estimated value.

Shapiro-Wilk test was applied to test the normality of the samples. Kruskal-Walis one-way analysis of variance non-parametric test was performed to test whether samples

originate from the same sample distribution. When a significant difference among the tested parameters mean were found, a post hoc test was performed to see which means are significant from the others. To test a small subset of all possible pairs, a Dunn's post hoc was performed. Conversely, for a larger pairwise comparison, Tukey honestly significant difference (HSD) test was performed. In addition, a sensitivity analysis was performed on Chapter 7 where it is more detailed.



## 4 BIO-OPTICAL VARIABILITY OF THE LOWER AMAZON WATERS

### 4.1 Introduction

The measured  $L_u$  from a water body is resultant of the inherent optical properties (absorption and scattering) of its optically significant constituents namely: the phytoplankton, non-algal particles (NAP) and coloured dissolved organic matter (CDOM) (PRIEUR; SATHYENDRANATH, 1981; SATHYENDRANATH, 2000). Over the years, empirical relationships between absorption coefficients and biogeochemical parameters such as  $a_{phy}$  and  $chl a$  (BRICAUD et al., 1995); and  $a_{nap}$  and SPM (BABIN et al., 2003), have been documented for ocean and coastal waters. Moving to inland waters, more studies are needed to confirm if these relationships are still reliable (MARTINEZ et al., 2015; BINDING, et al., 2008). In the same way, subproducts of absorption coefficients measurements as the slope of  $a_{CDOM}$  and  $a_{nap}$  ( $S_{CDOM}$  and  $S_{nap}$ , respectively) also require more studies on their applicability to retrieve qualitative information about the particles and dissolved material present in an optically complex water body. As a matter of fact, the slope  $S_{CDOM}$  assessed over different wavelength intervals, has been shown to be a relevant indicator of DOM molecular weight (FICHOT; BENNER, 2012; HELMS et al., 2008; BABIN et al., 2003), while  $S_{nap}$  can provide information on the relative contribution of organic and mineral particles in the absorption at coastal waters (BABIN et al., 2003).

Numerous semi-analytical algorithms have been proposed to assess IOPs and biogeochemical products in oceanic waters (where all IOPs are assumed to covary with  $chl a$ ) from ocean colour remote sensing (MOREL; GENTILI, 2009; MARITORENA et al., 2002; LEE et al., 2002; BARNARD et al., 1999; CARDER et al., 1999; GARVER; SIEGEL, 1997). These algorithms usually fail in turbid waters, where the contribution of NAP and CDOM can be higher and not driven only by phytoplankton dynamics (LOISEL et al., 2013).

Other factors are also responsible for the failure of standard ocean colour algorithms in optically complex waters such as inland waters: i) unsuccessful atmospheric correction (SHI and WANG, 2009); ii) adjacency effects that contaminate the remote sensing signal with land information (PALMER et al., 2015); iii) high spatiotemporal variability of hydrodynamic and biogeochemical processes (MOUW et al., 2015).

The choice of a non-suitable atmospheric correction in turbid waters can overestimate the total aerosol reflectance and mislead water colour products inducing for instance negative reflectance values (SHI; WANG, 2009). Studies are increasingly more focused in solving this issue, using different spectral bands and approaches already showing good progress as reported in the literature (MARTINS et al., 2017; WANG et al., 2012; STEINMETZ et al., 2011; SHI; WANG, 2009). The adjacency effect is still a considerable challenge in inland waters studies and advanced techniques are now being proposed such as, for instance, the separation of the forest signal from the water spectra (MARTINS et al., 2017; PALMER et al., 2015).

Studying the spatiotemporal bio-optical and radiometric variability in the Amazon River is not trivial and can unfold different spatial-temporal scales. The Lower Amazon has ~ 900 km of turbid waters in the mainstream course and receives the contribution of two important clearwater rivers: Tapajós and Xingu (SIOLI, 1984) which can influence the Amazon optical characteristics. The Amazon waters follow a strong seasonality, with the discharge season being characterized by Rising (RW) (Jan, Feb, Mar), High (HW) (Apr, May, Jun), Falling (FW) (Jul, Aug, Sep) and Low (LW) (Oct, Nov, Dec) waters conditions (SAWAKUCHI et al., 2017; WARD et al., 2015).

In addition to the latter main spatial and temporal patterns, small-temporal scale processes (e.g. tidal effect) occurring in the lower reaches of the Amazon river can represent another important source of radiometric and bio-optical variability. During the LW season, the oceanic tidal waves propagate, reaching Óbidos, 900 km upstream the Amazon mouth (KOSUTH et al., 2009). Near the river mouth, the semidiurnal tide



reverses the flow (FERRAZ, 1975; WARD et al., 2015), with great implications on SPM transport (WRIGHT; NITTROUER, 1995; JAEGER; NITTROUER, 1995) and DOM dynamics (WARD et al., 2015). The counteracting forces from tides and river create a unique and dynamic temporal variability.

The bathymetry and the width of a channel can also influence the bio-optical variability. The bathymetry of the channel impacts the velocity of the flowing water and it is a decisive force on the burial/resuspension dynamics of biogeochemical parameters (WARD et al., 2015). Therefore, the irregularities on the river floor can also influence water bio-optical characteristics and induce transversal and vertical variability.

These diverse scales of spatial-temporal variability can add a greater complexity to the development of inversion algorithms, which would need to properly take into account all the range of optical variability for then obtaining accurate OSCs measurements by remote sensing.

A synthetic representation of the water optical variability can be performed through the definition of optical water types (OWT) which is a recurrent research topic in water colour remote sensing since the pioneer work by Jerlov on marine waters (JERLOV, 1976). According to the concentration of biogeochemical parameters, Amazonian waters has been categorized as white, black or clearwater (SIOLI, 1984). White waters are associated with rivers characterized by high concentration of sediments, as the Amazon, Madeira and Solimões rivers; black waters are related to rivers with high concentration of CDOM as Negro River; and clearwaters, as observed in the Tapajós and Xingu, are linked to rivers with high transparency and high levels of in situ primary production.

The determination of OWT can be carried by a cluster analysis of in situ  $R_{rs}$  spectra. The cluster specific spectra can be applied to remote sensing data, providing information on the spatial distribution of the defined optical classes (ELEVELD et al., 2017;

KOPONEN et al., 2004). Bio-optical properties can be used to characterize the reflectance spectra clustered in an OWT, to provide a qualitative information on the bio-optical characteristics associated with this  $R_{rs}$  based optical typology. Further, OWT classification can provide a framework constraining the development of a suitable inversion algorithm for specific bio-optical environments. As a matter of fact, several recent studies have focused on the development of class specific inversion algorithms in coastal and inland waters (SPYRAKOS et al., 2017; SHEN et al., 2015; MOORE et al., 2014; SHI et al., 2014; VANTREPOTTE et al., 2012). In a global analysis, Spyrakos et al. (2017) has classified all Amazon waters within a single OWT with high reflectance across a wide interval of the spectrum due to an intense SPM dominance. However, the Amazon optical data utilized to develop the aforementioned classification were limited to a collection of spectra and bio-optical constituents sampled at the Lago Grande do Curuai floodplain lake, while no information about seasonal variability was considered or presented for this region.

The aim of this chapter is to characterize the OSCs spatiotemporal variability in the Lower Amazon considering different scales: the spatial variability along the 900 km of the Lower Amazon transect, seasonal variability, tidal variability and transversal variability across the margins. Further, a second aim of this chapter was to identify the different OWT composing the Lower Amazon and to characterize the associated bio-optical environments, contributing to a future development of inversion algorithms in this area.

## **4.2 Materials and methods**

### **4.2.1 In situ data**

The dataset used in this study consists in measurements of OSCs and IOPs performed in the Lower Amazon region over the 2014-2017 period, during all discharge seasons. The data were collected at the Amazon River and CW rivers (Table 4.1).

The computed  $R_{rs}$  spectra was corrected for sun glint interference according to Ruddick et al. (2006). The OSCs used in this study consist in SPM ( $\text{mg L}^{-1}$ ) and chl  $a$  ( $\text{mg L}^{-1}$ ). The IOPs consists in absorption coefficients of CDOM ( $a_{\text{CDOM}}(\lambda)$ ) ( $\text{m}^{-1}$ ), particulate matter ( $a_p(\lambda)$ ) ( $\text{m}^{-1}$ ), non-algal particles ( $a_{\text{nap}}(\lambda)$ ) ( $\text{m}^{-1}$ ) and phytoplankton  $a_{\text{phy}}(\lambda)$  ( $\text{m}^{-1}$ ). The slope of  $a_{\text{CDOM}}(\lambda)$  was computed over the 275-295 nm spectral domain (FICHOT; BENNER, 2012).

The slope of  $a_{\text{nap}}(\lambda)$ ,  $S_{\text{nap}}$ , computed over the 400-700 nm spectral domain ( $S_{\text{nap}400-800}$ ) (ESTAPA et al., 2012; VANTREPOTTE et al., 2007) potentially indicates the relative contribution of mineral and organic particles in the water (BABIN et al., 2003).

The  $a_{\text{phy}}(443)$  was also calculated using chl  $a$ , hereafter called  $a_{\text{phy}}(443)$  B95, according to Bricaud et al. (1995):

$$a_{\text{phy}}(443)\text{B95} = (0.0394 \cdot (\text{chl}a)^{0.3435}) \cdot \text{chl}a \quad (4.1)$$

The proportion of CDOM to the total absorption (except pure water) ( $a_{\text{CDOM}} : (a_{\text{CDOM}} + a_p)$ ) and particles to the total absorption (except pure water) ( $a_p : (a_{\text{CDOM}} + a_p)$ ) were also calculated at 443 nm. Likewise, the ratio of the  $a_{\text{phy}}$  B95 to  $a_p$  was also computed.

Table 4.1 - Total number of in situ data gathered during the years of 2014-2017.

Parameter	Amazon	CW	Total samples
$a_{\text{CDOM}}(\lambda)$ ( $\text{m}^{-1}$ )	116	14	130
Slope $a_{\text{CDOM}}(\lambda)$ ( $\text{nm}^{-1}$ )	116	14	130
$a_p(\lambda)$ ( $\text{m}^{-1}$ )	95	14	109
Slope $a_p(\lambda)$ ( $\text{nm}^{-1}$ )	95	14	109
$a_{\text{nap}}(\lambda)$ ( $\text{m}^{-1}$ )	95	14	109
$a_{\text{phy}}(\lambda)$ ( $\text{m}^{-1}$ )	95	14	109
SPM ( $\text{mg L}^{-1}$ )	90	12	102
chl $a$ ( $\text{mg L}^{-1}$ )	85	12	97

Source: Author's production.

## **4.2.2 Classification of the in situ $R_{rs}$ spectra**

### **4.2.2.1 Spectra normalization**

Each  $R_{rs}$  spectrum was normalized by its integrated value (LUBAC; LOISEL, 2007). The integration was computed by trapezoidal method, over a wavelength range of 400-800 nm. The goal of the normalization is to reduce the first order variability of reflectance and focus on the reflectance spectral shape, hence removing amplitude differences caused by concentration variation. The normalization is a common step that precedes the optical classification procedure in many studies (SPYRAKOS et al., 2017; SHEN et al., 2015; VANTREPOTTE et al., 2012). Vantrepotte et al. (2012) highlighted the importance of using normalized reflectance spectra instead of raw  $R_{rs}$  to perform an OWT classification. For example, if a water body has high concentrations of SPM (e.g. Amazon River), the use of raw  $R_{rs}$  would lead to a classification very much based on the relative concentration of sediments, and consequently, all the others OSC contribution would be neglected.

### **4.2.2.2 Cluster analysis**

Different supervised and unsupervised methods have been used for the classification of  $R_{rs}$  with the aim of defining OWT based upon differences in the magnitude and shape of the spectral curves (ELEVELD et al., 2017; SYPRAKOS et al., 2017; MÉLIN et al., 2015; SHEN et al., 2015; MOORE et al., 2014; SHI et al., 2014; VANTREPOTTE et al., 2012; LUBAC; LOISEL et al., 2007; KOPONEN et al., 2004; 2002). Unsupervised classification can be used when a priori knowledge is not available and  $R_{rs}$  data is used to define the clusters, this way being less subject to user errors. The  $k$ -means and fuzzy c-means are popular techniques among the unsupervised classification methods (ELEVELD et al., 2017; SPYRAKOS et al., 2017; SHEN et al., 2015; MARTINEZ et al., 2015; MOORE et al., 2014; VANTREPOTTE et al., 2012). When the clustering results of  $k$ -means are compared with fuzzy c-means and other unsupervised method (e.g. Ward algorithm), they can be very similar (SPYRAKOS et al., 2017; VANTREPOTTE et al.,

2012). Therefore, *k*-means was adopted in this study to cluster the data into homogeneous optical groups.

*K*-means technique requires a user-specified number of clusters (*K*), which are represented by their centroids (WILKS, 2006). The clusters are defined by measuring the square Euclidian distance of the centroids. The Silhouette width analysis (ROUSSEEUW, 1987) was used to determine the best number of clusters, by measuring how similar an individual point is to its own cluster.

### **4.3 Results and discussion**

#### **4.3.1 Bio-optical general characteristics of the Lower Amazon**

##### **4.3.1.1 CDOM absorption**

Amazon River  $a_{\text{CDOM}}(443)$  values ( $2.12 \pm 0.53 \text{ m}^{-1}$ ) are relatively lower in average when compared to values presented by Martinez et al. (2015) ( $a_{\text{CDOM}}(440)=3.3\pm1.0 \text{ m}^{-1}$ ) and Jorge et al. (2017) ( $a_{\text{CDOM}}(420) \cong 3.25 \pm 0.46 \text{ m}^{-1}$ ) from Amazon white waters. On the other hand, CW rivers had a higher average  $a_{\text{CDOM}}(443)$  value ( $3.21 \pm 1.46 \text{ m}^{-1}$ ) in comparison to values reported by Martinez et al. (2015) ( $a_{\text{CDOM}}(440)= 1.8\pm0.8 \text{ m}^{-1}$ ). CDOM discrepancies between studies can be attributed to the size of each dataset, alternative filtering methods and measurements (no baseline correction in Martinez et al, 2015 for instance), as well as different sampling locations.

Table 4.2 - Bio-optical characteristics of Amazon River and Clearwater rivers.

	Clearwater rivers			Amazon River		
	Average $\pm$ SD	CV %	RANGE	Average $\pm$ SD	CV %	RANGE
$a_{\text{CDOM}}(443) \text{ (m}^{-1}\text{)}$	$2.01 \pm 0.88$	42	0.74-3.53	$2.12 \pm 0.53$	28	0.89-4.40
$S_{275-295} \text{ (nm}^{-1}\text{)} \times 10^{-2}$	$1.50 \pm 0.17$	11	1.32-1.87	$1.45 \pm 0.05$	4	1.30-1.66
$a_p(443) \text{ (m}^{-1}\text{)}$	$1.68 \pm 2.44$	140	0.37-9.44	$3.16 \pm 2.11$	66	1.18-8.93
$S_{p400-800} \text{ (nm}^{-1}\text{)} \times 10^{-2}$	$1.05 \pm 0.13$	12	0.88-1.30	$1.05 \pm 0.08$	8	0.91-1.33
$a_{\text{nap}}(443) \text{ (m}^{-1}\text{)}$	<u><math>1.12 \pm 1.78</math></u>	154	<u>0.22-6.92</u>	<u><math>1.96 \pm 1.42</math></u>	72	<u>0.56-6.26</u>
$a_{\text{phy}}(443) \text{ (m}^{-1}\text{)}$	<u><math>0.61 \pm 0.68</math></u>	109	<u>0.19-2.53</u>	<u><math>1.29 \pm 0.84</math></u>	62	<u>0.57-4.93</u>
$a_{\text{phy}}(680) \text{ (m}^{-1}\text{)}$	<u><math>0.21 \pm 0.19</math></u>	85	<u>0.03-0.72</u>	<u><math>0.25 \pm 0.21</math></u>	82	<u>0.003-1.41</u>
SPM (mg L <sup>-1</sup> )	$14.0 \pm 18.1$	124	1.8-67.9	$69.7 \pm 33.8$	53	18.3-160.8
chl <i>a</i> (mg L <sup>-1</sup> )	$6.1 \pm 7.7$	122	1.5-31.3	$1.4 \pm 0.8$	57	0.5-6.3
$a_{\text{CDOM}} : (a_{\text{CDOM}} + a_p) (443)$	$0.64 \pm 0.19$	29	0.17-0.80	$0.44 \pm 0.12$	28	0.17-0.64
$a_p : (a_{\text{CDOM}} + a_p) (443)$	$0.36 \pm 0.19$	50	0.20-0.83	$0.56 \pm 0.12$	22	0.36-0.83
$a_{\text{phy}}(443) \text{ B95} : a_p(443)$	$0.19 \pm 0.15$	76	0.05-0.56	$0.02 \pm 0.012$	61	0.004-0.065
$a_{\text{phy}}(443) \text{ B95} : (a_{\text{CDOM}} + a_p) (443)$	$0.05 \pm 0.04$	80	0.02-0.13	$0.01 \pm 0.006$	60	0.003-0.033

SD – Standard Deviation; CV - Coefficient of Variation. Values *in italic* are considered inaccurate.

Source: Author's production.

$S_{275-295}$  had a higher average value ( $0.0150 \pm 0.0017 \text{ nm}^{-1}$ ) and higher variability (11%) for CW samples than for the Amazon River samples (4%). High  $S_{275-295}$  values indicate lower molecular weight of DOM (HELMS et al., 2008). This might suggest the higher impact of photobleaching rates in CW and less organic matter input from the margins.

Higher contribution of DOM from phytoplankton in CW might also explain the observed variation (GAGNE-MAYNARD et al., 2017; HELMS et al., 2008), although a recent study demonstrated that  $S_{275-295}$  is only slightly sensitive to the impact of phytoplankton derived DOM (DANHIEZ et al., 2017). The greater presence of phytoplankton at CW rivers can be evidenced by high values of chl $a$  in comparison to the Amazon River (Table 4.2).

The higher variability of  $S_{275-295}$ , as well as all other studied parameters (Table 4.2) at CW rivers might be related to the location where the samples were collected, very close to the Amazon mainstream, being potentially influenced by the overflow of the turbid Amazon waters according to the discharge season.

#### **4.3.1.2 Particulate matter absorption**

The results first emphasize the problematic related to the measurement of particulate absorption in the Amazon waters.

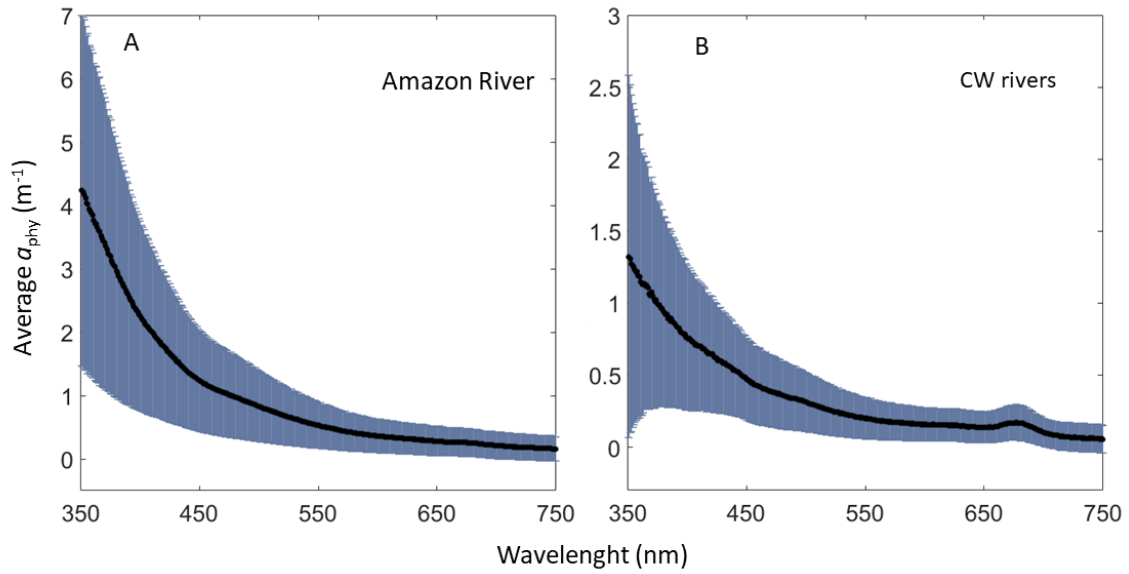
Specifically,  $a_{phy}$  measurements were not accurate for Amazon water. The common method in the literature and used in this study is based on the use of sodium hypochlorite (TASSAN; FERRARI, 1995) as an oxidizing agent. This method was not effective, and more than phytoplankton pigments were actually bleached. Further, for Amazon waters,  $a_p$  measured contained a large fraction that could not be attributed to phytoplankton pigments but to DOM adsorbed in the particles. Consequently, part of the absorption was taken erroneously as caused by phytoplankton, increasing the  $a_{phy}$  signal. Likewise, the same error signal was transferred to  $a_{nap}$ , leading to inaccurate low values considering the discounted  $a_{phy}$ . The observed methodological issue related to  $a_{phy}$  and  $a_{nap}$  measurements for the Lower Amazon is a source of uncertainty, and therefore, the corresponding data in Table 4.2 are underlined. It is worthy of note, however, that according to Binding et al. (2008), the enhanced absorption in the blue wavelengths by  $a_{phy}$  is not attributed to the bleaching of particulate organic detritus, since this fraction are not affected by the sodium hypochlorite bleaching (TASSAN;

FERRARI, 1995), but rather to the DOM adsorbed onto suspended sediments. Fine particles are better adsorption acceptors for DOM than coarse detritus (KAISER; ZECH, 1997; SUESS, 1970), and the mineral sediments in the Amazon River is predominantly silt and clay ( $< 64 \mu\text{m}$ ) (DUNNE et al., 1998).

For the Amazon River samples, an atypical  $a_{\text{phy}}$  spectrum is found with absorption increasing exponentially with decreasing wavelength without typical clear bumps corresponding to the photosynthetic pigments in the blue and red part of the spectrum (Figure 4.1.A). A similar situation was reported by other studies in inland waters with high CDOM concentration (BINDING et al., 2008; GALLEGOS et al., 2005). Binding et al. (2008) noted that stronger correlations between  $\text{chl}a$  and  $a_{\text{phy}}$  in the visible spectrum occurred in waters with low  $a_{\text{CDOM}}(440)$  ( $< 0.2 \text{ m}^{-1}$ ). In this study, the lower  $a_{\text{CDOM}}(443)$  was measured at the Tapajós River during the LW season ( $a_{\text{CDOM}}(443) = 0.74 \text{ m}^{-1}$ , Table 4.2), and was almost four times higher than the threshold suggested by Binding et al. (2008). In comparison to Amazon River,  $a_{\text{phy}}$  of CW rivers was less affected by CDOM (Figure 4.1.B). The corresponding average of  $a_{\text{phy}}$  spectrum presented the expected, although modest, signature of phytoplankton pigments, with a small and not well-defined absorption peak near 440 nm, and a more distinguished absorption peak on 680 nm (BRICAUD et al., 1995).



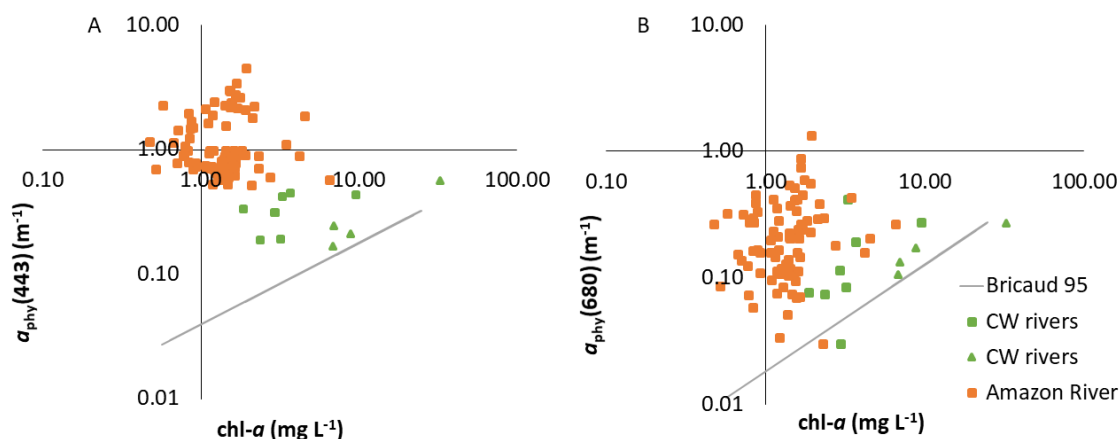
Figure 4.1 - Average  $a_{phy}$  and standard deviation spectrum for: A) Amazon River and, B) CW rivers.



Source: Author's production.

No significant correlation was found between  $a_{phy}(443)$  and  $chl a$  ( $N= 97$ ,  $R^2 = 0.03$ ,  $p>0.05$ ), when the whole dataset is used. When the data is partitioned into Amazon and CW waters, still no relationship is verified between  $a_{phy}(443)$  and  $chl a$  (Amazon:  $N= 85$ ,  $R^2 = 0.0004$ ,  $p>0.05$ ; CW  $N=12$ ,  $R^2 = 0.32$ ,  $p>0.05$ ), despite that some samples of CW are more in line with Bricaud et al. 1995's model (Figure 4.2.A). In fact, the samples closer to Bricaud et al 1995 relationship are those whose ratio of  $a_{phy}(443) : a_{CDOM}(443)$  are higher than 0.1 (Table 4.2). CDOM absorbs strongly at short wavelengths and should affect more  $a_{phy}(443)$  measurements than  $a_{phy}(680)$ , but still no relationship could be established between  $a_{phy}(680)$  and  $chl a$  ( $N= 97$ ,  $R^2 = 1.35 \cdot 10^{-5}$ ,  $p>0.05$ ) for the whole dataset. For the partitioned Amazon data, no correlation was observed ( $N= 85$ ,  $R^2 = 0.01$ ,  $p>0.05$ ) and for CW, only a relatively weak correlation was established ( $N= 12$ ,  $R^2 = 0.48$ ,  $p<0.05$ ).

Figure 4.2 - Correlation between chl-a and: A)  $a_{\text{phy}}(443)$ ; B)  $a_{\text{phy}}(680)$ , for the Lower Amazon.



Bricaud et al. (1995) fit in grey for comparison.

Source: Author's production.

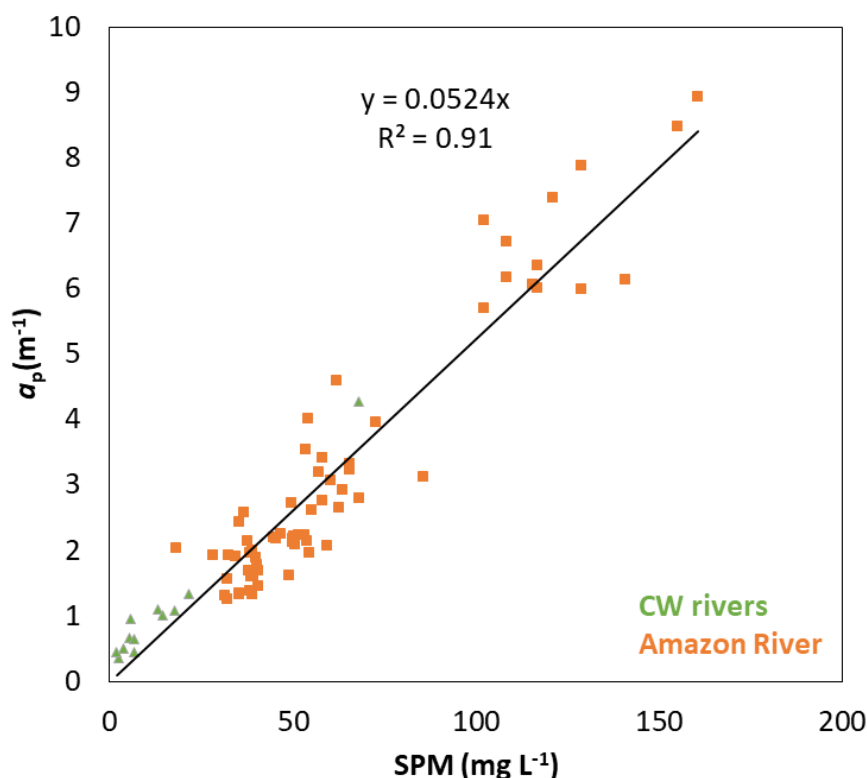
Considering the inaccuracy of  $a_{\text{phy}}$  from in situ data as mentioned above,  $a_{\text{phy}}(443)$  was calculated using chl-a data, according to Bricaud et al. (1995) (herein referred as B95).  $a_{\text{phy}}(443)$  B95 was used to approximate the proportion of the absorption by phytoplankton in the total particles absorption signal. On average,  $a_{\text{phy}}(443)$  contribution was very low for the Amazon (2% of  $a_p(443)$ , Table 4.2), while this contribution varies much more for CW samples (from 5 to 56%, Table 4.2) suggesting a greater heterogeneity on the constitution of the particulate matter stock present in these waters. The previous results clearly underline the practical difficulty to assess  $a_{\text{phy}}$  in the Amazon waters, where the contribution of phytoplankton to the total particles absorption signal is very low, while other processes such as CDOM adsorption can represent an additional issue (influencing  $a_p$ ,  $a_{\text{phy}}$  and  $a_{\text{nap}}$  measurements).

To assess the magnitude of the additional absorption potentially caused by CDOM in  $a_{\text{phy}}$  measurements, the absorption attributed to the adsorption of CDOM in the particle (defined here as CDOMp) was estimated by the difference of  $a_{\text{phy}}$  measured ( $a_{\text{phyM}}$ ) and  $a_{\text{phy}}$  B95. Thus, assuming that Bricaud et al. (1995) model is suitable for

complex waters and that chl $a$  was estimated properly, as well as disregarding a possible absorption due to package effect and pigment variability, the estimated absorption by CDOMp(443) for CW was on average 0.21 m<sup>-1</sup>, which results in an average overestimation in  $a_{\text{phy}}(443)$  of 165%. For Amazon waters the issue is even worst with  $a_{\text{phy}}(443)$  overestimation reaching up to 2447%. For  $a_{\text{phy}}(680)$  the percentage error was 914% for Amazon and 69% for CW rivers. CDOM samples were normalized by the average of 680-690 nm (BABIN et al., 2003) and even after the normalization,  $a_{\text{CDOM}}(680)$  signal although relatively smaller, is not neglectable ( $a_{\text{CDOM}}(680)$  = 0.05 and 0.08 m<sup>-1</sup> for Amazon and CW rivers, respectively). The combination of a small contribution of phytoplankton to the total absorption at the Amazon waters, the strong CDOM interference in  $a_{\text{phy}}$  measurements by adsorption in the suspended mineral particles, and CDOM absorption along higher wavelengths, challenges accurate  $a_{\text{phy}}$  measurements in optically complex waters requiring the development of further studies.

The major fraction of  $a_p$  is related to  $a_{\text{nap}}$  (Table 4.2, proportion of  $a_{\text{phy}}(443)$  B95 :  $a_p(443)$ ) and, since  $a_{\text{nap}}$  is impaired by an inaccurate  $a_{\text{phy}}$ , it was decided to consider in this study  $a_p$  as representative of NAP.  $a_p(443)$  is strongly correlated with SPM (N = 77, R<sup>2</sup> = 0.91, p<0.05) (Figure 4.3) as also reported by other studies in the Amazon basin (PINET et al., 2017). The slope of the regression between  $a_p$  and SPM (0.053) is much higher than what is reported for coastal waters (~0.031) (XI et al., 2013; BABIN et al., 2003) and for combusted particles (0.024) (BOWERS et al., 1996), possibly due to the major content of organic particles. CW  $a_p(443)$  are related to small concentrations of SPM and Amazon samples with SPM higher than 100 mg L<sup>-1</sup> were mainly obtained during the RW season. The average ratio of  $a_p(443)$  : SPM is higher for CW rivers (CW: 0.11 ± 0.05; Amazon: 0.05 ± 0.01) with a 49% of coefficient of variation (Amazon River CV: 25%), suggesting that CW rivers may have more organic particles and are more influenced seasonally by the Amazon mainstream.

Figure 4.3 - Scatterplot of  $a_p(443)$  as a function of SPM.



A linear regression with null intercept is shown.

Source: Author's production.

The slope of  $a_p$ ,  $S_p$ , is also considered as representative of the slope of  $a_{nap}$ ,  $S_{nap}$ .  $S_p$  showed similar values for Amazon and CW ( $S_{p400-800} \sim 0.010 \text{ nm}^{-1}$ ) with low variability for Amazon (8%) and CW rivers (12%) and lower values than what is usually reported for coastal and oceanic waters ( $> 0.011 \text{ nm}^{-1}$ ) (ZHANG et al., 2015; TZORTZIOU et al., 2007; VANTREPOTTE et al., 2007; BABIN et al., 2003; BRICAUD et al., 1998). Previous studies suggested that  $S_{nap}$  values of about  $0.011 \text{ nm}^{-1}$  are typical for mineral dominated waters (TZORTZIOU et al., 2007; BABIN et al., 2003; FERRARI et al., 2003; BOWERS et al., 1996), and higher  $S_{nap}$  ( $> 0.011 \text{ nm}^{-1}$ ) are related to organic particles (BABIN et al., 2003; FERRARI et al., 2003). Nevertheless, recent studies found an opposed trend in CDOM-rich waters, where steeper  $S_{nap}$  are in fact associated with more inorganic suspended matter by DOM adsorption in mineral surfaces (RIDDICK et

al., 2015; Xi et al., 2013; ESTAPA et al., 2012; BINDING et al., 2008). Considering the high values of CDOM in the study area, this situation may also apply in the Lower Amazon, where the low values of  $S_p$ , in comparison to the literature dedicated to coastal and oceanic waters, are in fact related to organic particles.

#### 4.3.1.3 Absorption budget

The absorption budget for Amazon River and CW at the Lower Amazon is governed by CDOM and total particles. At CW rivers,  $a_{phy}$  can have an expressive contribution to the total particulate absorption ( $a_{phy}(443)$  B95 :  $a_p(443)$  maximum = 56%, Table 4.2), but for the total absorption budget it is still very low when compared to  $a_{CDOM}$  and  $a_p$  ( $a_{phy}$ ,  $a_{CDOM}$ ,  $a_p$  maximum contribution to the absorption budget: 13%, 80% and 83%, respectively, Table 4.2).

CDOM is dominant with a large contribution to the total absorption in CW samples ( $a_{CDOM}(443) : a_{CDOM}(443) + a_p(443) = 0.64 \pm 0.19 \text{ m}^{-1}$ ) but its variability is similar to what is found for the Amazon River  $\cong 28\%$  (Table 4.2). At the Amazon River, although particulate matter has meaningful dominance, it is almost even with CDOM ( $a_{CDOM}$ : 44%;  $a_p$ : 56%, Table 4.2).

The balance proportion among  $a_{CDOM}$  and  $a_p$  at the Amazon River is even more evident when the absorption budget is assessed by season. Except for RW, when  $a_p$  is almost three-fold higher than  $a_{CDOM}$ , all other seasons are very equivalent (Table 4.3). The seasonal variability is also stronger during the RW for CW rivers, probably due to the influence of the overflow of the Amazon River waters (Table 4.3).

Table 4.3 - Absorption budget of the Amazon River (Am) and clearwater rivers (CW) for the seasons: Rising water (RW), High water (HW), Falling water (FW) and Low water (LW). SD – Standard Deviation; CV - Coefficient of Variation.

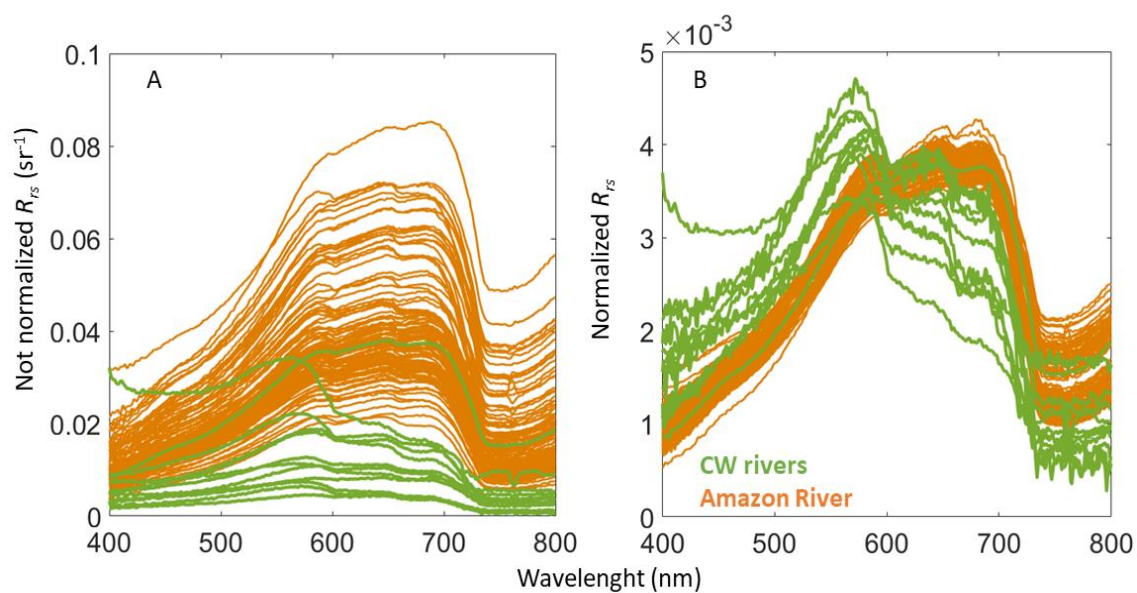
		$a_{\text{CDOM}} : (a_{\text{CDOM}} + a_p)$ (443)		$a_p : (a_{\text{CDOM}} + a_p)$ (443)		$a_{\text{phy}}(443) \text{ B95} : (a_{\text{CDOM}} + a_p)$ (443)	
		Average $\pm$ SD	CV %	Average $\pm$ SD	CV %	Average $\pm$ SD	CV %
RW	Am	0.26 $\pm$ 0.08	33	0.74 $\pm$ 0.08	11	0.008 $\pm$ 0.007	88
	CW	0.55 $\pm$ 0.26	47	0.45 $\pm$ 0.26	58	0.039 $\pm$ 0.026	67
HW	Am	0.48 $\pm$ 0.09	19	0.52 $\pm$ 0.09	18	0.006 $\pm$ 0.001	21
	CW	0.78 $\pm$ 0.03	4	0.22 $\pm$ 0.03	14	0.065 $\pm$ 0.065	99
FW	Am	0.50 $\pm$ 0.07	15	0.50 $\pm$ 0.07	15	0.007 $\pm$ 0.004	59
	CW	0.72 $\pm$ 0.06	8	0.28 $\pm$ 0.06	21	0.036 $\pm$ 0.016	45
LW	Am	0.50 $\pm$ 0.05	11	0.50 $\pm$ 0.05	11	0.014 $\pm$ 0.003	21
	CW	0.62 $\pm$ 0.06	10	0.38 $\pm$ 0.06	16	0.085 $\pm$ 0.056	65

Source: Author's production.

#### 4.3.2 Optical classification of the Lower Amazon waters

The normalization applied allowed to distinguish the spectra particularities, highlighting the heterogeneity in the OWT corresponding to the Amazon and CW rivers (Figure 4.4).

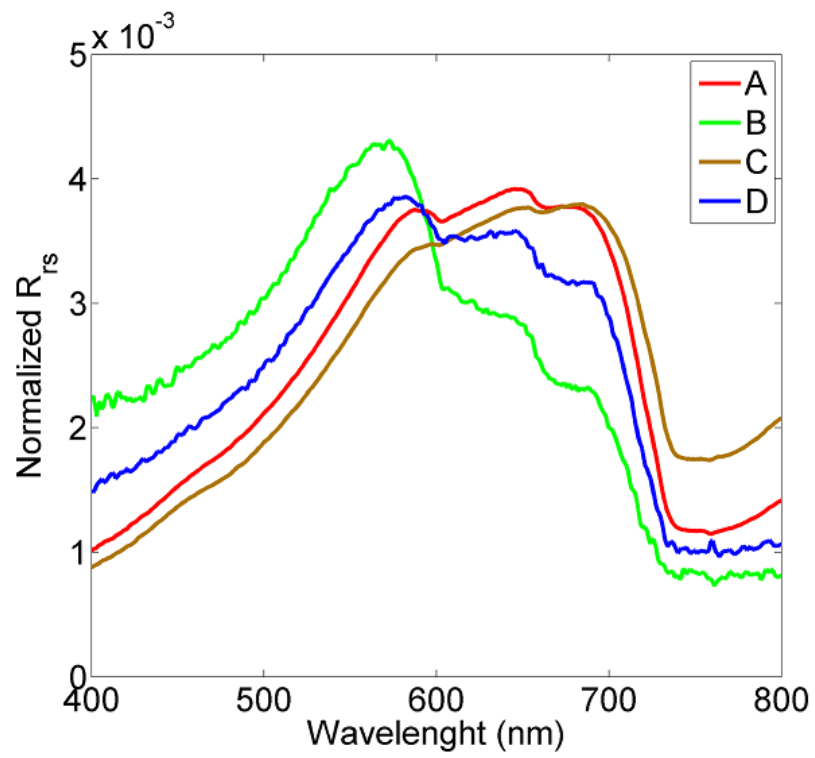
Figure 4.4 - Measured  $R_{rs}$  (A) not normalized and (B) normalized for the Lower Amazon region.



Source: Author's production.

The Silhouette analysis suggested four (A, B, C, D) as the optimal number of clusters for the *K*-means clustering analysis (Figure 4.5). Clusters A and C are representative of the Amazon River waters while clusters B and D are representative of CW tributaries from the Lower Amazon region. Table 4.4 summarizes the bio-optical properties corresponding to each cluster.

Figure 4.5 - Average normalized spectra resultant from the K-means clustering analysis of the Lower Amazon region.



Source: Author's production.



Table 4.4 - Bio-optical characteristics of the four optical water types for Lower Amazon.

	CLASS A (Amazon HW FW LW)		CLASS B (CW FW LW)		CLASS C (Amazon RW HW)		CLASS D (CW RW HW)	
	Average ± SD	Range	Average ± SD	Range	Average ± SD	Range	Average ± SD	Range
$a_{CDOM}$ (443) ( $m^{-1}$ )	$2.2 \pm 0.6$	1.3-4.2	$1.0 \pm 0.3$	0.7-1.3	$2.0 \pm 0.2$	1.6-2.7	$2.4 \pm 0.6$	1.3-3.1
$S_{275-295}$ ( $nm^{-1}$ ) $\times 10^{-2}$	$1.44 \pm 0.05$	1.32-1.54	$1.71 \pm 0.17$	1.51-1.87	$1.45 \pm 0.03$	1.40-1.50	$1.41 \pm 0.09$	1.32-1.57
$a_p(443)$ ( $m^{-1}$ )	$2.03 \pm 0.69$	1.18-4.74	$0.48 \pm 0.12$	0.37-0.64	$6.44 \pm 1.61$	2.72-9.44	$0.89 \pm 0.25$	0.50-1.11
$S_{p400-800}$ ( $nm^{-1}$ ) $\times 10^{-2}$	$1.04 \pm 0.06$	0.91-1.25	$0.93 \pm 0.04$	0.88-0.97	$1.05 \pm 0.07$	0.95-1.26	$1.14 \pm 0.14$	0.95-1.30
SPM ( $mg L^{-1}$ )	$43.6 \pm 9.9$	28.3-68.2	$4.4 \pm 2.7$	1.8-6.8	$102.5 \pm 40.6$	1.8-160.8	$10.0 \pm 5.8$	3.7-17.8
chl <i>a</i> ( $mg L^{-1}$ )	$1.5 \pm 0.8$	0.5-4.4	$5.1 \pm 2.9$	2.3-8.5	$1.4 \pm 0.4$	0.5-2.1	$9.1 \pm 11.2$	1.8-31.3
$a_{CDOM} :$ $a_{CDOM} +$ $a_p(443)$	$0.51 \pm 0.06$	0.28-0.64	$0.67 \pm 0.10$	0.55-0.78	$0.25 \pm 0.07$	0.17-0.50	$0.73 \pm 0.05$	0.66-0.80
$a_p : a_{CDOM}$ $+ a_p(443)$	$0.49 \pm 0.06$	0.36-0.72	$0.33 \pm 0.10$	0.22-0.45	$0.75 \pm 0.07$	0.50-0.83	$0.27 \pm 0.05$	0.20-0.34
$a_{phy}(443)$ B95 : $a_p$ (443)	$0.03 \pm 0.01$	0.01-0.06	$0.24 \pm 0.09$	0.15-0.36	$0.01 \pm 0.002$	0.00-0.013	$0.20 \pm 0.20$	0.05-0.57
$a_{phy}(443)$ B95 : ( $a_{CDOM} +$ $a_p(443)$ )	$0.01 \pm 0.005$	0.004-0.02	$0.08 \pm 0.04$	0.04-0.13	$0.006 \pm 0.0011$	0.00-0.008	$0.05 \pm 0.04$	0.02-0.11

Source: Author's production.

Besides the evident distinction between Amazon and CW waters, another prevailing difference is related to the seasonality. For CW, cluster B has a well-defined  $chl a$  peak at  $R_{rs}(570)$  and consists of  $R_{rs}$  spectra measured during the Falling-Low seasons. Cluster D represents the CW Rising-High water seasons and the reflectance spectrum has a less prominent  $chl a$  peak, even that during these seasons the average  $chl a$  measured was in higher concentrations (Table 4.4). The large variability of  $chl a$  and phytoplankton blooms during the Rising-High seasons within CW rivers (e.g. Tapajós) have been reported in the literature (ALBÉRIC, et al., 2017; COSTA et al., 2013), and it is likely caused by the optimal balance between the nutrients input from the Amazon River and the light availability. The clear water of these rivers allows sunlight penetrating the water, and therefore, enhances the primary production. Another characteristic of cluster D is a higher signal at the red-NIR spectrum when compared to cluster B. The overflow of the Amazon River into the CW tributaries during the Rising-High seasons carries a large load of CDOM and SPM (Table 4.4). CDOM is therefore responsible for a strong light absorption in the green part of the visible spectrum, reducing the reflectance attributed to  $chl a$ , while SPM also causes a higher signal in the red-NIR wavelengths. At the Amazon River (clusters A and C) there is no evident  $chl a$  signal and although the reflectance signal is dominated by SPM, it is possible to observe that cluster A has a more homogenous high signal over a wide part of the spectrum for the green to the NIR wavelengths, while cluster C has an increasing reflectance in the same interval (Figure 4.7). The spectra shape of clusters A and B are in agreement with other studies in the Amazon Basin (YEPEZ et al., 2018; JORGE et al., 2017; MARTINS, et al., 2017; CARVALHO et al., 2015; MARTINEZ et al., 2015; LOBO et al., 2012). Cluster C gathers spectra from the RW (T4) and the HW seasons of T6 campaign that had a shifted discharge timing (Figure 3.4). The bio-optical properties of cluster C indicate a considerable increase in SPM ( $102.5 \pm 40.6 \text{ mg L}^{-1}$ ),  $a_p(443)$  ( $6.44 \pm 1.61 \text{ m}^{-1}$ ), as well as in the relative contribution of  $a_p$  to the total absorption (75%) (Table 4.4). The impact of seasonality on the variability of radiometric and bio-optical properties of the Amazon basin was also discussed by other studies in the region,

especially during the RW season when the Amazon River reaches the highest SPM levels (PINET et al., 2017; PARK; LATRUBESSE, 2015; 2014; VILLAR et al., 2013). This study corroborates that the RW presents a specific optical signature and it is a hallmark for the Lower Amazon waters. In view of the influence of the rising waters, four unique classes with stable optical signature can be delineated, two for the turbid water of the Amazon River and two for CW rivers. It is worthy to note that, although in average the rising of the waters occurs during the first trimester of the year, it is subject to changes due to climatic events. Therefore, the classification proposed here can be used to monitor the nature of the water masses of the Amazon region taking into account the influence of possible unusual events (time-shifting of the hydrological seasonal pattern due to climatic events or other anomalous situation such as anthropogenic impacts).

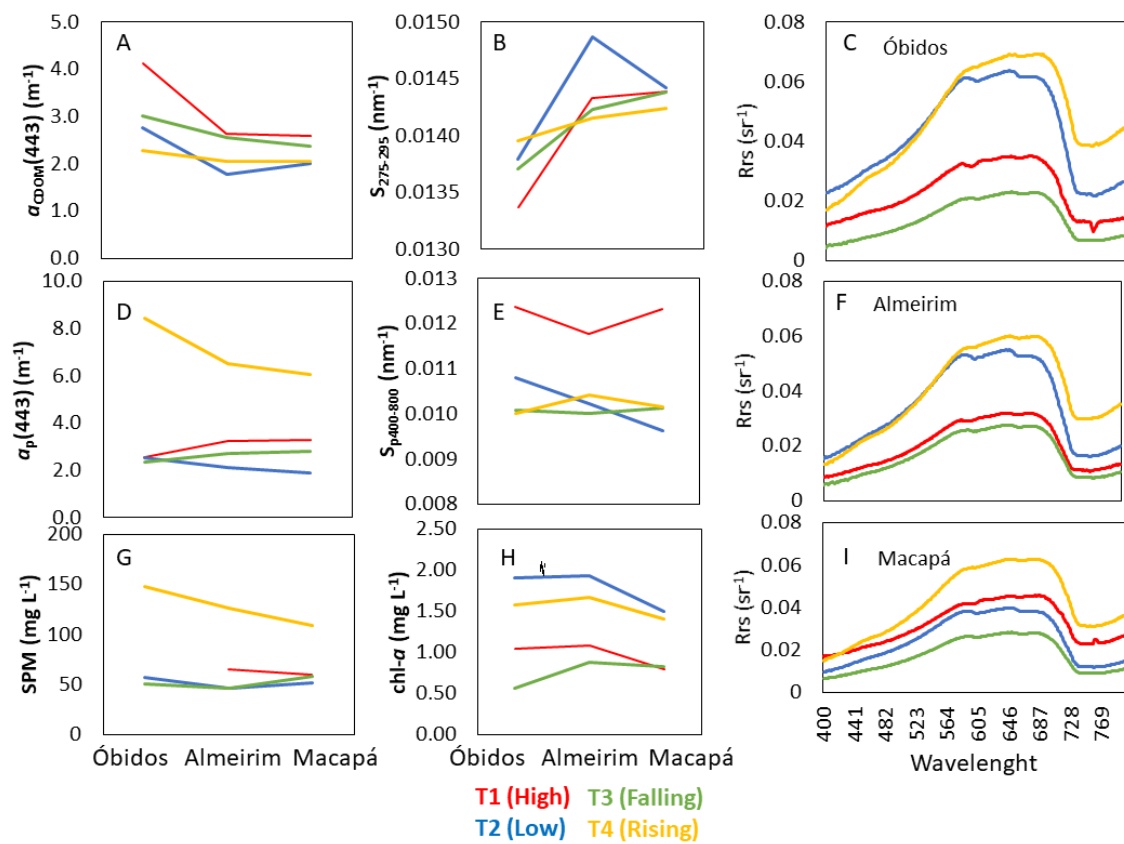
#### **4.3.3 Bio-optical spatial-seasonal variability along the river**

Radiometric and bio-optical spatial-seasonal variability from the Lower Amazon to the river's mouth are represented in Figure 4.8 showing average values of  $a_{CDOM}(443)$ ,  $S_{275-295}$ ,  $a_p(443)$ ,  $S_{p400-800}$ , SPM,  $chl a$  and  $R_{rs}$  for each station and season (campaigns: T1-T4). The spatial distribution shows that, for all seasons,  $a_{CDOM}(443)$  and  $chl a$  generally decrease from Óbidos to the river's mouth (Figure 4.6.A and 4.6.H), while the opposite trend is found for  $S_{275-295}$  that increases along the course of the river (Figure 4.6.B). The opposite trend of CDOM and  $S_{275-295}$  suggests a gradual decrease in DOM molecular weight by DOM degradation processes (especially bacterial) along the river course, as reported by other studies (WARD et al., 2016; 2013).

An inflexion point at Almeirim is observed for almost all parameters probably indicating the influence of Paru River waters, a CW river. Generally, SPM decreases and  $a_p(443)$  conjointly to  $S_{p400-800}$  are highly variable considering all the seasons for the study period. For all local stations, the radiometric spectra for RW season is elevated, with  $R_{rs}(670)$  close to  $0.05 \text{ sr}^{-1}$ , although the unique  $R_{rs}$  spectral shape (an increasing

reflectance on the green to NIR wavelength interval) discussed in the section 4.3.2 is less evident for Macapá. This may be related to a more diluted water, whereas Almeirim and Óbidos are closer to the reaches of Madeira and Solimões rivers. Both rivers are the main accountable for the sedimentary inputs at the Amazon River (PINET et al., 2017; FILIZOLA; GUYOT, 2009), and therefore, Almeirim and Óbidos stations could be under a stronger influence of SPM.

Figure 4.6 - Spatial distribution of bio-optical variability along the Amazon mainstream.



The parameters are averaged for each station per season. The first station is at Óbidos (~900 km from the mouth). The middle of the transect is at Almeirim (~450 km from the mouth). The transect ends at the Amazon mouth, in Macapá.

Source: Author's production.

The coefficient of variation per season along the transect (Óbidos-Almeirim-Macapá) shows an overall higher variability in  $R_{rs}(761)$  data translating modulation in the water masses bio-optical nature.  $R_{rs}(761)$  and  $a_{CDOM}(443)$  had also higher variability during

HW, while SPM and  $a_p(443)$  had during RW, and chl $a$  during FW. The slopes of CDOM and particles had a very low variability in all seasons ( $\leq 5\%$ ) (Table 4.5). During the FW the floodplains export particles to the Amazon River (ALCANTARA et al., 2011; NOVO et al., 2006), and therefore phytoplankton among sediments, that may enhance the variability of chl $a$  in the mainstream.

Table 4.5 - Coefficients of variation of  $a_{CDOM}(443)$ , SPM, chl $a$  and  $R_{rs}(761)$  along the Amazon River mainstream, during the different seasons: High Water (HW), Low water (LW), Falling water (FW) and Rising Water (RW).

	$a_{CDOM}(443)$	$S_{275-295}$	$a_p(443)$	$S_{p400-800}$	SPM	chl $a$	$R_{rs}(761)$
T1 (HW)	23%	3%	11%	2%	4%	14%	55%
T2 (LW)	19%	3%	12%	5%	9%	11%	20%
T3 (FW)	10%	2%	8%	0.5%	9%	18%	16%
T4 (RW)	5%	1%	15%	2%	13%	7%	11%

Source: Author's production.

Disregarding the season, the CV among the local stations shows that the variability decreases as the river flows downstream, emphasizing the gradual dilution of the tributaries inputs to the mainstream (Table 4.6). Despite the high variability, there is no statistically significant difference ( $p > 0.05$ , Kruskal-Wallis test) for all parameters among the local stations except for  $S_{275-295}$ . The latter parameter had a significant difference among samples measured at Óbidos and Macapá ( $p < 0.05$ , Dunn's post hoc), underlining the relevant action of the DOM degradation processes along the mainstream course.

Table 4.6 - Coefficients of variation of  $a_{\text{CDOM}}(443)$ ,  $S_{275-295}$ ,  $a_p(443)$ ,  $S_{p400-800}$ , SPM, chl $a$  and  $R_{rs}(761)$  along the Amazon River mainstream (considering all hydrological seasons together).

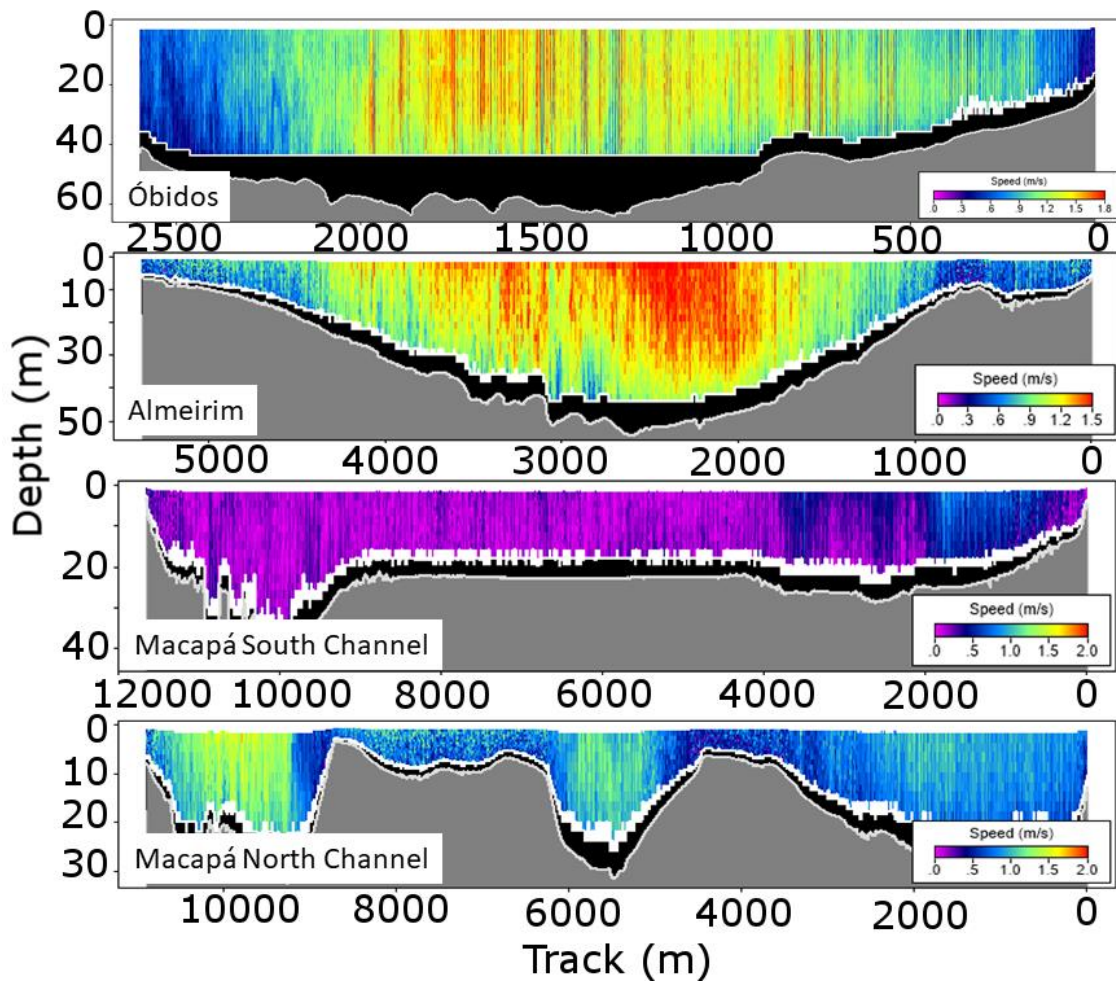
	Óbidos	Almeirim	Macapá
$a_{\text{CDOM}}(443)$	22%	16%	11%
$S_{275-295}$	2%	2%	0.50%
$a_p(443)$	65%	46%	44%
$S_{p400-800}$	9%	6%	10%
SPM	52%	46%	33%
chl $a$	40%	30%	28%
$R_{rs}(761)$	65%	50%	46%

Source: Author's production.

#### 4.3.4 River transversal bio-optical variability

Along the downstream path, the channel bed roughness of a river is usually irregular and governs the water velocity. The friction against the bottom and mudbanks decreases the water velocity. As a matter of fact, the water at the surface in middle of a river reaches its maximum speed while both at bottom and sides of a river the water moves slower (DOWNS et al., 2002). The Figure 4.7 explicitly shows how different are the river bathymetry at specific stations (Óbidos, Almeirim, Macapá South and Macapá North channels), and underline the higher velocity of the river flow in the middle of the channel.

Figure 4.7 - Bathymetry and velocity profile of the Amazon River at Óbidos, Almeirim, Macapá South and Macapá North channels.

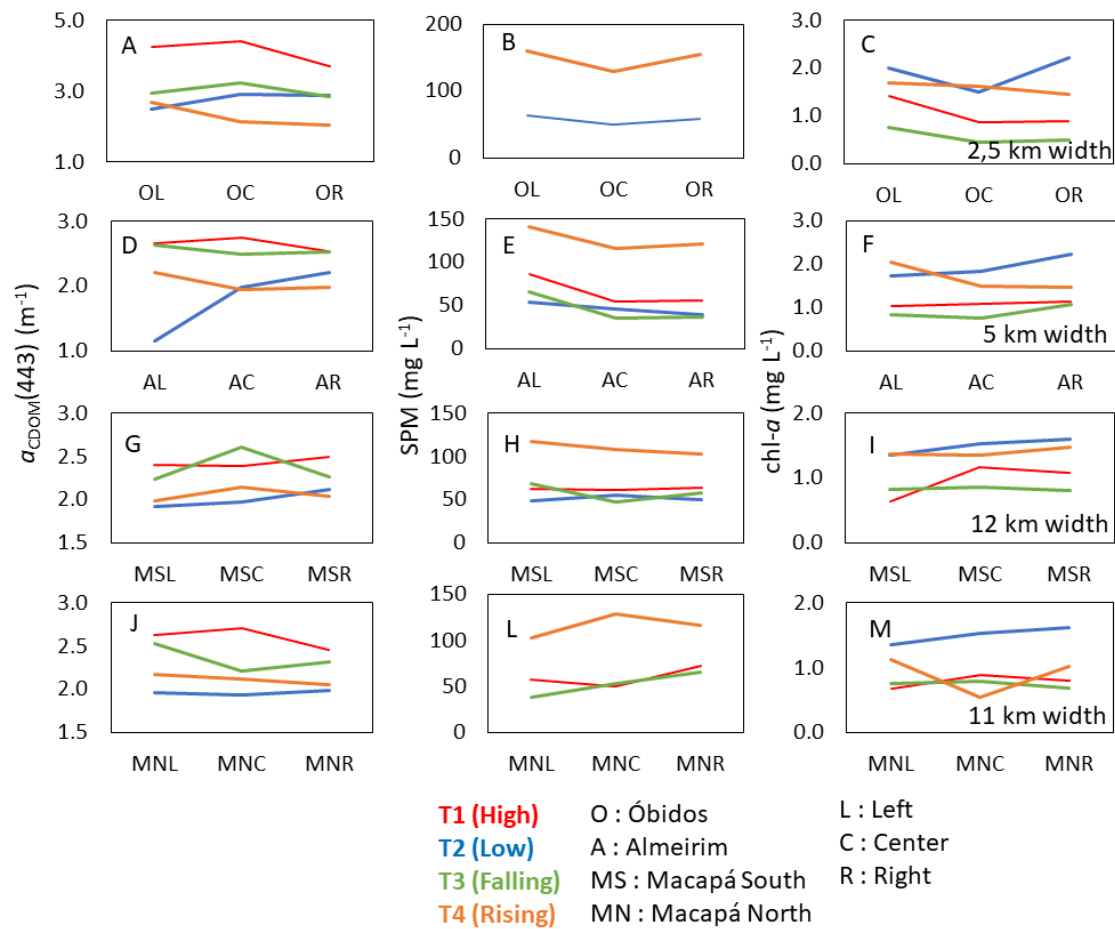


Measurement obtained using an Acoustic Doppler Current Profiler.

Source: Jeffrey Richey (2018), personal communication.

In a global perspective, the average of the parameters in each margin per season, demonstrates that the border of the mainstream has higher concentration of SPM and chl $a$ , and the center has a higher concentration of CDOM. This pattern is consistent in all local stations, except for SPM at Macapá North Channel, possibly associated with the high SPM measured during the RW season and an influence of the irregular bottom (Figure 4.8).

Figure 4.8 - Spatial distribution of bio-optical variability across the Amazon River channel at three sampling stations.



Three sampling stations: Óbidos (2,5 km of width), Almeirim (5 km of width), Macapá South (12 km of width) and Macapá North (11 km of width).

Source: Author's production.

It is plausible to argue that high SPM at the borders are related to terrestrial inputs (FILIZOLA; GUYOT, 2009; DUNNE et al., 1998) and that high chl-a are related to a decrease of velocity, as the related reduced turbulence favors phytoplankton growth (WU et al., 2011; SELLERS et al., 2003). Nevertheless, a statistic evaluation shows that the bio-optical properties  $a_{CDOM(443)}$ , chl-a and SPM, do not have a significant difference among the margins and the center ( $p > 0.05$ , Kruskal-Wallis test) for all locations studied (Óbidos, Almeirim, Macapá North and Macapá South channels). For



the entire period of cruises along the Lower Amazon (2014-2016),  $a_{\text{CDOM}}(443)$  had the lower variability at the margins, followed by SPM and chl *a* (6%, 11% and 13%, respectively). All the coefficients of variation are reported in Table 4.7.

Table 4.7 - Coefficients of variation of chl *a*,  $a_{\text{CDOM}}(443)$  and SPM for the margins along the mainstream Amazon River during different discharge seasons.

		Óbidos	Almeirim	Macapá North Channel	Macapá South Channel
T1 (HW)	chl <i>a</i> (mg L <sup>-1</sup> )	24%	3%	11%	24%
T2 (LW)		16%	11%	8%	7%
T3 (FW)		23%	15%	6%	2%
T4 (RW)		6%	16%	28%	4%
T1 (HW)	$a_{\text{CDOM}}(443)$ (m <sup>-1</sup> )	7%	3%	4%	2%
T2 (LW)		7%	26%	1%	4%
T3 (FW)		5%	2%	6%	7%
T4 (RS)		13%	6%	3%	3%
T1 (HW)	SPM (mg L <sup>-1</sup> )	--	--	--	--
T2 (LW)		9%	13%	7%	5%
T3 (FW)		1%	30%	22%	15%
T4 (RW)		9%	9%	9%	5%

Margins: left, center and right. Locations of stations: Óbidos, Almeirim, Macapá North and Macapá South Channel. Discharge seasons: High Water (HW), Low water (LW), Falling water (FW) and Rising Water (RW).

Source: Author's production.

#### 4.3.5 Tidal impact on the Amazon bio-optical variability

The tidal influence over biogeochemical parameters on the lower reaches of the Amazon River was the focus of the last two cruises (T5 and T6 campaigns). Tidal impact on river flow and biogeochemical parameters (e.g. SPM, dissolved organic carbon) at the Amazon River and other large rivers has been the subject of many studies reported in the literature (SAWAKUCHI et al., 2017; KOSUTH et al., 2009; UNCLES et al., 2002; JAEGER; NITTROUER et al., 1995). Near the Amazon mouth, the tide can completely

reverse the flow toward the river upstream, increasing the water residence time and turbulence (SAWAKUCHI et al., 2017).

The decrease in river discharge caused by the tidal effect is obvious during the LW (T5) and HW (T6) seasons for both Macapá South and North channels (Figure 4.9). On the other hand, the variation of the assessed optical and biogeochemical parameters was not so clear (Figure 4.9). Nevertheless, the parameters  $a_{CDOM}(443)$ , SPM and  $R_{rs}(671)$  has an oscillation throughout the 13 hours sampling period and generally, seems to be responding to the tidal cycle. During the LW the parameters had lower variability than during HW, and for the both seasons, CDOM had the lower CV (<10%) (Table 4.8).

Figure 4.9 - River discharge and tidal variability of radiometric and bio-optical properties.

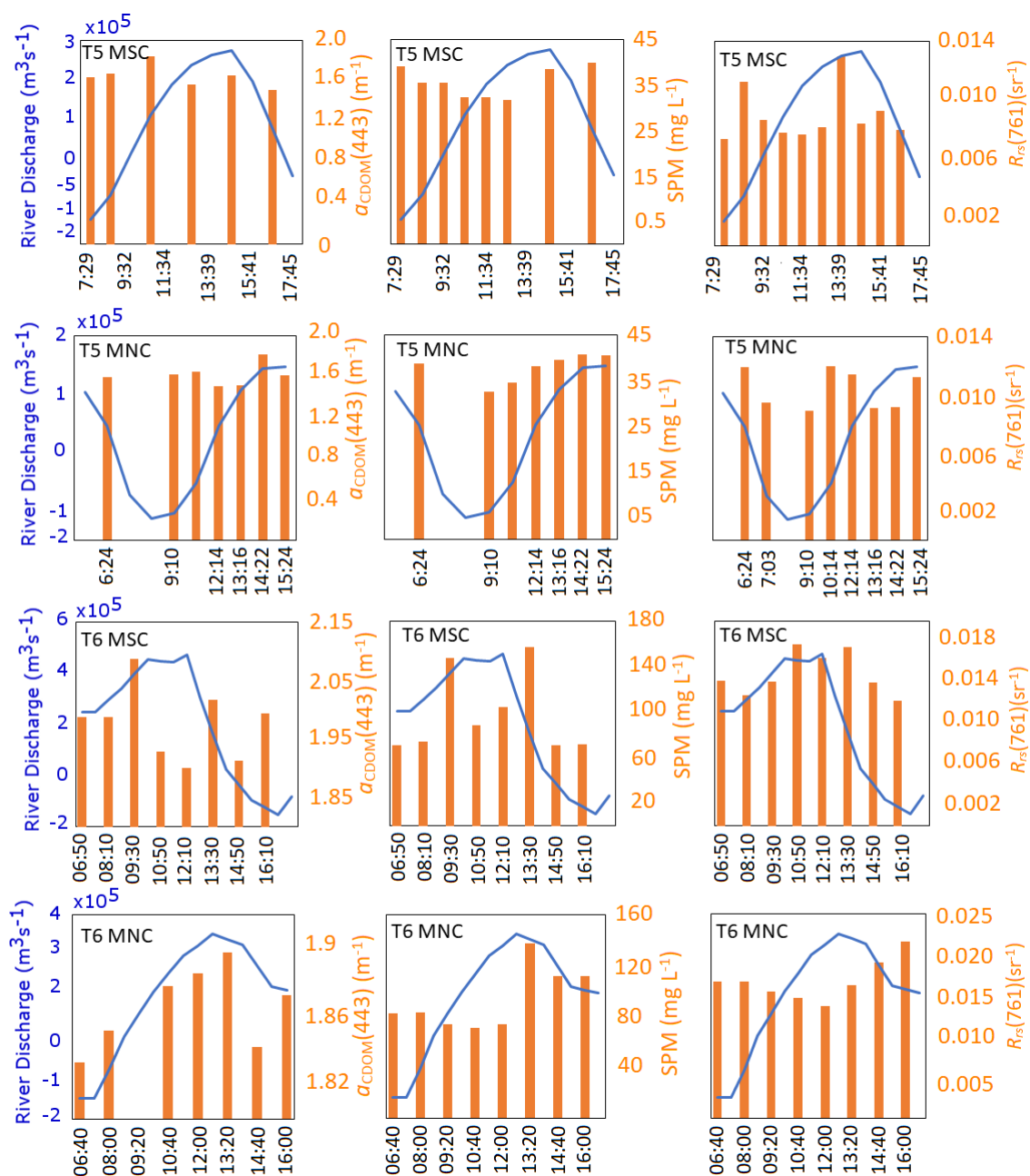


Table 4.8 - Coefficients of variation of  $a_{\text{CDOM}}(443)$ , SPM and  $R_{rs}(671)$  according to tidal cycle.

MSC/MNC	$a_{\text{CDOM}}(443)$	SPM	$R_{rs}(761)$
T5 (LW)	6%/6%	9%/8%	19%/12%
T6 (HW)	3%/1%	34%/24%	13%/14%

Stations: Macapá South (MSC) and Macapá North (MNC) channels. Discharge seasons: Low water (LW) and High water (HW).

Source: Author's production.

#### 4.4 Final considerations

The present chapter address the description of the bio-optical and radiometric variability along the Lower Amazon, considering different spatial-temporal scales. The main goal was to characterize this variability regarding the OWT. The practical issues related to regional in situ measurements are also discussed in the chapter.

In situ measurements of  $a_{\text{phy}}$  and  $a_{\text{nap}}$  represent a real challenge for the turbid waters of the Amazon River. The chosen method for particle depigment using sodium hypochlorite (TASSAN; FERRARI, 1995) was not suitable for the samples acquired in the study region likely due to a particle-bound DOM at the mineral particles. The same issue was observed by previous studies (see e.g. BINDING et al., 2008). Other methods such as the use of methanol was also described as not being effective to separate  $a_{\text{phy}}$  from  $a_{\text{p}}$  for all samples (GALLEGOS, 2005) and the use of combustion can cause changes in the particle absorption, and the sum of components are not conserved ( $a_{\text{p}} = a_{\text{phy}} + a_{\text{nap}}$ ) (WERDELL et al., 2018; ESTAPA et al., 2012). The depigment complication leads to inaccuracies in the measurement of  $a_{\text{phy}}$  and  $a_{\text{nap}}$ , requiring further studies to develop a compelling method to extract the signal of  $a_{\text{phy}}$  from  $a_{\text{p}}$ . One way to try to overcome this issue might be to the use of a derivative analysis on  $a_{\text{phy}}$ , enhancing the phytoplankton absorption when it removes the strong absorption related to CDOM. Nevertheless, the ratio of  $a_{\text{phy}} \text{ B95}$  and  $a_{\text{p}}$  shows that  $a_{\text{phy}}$  contribution is very low for

the Amazon River (2% on average), emphasizing the practical difficulty to assess phytoplankton signal. For CW  $a_{\text{phy}}$  was relatively close to Bricaud's model, although the interference of CDOM is still very high at the absorption coefficient.

Likewise, further studies are necessary to understand the variability of  $S_p$  observed at the Lower Amazon. At this point it is not clear if the slope found here is able to trace the relative proportion of organic and inorganic particles, while this potential was underlined for coastal waters (BABIN et al., 2003). The difficulty to assess reliable in situ  $a_{\text{phy}}$ ,  $a_{\text{nap}}$  clearly add difficulties for the development of a regional optical model dedicated to remote sensing inversion algorithms in the study area.

SPM measurements had a good relationship with  $a_p$  suggesting a high concentration of organic particles, especially in CW rivers. As expected, CW rivers had the lowest values of SPM, and the samples collected during the RW in the Amazon River had the higher values. The variability of  $a_p(443)$  : SPM at CW is also higher, indicating the influence of the Amazon mainstream onto the tributaries.

The optical classification presented here highlighted four distinct OWT for the Lower Amazon, regarding the seasonality. Aside from the evident difference of Amazon River and CW, these classes are subdivided in two branches: Rising-High waters and Falling-Low waters. During the Rising-High seasons, the Amazon River overflows and mixes with the water of tributaries, increasing the amount of SPM. In addition, the overflow of the Amazon River can promote phytoplankton bloom at CW rivers by achieving the optimal balance between the nutrients input coming from the Amazon waters and low turbidity of CW rivers that allows more light passing through the water. For the Amazon River one class gather samples of FW, LW as well as HW from  $R_{rs}$  measured during the first campaign (T1). The second class gathers samples of RW and HW from  $R_{rs}$  measured during the last campaign (T6). The difference between the HW from the first and last campaign can be related to a discharge time shifting (Figure 3.4, and see

discussion on Chapter 5, section 5.3). The class formed by Rising-High water presented an increase  $R_{rs}$  signal from green to NIR related to the considerable increase in SPM.

The spatial variability along the mainstream shows a concentration decrease of CDOM, SPM and chl $a$  downstream, suggesting a dilution of the waters as the contribution of the inputs from the Amazon tributaries is increasing. The variability of the assessed parameters through the seasons as well as among local sampling at the river course, didn't present a significative difference, except for the  $S_{275-295}$  indicating a decrease in DOM molecular weight by DOM degradation processes.

Finally, the assessment of small-scale regarding the spatial and temporal variability, shown some slight higher values of SPM and chl $a$  at the Amazon River margins, and CDOM at the center of the river, but this difference is not statistically significant. The same conclusion can be performed regarding the tidal influence. Although the bio-optical parameters tend to follow the tide cycle, no meaningful difference can be evidenced could have been evidenced from the current data set.

## 5 USING CDOM OPTICAL PROPERTIES FOR ESTIMATING DOC CONCENTRATIONS AND $p\text{CO}_2$ IN THE LOWER AMAZON RIVER

### 5.1 Introduction

Terrestrial humic substances are the dominant contributor to DOM in freshwaters (WETZEL; LIKENS, 2000). DOC is the major fraction of DOM active in the global carbon cycle, with fluvial export of DOC providing the largest flux of reduced carbon ( $0.25 \text{ Pg C yr}^{-1}$ ) from land to ocean (BATTIN et al., 2008). The fraction of DOM that absorbs ultraviolet (UV) and visible light, CDOM, is one of the major contributors to the absorption budget of most freshwaters. Freshwater systems also contain large amounts of  $\text{CO}_2$  relative to the atmosphere (WARD et al., 2017). In small streams most  $\text{CO}_2$  is derived from soils and groundwater inputs (JOHNSON et al., 2006), whereas in large riverine systems the input and in situ degradation of DOM by both microbes (WARD et al., 2018) and UV light (KOEHLER et al., 2014) is a major source of  $\text{CO}_2$ , which is subsequently outgassed to the atmosphere.

The importance of freshwater systems on controlling the export and transformation of terrestrial DOM and the intimate relationship between these dynamics and  $p\text{CO}_2$  is well recognized (SAWAKUCHI et al., 2017; WARD et al., 2017, 2015; RICHEY et al., 2002). However, there is still a lack in the detailed understanding of how these dynamics vary in space and time, particularly in the tropics, which contribute disproportionately to global  $\text{CO}_2$  emissions and DOM export from inland waters (LAUERWALD et al., 2015; RICHEY et al., 2002). The rivers in the Amazon basin, for example, are estimated to outgas from  $0.5$  to  $1.39 \text{ Gt C yr}^{-1}$  (SAWAKUCHI et al., 2017; ABRIL et al., 2014).

The dynamics of CDOM, DOC and  $p\text{CO}_2$  in the Amazon River are largely influenced by the seasonal changes in the river discharge (CURTARELLI et al., 2016; VIHERRMAA et al., 2016; WARD et al., 2015; MOREIRA-TURCQ et al., 2013; RUDORFF et al., 2011; RICHEY et al., 2002). Seasonal variation in the rainfall intensity over the Amazon basin can also

induce strong modulation in the quality (lability) of the DOC delivered to the river (RICHEY et al., 2013; NEU et al., 2011; JOHNSON et al., 2006). Several recent studies have emphasized trends towards the occurrence of extreme climatic events in some regions of the Amazon basin, illustrating the potential impact of such events on rain and river discharge patterns in the area (CORREA et al., 2017; JIMÉNEZ-MUÑOZ et al., 2016; MARENGO; ESPINOZA, 2016; ESPINOZA et al., 2014).

Sawakuchi et al. (2017) estimated that  $\sim 0.48 \text{ Pg C year}^{-1}$  of  $\text{CO}_2$  could be outgassed just from the Lower Amazon River, if the entire spatial extent of the geographical mouth is considered, fueled primarily by the metabolism of DOM (WARD et al., 2018; 2013). But the extreme heterogeneity and vast scales of the region make it difficult to interpolate over space and time, suggesting that suitable means of remote sensing could provide much-needed insight into the dynamics of this complex region.

The objective of this chapter is to investigate the potential use of CDOM absorption coefficient for estimating DOC concentration and  $p\text{CO}_2$  in the Lower Amazon River along a 900 km transect from the historic downstream gauging station, Óbidos, to the river mouth with samples collected in contrasting water types (clear and turbid waters) under different discharge conditions. This chapter provides the first bio-optical approach for assessing the carbon content at the Lower Amazon, a region recently pointed out as one of the most active  $\text{CO}_2$  emission areas among inland waters (SAWAKUCHI et al., 2017).

Numerous studies have aimed to relate  $a_{\text{CDOM}}$  to DOC content in estuarine and coastal waters (BREZONIK et al., 2015; VANTREPOTTE et al., 2015; FICHOT; BENNER, 2012; SPENCER et al., 2012; MANNINO et al., 2008; CHEN et al., 2004; VODACEK et al., 1997; FERRARI et al., 1996) to use the latter optical proxy assessing DOC distribution through in situ or satellite observations. More recent studies have clearly emphasized the presence of highly significant linear relationships between  $a_{\text{CDOM}}$  and DOC in coastal waters dominated by terrestrial inputs of DOM, further illustrating the strong seasonal



and regional dependency in the link between CDOM and organic carbon content (VANTREPOTTE et al., 2015; FICHOT; BENNER, 2012). While CDOM absorption at a defined wavelength is providing quantitative information on DOM concentration, the spectral slope of the CDOM absorption spectra in the UV domain [275-295 nm] ( $S_{275-295}$ ) has been shown to provide relevant insights into DOM composition and origin (FICHOT; BENNER, 2012; HELMS et al., 2008). The potential use of  $S_{275-295}$  as a relevant optical proxy for the DOC-normalized absorption coefficient of CDOM have been further demonstrated, emphasizing the interest of this descriptor for better constraining the natural variability in the CDOM to DOC relationship at both seasonal (FICHOT; BENNER, 2011) and regional (DANHIEZ et al., 2017; VANTREPOTTE et al., 2015) scales. High  $S_{275-295}$  values are usually related to highly (biologically or photochemically) degraded DOM (NELSON; SIEGEL, 2013; FICHOT; BENNER, 2012; HELMS et al., 2008). Helms et al. (2008) have further documented the interest of the ratio of two narrow spectral slopes ( $S_R$ ;  $S_{275-295}/S_{350-400}$ ) for assessing the molecular weight of the DOM within CDOM-rich waters.

Various potential descriptors of  $p\text{CO}_2$  variability in inland ecosystems have been recently documented. A strong linear dependency between  $p\text{CO}_2$  and DOC content has been for instance emphasized within diverse boreal and temperate inland waters (LAPIERRE; DEL GIORGIO, 2012; LARSEN et al., 2011; SOBEK et al., 2005). The presence of such relationship in tropical regions was conversely not confirmed, including some Brazilian lakes of the Amazon basin (PINHO et al., 2015; MAROTTA et al., 2010). CDOM, more likely adapted to the development of ocean colour remote sensing based  $p\text{CO}_2$  inversion algorithms, has been also considered as a potential proxy for  $p\text{CO}_2$  (KUTSER et al., 2015; LOHRENZ et al., 2006; CLARK et al., 2004). However, the potential use of CDOM for estimating  $p\text{CO}_2$  in the Amazon waters still need to be evaluated.

## 5.2 Materials and methods

The dataset used in this chapter consists in CDOM and its subproducts ( $S_{275-295}$ ,  $S_{350-400}$  and  $S_R$ ), DOC,  $pCO_2$ , temperature and chl $a$  measurements for the Lower Amazon region, during the years of 2014-2017, contemplating all discharge seasons (TROCAS campaigns: T1 (HW), T2 (LW), T3 (FW), T4 (RW), T5 (LW) and T6 (HW)). The data were collected at the Amazon River and other CW rivers. CDOM, DOC,  $pCO_2$ , chl $a$  and temperature data are not available for T6. Since the number of DOC and  $pCO_2$  measurements is lower than CDOM and chl $a$ , the dataset was reduced to equal the number of samples (Table 5.1).

Table 5.1 - Total of in situ data for the campaigns during the years of 2014-2017.

Parameter	Total samples
$a_{CDOM}(\lambda)$ ( $m^{-1}$ )	80
DOC ( $\mu mol\ L^{-1}$ )	80
$pCO_2$ ( $\mu atm$ ) *	69
chl $a$ ( $mg\ L^{-1}$ )*	69
Temperature ( $^{\circ}C$ )*	69

\* Data not available for TROCAS 6 campaign

Source: Author's production.

## 5.3 Results and discussion

### 5.3.1 Optical and biogeochemical variability of the Lower Amazon River and tributary waters

Over the studied period, the average values of chl $a$  ( $1.2 \pm 0.45\ mg\ L^{-1}$ ), DOC ( $306 \pm 27\ \mu mol\ L^{-1}$ ),  $pCO_2$  ( $2777 \pm 1719\ \mu atm$ ) and temperature ( $29.8 \pm 0.8\ ^{\circ}C$ ) recorded over the Lower Amazon River were in the range of observations previously reported in the

region (SAWAKUCHI et al., 2017; PINHO et al., 2015; WARD et al., 2015; MOREIRA-TURCQ et al., 2013). The average  $a_{\text{CDOM}}(412)$  ( $\text{m}^{-1}$ ) for the Amazon River during these cruises ( $3.6 \pm 1.0 \text{ m}^{-1}$ ) was similar to the  $a_{\text{CDOM}}(400)$  value ( $2.97 \text{ m}^{-1}$ ) reported for the Curuai floodplain (KUTSER et al., 2016) (Table 5.2).

Table 5.2 - General statistics for clearwater (CW) and Amazon River stations considering all sampling periods (2014-2017).

	CW			Amazon River		
	Average $\pm$ SD	CV %	Range	Average $\pm$ SD	CV %	Range
DOC ( $\mu\text{mol L}^{-1}$ )	271 $\pm$ 103	40	134-503	306 $\pm$ 27	9	266-377
$a_{\text{CDOM}}(412)(\text{m}^{-1})$	3.3 $\pm$ 1.5	45	1.0-5.9	3.6 $\pm$ 1.0	28	2.5-7.0
$a^*_{\text{CDOM}}(412)$ ( $\text{m}^2.\text{mmol}^{-1}$ )	0.012 $\pm$ 0.004	34	0.005- 0.019	0.012 $\pm$ 0.002	20	0.009- 0.018
$S_{275-295}$ ( $\text{nm}^{-1}$ )	0.015 $\pm$ 0.002	11	0.013- 0.019	0.014 $\pm$ 0.0004	3	0.013- 0.015
$S_{350-400}$ ( $\text{nm}^{-1}$ )	0.017 $\pm$ 0.001	8	0.014- 0.018	0.016 $\pm$ 0.001	4	0.015- 0.018
Slope Ratio	0.91 $\pm$ 0.16	16	0.77-1.26	0.87 $\pm$ 0.03	3	0.80- 0.94
$p\text{CO}_2$ ( $\mu\text{atm}$ )	2010 $\pm$ 1472	73	451-5030	2777 $\pm$ 1789	62	1045- 6474
chl $a$ ( $\text{mg L}^{-1}$ )	6.4 $\pm$ 7.6	118	1.7-31.3	1.29 $\pm$ 3.8	30	0.6-2.2
Temp ( $^{\circ}\text{C}$ )	30.1 $\pm$ 0.7	2	28.9-31.6	29.8 $\pm$ 0.8	3	28.5- 30.7

General Statistics: maximum, minimum, mean, standard deviation – SD, and coefficient of variation – CV.

Source: Author's production.

Amazon River samples had slightly lower temperature and chl  $a$  values than the CW tributaries, with their higher primary production rates and lower turbidity (GAGNE-

MAYNARD et al., 2017) (Table 5.2). All parameters other than temperature generally presented a higher seasonal variability for the CW stations compared to the mainstream. Average  $a_{\text{CDOM}}(412)$  values were similar between Amazon River and CW samples (3.6 vs 3.3  $\text{m}^{-1}$ , respectively). However, higher DOC and  $p\text{CO}_2$  were observed in the Amazon River waters when compared to the other rivers. On the other hand, CW rivers generally had higher values of  $S_{275-295}$  and  $S_R$  (0.015  $\text{nm}^{-1}$  and 0.91, respectively,  $p < 0.01$ ) indicating differences in DOM quality between these different waters of the Amazon basin. The highest values for  $S_{275-295}$  and  $S_R$  were found in CW tributaries when compared to those collected within the Amazon River (0.014 and 0.87  $\text{nm}^{-1}$ , respectively), indicating the presence of lower molecular weight DOM that could be attributed to the higher abundance of algae (HELMS et al., 2008). These results are similar to molecular level differences in DOM composition previously observed in the Tapajós and Amazon rivers (SEIDEL et al., 2016).

All parameters other than temperature generally presented a higher temporal variability for the CW stations, emphasizing the seasonal modulation in the intensity of the water mixing of the clearwater rivers and Amazon River according to the discharge season (Table 5.2).

Two different seasonal patterns regarding the DOM dynamics could be identified in the Amazon River. First, average CDOM and DOC values for samples corresponding to T1, T2, T3 and T5 cruises are following the discharge patterns with a clear co-variation between CDOM and DOC levels. The highest CDOM and DOC average values (Table 5.3, 4.6 and 4.7  $\text{m}^{-1}$ , 297 and 337  $\mu\text{mol L}^{-1}$  for CW and Amazon River, respectively) were found during HW discharges conditions (T1), while the lowest ones (Table 5.3, 2.8  $\text{m}^{-1}$  and 287  $\mu\text{mol L}^{-1}$  for the Amazon River) are occurring during low discharge conditions (T2 and T5), especially during T5 due to a severe drought in 2016 related to an El Niño event (JIMÉNEZ-MUÑOZ et al., 2016). Intermediary values (Table 5.3, 2.6 and 4.2  $\text{m}^{-1}$ , 171 and 313  $\mu\text{mol L}^{-1}$  for CW and Amazon River, respectively) are found during transition period (falling conditions, T3). The latter pattern tends to suggest that the

DOM concentration of the Lower Amazon region is mainly driven by the intensity of the river discharge and therefore the inputs from land-floodplains.

Table 5.3 - Average of parameters for each sampling campaign for the clearwaters (CW) and Amazon River (Am) samples.

	T1 HW		T2 LW		T3 FW		T4 RW		T5 LW	T6 HW
	CW	Am	CW	Am	CW	Am	CW	Am	Am	Am
DOC ( $\mu\text{mol L}^{-1}$ )	297 $\pm$ 72	337 $\pm$ 20	186 $\pm$ 41	303 $\pm$ 22	171 $\pm$ 22	313 $\pm$ 64	371 $\pm$ 80	381 $\pm$ 15	287 $\pm$ 12	420 $\pm$ 24
$a_{\text{CDOM}}$ (412) ( $\text{m}^{-1}$ )	4.6 $\pm$ 0.3	4.7 $\pm$ 1.1	1.7 $\pm$ 1.0	3.3 $\pm$ 0.7	2.6 $\pm$ 0.7	4.2 $\pm$ 0.4	3.9 $\pm$ 1.3	3.6 $\pm$ 0.3	2.8 $\pm$ 0.3	3.3 $\pm$ 0.1
$a^*_{\text{CDOM}}$ (412) ( $\text{m}^2 \cdot \text{m}^{-1}$ )	0.01 $\pm$ 0.00 28	0.0 14 $\pm$ 0.0 023	0.0 10 $\pm$ 0.0 051	0.0 11 $\pm$ 0.0 017	0.0 15 $\pm$ 0.0 023	0.0 14 $\pm$ 0.0 03	0.0 10 $\pm$ 0.0 022	0.0 09 $\pm$ 0.0 005	0.01 0 $\pm$ 0.00 07	0.008 $\pm$ 0.000 5
$S_{275-295}$ ( $\text{nm}^{-1}$ )	0.01 $\pm$ 0.00 06	0.0 14 $\pm$ 0.0 004	0.0 17 $\pm$ 0.0 019	0.0 14 $\pm$ 0.0 006	0.0 15 $\pm$ 0.0 011	0.0 14 $\pm$ 0.0 003	0.0 14 $\pm$ 0.0 007	0.0 14 $\pm$ 0.0 003	0.01 5 $\pm$ 0.00 3	0.015 $\pm$ 0.000 2
$S_{350-400}$ ( $\text{nm}^{-1}$ )	0.01 $\pm$ 0.00 04	0.0 16 $\pm$ 0.0 005	0.0 15 $\pm$ 0.0 007	0.0 16 $\pm$ 0.0 01	0.0 17 $\pm$ 0.0 001	0.0 17 $\pm$ 0.0 003	0.0 18 $\pm$ 0.0 005	0.0 17 $\pm$ 0.0 004	0.01 7 $\pm$ 0.00 03	0.018 $\pm$ 0.000 1
Slope Ratio	0.85 $\pm$ 0.01 1	0.8 6 $\pm$ 0.0 1	1.1 8 $\pm$ 0.0 8	0.8 9 $\pm$ 0.0 4	0.8 7 $\pm$ 0.0 6	0.8 5 $\pm$ 0.0 2	0.8 1 $\pm$ 0.0 4	0.8 2 $\pm$ 0.0 2	0.88 $\pm$ 0.02	0.82 $\pm$ 0.01
$p\text{CO}_2$ ( $\mu\text{atm}$ )	334 5 $\pm$ 1685	477 9 $\pm$ 106 0	853 $\pm$ 529	159 0 $\pm$ 458	210 4 $\pm$ 6	398 1 $\pm$ 4	211 5 $\pm$ 3	188 8 $\pm$ 495	114 6 $\pm$ 93	-----

chl $a$ (mg L <sup>-1</sup> )	17.1 ± 14.2	1.0 ± 0.2	6.2 ± 2.0	1.7 ± 0.3	2.4 ± 0.5	0.8 ± 0.2	4.7 ± 2.8	1.4 ± 0.4	1.4 ± 0.1	-----
Temp (°C)	29.7 ± 0.05	28. 8 ± 0.2	30. 8 ± 0.6	30. 3 ± 0.3	29. 4 ± 0.4	29. 0 ± 0.2	30. 3 ± 0.4	30. 1 ± 0.6	30.3 ± 0.5	-----
Dischar ge (m <sup>3</sup> /s)	284100 ± 2769	117785 ± 835		265028 ± 1731		205013 ± 965		982 37 ± 164		2690 48 ± 451

Average ± standard deviation

Source: Author's production.

Specific situations departing from such general seasonal modulations were, however, observed during T4 and T6. For these two cruises  $a_{\text{CDOM}}(412)$  values remained relatively low (3.6 and 3.3 m<sup>-1</sup>, respectively), when compared to the corresponding DOC contents (381 and 420 µmol L<sup>-1</sup>), leading for these two cruises to the lowest  $a^*_{\text{CDOM}}(412)$  average values (0.009 and 0.008 m<sup>2</sup>.mmol<sup>-1</sup>, for T4 and T6, respectively, see Table 5.3). The patterns observed for T4 and T6 tend to indicate that the terrestrial inputs of DOC and CDOM to the Lower Amazon are not fully co-varying with the river discharge. As a matter of fact, the correlation between DOC average values and the discharge data are much higher when excluding rising condition measurements ( $R^2=0.16$  considering all the cruises and 0.79 excluding T4 and T6, data not shown), with relatively high DOC contents with respect to the corresponding Amazon discharge levels for these two cruises (Table 5.3).

The latter peculiar feature tends to indicate the presence of strong seasonal modulation in the DOM quality according to the timing of discharge and not only its intensity. T4 is corresponding to the RW season. In this case, the low CDOM-high DOC situation might reflect a difference in the quality (lability) of the DOM accumulated in source areas (e.g. floodplains, flooded forest, seasonally isolated lakes, see e.g., ABRIL et al. 2014) and then mobilized during the increase of the Amazon waters level. The

situation for the T6 samples (April 2017, beginning of the high season) is globally similar to the one found during T4 (February 2016). During the year of 2017 a modification occurs in the general river discharge pattern, probably linked to the El Niño event of 2015-2016 (CUNHA; STERNBERG, 2018; JIMÉNEZ-MUÑOZ et al., 2016), as illustrated here by the decay of about one month in the maximal discharge values recorded at Óbidos in 2017 (beginning of May), when compared to the conditions observed from 2014 to 2016 (late May, Fig. 3.4). This suggests that besides seasonal modulation, inter-annual variability in the timing of the hygrometric regime can modulate the quality of the DOM mobilized from land-floodplain flush and delivered to the river. Note that short time scale processes such as heavy rain event might also represent another source of variability in the quality of the terrestrial DOM inputs, as emphasized in other tropical environments (PEREIRA et al., 2014). Temporal variability in the average  $S_{275-295}$  and  $S_R$  are relatively narrow when compared to the variability found at spatial scale between the different water types (CW, Amazon) investigated in the frame of this study (Tables 5.2 and 5.3). The slightly lowest  $S_R$  values found for T4, T6 might suggest the presence of DOM with a higher molecular weight for these two cruises when compared to the other cruises. However, the understanding of the source and sink mechanisms driving this apparent heterogeneity in the DOM characteristics of the Lower Amazon according to the discharge conditions (intensity and timing), would require additional measurements including some specifically dedicated to the characterization of the seasonal DOM dynamics within the diversity of source areas surrounding the Lower Amazon.

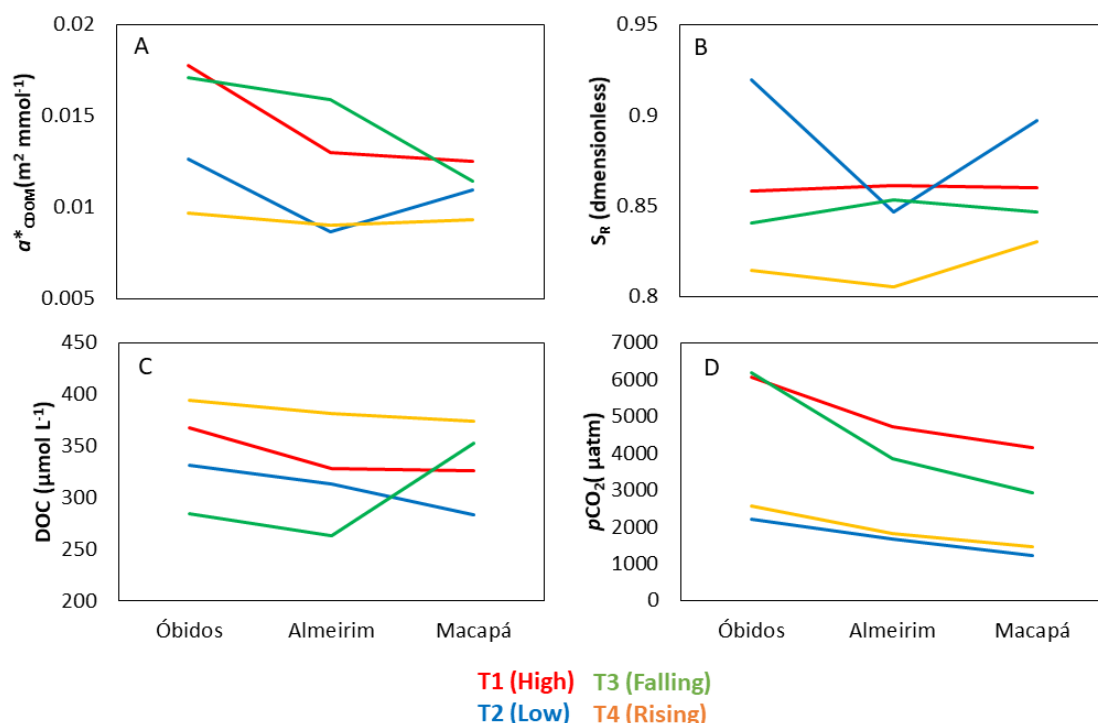
The latter temporal patterns were not observed for the  $pCO_2$  values. An ANOVA of  $pCO_2$  between different seasons, combined with a post-hoc test (Tukey HSD for unequal N), reveals that  $pCO_2$  for the stations of the Amazon was higher during the HW (T1) and FW (T3) seasons while the data for the other cruises showed the same mean values ( $p > 0.05$ ). In contrast with the Amazon samples, no clear seasonal pattern can be found regarding the biogeochemical and bio-optical properties of the CW samples. This might be related to the higher complexity of the factors driving DOM

dynamics for the corresponding water masses which result for the balanced effects of autochthonous and allochthonous DOM inputs, mixing processes between CW and Amazon River waters and modulation related to both bacterial and photochemical degradation processes. Low CDOM and DOC values are found during the LW and FW seasons (T2 and T3, respectively) translating the combined action of low allochthonous (low land flush) and autochthonous (low chl $a$ ) sources of DOM. As observed for the Amazon River, high DOC values recorded for CW during T4 were not associated with an equivalent raise in the CDOM values reinforcing the peculiar characteristics of the DOM input during the rising season. No seasonal difference was found in the  $p\text{CO}_2$  recorded for the CW samples ( $p > 0.05$ ).

In order to illustrate the spatial variability from the Lower Amazon to the river's mouth, averaged DOC,  $p\text{CO}_2$ ,  $a^*_{\text{CDOM}}(412)$  and  $S_R$  are represented for each cruise in Figure 5.1. Since  $a_{\text{CDOM}}(412)$  spatial variability is proportional to  $a_{\text{CDOM}}(443)$  presented in Chapter 4 (section 4.3.3),  $a_{\text{CDOM}}(412)$  and  $S_{275-295}$  spatial distribution are not represented in Figure 5.1. The spatial distribution shows that the carbon content (DOC: Figure 5.1.C, and  $p\text{CO}_2$  Figure 5.1.D) generally decreased from Óbidos to the river mouth. This general pattern remained consistent for all the seasons sampled, except for DOC during the falling season (T3), which tended to increase towards the mouth of the river (Macapá), while no similar pattern could be observed for CDOM (Chapter 4, section 4.3.3, Figure 4.8.A). The increase of DOC along the transect Óbidos-Macapá was reported by Ward et al. (2015) as a result of the combination of strong organic matter inputs from tributaries and floodplains and the degradation of particulate carbon into dissolved molecules. Such high export rates of labile organic matter from floodplains to the river during the FW season, was also reported by Moreira-Turcq et al. (2013). However, this labile material does not persist further out into the plume once exported to the ocean, leaving behind a background of recalcitrant DOM (MEDEIROS et al., 2015; SEIDEL et al., 2015).



Figure 5.1 - Spatial distribution of biogeochemical parameters along the Amazon mainstream.



The parameters were averaged for each station per season. The first station is at Óbidos (~900 km from the mouth). The middle of the transect is at Almeirim (~450 km from the mouth). The transect ends at the Amazon mouth, in Macapá, and T5 and T6 were sampled at the river mouth only.

Source: Author's production.

The opposite trend of CDOM and  $S_{275-295}$ , discussed in the previous chapter (Chapter 4, section 4.3.3, Figure 4.8.A), is also illustrated here by the general sharp decreasing patterns in  $a^*_{CDOM}(412)$ , translating differences in the intensity of the degradation rates for DOC and CDOM along the Amazon water course (Figure 5.1.A).

Note that the carbon content, DOC and  $pCO_2$  spatial distribution, also has a slight inflexion point at Almeirim (Figure 5.1), emphasizing a potential influence of inputs of the CW from the Paru River on the biogeochemical characteristics of this area (WARD et al., 2016) (Table 5.2). The decrease in the  $CO_2$  degassing along the Lower Amazon

River region reported here, is consistent with previous observations provided by Sawakuchi et al. (2017).

### 5.3.2 $a_{\text{CDOM}}(412)$ to DOC relationships

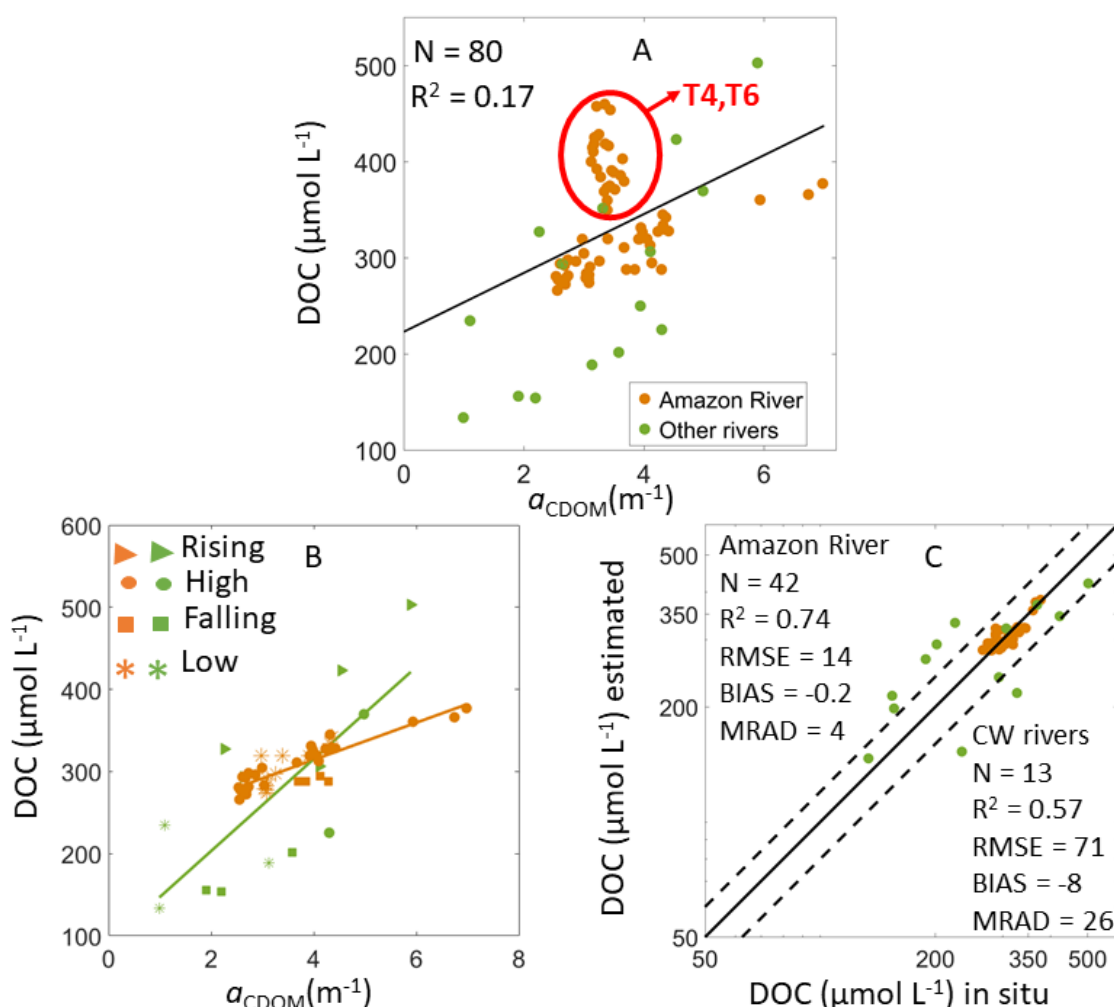
Considering the whole data set gathered in the frame of this study, the direct relationship between  $a_{\text{CDOM}}(412)$  and DOC ( $N = 80$ ;  $R^2 = 0.17$ ,  $p < 0.05$ ) had a low accuracy (Figure 5.2.A). This absence of general co-variation between CDOM and DOC can be related to two specific features, as explained below

First, Amazon River water samples for T4 and T6 present a pattern very different from the other cruises, with a general decoupling between CDOM and DOC data (Figure 5.2.A). This absence of co-variation between CDOM and DOC for T4 and T6 can be related to the peculiar characteristics of the terrestrial DOM inputs induced by land-floodplain flush during the rising of the Amazon waters. Here, the decoupling observed between CDOM and DOC could translate a spatial heterogeneity in the DOM sources mobilized during such discharge conditions. Floodplain areas surrounding the Amazon have been for instance showed to be extremely heterogeneous in terms of vegetation-water connections (CUNHA; STERNBERG, 2018; ABRIL et al., 2014). However, no information about the DOM dynamics in the latter water bodies is currently available.

Second, a clear discrepancy in the link between CDOM and DOC exists when considering the CW (whole data set) and Amazon samples (for T1, T3 and T5) separately (Figure 5.2.A). When splitting these data (Figure 5.2.B), two different significant linear relationships between  $a_{\text{CDOM}}(412)$  and DOC can be drawn (Figure 5.2.C, Amazon River:  $N=42$ ,  $R^2=0.74$ ,  $p<0.05$  ; CW:  $N= 13$ ,  $R^2 = 0.57$ ,  $p<0.05$ ) underlining the strong biogeochemical heterogeneity of the Amazon basin water masses. The dispersion around these two relationships can be partly attributed to seasonal modulation in DOM quality; however, more data are needed to clarify the impact of these seasonal patterns, especially for the CW data set which is relatively small ( $N=13$ ). Note that the presence of such linear dependency between CDOM and DOC is not due,

unlike coastal waters, to mixing processes, but more likely to a parallel (biological and photochemical) degradation of both CDOM and DOC along the Amazon River course.

Figure 5.2 - Direct relationship between  $a_{\text{CDOM}}(412)$  and [DOC].



A) All data from the Lower Amazon (N = 80;  $R^2 = 0.17$ ,  $p < 0.05$ ); B) Amazon River (T1-T3, T5), (N = 42,  $R^2 = 0.74$ ,  $p < 0.05$ ) and CW rivers (N = 13,  $R^2 = 0.57$ ,  $p < 0.05$ ); C) Scatter plot of estimated [DOC] as a function of the direct relationship of in situ [DOC] and  $a_{\text{CDOM}}(412)$  (Amazon River: N = 42,  $R^2 = 0.74$ , RMSE = 14, Bias = -0.2; MRAD = 4; CW rivers: N = 13,  $R^2 = 0.57$ , RMSE = 71, Bias = -8; MRAD = 26). Data from T4 and T6 (N=25) are not showed in a separated panel due the absence of significant direct CDOM-DOC relationship. Solid lines represent 1:1 line and dashed lines represent the 20% error lines.

Source: Author's production.

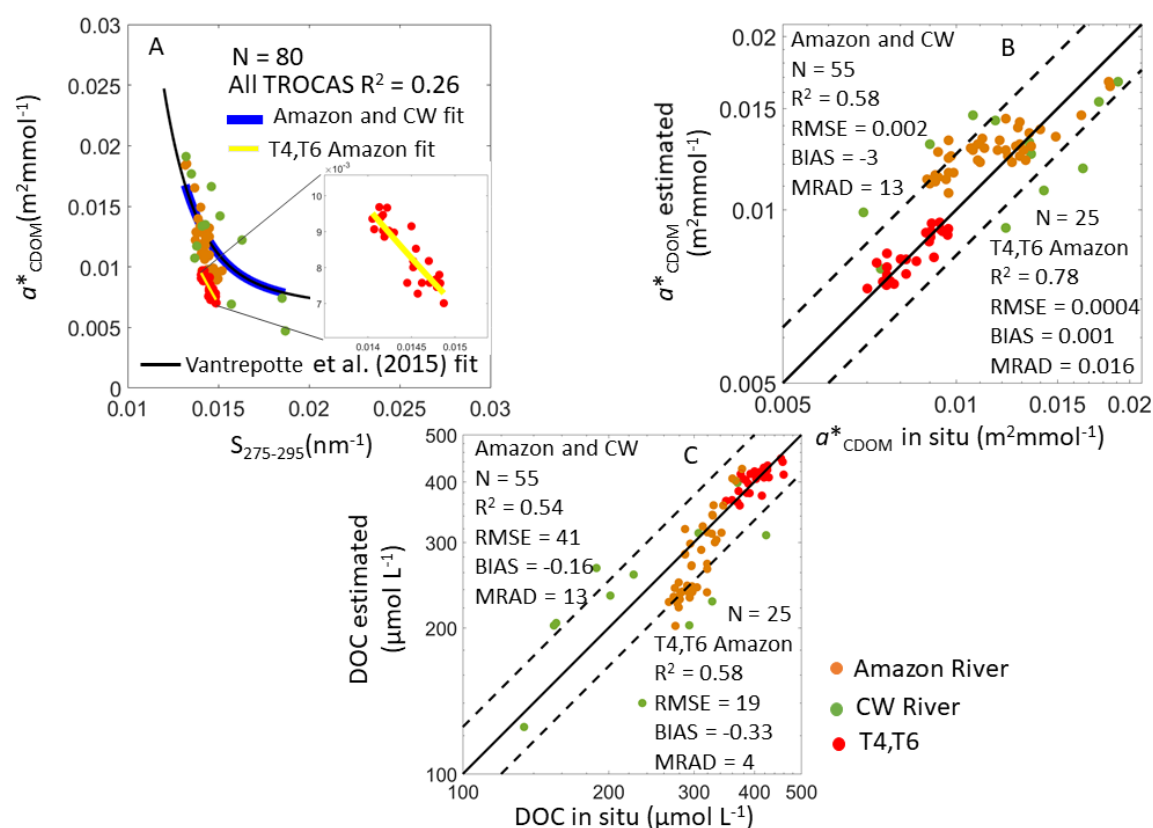
The differences in the slope and offset values for the CDOM to DOC relationships derived for the Amazon and CW samples (22.6 and 224  $\mu\text{mol L}^{-1}$ , 54 and 91.3  $\mu\text{mol L}^{-1}$ , respectively) suggest differences regarding the source and sink factors acting on DOM dynamics in these two optically different water types of the Amazon basin. The higher average  $S_{275-295}$  and  $S_R$  for the CW samples (Table 5.2) tend to indicate the presence of DOM with lower molecular weight than for the Amazon samples. Such differences might be attributed to variation in the DOM origin as larger contribution of the phytoplankton derived DOM in CW (WARD et al., 2015) as well as variation in the intensity of the photo-degradation processes (greater in the less turbid and more stagnating CW samples of the Xingu and Tapajós rivers).

These results suggest that the estimation of DOC from CDOM absorption coefficient using a simple linear model might be possible taking into account specific information about the optical water type, and thus biogeochemical quality (Fig. 5.2.B, C). This might be achieved using optical classification-based approaches whose advantages have been demonstrated for diverse applications dealing with the estimation of various biogeochemical products from ocean colour remote sensing (e.g. MOORE et al., 2014; VANTREPOTTE et al., 2012; MÉLIN et al., 2011). However, the results from this study also emphasize that such direct CDOM to DOC models are invalid and would result in inaccurate estimations of DOC (e.g. T4: rising conditions, T6: shift in the discharge timing).

Several studies have emphasized the use of spectral slope  $S_{275-295}$  for assessing  $a^*_{\text{CDOM}}$  and thus better constraining the natural variability in the dependency between CDOM and DOC at both seasonal (FICHOT; BENNER, 2011) and regional (DANHIEZ et al., 2017; VANTREPOTTE et al., 2015) scales. The interest of using  $S_{275-295}$  for estimating DOC from CDOM was also evaluated in the frame of this study. As previously observed for the direct CDOM-DOC relationship, a low correlation between  $a^*_{\text{CDOM}}(412)$  and  $S_{275-295}$  is observed when the whole data set is considered ( $N = 80$ ;  $R^2=0.26$ ,  $p<0.05$ ). When excluding the peculiar samples corresponding to T4, T6, a significant nonlinear

relationship can however be drawn between  $a^*_{\text{CDOM}}(412)$  and  $S_{275-295}$  for T1 to T3 and T5 considering both Amazon and CW samples (Figure 5.3.A).

Figure 5.3 - Relationship between  $S_{275-295}$  and  $a^*_{\text{CDOM}}(412)$  for the Lower Amazon region.



A) Relationship between  $S_{275-295}$  and  $a^*_{\text{CDOM}}(412)$  for Amazon River (T1-T3, T5), clearwater rivers and T4, T6 Amazon samples (N = 80, R<sup>2</sup> = 0.26, p<0.05), and zoom for the relationship between  $a^*_{\text{CDOM}}(412)$  and  $S_{275-295}$  for T4, T6 Amazon samples (N = 25), Vantrepotte et al. (2015) fit for comparison; B) Estimated  $a^*_{\text{CDOM}}(412)$  ( $S_{275-295}$  method) as a function of the measured  $a^*_{\text{CDOM}}(412)$  for Amazon + clearwater rivers (N = 55, R<sup>2</sup> = 0.58, p<0.05, RMSE = 0.002, Bias = -3; MRAD = 13), and for T4, T6 Amazon samples (N = 25, R<sup>2</sup> = 0.78, p<0.05, RMSE = 0.0004, Bias = 0.001; MRAD = 0.016) in log10 scale; C) Estimated [DOC] as a function of the  $a^*_{\text{CDOM}}(412)$  and  $S_{275-295}$  for Amazon + clearwater rivers (N = 55, R<sup>2</sup> = 0.54, p<0.05, RMSE = 41, Bias = 0.16; MRAD = 13), and for T4, T6 Amazon samples (N = 25, R<sup>2</sup> = 0.58, p<0.05, RMSE = 19, Bias = -0.33; MRAD = 4) in log10 scale. Solid lines represent 1:1 line and dashed lines represents the 20% error lines.

Source: Author's production.

This non-linear model is very close to the one proposed by Vantrepotte et al. (2015), from a large data set gathering data collected within highly contrasting coastal waters dominated by terrestrial inputs of DOM. Further, the general validity of this model, when considering the data of Amazon River (T1-T3, T5) and CW rivers, emphasizes the interest of such  $S_{275-295}$  based approach for avoiding issues related to the use of water masses information as suggested for direct CDOM to DOC linear models. It is worth noting, however, that such a  $S_{275-295}$  based model might induce a decrease of performance in the DOC retrieval when compared to direct CDOM-DOC relationships, as observed here especially for the samples collected during low water conditions (relative errors reaching 20%, Figure 5.3.C). The results presented here further indicate that a unique  $S_{275-295}$  vs  $a^*_{CDOM}(412)$  model is not sufficient to take into account the occurrence of very specific conditions such as the ones identified for the samples collected during T4 and T6, for which a specific model is required (Figure 5.3.A).

Note that a significant relationship between  $S_{275-295}$  vs  $a^*_{CDOM}(412)$  was found for these samples ( $N= 25$ ,  $R^2 = 0.78$ ,  $p<0.05$ ,  $RMSE = 0.0004$ ,  $Bias = 0.001$ ,  $MRAD = 0.016$ ) (Figure 5.3.B) whereas a general scattering was conversely observed when looking to the direct link between CDOM and DOC for the corresponding data (Figure 5.2.B). The better result for T4, T6 in comparison to Amazon and CW ( $R^2 = 78$  and  $R^2 = 58$ , respectively, Figure 5.3.B) can be explained by the data set of similar bio-optical characteristics. Amazon and CW gather samples from contrasted turbidity while T4 and T6 were sampled only on Amazon waters with similar optical constituents.

Interestingly, a sharp non-linear relationship was found between  $a_{CDOM}(412)$  and  $S_{275-295}$  (Figure 5.4) as reported by other authors (VANTREPOTTE et al., 2015). This unique relationship derived from the whole data set indicates the link between CDOM quality and quantity, and suggests the possible assessment of  $S_{275-295}$  from  $a_{CDOM}(412)$  for remote sensing applications.

The expressions and coefficients used to develop the relationship of CDOM-DOC are documented in Table 5.4.

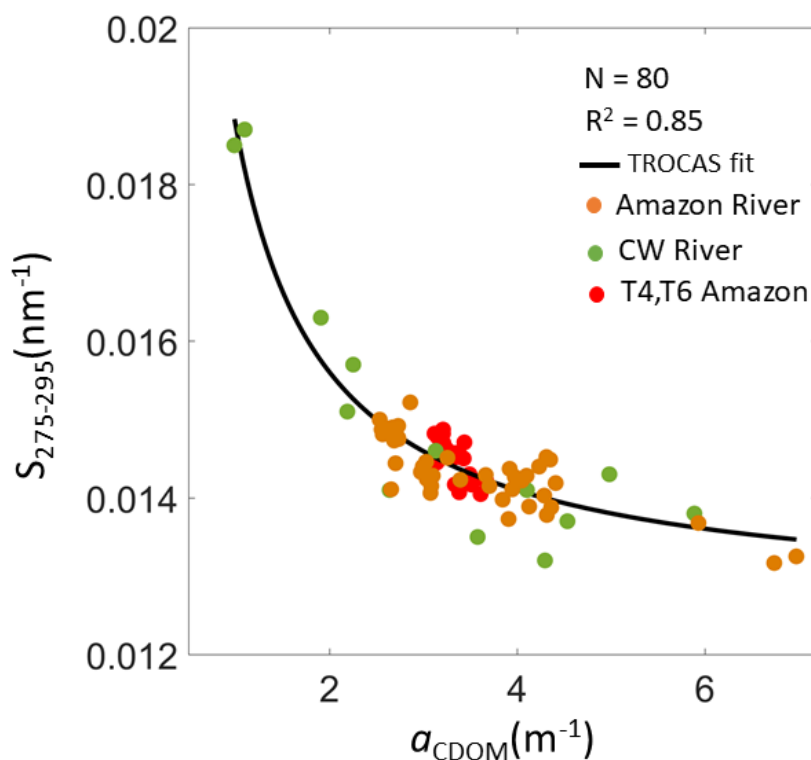
Table 5.4 - Expressions and coefficients for the relationship  $a^*_{CDOM}(412)$  vs  $S_{275-295}$ ,  $S_{275-295}$  vs  $a_{CDOM}(412)$  and  $a_{CDOM}(412)$  vs DOC.

Coefficients and R <sup>2</sup>					
Expression	General (Am + CW+T4,T6)	General (Am + CW)	Regional Am	Regional CW	Regional T4,T6
$a^*_{CDOM}(412)$	a= -6.99	a= 6.00	---	---	a= 2.974
$= a$					
$\cdot (e^{(b \cdot S_{275-295})})$	b= -54.4	b= -	---	---	b= -38.83
$- e^{(c \cdot S_{275-295})})$		60.93			
$+ d$					
(Figure 5.3)	c= -63.4	c= -	---	---	c= -35.46
	d= 0.40	d= 0.30	---	---	d= 0.09
	R <sup>2</sup> = 0.26	R <sup>2</sup> =	---	---	R <sup>2</sup> = 0.78
		0.58			
$S_{275-295} =$	a= 0.0425	---	---	---	---
$\frac{(a+b \cdot (a_{CDOM}(412)))}{(c+d \cdot (a_{CDOM}(412)))}$	b= 0.1061	---	---	---	---
	c= 1	---	---	---	---
(Figure 5.4)	d= 9.238	---	---	---	---
	R <sup>2</sup> = 0.85	---	---	---	---
$DOC = a \cdot$	a = 30.59	a =	a = 22.61	a =	a = -69.76
$a_{CDOM} + b$		32.59		54.64	
(Figure 5.2)	b = 223.2	b =	b = 223.9	b =	b = 635.8
		176.48		96.56	
	R <sup>2</sup> = 0.17	R <sup>2</sup> =	R <sup>2</sup> = 0.74	R <sup>2</sup> =	R <sup>2</sup> = 0.14
		0.51		0.57	

Am – Amazon samples; CW – clearwater samples.

Source: Author's production.

Figure 5.4 - Relationship between  $a_{\text{CDOM}}(412)$  and  $S_{275-295}$  for all sampling campaigns (N = 80,  $R^2 = 0.85$ ,  $p < 0.05$ ).



Source: Author's production.

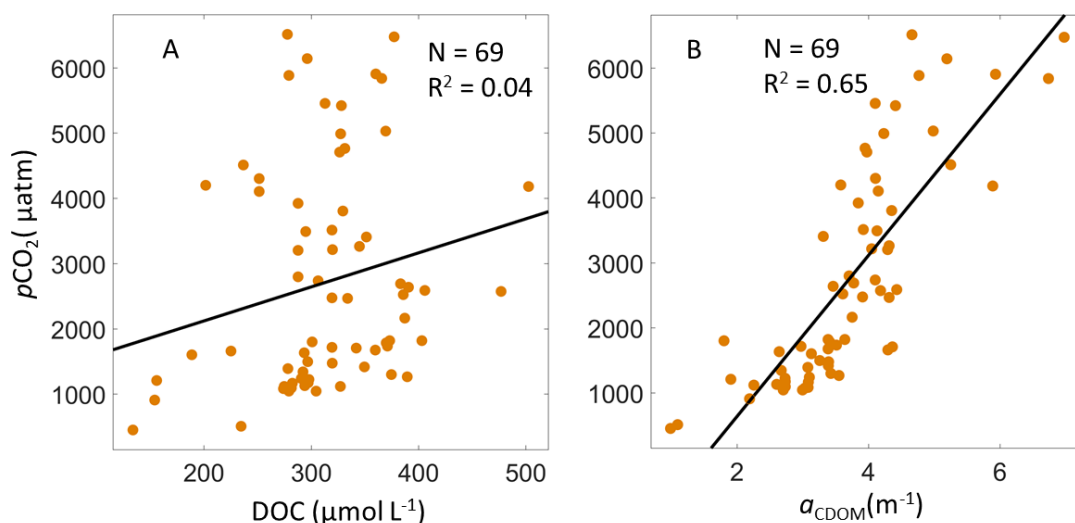
### 5.3.3 $a_{\text{CDOM}}(412)$ and $p\text{CO}_2$ relationships

Various studies have documented significant relationships between  $p\text{CO}_2$  and DOC in boreal and temperate inland waters (LAPIERRE; DEL GIORGIO, 2012; LARSEN et al., 2011; SOBEK et al., 2005). Based on results from this study, we have not observed such a link between  $p\text{CO}_2$  and DOC in the Lower Amazon River waters (N=69,  $R^2=0.04$ ,  $p>0.05$ , Figure 5.5.A). This result is consistent with other studies in tropical inland waters (PINHO et al., 2015; MAROTTA et al., 2010; MAROTTA et al., 2009), also emphasizing an absence of correlation between these two parameters in various Brazilian lakes, including some located in the Amazon basin. Rather, the  $p\text{CO}_2$  has been related to rainfall and temperature (FONTES et al., 2015; MAROTTA et al., 2010; MAROTTA et al., 2009). In contrast, a strong linear positive relationship was found here



between  $a_{\text{CDOM}}(412)$  and  $p\text{CO}_2$  (Figure 5.5.B and 5.6.A, ( $p\text{CO}_2 = 1240 * a_{\text{CDOM}}(412) - 1845$ ;  $N=69$ ,  $R^2=0.65$ ,  $\text{RMSE}= 979$ ,  $p<0.05$ ). This general relationship between  $a_{\text{CDOM}}(412)$  and  $p\text{CO}_2$  seems to be less affected by the optical water type or river discharge conditions, when compared to the results previously obtained regarding CDOM to DOC relationship.

Figure 5.5 - Estimative of  $p\text{CO}_2$  in the Lower Amazon region.



A) DOC- $p\text{CO}_2$  linear relationship ( $N = 69$ ,  $R^2 = 0.04$ ,  $p>0.05$ ) and; B)  $a_{\text{CDOM}}(412)$ - $p\text{CO}_2$  linear relationship ( $N = 69$ ,  $R^2 = 0.65$ ,  $p<0.05$ ) in the Lower Amazon region.

Source: Author's production.

Several studies have demonstrated the use of  $\text{chl}a$  and surface temperature data ( $T$ ) as a predictor for  $p\text{CO}_2$  in diverse river-dominated coastal areas (HALES et al., 2012; ZHU et al., 2009). CDOM has also been used in combination with the aforementioned parameters as a proxy for salinity or humic substances (BAI et al., 2015; KOSTEN et al., 2010; LOHRENZ; CAI, 2006). The  $\text{chl}a$  measurement indicates the presence of phytoplankton and therefore primary production that fixes  $\text{CO}_2$ , leading to lower values of  $p\text{CO}_2$  (SUBRAMANIAM et al., 2008). Inversely, higher temperatures decrease the solubility of  $\text{CO}_2$  (ZREDA et al., 1999) and DOM availability enhances bacterial respiration leading to higher  $p\text{CO}_2$  (SAWAKUCHI et al., 2017; ELLIS et al., 2012; MAROTTA et al., 2009; RICHEY et al., 2002).

Individual regressions (Table 5.5) indicate that degassing fluxes related to CDOM-degradation processes are the main factor driving  $p\text{CO}_2$  dynamics in the Lower Amazon explaining 65% of  $p\text{CO}_2$  variability through a linear relationship (Figure 5.6.A). Conversely, temperature and  $\text{chl}a$  explain 49% and 30% of  $p\text{CO}_2$  variability, respectively, and  $p\text{CO}_2$  exhibit a non-linear dependency with the latter two parameters (Table 5.5).

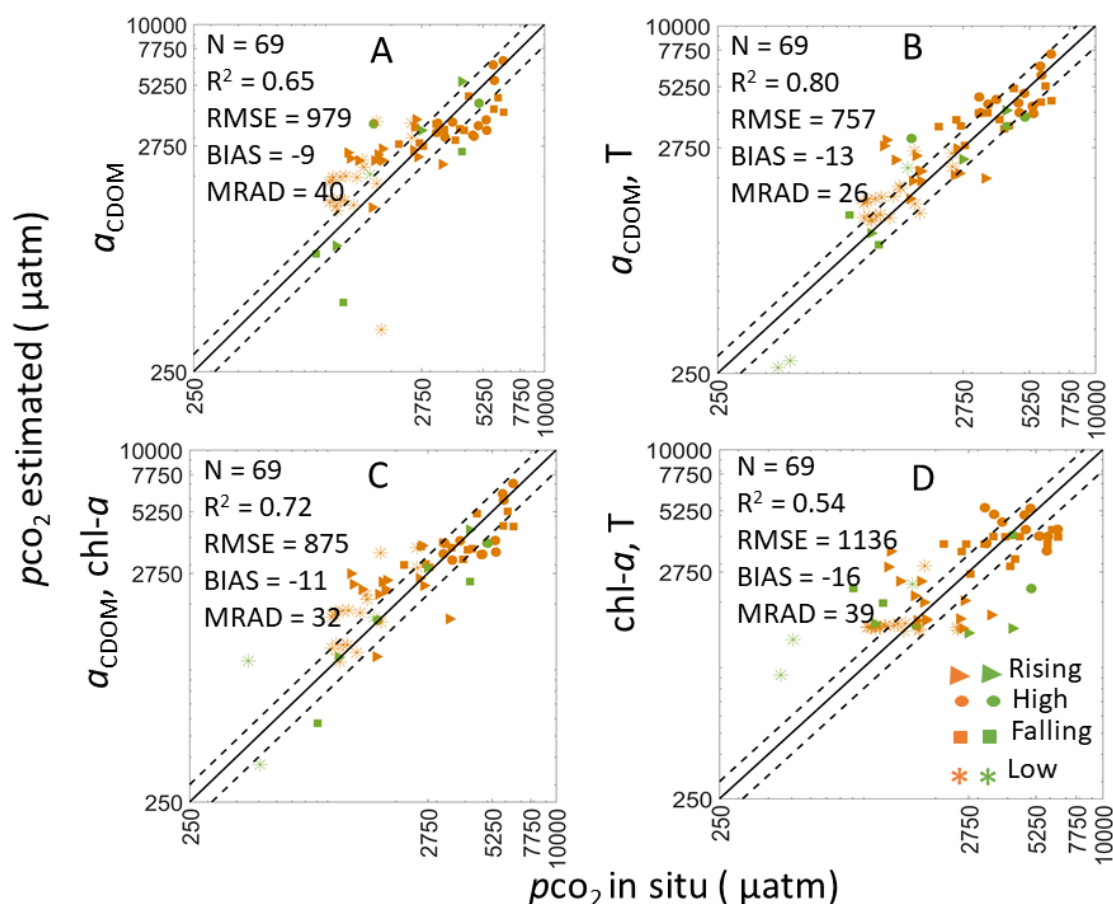
Table 5.5 - Simple regression models describing the relationship of  $p\text{CO}_2$  and CDOM, temperature (T) and  $\text{chl}a$  at the Lower Amazon.

Model	$p\text{CO}_2 =$	$R^2$	RMSE	N
1	$1240 \cdot a_{\text{CDOM}}(412) - 1845$	0.65	979	69
2	$1.48 \cdot 10^{30} \cdot T^{-18.2}$	0.49	1200	69
3	$3180 \cdot \text{chl}a^{-0.68}$	0.3	1411	69

Source: Author's production.

The value added when including these two additional descriptors for estimating  $p\text{CO}_2$  was specifically assessed using polynomial multivariate regression considering  $a_{\text{CDOM}}(412)$ , T and  $\text{chl}a$  as descriptive variables. Results indicate that the inclusion of both CDOM and temperature provide better  $p\text{CO}_2$  estimates (N=69;  $R^2 = 0.80$ ; RMSE= 757  $\mu\text{atm}$ , Bias = -13, MRAD = 26) than a model based on CDOM and  $\text{chl}a$  (N=69;  $R^2 = 0.72$ ; RMSE= 875  $\mu\text{atm}$ , Bias = -11 %, MRAD = 32 %). A  $\text{chl}a$  and temperature-based model provides the lower  $p\text{CO}_2$  retrieval accuracy (N=69;  $R^2 = 0.54$ ; RMSE= 1136  $\mu\text{atm}$ , Bias = -16 %, MRAD = 39 %). Further, the consideration of CDOM, T and  $\text{chl}a$  only slightly improve  $p\text{CO}_2$  retrieval (N=69;  $R^2 = 0.83$ ; RMSE= 749  $\mu\text{atm}$ , data not shown) when compared to the CDOM and T based model (Figure 5.6.B).

Figure 5.6 - Estimative of  $p\text{CO}_2$  for different sampling seasons, clearwater and Amazon River.



A) Estimated  $p\text{CO}_2$  as a function of the  $a_{\text{CDOM}}(412)$  ( $N = 69$ ,  $R^2 = 0.65$ ,  $p < 0.05$ ,  $\text{RMSE} = 979 \mu\text{atm}$ ,  $\text{Bias} = -9$ ,  $\text{MRAD} = 40$ ,  $p\text{CO}_2 = 1240 * a_{\text{CDOM}}(412) - 1845$ ); B) Estimated  $p\text{CO}_2$  as a function of  $a_{\text{CDOM}}(412)$  and temperature ( $N = 69$ ,  $R^2 = 0.80$ ,  $p < 0.05$ ,  $\text{RMSE} = 757 \mu\text{atm}$ ,  $\text{Bias} = -13$ ,  $\text{MRAD} = 26$ ); C) Estimated  $p\text{CO}_2$  as a function of  $a_{\text{CDOM}}(412)$  and  $\text{chl}a$  ( $N = 69$ ,  $R^2 = 0.72$ ,  $p < 0.05$ ,  $\text{RMSE} = 875 \mu\text{atm}$ ,  $\text{Bias} = -11$ ,  $\text{MRAD} = 32$ ); D) Estimated  $p\text{CO}_2$  as a function of temperature and  $\text{chl}a$  ( $N = 69$ ,  $R^2 = 0.54$ ,  $p < 0.05$ ,  $\text{RMSE} = 1136 \mu\text{atm}$ ,  $\text{Bias} = -16$ ,  $\text{MRAD} = 39$ ). All the figures are in log10 scale. Solid lines represent 1:1 line and dashed lines represent the 20% error lines.

Source: Author's production.

The estimation of  $\text{chl}a$  concentration from ocean colour remote sensing in very turbid waters such as those from the Amazon River remains very challenging (SUN et al., 2014; LE et al., 2013). The performance of models based on reflectance bands are more suitable to retrieve  $\text{chl}a$  in turbid environments (i.e. red and NIR) and has already

been shown to provide a relevant alternative for this application, at least when chl*a* concentration is > 2mg m<sup>-3</sup> (LE et al., 2013; 2009; GITELSON et al., 2008; DALL'OMO; GITELSON, 2005]. Such chl*a* levels were rarely reached in this data set, with Amazon River samples showing an average chl*a* concentration of 1.24 ± 0.45 mg m<sup>-3</sup> and maximum value of 2.2 mg m<sup>-3</sup> (Table 5.2). Conversely, various studies have emphasized the possibility of using remotely-sensed temperature estimations in inland waters with a relatively high accuracy (DÖRHNHÖFER; OPPELT, 2016; DUGDALE, 2016; HANDCOCK et al., 2012; ALCÂNTARA et al., 2010). Considering these issues, a formulation based on CDOM and T for estimating *p*CO<sub>2</sub> in the Lower Amazon region could be developed:

$$pCO_2 = a. (a_{CDOM}(412))^2 + b. a_{CDOM}(412) + c + d. (T^2) + e. T + f. (a_{CDOM}(412). T) \quad (5.1)$$

where T and *a*<sub>CDOM</sub>(412) represents the in situ river surface temperature and CDOM absorption coefficient, with the equation coefficients equivalent to: a = 49.24, b= 3001, c = 4.828 x 10<sup>5</sup>, d = 526.6, e = -3.19 x 10<sup>4</sup>, f = -83.52.

Similarly, various CDOM absorption inversion algorithms adapted to coastal or freshwaters environments have been also recently documented (e.g. Cao et al., 2018). Considering the latter feature, a formulation based on CDOM and T for estimating *p*CO<sub>2</sub> in the Amazon waters is here proposed for assessing *p*CO<sub>2</sub> content, potentially applicable for further applications of water colour remote sensing.

Interestingly, in contrast with the previous results on DOC, these results suggest that a unique relationship can be used without distinguishing Amazon and CW data, or considering specific rain conditions (T4, T6), highlighting a greater stability in the factors driving CO<sub>2</sub> production, consumption, and outgassing.

## 5.4 Final considerations

The major aim of this chapter was to assess the potential use of  $a_{\text{CDOM}}(412)$  for estimating DOC and  $p\text{CO}_2$  content within the poorly-investigated region of the Lower Amazon River. To achieve the main goal, the spatial-seasonal variability of the carbon content was documented for the study period.

The heterogeneity of the DOM dynamics between clear and turbid water bodies of the Lower Amazon River region was clearly observed. The prevalent impact of degradation processes more likely related to bacterial activity has been further highlighted by the changing optical properties of CDOM along the course of the Amazon River that agree well with past observations of more degraded DOM molecular composition towards the river's mouth. Besides these general spatial features, a strong seasonal variability was found for both CDOM and DOC values. While the seasonality in the Amazon River discharge represents a major controlling factor for the DOM annual variation, results also illustrate the complexity of the DOM temporal dynamics in the Lower Amazon. Significant modulations in the DOM quality were specifically observed according to the discharge timing at either seasonal (rising conditions) or inter-annual (El Niño event) scales. The understanding of the CDOM and DOC dynamics depicted here in the Amazon mainstream would however need additional information specifically regarding the seasonal variation in the quality of DOM inputs, considering the diverse source areas surrounding the Lower Amazon (floodplains, flooded forest, seasonally isolated lakes).

The potential for the assessment of DOC loads from a CDOM inversion algorithm was investigated. Results demonstrate the strong heterogeneity of the water masses of the Lower Amazon region with its clear and turbid waters, suggesting that assuming a single direct CDOM to DOC relationship is problematic. While the use of  $S_{275-295}$  based approach has been shown to represent a relevant alternative for assessing DOC from CDOM in coastal waters, results here tend to indicate that such optical proxy can only

partly describe the natural variability of the CDOM to DOC ratio in the inner Amazon. A single  $S_{275-295}$  based model is not able to capture the impact of DOM inputs potentially related to the seasonal modulation in the quality of the DOM delivered to the river from land–floodplain flush.

Finally, the results have demonstrated that CDOM absorption can be considered as a relevant proxy of the  $p\text{CO}_2$  in the Lower Amazon. A model based on CDOM and temperature seems to provide the most reliable  $p\text{CO}_2$  estimates (relative error of 26% on average). The assessment of the  $\text{CO}_2$  flux from the entire Amazon River, including the lower reaches that are tidal-influenced, is crucial to understand the role of inland waters to the carbon budget. For example, past global estimates of  $\text{CO}_2$  emissions do not include tidal rivers, and including the tidal reaches of the Amazon River, alone, increase global  $\text{CO}_2$  outgassing estimates by ~43% (SAWAKUCHI et al., 2017). Widely applying the optical approach used here will allow a broader assessment of the lower reaches of rivers worldwide and allow for more persistent monitoring of alterations to aquatic carbon cycling under a changing climate.

## **6 EVALUATION OF CDOM EMPIRICAL ALGORITHMS AND CARBON CONTENT MAPPING USING MERIS IMAGES**

### **6.1 Introduction**

The accurate retrieval of CDOM information from remote sensing of optically complex waters is not trivial. CDOM is measured by its absorption property and does not scatter or reflect light (BRICAUD et al., 1981). CDOM has an exponential absorption curve that increases as the wavelength decreases without peaks or troughs, such as the ones observed for phytoplankton pigments absorption curve, can be evidenced (BRICAUD et al., 1995; BRICAUD et al., 1981). A major issue for estimating CDOM from water colour remote sensing information is the need to properly discriminate the CDOM absorption from that related to NAP, which absorption spectra present a very similar shape. Additionally, water colour remote sensing is based on the visible/NIR spectrum domain (400~900 nm) where generally the sensors do not have a wavelength band dedicated to monitor CDOM exclusively (BREZONIK et al., 2015). Although many studies used the bands in the blue region (e.g. 412 and 443 nm) to assess CDOM, these bands are more sensible to atmospheric correction issues specially over turbid waters (SHANMUGAM, 2012; SHI; WANG, 2009; WANG; SHI, 2007; RUDDICK et al., 2000).

Several efforts to retrieve CDOM information from satellite imagery have led to the development of empirical inversion algorithms based on simple or multiple, linear and nonlinear regressions. These empirical relationship between CDOM and reflectance are usually based on band ratios (JOSHI et al., 2017; FICEK et al., 2011; DEL CASTILLO; MILLER, 2008; D'Sa et al., 2006; KUTSER et al., 2005) although recent studies also uses a combination of multiple bands (CAO et al., 2018).

The blue/green (green/blue) ratios are usually used for oceanic waters and/or waters with similar optical characteristics, with a higher absorption of CDOM at blue wavelengths compared to the chl $a$ , as well as lower contribution of CDOM in the green spectra (MANNINO et al., 2014; GRIFFIN et al., 2011; SISWANTO et al., 2011;

MANNINO et al., 2008; KARHU; MITCHELL, 2001; TASSAN, 1994). In waters with high CDOM, as in coastal and inland waters, the use of the ratios based on the blue and red wavelengths have shown better results for some investigations (KEITH et al., 2016; MANNINO et al., 2014; TIWARI et al., 2011).

For inland waters monitoring purposes, the use of a suitable spatial resolution can be a determinant aspect regarding the choice of an adequate sensor. For that, the Landsat-8/OLI (30 m) and Sentinel-2/MSI (10-20 m) represent good alternatives to map CDOM in terms of spatial resolution. Over inland waters, Brezonik et al. (2005, 2015) illustrated the interest of considering band ratios partly based on the NIR information for applications dedicated to Landsat TM (BREZONIK et al., 2005) or more recently to Sentinel-2/MSI (BREZONIK et al., 2015).

The green/red band ratio is also often used for inland turbid waters applications. Although the CDOM has a higher contribution to blue than green spectra, there are other reasons why the green band is preferred. Atmospheric correction of blue wavelengths is often problematic, especially in turbid waters (SHANMUGAM, 2012; SHI; WANG, 2009; WANG; SHI, 2007; RUDDICK et al., 2000). Additionally, chl<sub>a</sub> absorption also influences blue band more than the green one (KUTSER et al., 2005). Several studies show a good relationship between CDOM and green/red band ratio in optically complex waters using a variety of remote sensing sensors with different spatial and spectral resolutions (JOSHI et al., 2017; BREZONIK et al., 2015; KUTSER et al., 2015; FICEK et al., 2011; DEL CASTILLO; MILLER, 2008).

The reason why the performance of some band ratios is varying according to the study considered is not fully understood (BREZONIK et al. 2005). One possible explanation about the variability in the CDOM-reflectance relationship is the fluctuant proportion of other bio-optical constituents that also rules the radiometric response of the water system. Nevertheless, this non-uniformity increases prediction uncertainties at high CDOM levels. Zhu et al. (2014) indicate that the selection of bands with relatively



longer wavelengths ( $> 600$  nm) is more appropriate for inland CDOM-rich waters due to the influence of DOM from terrestrial vegetation as well as to the presence of significant amounts of particulate matter.

An accurate retrieval of CDOM optical properties from water colour remote sensing represent a prerequisite for synoptically monitoring water carbon content (e.g. DOC and  $p\text{CO}_2$ ) and studying its variability across different spatiotemporal scales. Nevertheless, studies dealing with CDOM-based retrieval of DOC and  $p\text{CO}_2$  in the context of remote sensing applications are still scarce in optically complex waters, the latter statement being especially true for rivers and transitional zones between fresh and saline waters (CAO et al., 2018; JOSHI et al., 2017; VANTREPOTTE et al., 2015).

In this general context, the main objective of this chapter is to evaluate the performance of empirical algorithms currently available in the literature to retrieve CDOM from the remote sensing reflectance. The best performing CDOM algorithm was applied to MERIS data to generate distribution maps of CDOM in the Lower Amazon region. Using the algorithms developed in the previous chapter (Chapter 5),  $S_{275-295}$ , DOC and  $p\text{CO}_2$  maps are also generated for the study area. The spatiotemporal variability of the carbon content is illustrated and discussed using MERIS images for 2010 and 2011.

## **6.2 Material and methods**

### **6.2.1 Empirical algorithms**

The performance of seven (7) selected empirical algorithms from the literature was evaluated based on the  $R_{rs}$ -CDOM coupled data gathered in the Lower Amazon. Although each algorithm was developed for assessing  $a_{\text{CDOM}}$  at various specific wavelengths, this study specifically focused on the retrieval of  $a_{\text{CDOM}(412)}$  considering formulations based on different input variables. All the following algorithms were fitted to the Lower Amazon in situ regional data set (N=100):

$$a_{CDOM}(412) = 1.5 \cdot 10^{(c_0 + c_1 R_{15} + c_2 R_{15}^2 + c_3 R_{25} + c_4 R_{25}^2)} \quad (6.1)$$

where:  $R_{15} = \log_{10} \left( \frac{R_{rs412}}{R_{rs555}} \right)$ ,  $R_{25} = \log_{10} \left( \frac{R_{rs443}}{R_{rs555}} \right)$  (CARDER et al., 2003)

$$a_{CDOM}(412) = 10^{(c_0 + c_1 R_{15} + c_2 R_{15}^2 + c_3 R_{25} + c_4 R_{25}^2)} \quad (6.2)$$

where:  $R_{25} = \log_{10} \left( \frac{R_{rs443}}{R_{rs555}} \right)$ ,  $R_{35} = \log_{10} \left( \frac{R_{rs488}}{R_{rs555}} \right)$ ,  $R_{65} = \log_{10} \left( \frac{R_{rs667}}{R_{rs555}} \right)$  (CARDER et al., 2004)

$$\ln(a_{CDOM}(412)) = a_0 + a_1(R_1) + a_2(R_2) \quad (6.3)$$

where: A:  $R_1 = R_{rs483}$  and  $R_2 = \frac{R_{rs483}}{R_{rs830}}$  ; B:  $R_1 = R_{rs565}$  and  $R_2 = \frac{R_{rs483}}{R_{rs830}}$  (BREZONIK et al., 2005)

$$a_{CDOM}(412) = \exp(-a + b \cdot R_1 + c \cdot R_2) \quad (6.4)$$

where:  $R_1 = R_{rs660}$  and  $R_2 = \frac{R_{rs565}}{R_{rs483}}$  (GRIFFIN et al., 2011)

$$a_{CDOM}(\lambda) = a \cdot X^b \quad (6.5)$$

where:  $X = \frac{R_{rs510}}{R_{rs555}}$  (D'SA et al., 2006);  $X = \frac{R_{rs570}}{R_{rs655}}$  (FICEK et al., 2011);  $X = \frac{R_{rs565}}{R_{rs660}}$  (KUTSER et al., 2005);  $X = \frac{R_{rs560}}{R_{rs655}}$  (SLONECKER et al., 2016; JOSHI et al., 2015 );  $X = \frac{R_{rs560}}{R_{rs665}}$  (KUTSER et al. 2015);  $X = \frac{551}{671}$  (JOSHI et al., 2017)

$$a_{CDOM}(412) = a + bX \quad (6.6)$$

where:  $X = \frac{R_{rs510}}{R_{rs670}}$  (CASTILLO et al., 2008);  $X = \frac{R_{rs665}}{R_{rs489}}$  (KEITH et al., 2016);  $X = \frac{R_{rs667}}{R_{rs488}}$  (SCHAEFFER et al., 2015);  $X = \frac{R_{rs670}}{R_{rs490}}$  (TIWARI et al., 2011)

$$\ln(a_{CDOM}(\lambda)) = \alpha \cdot \ln(R_{rs}(443)) + \beta \cdot \ln(R_{rs}(488)) + \gamma \cdot \ln(R_{rs}(531)) + \delta \cdot \ln(R_{rs}(555)) + \varepsilon \cdot \ln(R_{rs}(667)) + \zeta \quad (\text{CAO et al., 2018}) \quad (6.7)$$

## 6.2.2 Satellite-based carbon content maps

The best performing empirical  $a_{CDOM}(412)$  algorithm, based on statistical metrics ( $R^2$ , RMSE, MRAD and Bias) was applied on MERIS images for the years of 2010 and 2011. Likewise,  $S_{275-295}$ ,  $pCO_2$  and DOC algorithms developed on Chapter 5 were also applied on MERIS images. More information about MERIS imagery used in this study are provided on Chapter 3, section 3.6.1.

## 6.3 Results and discussion

### 6.3.1 CDOM optical properties empirical inversion algorithms performance

#### 6.3.1.1 CDOM absorption estimates

The performance of the selected CDOM inversion algorithms was assessed considering coefficients calibrated with the in situ Lower Amazon data set. In general, the algorithms that used band ratio with blue wavelengths had a poor performance ( $R^2 = 0.02-0.47$ , Type of algorithms: Blue/Green, Blue/NIR, Red/Blue, Table 6.1). The best regional empirical algorithms ( $R^2 > 0.6$ ) are shown in bold letters on Table 6.1. Green/Red band ratio-based algorithms together with multilinear relationship as proposed by Carder et al., 2004 and Cao et al., 2018 provided the best fitting accuracies ( $R^2 = 0.66$  and  $0.67$ , respectively (Table 6.1).

Table 6.1 - Empirical algorithms for estimating CDOM with the coefficients calibrated for the Lower Amazon region.

Type of algorithm	Name	R <sup>2</sup>	Function	R <sub>rs</sub> band (nm)
Blue/Green (multiband)	Carder03	0.3	linear	412/555, 443/555
<b>Blue/Green (multiband)</b>	<b>Carder04</b>	<b>0.6</b>	<b>linear</b>	<b>443/555, 488/555, 667/555</b>
Blue/NIR (multiband)	Brezonik05A	0.4	linear	R483, 483/830
Blue/NIR (multiband)	Brezonik05B	0.4	linear	R560, 483/830
Green/Blue (multiband)	Griffin11	0.0	linear	R660, 565/483
Green/Green	D'Sa06	0.0	power	510/555
Green/Red	Castillo08	0.4	linear	510/670
<b>Green/Red</b>	<b>Ficek11</b>	<b>0.6</b>	<b>power</b>	<b>570/655</b>
<b>Green/Red</b>	<b>Kutser05</b>	<b>0.6</b>	<b>power</b>	<b>565/660</b>
<b>Green/Red</b>	<b>Slonecker16</b>	<b>0.6</b>	<b>power</b>	<b>560/655</b>
<b>Green/Red</b>	<b>/Joshi15</b>	<b>0.6</b>	<b>power</b>	<b>560/655</b>
<b>Green/Red</b>	<b>Kutser15</b>	<b>0.6</b>	<b>power</b>	<b>560/665</b>
<b>Green/Red</b>	<b>Joshi17</b>	<b>0.6</b>	<b>power</b>	<b>551/671</b>
<b>Multiband</b>	<b>Cao18</b>	<b>0.6</b>	<b>linear</b>	<b>443, 488, 531, 555, 667</b>
Red/Blue	Keith16	0.3	linear	665/489
Red/Blue	Schaeffer15	0.4	linear	667/488
Red/Blue	Tiwari11	0.4	linear	670/490

Source: Author's production.

Cao18 was developed based on many spectral bands available on MERIS and MODIS sensors. Nevertheless, is also worthy to note that the algorithms developed using ALI (Kutser05), Landsat-8 OLI (Slonecker16, Joshi15) and VIIRS (Joshi17) spectral bands also

showed a good performance (Table 6.1). Likewise, Kutser et al. (2015) formulation using the spectral bands of Sentinel 3 OLCI (equivalent to MERIS bands) based on green/red band ratio was also satisfying (Table 6.1).

According to Cao et al. (2018), the proposed model has the advantage to not be sensitive to NAP variability since it is based on the  $R_{rs}$  and not on the absorption spectral shape. In this study, a regional adaptation of Cao18 was therefore considered to retrieve  $a_{CDOM}(412)$  in the Lower Amazon region from MERIS data as follows:

$$\begin{aligned} \ln(a_{CDOM}(412)) = & \alpha \cdot \ln(R_{rs}(443)) + \beta \cdot \ln(R_{rs}(490)) + \gamma \cdot \\ & \ln(R_{rs}(510)) + \varepsilon \cdot \ln(R_{rs}(665)) + \zeta \end{aligned} \quad (6.8)$$

where  $\alpha = 1.006$ ,  $\beta = -1.212$ ,  $\gamma = -0.486$ ,  $\delta = -0.704$ ,  $\varepsilon = 1.396$ ,  $\zeta = 0.943$

This multiband relationship could retrieve satisfactorily  $a_{CDOM}(412)$  for the study area (N = 100,  $R^2 = 0.67$ ,  $p < 0.05$ , RMSE = 0.4, Bias = 0.4, MRAD = 8.2) (Figure 6.1.A)

Cao et al. (2018) aimed to retrieve  $a_{CDOM}(355)$  across different estuarine and coastal waters and therefore, in order to compare with the original algorithm provided by this authors,  $a_{CDOM}$  data measured for this study area at 355 nm were also considered leading to the following regional algorithm:

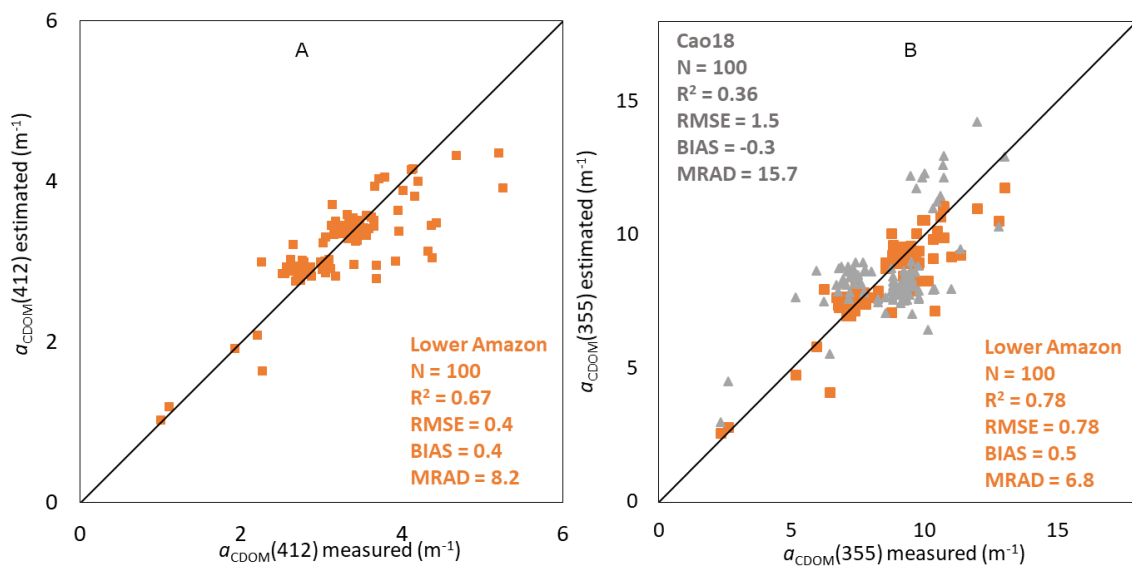
$$\begin{aligned} \ln(a_{CDOM}(355)) = & \alpha \cdot \ln(R_{rs}(443)) + \beta \cdot \ln(R_{rs}(488)) + \gamma \cdot \\ & \ln(R_{rs}(555)) + \varepsilon \cdot \ln(R_{rs}(667)) + \zeta \end{aligned} \quad (6.9)$$

where  $\alpha = 0.038$ ,  $\beta = -0.871$ ,  $\gamma = -0.035$ ,  $\delta = -0.274$ ,  $\varepsilon = 0.959$ ,  $\zeta = -0.107$  (Cao et al., 2018).

When Cao18 model is calibrated for the Lower Amazon region for  $a_{CDOM}(355)$ , the performance of the regionally tuned model is improved (N = 100,  $R^2 = 0.78$ ,  $p < 0.05$ , RMSE = 0.78, Bias = 0.5, MRAD = 6.8) when compared to the original Cao et al. 2018 algorithm (N = 100,  $R^2 = 0.36$ ,  $p < 0.05$ , RMSE = 1.5, Bias = -0.3, MRAD = 15.7), as

expected (Figure 6.1.B). Note however that the performance of the original method by Cao et al. (2018) ( $\alpha = 0.038$ ,  $\beta = -0.871$ ,  $\gamma = -0.035$ ,  $\delta = -0.274$ ,  $\varepsilon = 0.959$ ,  $\zeta = -0.107$ ) is relatively poor especially for the medium CDOM ranges observed in the study site (between 5 and 10  $\text{m}^{-1}$ , Figure 6.1.B) where the retrieved CDOM show a low dynamic range, although the authors were emphasizing the generalizable feature of their proposed formulation.

Figure 6.1 - Estimative of  $a_{\text{CDOM}}$  in the Lower Amazon region.



A) Estimated  $a_{\text{CDOM}}(412)$  as function of a multivariate linear relationship adapted from Cao et al. 2018 utilizing MERIS bands for the Lower Amazon (N = 100,  $R^2 = 0.67$ ,  $p < 0.05$ , RMSE = 0.4, Bias = 0.4, MRAD = 8.2); B) Estimated  $a_{\text{CDOM}}(355)$  as function of a multivariate linear relationship Cao18 for the Lower Amazon using Cao et al. 2018 coefficients (N = 100,  $R^2 = 0.36$ ,  $p < 0.05$ , RMSE = 1.5, Bias = -0.3; MRAD = 15.7) and this study coefficients (N = 100,  $R^2 = 0.78$ ,  $p < 0.05$ , RMSE = 0.78, Bias = 0.5; MRAD = 6.8);

Source: Author's production.

Note that the dispersion of the samples observed along the fit line (Figure 6.1 A and B) was not related to the seasonality or the optical classes developed on Chapter 4. Therefore, a single algorithm could be used to assess the spatial and seasonal variability of the Lower Amazon region.

### 6.3.1.2 CDOM spectral slope retrieval

Besides  $a_{CDOM}(355)$ , Cao et al. (2018) also estimated  $S_{275-295}$  based on a multiple linear regression using the same spectral bands applied for CDOM calculation. For the purpose of comparison with the method proposed by Vantrepotte et al. (2015) described in Chapter 5 (section 5.3.2), Cao et al. (2018) approach to estimate  $S_{275-295}$  was also applied for the study area. Therefore, the following approaches were applied (Figure 6.2): i) using the same wavelengths and coefficients developed by Cao et al., 2018 for estuarine and coastal waters; ii) Cao18 model using MERIS bands and coefficients calibrated for the Lower Amazon and; iii) Vantrepotte et al., 2015 (Vantrepotte15) model calibrated for the Lower Amazon

- i) Multilinear reflectance formulation Cao et al. (2018)

$$\ln(S_{275-295}) = \alpha \cdot \ln(R_{rs}(443)) + \beta \cdot \ln(R_{rs}(488)) + \gamma \cdot \ln(R_{rs}(555)) + \varepsilon \cdot \ln(R_{rs}(667)) + \zeta \quad (6.10)$$

where:  $\alpha = -0.0537$ ,  $\beta = 0.2689$ ,  $\gamma = 0.1017$ ,  $\delta = -0.2097$ ,  $\varepsilon = -0.0893$ ,  $\zeta = -3.685$

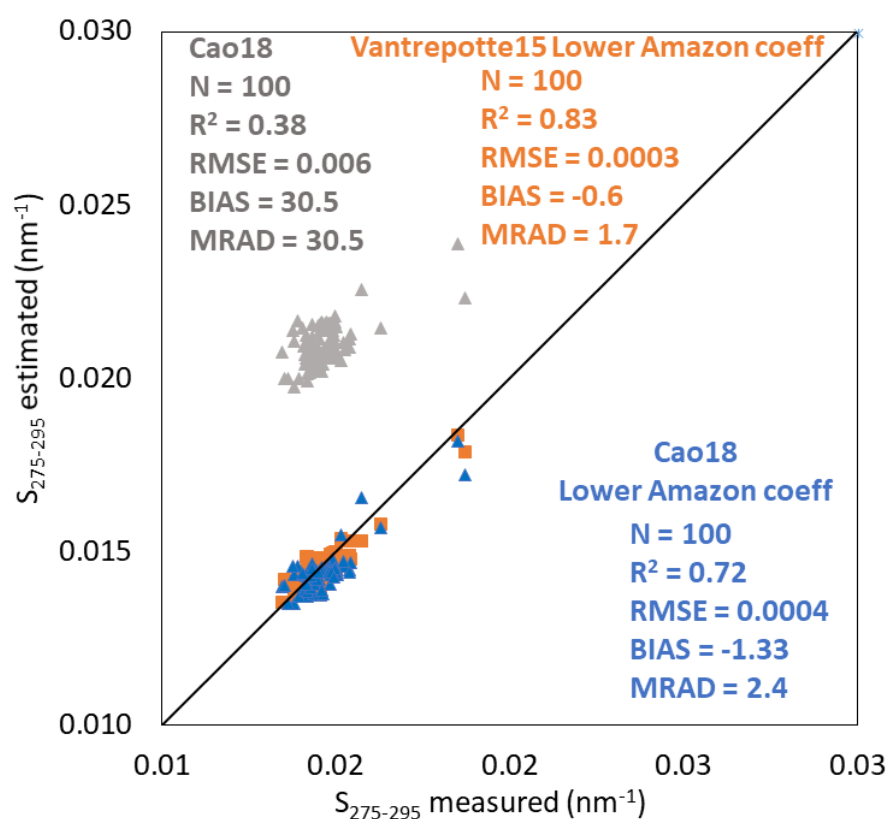
- ii) *This study*: same as equation 6.10 with  $\alpha = -0.257$ ,  $\beta = 0.751$ ,  $\gamma = -0.343$ ,  $\delta = 0.111$ ,  $\varepsilon = -0.261$ ,  $\zeta = -4.140$

- iii) This study ( $a_{CDOM}(412)$  based), Vantrepotte et al., 2015-like)

$$S_{275-295} = \frac{(a+b \cdot (a_{CDOM}(412)))}{(c+d \cdot (a_{CDOM}(412)))} \quad (6.11)$$

where:  $a = 0.0341$ ,  $b = 0.031$ ,  $c = 0.9716$ ,  $d = 2.579$

Figure 6.2 - Estimative of  $S_{275-295}$  in the Lower Amazon region.



Estimated  $S_{275-295}$  as function of a multivariate linear relationship Cao18 using its coefficients ( $N = 100$ ,  $R^2 = 0.38$ ,  $p < 0.05$ ,  $\text{RMSE} = 0.006$ ,  $\text{Bias} = 30.5$ ;  $\text{MRAD} = 30.5$ ) and calibrated to the Lower Amazon ( $N = 100$ ,  $R^2 = 0.72$ ,  $p < 0.05$ ,  $\text{RMSE} = 0.0004$ ,  $\text{Bias} = -1.33$ ;  $\text{MRAD} = 2.4$ ); and nonlinear relationship Vantrepotte et al., 2015 calibrated for the Lower Amazon ( $N = 100$ ,  $R^2 = 0.83$ ,  $p < 0.05$ ,  $\text{RMSE} = 0.0003$ ,  $\text{Bias} = -0.6$ ;  $\text{MRAD} = 1.7$ ).

Source: Author's production.

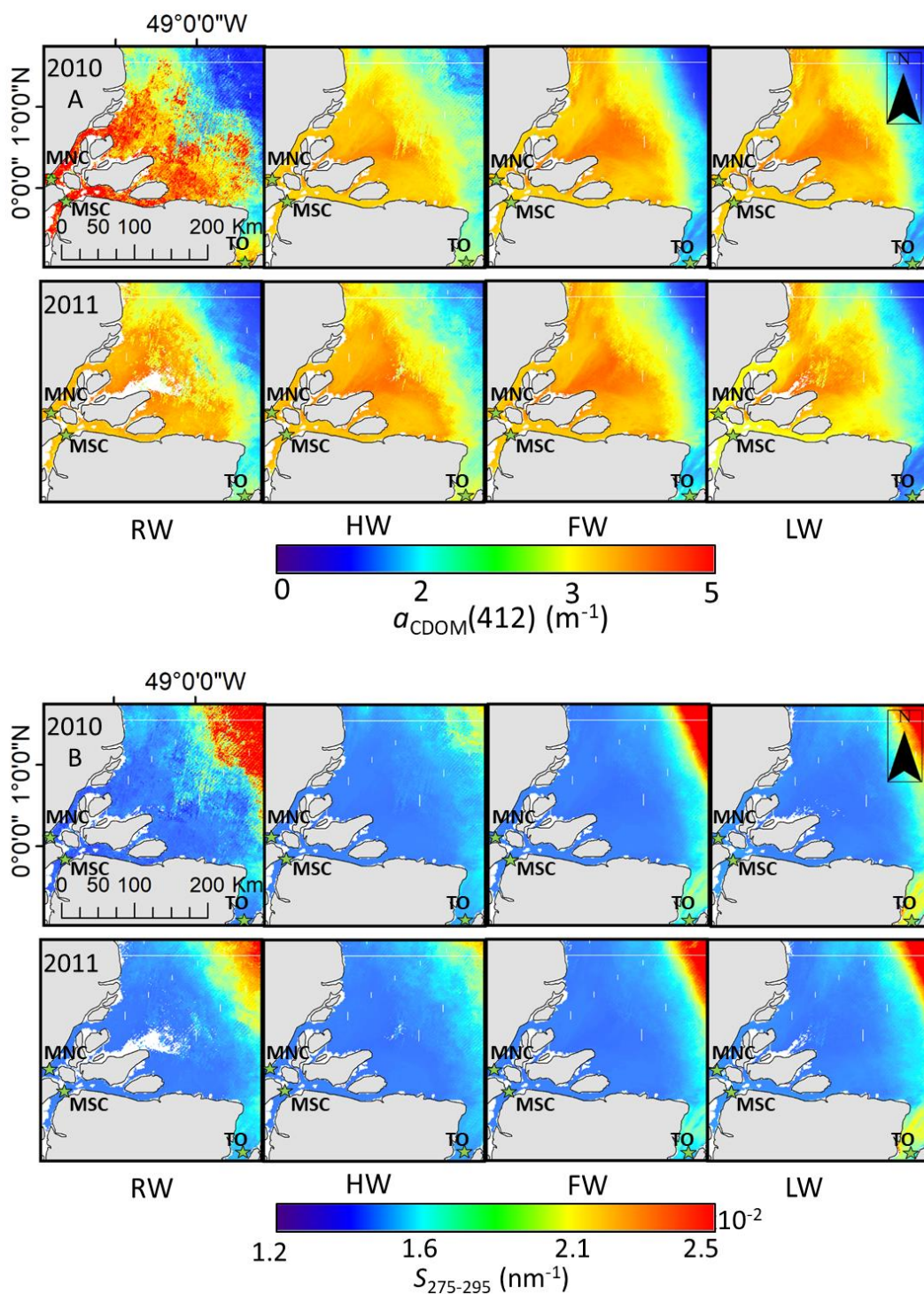
The nonlinear algorithm proposed by Vantrepotte et al., 2015 ( $N = 100$ ,  $R^2 = 0.83$ ,  $p < 0.05$ ,  $\text{RMSE} = 0.0003$ ,  $\text{Bias} = -0.6$ ;  $\text{MRAD} = 1.7$ ) showed a better performance than the Cao18 approach ( $N = 100$ ,  $R^2 = 0.72$ ,  $p < 0.05$ ,  $\text{RMSE} = 0.0004$ ,  $\text{Bias} = -1.33$ ;  $\text{MRAD} = 2.4$ ), both calibrated for the Lower Amazon.

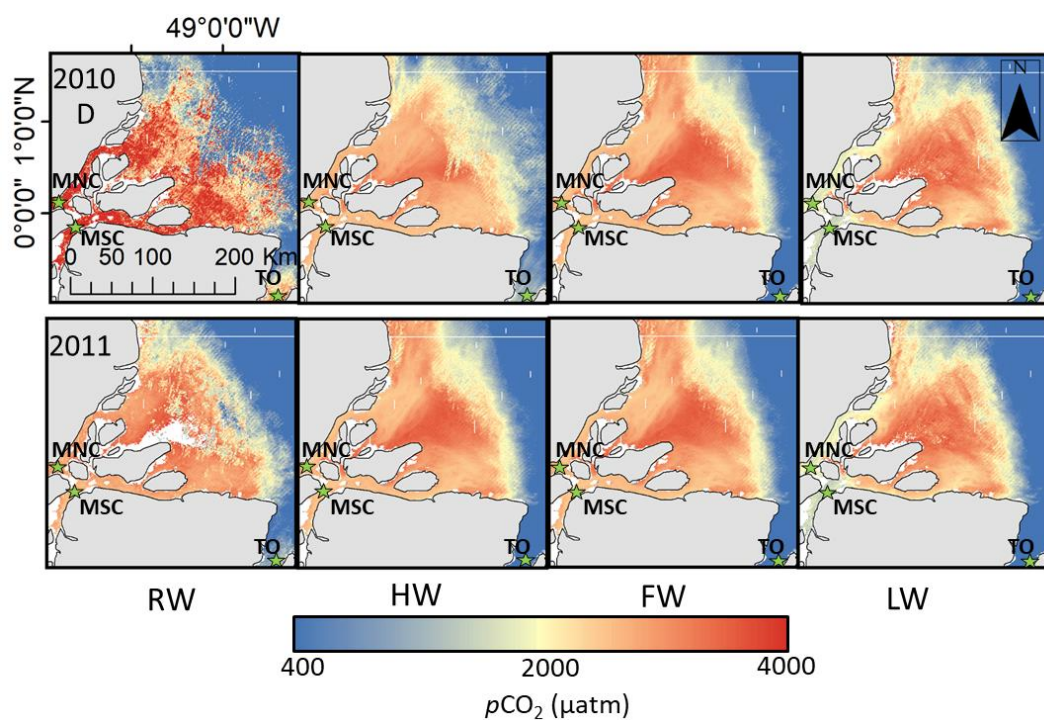
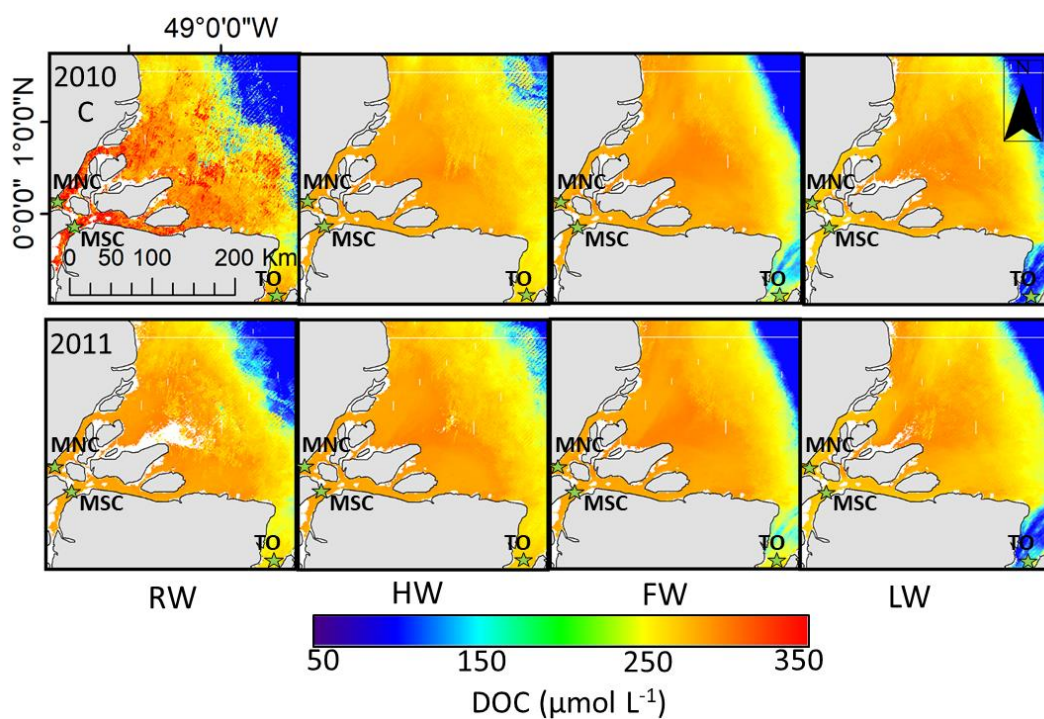


### 6.3.2 Satellite-based carbon content maps

With the use of Cao18 and Vantrepotte15 approaches calibrated for the Lower Amazon it was possible to generate  $a_{\text{CDOM}}(412)$  and  $S_{275-295}$  maps for 2010-2011 using MERIS images (Figure 6.3 A and B). Likewise, the models developed on Chapter 5 are also used to compute DOC and  $p\text{CO}_2$  maps (Figure 6.3 C and D). The maps of DOC were computed using the general algorithm for DOC inversion from CDOM optical properties including the RW season developed previously (General Am+CW, Chapter 5, Section 5.3.2, Table 5.4). The MERIS reflectance data used in the frame of this study over the Amazon region cover the Amazon River mouth, Tocantins River mouth and the coastal waters of the Atlantic Ocean (Globcoast data, <https://www.hygeos.com/project/globcoast>). Therefore, the general algorithm was here adopted for all seasons due to its similarity to the algorithm developed by Vantrepotte et al. (2015) which allow a representation of a larger range of DOC natural variability considering that it has been developed over a data set covering very contrasted coastal waters under riverine waters influence.

Figure 6.3 - Lower Amazon transitional water seasonal MERIS composites illustrating the distribution of: A)  $a_{\text{CDOM}}(412)$  ( $\text{m}^{-1}$ ); B)  $S_{275-295}$  ( $\text{nm}^{-1}$ ); C) DOC concentration ( $\mu\text{mol L}^{-1}$ ); D)  $p\text{CO}_2$  ( $\mu\text{atm}$ ) in 2010 and 2011.





Rising water (RW), High Water (HW), Falling Water (FW) and Low Water (LW). The green polygon located at the Amazon River in the Macapá north channel (MNC) and Macapá south channel (MSC) and at the Tocantins River (TO) represents an area of 5x3 pixels where the information of carbon content was extracted.

Source: Author's production.

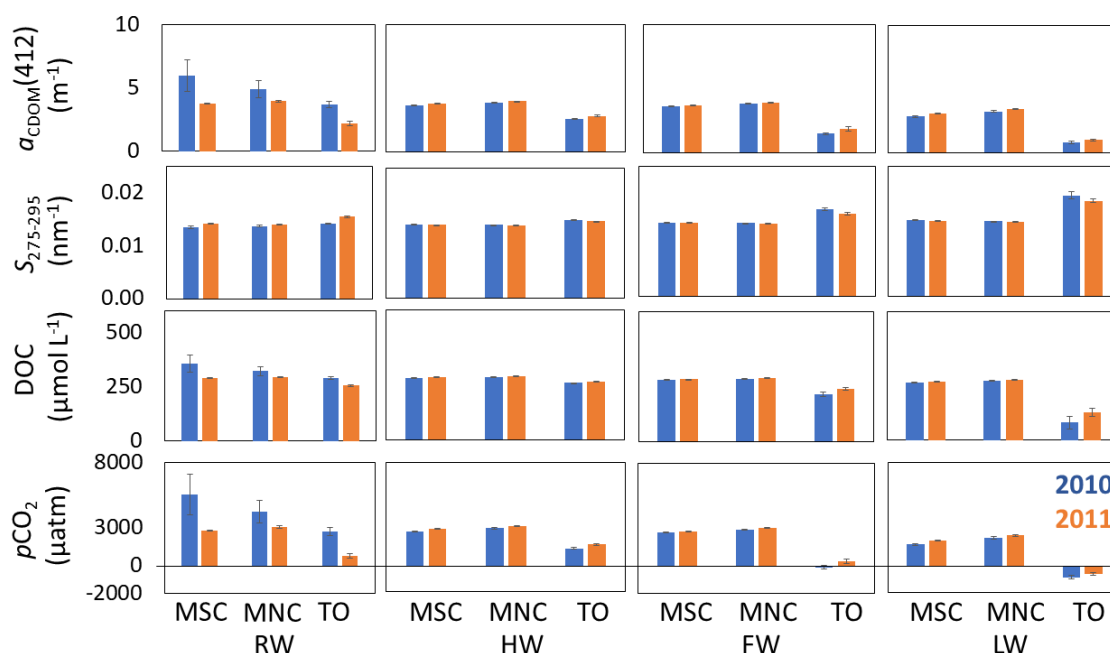
The maps in Figure 6.3 illustrate the gradation of the distribution in the considered parameters and the contrast of the water masses at the meeting of the Amazon River and the ocean. The RW of 2010 presented higher values of all carbon contents estimated with lower  $S_{275-295}$  indicating higher molecular weight of DOM. RW of 2010 aside, for the ranges determined on the maps, the seasonality on the observed area doesn't seem to have a significant variability for the Amazon River mouth. However, when 15 pixels located on Macapá South Channel and Macapá North Channel (Figure 6.3) on the Amazon River's mouth are extracted (total: 30 pixels), the seasonality can be drawn and the LW and RW seasons are statistically different from other seasons ( $p < 0.05$ , Dunn's post hoc) for all variables ( $a_{CDOM}(412)$ ,  $S_{275-295}$ , DOC,  $pCO_2$ ) for the MERIS years considered (2010-2011). For the in situ data (2014-2017) at MSC and MNC,  $a_{CDOM}(412)$  during the LW is statistically different from other seasons as well as HW is different from FW ( $p < 0.05$ , Dunn's post hoc). Additionally, there is no statistical difference of  $S_{275-295}$  and DOC during all seasons ( $p > 0.05$ , Kruskal-Wallis test); and  $pCO_2$  during the LW is statistically different from HW and FW, as well as  $pCO_2$  during RW is different from HW season ( $p < 0.05$ , Dunn's post hoc), for the in situ samples.

In contrast, the seasonality patterns on the computed MERIS maps were more obvious on the Tocantins River mouth, where the RW-HW was marked by higher  $a_{CDOM}$  and DOC and FW-LW was marked by a higher  $S_{275-295}$ . Tocantins River is a clearwater river similar to Tapajós and Xingu (HIERONYMUS et al., 1995) and during the RW-HW seasons, the river receives a higher concentration of allochthonous DOC coming from the surrounding environment (ARAÚJO, 2017). Other authors also documented the higher concentration of DOC during the RW-HW seasons with values close to  $240 \mu\text{mol L}^{-1}$  (ARAÚJO, 2017) similar to the average for 2010 and 2011 estimated by this study ( $269 \pm 12 \mu\text{mol L}^{-1}$ ). For the whole period the Amazon River mouth was outgassing  $CO_2$  and the Tocantins River mouth (TO) acted as a carbon sink during FW-LW ( $pCO_2 < 400 \mu\text{atm}$ ). Even though the River Tocantins was not sampled in situ in the context of this study, it was observed by remote sensing that the concentration of the assessed carbon content was much lower in comparison to the Amazon River.

The comparison among the three locations (MSC, MNC and TO, Figure 6.4) confirms that the Amazon River has higher values of carbon content in comparison to Tocantins River. During the RW season of 2010, the rivers outgassed more CO<sub>2</sub> and delivered more DOM to the ocean, but also had a higher spatial variability. Araújo (2017) documented an average  $p\text{CO}_2$  of 1445  $\mu\text{atm}$  during the RW-HW for the Tocantins River, close to what was estimated by this study algorithm applied to MERIS images ( $1651 \pm 694 \mu\text{atm}$ ,  $p\text{CO}_2$  average and standard deviation for RW-HW of 2010 and 2011).

During the other seasons of 2010 and 2011, the spatial and temporal patterns observed were globally homogeneous with slightly higher values for the year of 2011. Apart from the RW of 2010, the north channel of the Amazon (MNC) also presented slightly higher values in comparison to the south channel (MSC) (Figure 6.4).

Figure 6.4 - Average and standard deviation of  $a_{\text{CDOM}}(412)$  ( $\text{m}^{-1}$ ),  $S_{275-295}$  ( $\text{nm}^{-1}$ ), DOC concentration ( $\mu\text{mol L}^{-1}$ ) and  $p\text{CO}_2$  ( $\mu\text{atm}$ ) for the extracted area of the Macapá south (MSC) and Macapá north (MNC) channel of the Amazon River and Tocantins River (TO).



Source: Author's production.

The comparison among averaged values of  $a_{\text{CDOM}}(412)$ ,  $S_{275-295}$ , DOC and  $p\text{CO}_2$  measured in situ at MSC and MNC and estimated in the same areas from MERIS images shows a general agreement especially in terms of seasonal variation, despite differences regarding of the time period considered due to the unavailability of MERIS data during the in situ sampling period (in situ: 2014-2017; MERIS data 2002-2012) (Table 6.2). Except for the measurements gathered during the LW, all the other seasons show an overall underestimation of DOC values by MERIS (Table 6.2). This fact might be related to exceptional climate events over the years. The year of 2010 here considered for MERIS data was marked by a severe drought (MARENGO et al., 2011) while the year of 2014, when was performed the sampling, was instead marked by a record flood (MARENGO; ESPINOZA, 2016). The rainfall and, consequently, hydrological variation can explain the observed modulation in the amount of DOC within the river (NEU et al., 2016). Likewise, averaged  $p\text{CO}_2$  of in situ data and MERIS data showed a higher discrepancy compared to other parameters.



Table 6.2 - Average and standard deviation ( $\pm$ ) of  $a_{\text{CDOM}}(412)$  ( $\text{m}^{-1}$ ),  $S_{275-295}$  ( $\text{nm}^{-1}$ ), DOC concentration ( $\mu\text{mol L}^{-1}$ ) and  $p\text{CO}_2$  ( $\mu\text{atm}$ ) measured at the Amazon's River mouth by in situ sampling and MERIS images extracted samples, for comparison.

		$a_{\text{CDOM}}(412)$ ( $\text{m}^{-1}$ )		$S_{275-295}$ ( $\text{nm}^{-1}$ )		DOC ( $\mu\text{mol L}^{-1}$ )		$p\text{CO}_2$ ( $\mu\text{atm}$ )	
		in situ	MERIS	in situ	MERIS	in situ	MERIS	in situ	MERIS
RW	MSC	$3.3 \pm 0.3$	$4.9 \pm 0.7$	$0.0144 \pm 0.0003$	$0.0138 \pm 0.0001$	$364 \pm 12$	$322 \pm 21$	$1645 \pm 198$	$4189 \pm 811$
	MNC	$3.8 \pm 0.7$	$4.4 \pm 0.4$	$0.0143 \pm 0.0001$	$0.0139 \pm 0.0001$	$385 \pm 9$	$307 \pm 11$	$1282 \pm 22$	$3632 \pm 484$
HW	MSC	$3.4 \pm 0.3$	$3.7 \pm 0.02$	$0.0145 \pm 0.0002$	$0.0142 \pm 0.00001$	$394 \pm 53$	$288 \pm 1$	$3831 \pm 822$	$2766 \pm 28$
	MNC	$3.4 \pm 0.4$	$3.9 \pm 0.04$	$0.0147 \pm 0.0003$	$0.0141 \pm 0.00002$	$400 \pm 50$	$293 \pm 1$	$4500 \pm 619$	$3001 \pm 47$
FW	MSC	$3.9 \pm 0.2$	$3.7 \pm 0.01$	$0.0144 \pm 0.0002$	$0.0142 \pm 0.00001$	$416 \pm 53$	$287 \pm 0.3$	$2475 \pm 276$	$2718 \pm 15$
	MNC	$3.9 \pm 0.2$	$3.9 \pm 0.04$	$0.0140 \pm 0.0001$	$0.0141 \pm 0.00002$	$290 \pm 4$	$292 \pm 1$	$3404 \pm 567$	$2961 \pm 48$
LW	MSC	$2.8 \pm 0.2$	$3.0 \pm 0.05$	$0.0148 \pm 0.0003$	$0.0146 \pm 0.00001$	$293 \pm 8$	$272 \pm 1$	$1215 \pm 149$	$1859 \pm 60$
	MNC	$2.8 \pm 0.2$	$3.3 \pm 0.06$	$0.0146 \pm 0.0004$	$0.0144 \pm 0.00001$	$277 \pm 5$	$279 \pm 1$	$1149 \pm 125$	$2298 \pm 72$

Locations: Macapá south channel (MSC) and Macapá north channel (MNC). The statistics are computed by season: Rising water (RW), High water (HW), Falling water (FW) and Low water (LW). In situ data comprehends the years of 2014-2017 and MERIS images the years of 2010 and 2011.

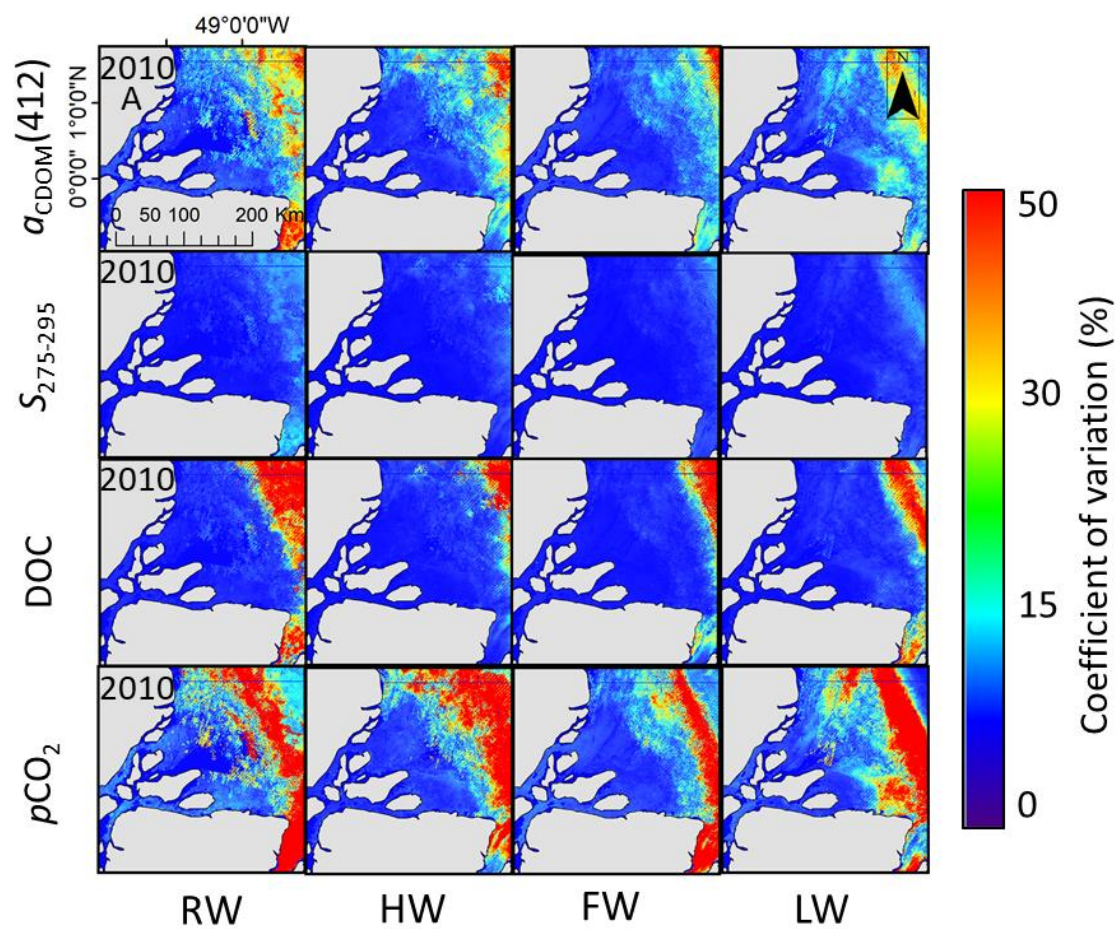
Source: Author's production.

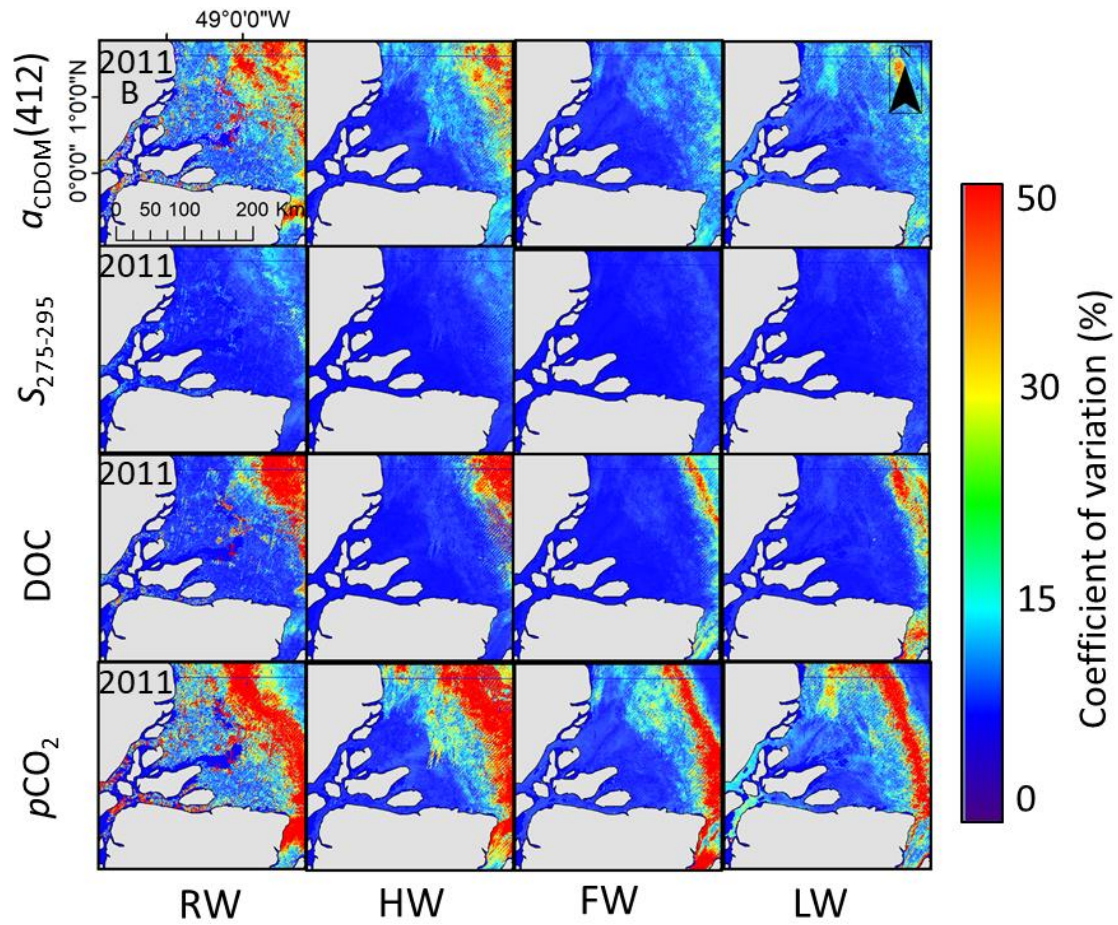
The intra-seasonal variability was illustrated from the coefficient of variation computed for  $a_{\text{CDOM}}(412)$ ,  $S_{275-295}$ , DOC and  $p\text{CO}_2$  for the years 2010 and 2011 (Figure 6.5 A and B). The spatial patterns observed were highly homogeneous from one year

to another with the higher variability observed at the transitional area where the riverine and ocean water meet. Conversely the data corresponding to the Amazon waters were highly homogeneous over the 3 months composing each HW, FW and LW season with  $CV < 10\%$  for all the considered parameters. A higher spatial variability is however found during the RW for all parameters.  $pCO_2$  was the parameter that presented the higher intra-seasonal variability for all seasons considered. Note that the global low intra-seasonal variability of the Amazon waters contrast with the higher coefficients of variation observed for the Tocantins water ( $> 40\%$  for instance for the  $pCO_2$  and DOC which emphasizes the higher dynamics of this riverine system and thus of the environmental factors driving carbon fluxes in this area.



Figure 6.5 - Coefficient of variation (%) for  $a_{CDOM}(412)$ ,  $S_{275-295}$ , DOC and  $pCO_2$  by hydrological season: A) 2010 and; B) 2011.





Rising water (RW), High Water (HW), Falling Water (FW) and Low Water (LW)

Source: Author's production.

#### 6.4 Final considerations

The objective of this chapter was to develop a regional inversion algorithm of CDOM optical properties ( $a_{\text{CDOM}(412)}$  and  $S_{275-295}$ ) selecting the best empirical algorithm among current formulations proposed in the literature. The multilinear model developed by Cao et al., 2018, calibrated for the Lower Amazon data was the most appropriated algorithm at regional scale. The approaches developed by Cao et al., 2018 and Vantrepotte et al., 2015 to retrieve  $S_{275-295}$  were also compared, leading to the selection of Vantrepotte15 for assessing  $S_{275-295}$  in the Lower Amazon. These algorithms were used for computing 2010 and 2011 MERIS seasonal composite of

$a_{\text{CDOM}}(412)$  and  $S_{275-295}$  and then map DOC and  $p\text{CO}_2$ , using the algorithms developed in the Chapter 5.

The final maps allowed a description of the distribution of  $a_{\text{CDOM}}(412)$ ,  $S_{275-295}$ , DOC and  $p\text{CO}_2$  at the Amazon River's mouth, Tocantins River's mouth as well as the meeting of fresh and ocean waters. The seasonal variability in the Amazon water was found to be relatively restricted contrasting with the clear waters of the Tocantins River's mouth, where a higher temporal variability can be evidenced. Amazon River is a source of carbon during all seasons, as expected, while the Tocantins is a source of  $\text{CO}_2$  during the RW and HW and a net sink of  $\text{CO}_2$  during the FW and LW. The intra seasonal variability inside each of the 3-month composites considered for each season, shows the higher dynamical patterns of the region where river mixes with ocean. The latter intra seasonal variability is caused by high standard deviations from the average situation that characterize the season. This could mean that the assumed seasonal hydrologic pattern cannot be considered as a "closed package" of 3 months through the years. Instead, the observed patterns in the corresponding area seem to more likely indicate "moving seasons" translating the importance of other external forcing (e.g. extreme climate events). In addition, the high variability on the region where river mixes with ocean shows, besides the contrasting waters, that less is known about this particular region and more studies are necessary to understand the river-ocean dynamic.

Notwithstanding, this chapter presents the potential of using the proposed algorithms calibrated for the Lower Amazon, to retrieve the carbon content and  $S_{275-295}$  for the land-to-ocean aquatic continuum of the Amazon River, using water colour remote sensing. A future work will focus on the use of adapted temporal analysis (e.g. Census X11 method, Vantrepotte et al., 2011) applied to a longer satellite time series (e.g. 2002-2012 for MERIS) in order to better characterize the spatiotemporal variability patterns of DOC and  $p\text{CO}_2$  over different time scale (intra-annual, annual, interannual) and relate this with the impact of environmental forcing (e.g. climate events such as El

Niño, as already evidenced from in situ observation presented in Chapters 5 and 7). In addition to CDOM algorithm for the Lower Amazon, this study also assessed the retrieval of SPM by reflectance, comparing the results with algorithms documented in the literature (Appendix A).

## **7 SEASONAL AND INTER-ANNUAL VARIABILITY OF CARBON DIOXIDE FLUXES IN THE AMAZON RIVER PLUME BASED ON SOIL MOISTURE AND OCEAN SALINITY SATELLITE DATA**

### **7.1 Introduction**

Inland waters and coastal oceans are becoming increasingly recognized as an integrated water system through which geochemical constituents are constantly transformed providing unique biogeochemical influences in different sectors along the continuum (WARD et al., 2017; MEDEIROS et al., 2015; DAGG et al., 2004; HEDGES et al. 1997). However, few studies have addressed the spatial and temporal dynamics of water and carbon fluxes from the mouth of major river systems out into marine receiving waters. While rivers usually act as a pump of CO<sub>2</sub> that transfers carbon dioxide from the water to the atmosphere (RAYMOND et al., 2013; TRANVIK et al., 2009; COLE et al., 2007) largely due to the breakdown of terrestrially-derived organic matter (WARD et al., 2013) and floodplain inputs (ABRIL et al., 2014), river-dominated coastal areas such as the Amazon River Plume (ARP) are typically thought to remove CO<sub>2</sub> from the atmosphere due to enhanced primary production driven by fluvial nutrients (GOES et al., 2014; YEUNG et al., 2012; SUBRAMANIAM et al., 2008; COOLEY et al., 2007).

Draining an area of ~6.5 million km<sup>2</sup>, the Amazon basin represents ~20% of all freshwater discharge to the global ocean and ~25% of global evasive CO<sub>2</sub> gas flux from inland waters (RAYMOND et al., 2013; RICHEY et al., 1990, 2002). Flowing into the Western Tropical North Atlantic (WTNA), Amazon River water merges with the North Brazil Current and its waters are transported northwestward along the Brazilian North Shelf in the direction of the Guyana Current, forming the ARP. During the FW to LW seasons, a fraction of the ARP is retroflected and carried eastward by the North Equatorial Counter Current. During the RW the water is trapped in the river mouth (recirculation current), due to the onshore trade winds against the coast (LENTZ;

LIMEBURNER, 1995). The dispersal of the ARP can extend offshore to an area of 106 km<sup>2</sup> (MOLLERI et al., 2010)

This seasonal behavior of the ARP has an ecological significance on the WTNA considering the response of the phytoplankton community to changing nutrients availability, river inputs, and consequently affects the carbon dioxide flux. Based on measurements of the outer plume, a net carbon sequestration as high as ~27 Tg C yr<sup>-1</sup> from the atmosphere due to primary production in the mesohaline area (salinity = 30-35 psu) has been measured (SUBRAMANIAM et al., 2008; COOLEY et al., 2007). Lefèvre et al. (2010) estimated an annual CO<sub>2</sub> flux of 5 Tg C yr<sup>-1</sup> from the atmosphere into the ARP. Conversely, the Amazon River basin outgasses ~500 Tg C yr<sup>-1</sup> CO<sub>2</sub> from the river to the atmosphere (RICHEY et al., 2002), with more recent estimates exceeding this estimative by several fold when the entire extent of the river is considered (SAWAKUCHI et al., 2017). This poses the question, what happens to CO<sub>2</sub> fluxes across the continuum, from river export to the overall ARP, on a seasonal basis?

This question poses the significant logistical challenge of enough spatiotemporal coverage to adequately characterize overall flux patterns. The ability to estimate the *p*CO<sub>2</sub> with the use of satellite data allows a more holistic view of the variability and dynamics of net sea-air CO<sub>2</sub> fluxes than ship in situ measurements alone and, as such, more accurate estimations of large-scale regional fluxes. Further, if an established relationship between *p*CO<sub>2</sub> and remotely sensed parameters is robust and well representative of a particular region beyond a particular sampling period, long term variability can be assessed both in present and in past times to assess the influence of environmental factors such as flood/drought cycles and climate variations such as El Niño Southern Oscillation (ENSO) on CO<sub>2</sub> fluxes. The aim of this chapter is to quantify the net flux of CO<sub>2</sub> to/from the river plume and WTNA based on the correlation between remotely sensed parameters and in situ *p*CO<sub>2</sub> measurements. This study considered the area closer to the river mouth that was not included in previous studies at the region (IBÁNHEZ et al., 2016;2015; SUBRAMANIAM et al., 2008; COOLEY et al.,

2007), leading to the hypothesis that the high CO<sub>2</sub> input from the mouth of the Amazon River to the ARP in this area near to the mouth is high enough to offset the absorption of CO<sub>2</sub> in the outer plume.

Quantitative linkages between remotely sensed parameters and  $p\text{CO}_2$  measured in situ has the potential to provide a synoptic view of these processes over a large spatial extent. Several studies have attempted to estimate  $p\text{CO}_2$  from remote sensing and later compute the sea-air CO<sub>2</sub> flux. Sea Surface Temperature (SST) (BAI et al., 2015; ZHU et al., 2009; LOHRENTZ; CAI, 2006) and or  $\text{chl}a$  (BAI et al., 2015; HALES et al., 2012; ZHU et al., 2009; LOHRENTZ; CAI, 2006) are usually the remotely-sensed products used to relate with in situ  $p\text{CO}_2$  by linear or multiple regression. To improve the relationship, other remote sensing parameters have been taken into account such as Sea Surface Salinity (SSS) (BAI et al., 2015; IBÁÑHEZ et al., 2015), wind (LOHRENTZ et al., 2018; ZHU et al., 2009) and CDOM (LOHRENTZ; CAI, 2006). In this study, SMOS products SSS, SST and wind are used to develop  $p\text{CO}_2$  and CO<sub>2</sub> flux maps.

## **7.2 Materials and methods**

### **7.2.1 $p\text{CO}_2$ predictive algorithm**

A predictive algorithm was developed exploring the relationship between in situ SSS, SST and  $p\text{CO}_2$  data using a multiple polynomial regression model. SSS and SST have been described to have a relationship with the variability of  $p\text{CO}_2$  (IBÁÑHEZ et al., 2015; BAI et al., 2015; ZHU et al., 2009; LOHRENTZ; CAI, 2006), although the relationship between SSS and  $p\text{CO}_2$  is much more evident in the ARP (TERNON et al., 2000). While many different approaches have been used to estimate and map coastal  $p\text{CO}_2$ , they are all relatively consistent with previous estimations for the same region and season (RÖDENBECK et al., 2015). These estimations of  $p\text{CO}_2$  are often performed for oceanic waters and when developed for river plumes, usually samples are collected at the distal plume area. In this border region, nutrient and sediment rich river water is more dilute and provides a better environment for phytoplankton blooms, and

consequently, CO<sub>2</sub> consumption, resulting in the transfer of atmospheric CO<sub>2</sub> into the water. This is an important bias to be considered when developing a predictive algorithm of *p*CO<sub>2</sub>, and for that reason, it was developed a new algorithm that takes into account a proximal area of the Amazon River Plume at the river mouth.

SSS, SST and *p*CO<sub>2</sub> measurements along the tracks of the three oceanographic cruises (N=15,392 data points) were averaged for every pixel of the SMOS daily products (N= 318) for the respective cruise date ( $\pm 1$ day), and from now on these variables will be here denominated as SSSa, SSTa and *p*CO<sub>2</sub>a. The variability of these in situ data within the SMOS pixel was calculated using the coefficient of variation.

A limitation faced in this work is the poor performance of SMOS to retrieve lower values of salinity (<30 psu). Advancing into the river mouth the error of SSS increased. Therefore, a part of the in situ salinity samples considered outliers had to be discarded after a Cook's distance analysis, resulting in 253 samples (pixels with in situ integrated data), where 70% of the samples were partitioned to generate the model using the multiple polynomial regression model and 30% were used for validation ( $N_{\text{model}}=177$ ;  $N_{\text{validation}} = 76$ ).

The resultant formula was applied to SMOS daily data of the same dates of in situ sampling to generate *p*CO<sub>2</sub> remote sensing products and to validate the model. Later, the predictive algorithm was applied to three-month composites of SMOS data for the years of 2010-2014. Unfortunately, to develop the model, the samples from 2012 obtained at less than 100 km from the shoreline were excluded because they were outside the limits of SMOS products.

### 7.2.2 Sea-air CO<sub>2</sub> flux

The CO<sub>2</sub> flux from the sea-air CO<sub>2</sub> exchange,  $F_{\text{CO}_2}^{\text{sea}}$  ( $\mu\text{mol m}^{-2} \text{s}^{-1}$ ) in the WTNA, was calculated according to Wanninkhof (1992):

$$F_{\text{CO}_2}^{\text{sea}} = k_{\text{CO}_2} K_0 (p\text{CO}_2^{\text{sea}} - p\text{CO}_2^{\text{air}}) \quad (7.1)$$



where  $p\text{CO}_2$  is the partial pressure of  $\text{CO}_2$  ( $\mu\text{atm}$ ),  $k_{\text{CO}_2}$  ( $\text{cm hr}^{-1}$ ) is the gas transfer coefficient and  $K_0$  ( $\text{mol L}^{-1}\text{atm}^{-1}$ ) is the solubility of  $\text{CO}_2$ . Negative values of  $F_{\text{CO}_2}^{\text{sea}}$  indicate that the water acts as a carbon sink while positive values indicate that water acts as a source of carbon to the atmosphere.  $p\text{CO}_2^{\text{air}}$  was obtained from Barbados ( $13.17^\circ\text{N}$ - $59.43^\circ\text{W}$ ), the closest station of the NOAA Earth System Research Laboratory (ESRL) Global Monitoring Division.

The  $k_{\text{CO}_2}$  was calculated as a quadratic function of wind speed ( $\text{m s}^{-1}$ ) updated by Wanninkhof (2014) which has a 20% uncertainty:

$$k_{\text{CO}_2}^{\text{sea}} = 0.251 U_{10}^2 \left( \sqrt{\frac{660}{Sc}} \right) \quad (7.2)$$

where  $U_{10}$  is the wind speed ( $\text{m s}^{-1}$ ) at 10 m above the water surface and  $Sc$  is the Schmidt dimensionless number determined accordingly to Wanninkhof (2014). For the calculation of  $Sc$  water temperature ( $T$ ) is required.  $T$  and  $U_{10}$  were provided by the SMOS product chosen for this study.

To convert partial pressures into molar units, the solubility of  $\text{CO}_2$ ,  $K_0$  ( $\text{mol L}^{-1} \text{atm}^{-1}$ ) was calculated according to Weiss (1974). All formulae to calculate  $K_0$ ,  $k$ ,  $Sc$  and  $F_{\text{CO}_2}^{\text{sea}}$ , were applied to the SMOS seasonal discharge composites.

The annual net sea-air dissolved  $\text{CO}_2$  ( $\text{Tg C y}^{-1}$ ) was calculated by using the molar mass of C, the fraction of a second in a year, and the area of the plume for each SMOS seasonal discharge composite.

### 7.2.3 Sensitivity analysis

After the adjustment of the multiple polynomial model, a sensitivity analysis (SA) was conducted to identify which model coefficient exert the most influence on the model results. It compares changes in the simulated values against changes in the model coefficient. A sensitivity index was computed to assess the SA (SMITH; SMITH, 2007):

$$S_i = \frac{(Max(P_i) - Min(P_i))}{Max(P_i)} \quad (7.3)$$

where  $P_i$  is each model coefficient. After obtaining  $S_i$  values, a standardization [ $0 \leq S_i \leq 1$ ] was carried out to compare their relative proportions ( $S_i/S_{i\max}$ ) on the model response.

#### **7.2.4 Amazon River Plume area**

The area of the Amazon River plume was delimited and computed by using a threshold algorithm to map water masses with SSS < 35 psu in the WTNA. The computing was performed using QGIS v. 2.18.12, free software.

### **7.3 Results and discussion**

#### **7.3.1 Remote sensing SST and SSS variability**

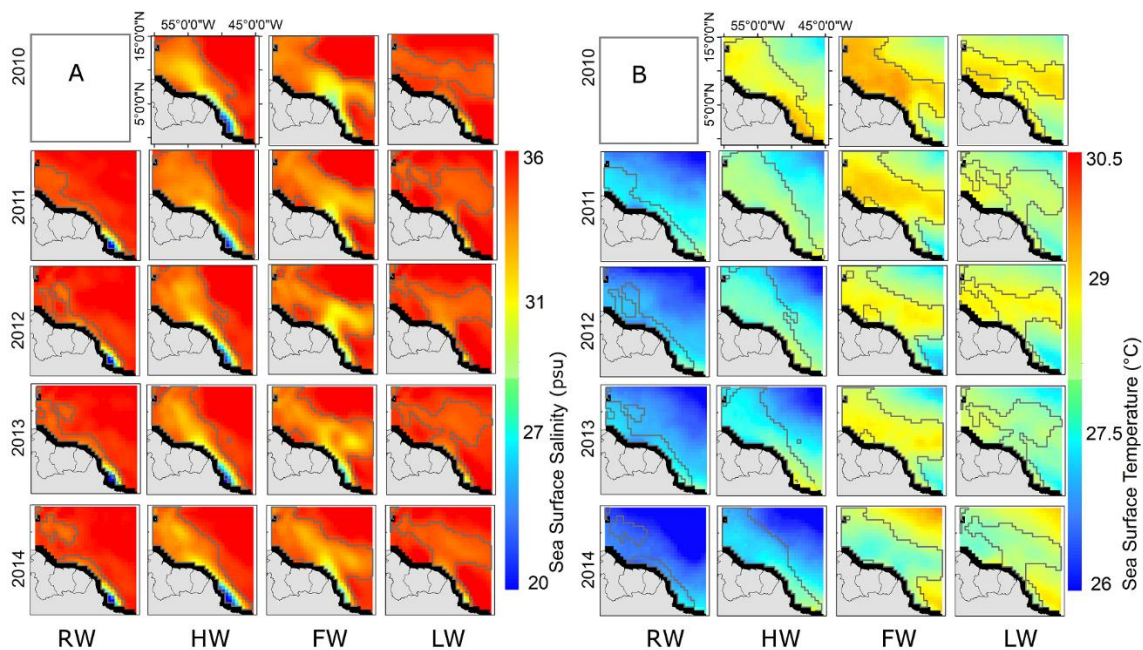
Composites of averaged three months images from SMOS products of SSS and SST (Figure 7.1), shows in general, a colder water for the whole WTNA region for every RW over the study period. The ARP follows the north coast of Brazil in direction to the Guianas, and with lower temperatures ( $\sim 27^\circ\text{C}$ ) during all RW seasons, as well as the lowest SSS values registered by SMOS. It is also interesting to note that, within the plume, the SSS has a higher variation during the RW season, except for the year of 2013 (Table 7.1).

During the HW, the temperature starts to increase in the plume region due to the major discharge of warm waters from the river. The SST product provided by SMOS is consistent with the temperature measured by Lefèvre et al. (2017), with values higher than  $27.8^\circ\text{C}$ . The spread of the riverine water in the plume indicate a larger area presenting SSS < 35 psu. The FW expressed the largest plume area (Figure 7.2) and the temperature reaches its maximum. During the LW, the plume starts to shrink and within the ARP the temperature and SSS are higher in comparison to other seasons, suggesting a mixing of ocean and riverine water (Table 7.1 and Table 7.2). For all

seasons, the latitudinal region below the river mouth has SSS similar to oceanic waters, which is consistent with the observations of Lentz and Limeburner (1995) who observed that the ARP does not extend southeastward beyond the mouth of the Tocantins River, Pará, Brazil.

Previous works described the WTNA as a source of CO<sub>2</sub> (LANDSCHÜTZER et al., 2014; TAKAHASHI et al., 2009). For the studied RW seasons, the WTNA, including the ARP, is in major part dominated by “oceanic alike water” with lower temperatures and higher salinity (Figure 7.1) in comparison to other seasons. However, the lowest values of SSS are also found during the RW season (Table 7.1).

Figure 7.1 - SMOS 3 months composite products of: A) Sea Surface Salinity and B) Sea Surface Temperature for the Western Tropical North Atlantic, according to the discharge season for the years of 2010-2014.



Rising water (RW), high water (HW), falling water (FW) and low water (LW). The gray line refers to the Amazon River Plume (SSS<35) and the black area refers to no-data (maximum distance of 100 km from the coast). The RW of 2010 was not represented in the spatial analyses because SMOS mission only began providing data in May of 2010.

Source: Author's production.

Table 7.1 - Statistics for the SSS (psu) at the Amazon River Plume.

		Min	Max	Mean $\pm$ Std
2010	High	20.78	34.99	32.6 $\pm$ 2.6
	Falling	26.64	34.99	33 $\pm$ 1.7
	Low	27.24	35.00	34.5 $\pm$ 0.8
2011	Rising	15.71	34.99	33.6 $\pm$ 3.2
	High	20.10	34.99	33.2 $\pm$ 2.2
	Falling	26.54	34.98	33.3 $\pm$ 1.3
	Low	30.01	35.00	34.5 $\pm$ 0.6
2012	Rising	16.26	34.99	33.3 $\pm$ 3.4
	High	20.93	35.00	33.1 $\pm$ 2.2
	Falling	26.29	35.00	33.2 $\pm$ 1.5
	Low	30.66	35.00	34.4 $\pm$ 0.6
2013	Rising	21.65	35.00	33.9 $\pm$ 2.2
	High	20.52	34.99	32.9 $\pm$ 2.3
	Falling	25.33	35.00	33.3 $\pm$ 1.5
	Low	28.49	35.00	34.6 $\pm$ 2.8
2014	Rising	14.70	34.97	33.2 $\pm$ 3.5
	High	17.93	35.00	32.6 $\pm$ 2.8
	Falling	26.09	35.00	33.4 $\pm$ 1.5
	Low	27.67	35.00	34.4 $\pm$ 0.7

General statistics: minimum (Min), maximum (Max), Mean and standard deviation ( $\pm$ ).

Source: Author's production.

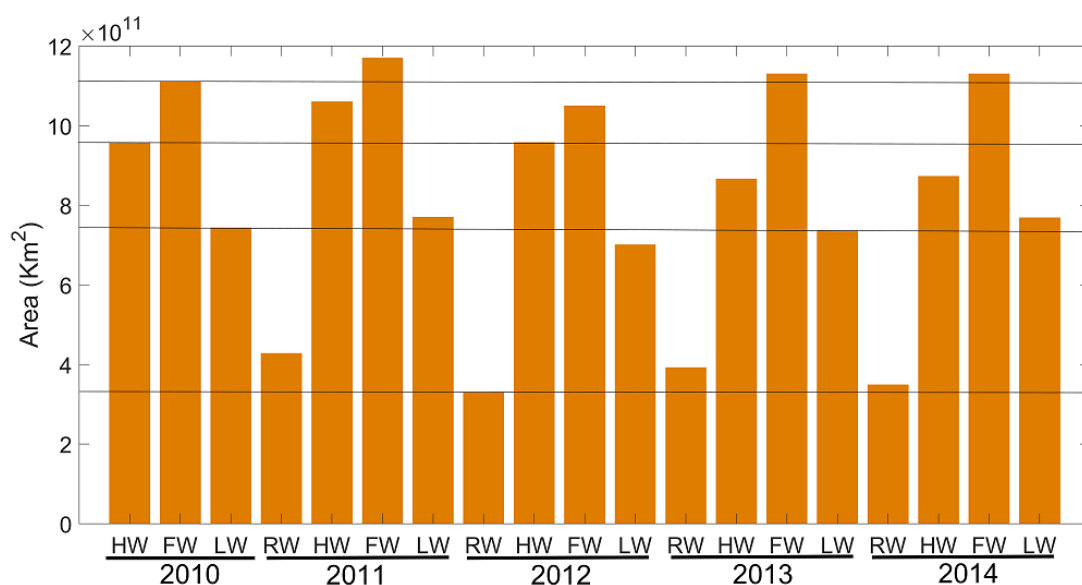
Table 7.2 - Statistics for the SST (°C) at the Amazon River Plume.

		Min	Max	Mean $\pm$ Std
2010	High	28.35	29.60	28.9 $\pm$ 0.2
	Falling	28.30	29.71	29.36 $\pm$ 0.2
	Low	28.33	29.28	29.02 $\pm$ 0.2
2011	Rising	26.85	28.30	27.46 $\pm$ 0.3
	High	27.60	28.60	28.16 $\pm$ 0.2
	Falling	27.82	29.43	29.05 $\pm$ 0.3
	Low	28.00	28.86	28.43 $\pm$ 0.1
2012	Rising	26.46	28.01	27.19 $\pm$ 0.3
	High	27.13	28.58	27.81 $\pm$ 0.3
	Falling	27.45	29.13	28.76 $\pm$ 0.3
	Low	27.86	29.06	28.84 $\pm$ 0.2
2013	Rising	26.84	28.06	27.25 $\pm$ 0.2
	High	26.82	28.72	27.66 $\pm$ 0.4
	Falling	27.72	29.18	28.78 $\pm$ 0.2
	Low	27.83	28.61	28.21 $\pm$ 0.2
2014	Rising	26.29	27.51	26.75 $\pm$ 0.3
	High	26.64	28.51	27.37 $\pm$ 0.4
	Falling	27.48	28.87	28.44 $\pm$ 0.3
	Low	27.67	28.63	28.26 $\pm$ 0.2

General statistics: minimum (Min), maximum (Max), Mean and standard deviation ( $\pm$ ).

Source: Author's production.

Figure 7.2 - Computed area for the Amazon River Plume by discharge season during 2010-2014.



The black lines correspond to the smaller area of each season.

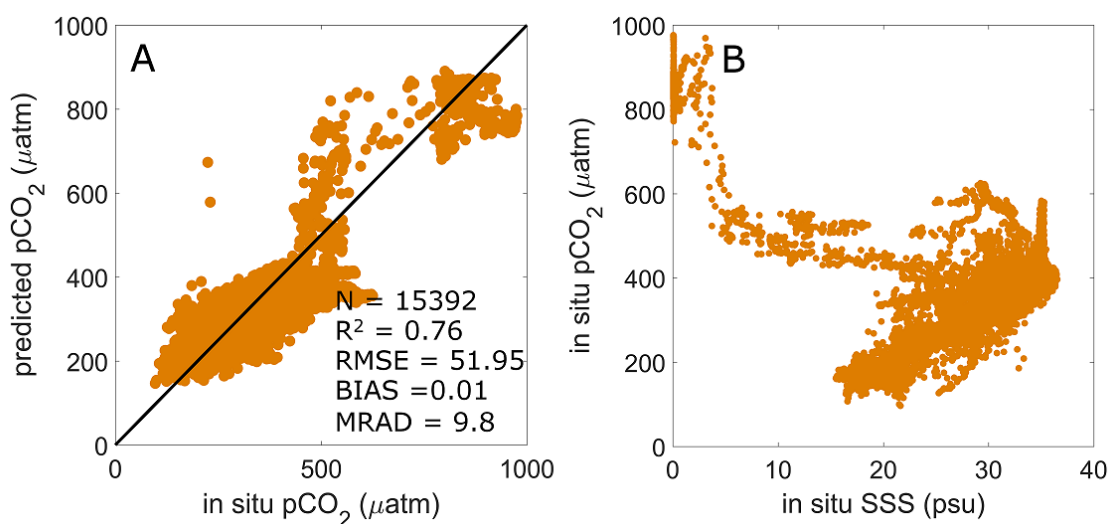
Source: Author's production.

### 7.3.2 Correlation among measured parameters in the ARP and validation of modeled $p\text{CO}_2$

In situ measurements of SST and SSS had a significant positive correlation with  $p\text{CO}_2$  along the oceanographic cruise boundaries (Figure 7.3.A) ( $N = 15392$ ,  $R^2 = 0.76$ ,  $\text{RMSE} = 51.95 \mu\text{atm}$ ,  $\text{BIAS} = 0.01$ ,  $\text{MRAD} = 9.8$ ,  $p < 0.005$ ) using a multiple polynomial regression ( $p\text{CO}_2 = 0.82 (\text{SSS})^2 + 1.7(\text{SST})^2 + 7.7(\text{SSS} * \text{SST}) + 9770.7 - 262.65(\text{SSS}) - 360.14(\text{SST})$  (Equation 7.4)). The in situ  $p\text{CO}_2$  ranged between 97-976  $\mu\text{atm}$ , in which most part of the measurements along the WTNA ranged between 120-500  $\mu\text{atm}$  (94% of this study  $p\text{CO}_2$  dataset); these values are similar to measurements shown by Cooley et al. (2007). The weakness of the relationship at the interval 500-750  $\mu\text{atm}$  (high residual values) is likely due to a strong influence of the river. When in situ data from all the three cruises are compiled (Figure 7.3.B), two very distinct water masses are observed: river and ocean; additionally, it is possible to observe the non-linear behavior of riverine water in both relationships (predicted  $p\text{CO}_2$  x in situ  $p\text{CO}_2$  and in

situ  $p\text{CO}_2$  x in situ SSS, Figure 7.3). Despite this issue, the samples between 500-750  $\mu\text{atm}$  represent only 3% (N= 467) of the total dataset and do not compromise the overall results.

Figure 7.3 - Relationships of in situ  $p\text{CO}_2$ , SSS and SST in the Amazon River plume.



- A) Multiple polynomial regression between in situ SSS, SST and  $p\text{CO}_2$  (N = 15392,  $R^2 = 0.76$ , RMSE = 51.95  $\mu\text{atm}$ , BIAS = 0.01, MRAD = 9.8,  $p < 0.005$ ;  $p\text{CO}_2 = 0.82 (\text{SSS})^2 + 1.7(\text{SST})^2 + 7.7(\text{SSS} * \text{SST}) + 9770.7 - 262.65(\text{SSS}) - 360.14(\text{SST})$ );  
 B) Correlation between in situ salinity and in situ  $p\text{CO}_2$  (2010-2012).

Source: Author's production.

Although all three cruises were crossing within the Amazon plume, they had different routes as can be seen in Figure 3.3 (see chapter 3, section 3.2.2). The cruise of 2012 was much closer to the coast and the  $p\text{CO}_2$  values are much higher when compared to the other two cruises (Table 7.3).

Table 7.3 - General statistics of in situ  $p\text{CO}_2$  sampled during the three oceanographic cruises (2010-2012).

Sampling years of $p\text{CO}_2$ ( $\mu\text{atm}$ )	Min	Max	Mean $\pm$ Std
2010	97.0	477.0	320.4 $\pm$ 76.6
2011	126.3	477.5	349.0 $\pm$ 40.6
2012	152.5	976.0	396.45 $\pm$ 129.3

General statistics: minimum (Min), maximum (Max), Mean and standard deviation ( $\pm$ ).

Source: Author's production.

To match the SMOS pixel spatial resolution of  $0.5^\circ$ , in situ data were averaged and after a Cook's analysis, some outliers were discarded. Basic statistics calculated before and after the averaging are shown in Table 7.4. Even though a great number of in situ data points were averaged, the coefficient of variation shows consistency of SSS, SST and  $p\text{CO}_2$  values within each pixel.



Table 7.4 - General statistics of the variables used to develop the model for the Amazon River Plume, before and after averaging to match the SMOS spatial resolution of 0.5°.

Variable name	Variable description	Min	Max	Mean $\pm$ SD	Median	C.V. min (%)	C.V. max (%)	C.V. mean (%)
SSS in situ	In situ sea surface salinity	0.04	36.5	30.2 $\pm$ 6.9	32.2	--	--	--
SST in situ (°C)	In situ sea surface temperature	26.9	30.8	29.0 $\pm$ 0.7	29.0	--	--	--
pCO <sub>2</sub> in situ (µatm)	In situ sea pCO <sub>2</sub>	96.7	976.0	370.6 $\pm$ 106.6	372.3	--	--	--
SSS <sub>a</sub>	In situ sea surface salinity averaged	20.7	36.3	31.8 $\pm$ 3.4	32.5	0.002	20.2	1.6
SST <sub>a</sub> (°C)	In situ sea surface temperature averaged	27.1	30.4	29.2 $\pm$ 0.6	29.3	0.007	3.5	0.3
pCO <sub>2a</sub> (µatm)	In situ sea pCO <sub>2</sub> averaged	150.1	433.0	349.1 $\pm$ 49.4	360.1	0.03	21.3	2.8

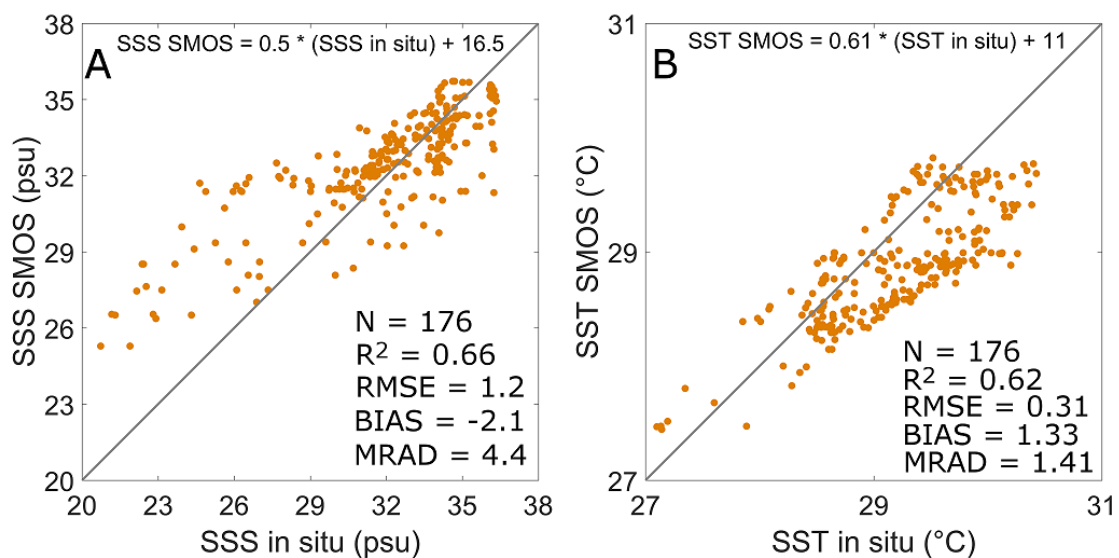
General statistics: minimum (Min), maximum (Max), Mean and standard deviation ( $\pm$ ), Median and coefficient of variation (CV). The first three parameters (SSS in situ, SST in situ (°C) and pCO<sub>2</sub> in situ (µatm)) (N=15392) were measured at surface during three oceanographic cruises and the later three (SSS<sub>a</sub>, SST<sub>a</sub> (°C) and pCO<sub>2a</sub> (µatm)) are the

parameters subsequent the average to match the SMOS spatial resolution of 0.5° (N = 318).

Source: Author's production.

The  $SSS_a$  and  $SST_a$  values used to generate the model are linearly correlated to  $SSS_{SMOS}$ , and  $SST_{SMOS}$  (Figure 7.4.A and Figure 7.4.B, respectively). It is possible to observe that  $SSS_{SMOS}$  overestimates in situ SSS for values < 30 psu, while  $SST_{SMOS}$  has an underestimate bias of the in situ SST. Reul et al. (2012) also observed a SSS bias where SMOS data are too salty in coastal waters with in situ salinity below 33 psu.

Figure 7.4 - Linear relationship between in situ and SMOS parameters in the Amazon River plume.



A) in situ  $SSS_a$  and  $SSS_{SMOS}$  (N = 176,  $R^2 = 0.66$ , RMSE = 1.23, BIAS = -2.1, MRAD = 4.4,  $p < 0.005$ ); B)  $SST_a$  and  $SMOS_{SST}$  (N = 176,  $R^2 = 0.62$ , RMSE = 0.31 °C, BIAS = 1.33, MRAD = 1.41,  $p < 0.005$ ).

Source: Author's production.

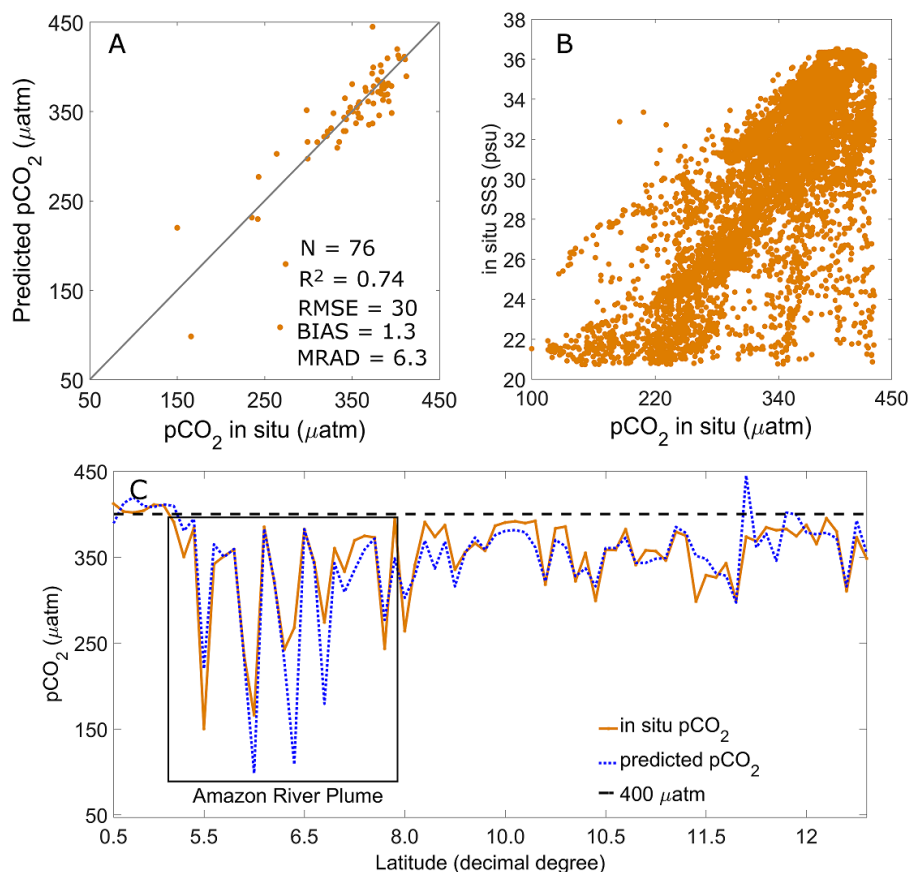
By applying the multiple polynomial regression to SMOS-derived SSS and SST it was possible to generate an empirical function to estimate  $pCO_2$  as follows:

$$pCO_2 = a (SSS)^2 + b(SST)^2 + c(SSS * SST) + d - e(SSS) - f(SST) \quad (7.5)$$

where  $a = 0.05$ ;  $b = 34.81$ ;  $c = 19.71$ ;  $d = 48792.07$ ;  $e = 560.47$ ;  $f = 2694.56$

The empirical model obtained by Equation 7.5 was applied to an independent dataset and it was acceptably validated (Figure 7.5.A,  $N = 76$ ,  $R^2 = 0.74$ ,  $RMSE = 30 \mu atm$ ,  $BIAS = 1.3$ ,  $MRAD = 6.3$ ,  $p < 0.005$ ), although it was identified an underestimation of values below  $300 \mu atm$ .  $pCO_2$  values  $< 300 \mu atm$  were correlated with salinity  $< 30$  psu (Figure 7.5.B) and as shown previously, SMOS has limitations for estimating SSS below this threshold. Nevertheless, the model had a good accuracy representing the  $pCO_2$  distribution throughout ARP (Figure 7.5.C).

Figure 7.5 - Estimative of  $p\text{CO}_2$  using SMOS in the Amazon River plume and Western Tropical North Atlantic.

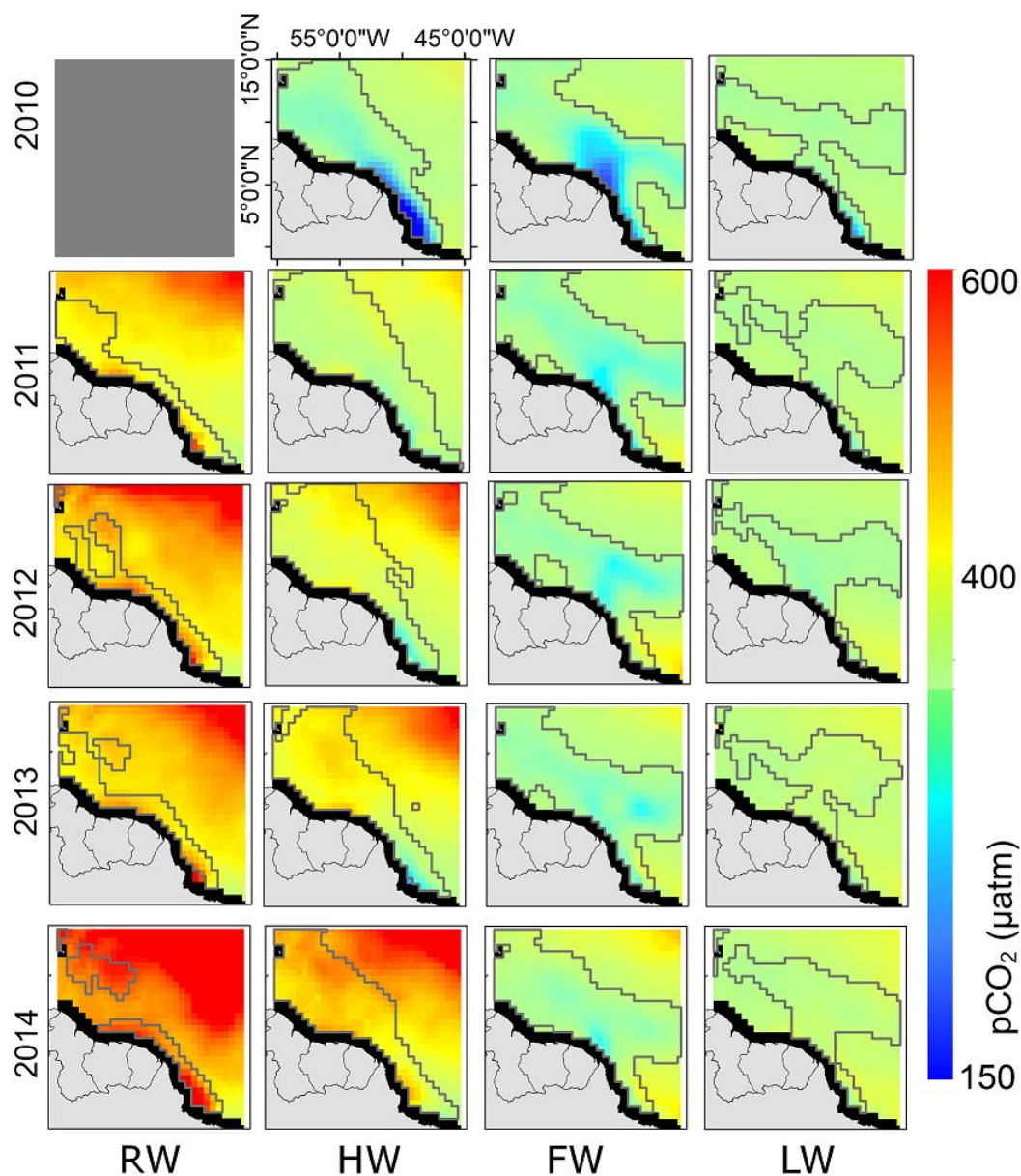


A) Validation of the multiple polynomial regression function of SMOS-derived SSS and SST to estimate  $p\text{CO}_2$  at the Amazon River Plume ( $N = 76$ ,  $R^2 = 0.74$ ,  $\text{RMSE} = 30 \mu\text{atm}$ ,  $\text{BIAS} = 1.3$ ,  $\text{MRAD} = 6.3$ ,  $p < 0.005$ ); B) Correlation between in situ SSS and  $p\text{CO}_2$  within the interval of  $150\text{--}450 \mu\text{atm}$  (Pearson's correlation,  $r = 0.78$ ,  $p < 0.05$ ,  $N = 13940$ ); C) Latitudinal distribution of in situ  $p\text{CO}_2$  and estimated- $p\text{CO}_2$  for the Western Tropical North Atlantic area using SMOS products.

Source: Author's production.

The derived  $p\text{CO}_2$  function was applied to a 3-month composition of SMOS products, grouped according to the seasonal discharge of the Amazon River (Figure 7.6). Except for all RW and HW seasons of 2012-2014, the ARP presented comparatively lower values of estimated- $p\text{CO}_2$  at the WTNA, ranging between  $65\text{--}841 \mu\text{atm}$  ( $\mu = 406 \pm 24 \mu\text{atm}$ ) during the five-year period (Table 7.5).

Figure 7.6 - Estimated- $p\text{CO}_2$  for the Western Tropical North Atlantic area using SMOS products according to the discharge season for the years of 2010-2014.



Rising water (RW), High water (HW), Falling water (FW) and Low water (LW). The gray line refers to the Amazon River Plume (SSS<35) and the black area refers to no-data (maximum distance of 100 km from the coast). The RW of 2010 was not represented in this spatial analysis because SMOS mission only began providing data in May of 2010.

Source: Author's production.

The results from this study for the ARP agree with other  $p\text{CO}_2$  values derived from remote sensing studies in coastal areas dominated by rivers, where the mixing between river and ocean waters decreases  $p\text{CO}_2$  values observed in the plume due to rates of biological uptake and degassing that exceed biological and photo-oxidative organic matter decomposition (BAI et al., 2015; LOHRENZ; CAI, 2006). Considering all studies years,  $p\text{CO}_2$  values were higher during the RW season in comparison to other seasons, suggesting a minor contribution from the ARP.

During the HW season the ARP is driven northwestward by the North Brazil Current, and during the FW season a retroflexion of the ARP has been observed driving nutrient-rich waters eastwards (LENTZ; LIMEBURNER, 1995) and leading to lower values of  $p\text{CO}_2$  due to biological uptake. Lefèvre et al. (2017) also observed a sink of  $\text{CO}_2$  at the French Guiana shelf during the FW season (August). The overall seasonal  $p\text{CO}_2$  values obtained in this study in the ARP are similar to values previously reported by Cooley et al. (2007) and Ibánhez et al. (2016). However, it is also observed higher values ( $> 500 \mu\text{atm}$ ) during the RW season of 2011 and 2012 and during the RW and HW of 2013 and 2014 (Table 7.5).

Table 7.5 - Statistics for the estimated  $p\text{CO}_2$  ( $\mu\text{atm}$ ) for the Amazon River Plume.

Year	Seasonal Discharge	Min	Max	Mean $\pm$ Std
2010	HW	65.0	380.7	$338.2 \pm 55.2$
	FW	192.4	384.4	$342.0 \pm 38.8$
	LW	247.5	380.9	$369.0 \pm 12.9$
2011	RW	382.2	576.3	$451.9 \pm 27.7$
	HW	324.6	428.8	$389.0 \pm 14.2$
	FW	285.4	411.7	$353.2 \pm 19.8$
	LW	338.3	396.5	$377.2 \pm 6.3$
2012	RW	408.7	599.6	$489.8 \pm 30.3$
	HW	313.3	480.0	$419.0 \pm 27.7$
	FW	302.8	438.8	$358.8 \pm 22.6$
	LW	348.4	404.8	$368.3 \pm 6.8$
2013	RW	426.8	553.5	$474.3 \pm 20.3$
	HW	290.3	509.7	$436.8 \pm 36.6$
	FW	305.3	422.6	$358.2 \pm 15.8$
	LW	350.2	407.8	$386.9 \pm 7.7$
2014	RW	440.8	841.2	$561.9 \pm 49.3$
	HW	358.1	545.0	$479.9 \pm 35.5$
	FW	307.9	436.5	$373.1 \pm 18.0$
	LW	367.8	421.2	$385.1 \pm 8.8$

Average 2010- 2014	405.9 ± 23.9
--------------------------	--------------

General statistics: minimum (Min), maximum (Max), Mean and standard deviation ( $\pm$ ).  
Rising water (RW), High water (HW), Falling water (FW) and Low water (LW).

Source: Author's production.

### 7.3.3 Sensitivity analysis

Each coefficient of the model (Equation 7.5) was altered in steps of  $\pm 5\%$  in a range between  $\pm 20\%$ . The changes in a given input into the model varied according to the temperature (26-30°C). The maximum sensitivity index reached was reported as the coefficient "e" (SSS) for 26°C ( $S_i = 8.93$ , Table 7.6) with a maximum value of 100% being attributed. All the other absolute values of  $S_i$  were related to this maximum, resulting in the values presented in Table 7.7.

Table 7.6 - Sensitivity index for each coefficient of the model, in the interval of 26-30°C

Temperature Coefficients	26	27	28	29	30
a	0.62	0.54	-0.31	0.54	<b>1.03</b>
b	0.42	0.42	0.42	0.42	0.42
c	0.42	0.42	0.42	0.42	0.42
d	----	----	----	----	----
e	<b>8.93</b>	<b>-5.83</b>	<b>-1.74</b>	-0.85	<b>1.03</b>
f	0.61	0.53	0.21	0.54	<b>1.03</b>

The bold letters highlight the most sensitive coefficients according to the temperature interval.

Source: Author's production.



Table 7.7 - Standard values relative to the higher sensitivity index (%) for each coefficient of the model, in the interval of 26-30°C.

Temperature Coefficients	26	27	28	29	30
a	7	6	3	6	12
b	5	5	5	5	5
c	5	5	5	5	5
d	----	----	----	----	----
e	<b>100</b>	65	19	10	12
f	7	6	2	6	12

Source: Author's production.

Therefore, the coefficient “e” is the most sensitive followed by the coefficients “a” and “f”. The coefficient “e” represents the SSS (Equation 7.5) and according to this analysis, is more sensitive for lower temperatures (26-28°C). The coefficients “a” and “f” were more sensitive only when the temperature reaches 30°C, but such temperature was not registered by SMOS SST product used in this study ( $SST \leq 29.71$ , Table 7.2). The interval of 26-28°C is observed predominately during the RW for all studied years. This interval is also characteristic of the ocean water observed in Figure 7.1.B.

During the RW season, the extent of the ARP is constrained by ocean currents and trade winds. This can promote two situations. The first is that it might decrease the input of nutrients into the ocean. Furthermore, as the Amazon River takes about 1 month from the last discharge measurement station at Óbidos to reach the open ocean, and about 2 months to reach the distal part of the plume (KOROSOV et al., 2015; HELLWEGER; GORDON, 2002), the RW water season of the ARP still has a lower nutrient input of the river from its respective LW season. Likewise, the results from the

RW of this study are consistent with Lefèvre et al. (2017). In cruises across the border of the plume, during January and March (years: 2006, 2009, 2011-2016) they found that the French Guiana shelf was a source of CO<sub>2</sub>, with transects registered mean salinities higher than 34 psu. The second situation is that the inner shelf water is less diluted with ocean water, therefore predominantly riverine (lowest values of SSS, Table 7.1). CO<sub>2</sub> oversaturation in coastal waters due to riverine carbon input has been reported recently and shows a seasonality dependence (LOHRENZ et al., 2018; XUE et al., 2016).

The optimal-growth zone of phytoplankton in the Amazon shelf occurs mainly seaward of the high-turbidity plume as well as shoreward of the nutrient-depleted offshore water. DeMaster et al. (1983, 1986) reported that the nutrient uptake happens when the turbidity decreases, and the blooms occurred shoreward of the 33 isohaline. In this study period, within the plume, it is likely that the lower salinity values (Table 7.1) of the RW season didn't provide an optimal-growth zone for phytoplankton blooms. Additionally, the nearshore region between Amazon river mouth and the Guianas has been reported as a relevant area of remineralization (ALLER; BLAIR, 2006). The combined biogeochemical-physical conditions suggested here might be causing the increased  $p\text{CO}_2$  during the RW season. Nevertheless, the RW is the most problematic season according to the sensitivity analysis, and although the model was validated, this particular season was not contemplated with in situ data.

#### **7.3.4 Spatiotemporal distribution of CO<sub>2</sub> fluxes in the WTNA**

Calculated monthly sea-air CO<sub>2</sub> fluxes for the ARP ranged from -0.203  $\mu\text{mol m}^2 \text{s}^{-1}$ , during the HW period of 2010 to 0.502  $\mu\text{mol m}^2 \text{s}^{-1}$  during the RW period of 2014 (Table 7.8).  $F_{\text{CO}_2}^{\text{sea}}$  results are in agreement with values presented by Ibáñez et al. (2015) (-0.127 to 0.034  $\mu\text{mol m}^2 \text{s}^{-1}$ ), also indicating that most of the CO<sub>2</sub> outgassing occurs in lower latitudes. Likewise, both results agree that the highest levels of CO<sub>2</sub>

outgassing in the ARP occur during the RW period, whereas the highest levels of CO<sub>2</sub> uptake occur during LW.

Table 7.8 - Statistics for the Sea-air CO<sub>2</sub> flux ( $\mu\text{mol m}^2 \text{s}^{-1}$ ) for the Amazon River Plume.

Year	Seasonal Discharge	Min	Max	Mean $\pm$ Std
2010	HW	-0.203	-0.005	-0.041 $\pm$ 0.032
	FW	-0.117	-0.002	-0.026 $\pm$ 0.021
	LW	-0.115	-0.005	-0.016 $\pm$ 0.010
2011	RW	-0.004	0.155	0.08 $\pm$ 0.031
	HW	-0.047	0.047	-0.003 $\pm$ 0.015
	FW	-0.088	0.025	-0.022 $\pm$ 0.013
	LW	-0.055	0.011	-0.010 $\pm$ 0.006
2012	RW	0.020	0.353	0.139 $\pm$ 0.049
	HW	-0.069	0.138	0.046 $\pm$ 0.038
	FW	-0.046	0.053	-0.016 $\pm$ 0.013
	LW	-0.031	0.010	-0.016 $\pm$ 0.005
2013	RW	0.047	0.206	0.123 $\pm$ 0.030
	HW	-0.074	0.204	0.078 $\pm$ 0.055
	FW	-0.062	0.029	-0.019 $\pm$ 0.010
	LW	-0.042	0.022	-0.001 $\pm$ 0.010
2014	RW	0.055	0.502	0.270 $\pm$ 0.072
	HW	-0.026	0.258	0.143 $\pm$ 0.063
	FW	-0.054	0.058	-0.011 $\pm$ 0.016

	LW	-0.024	0.035	-0.003 ± 0.010
Average				
2010-2014				0.035 ± 0.027

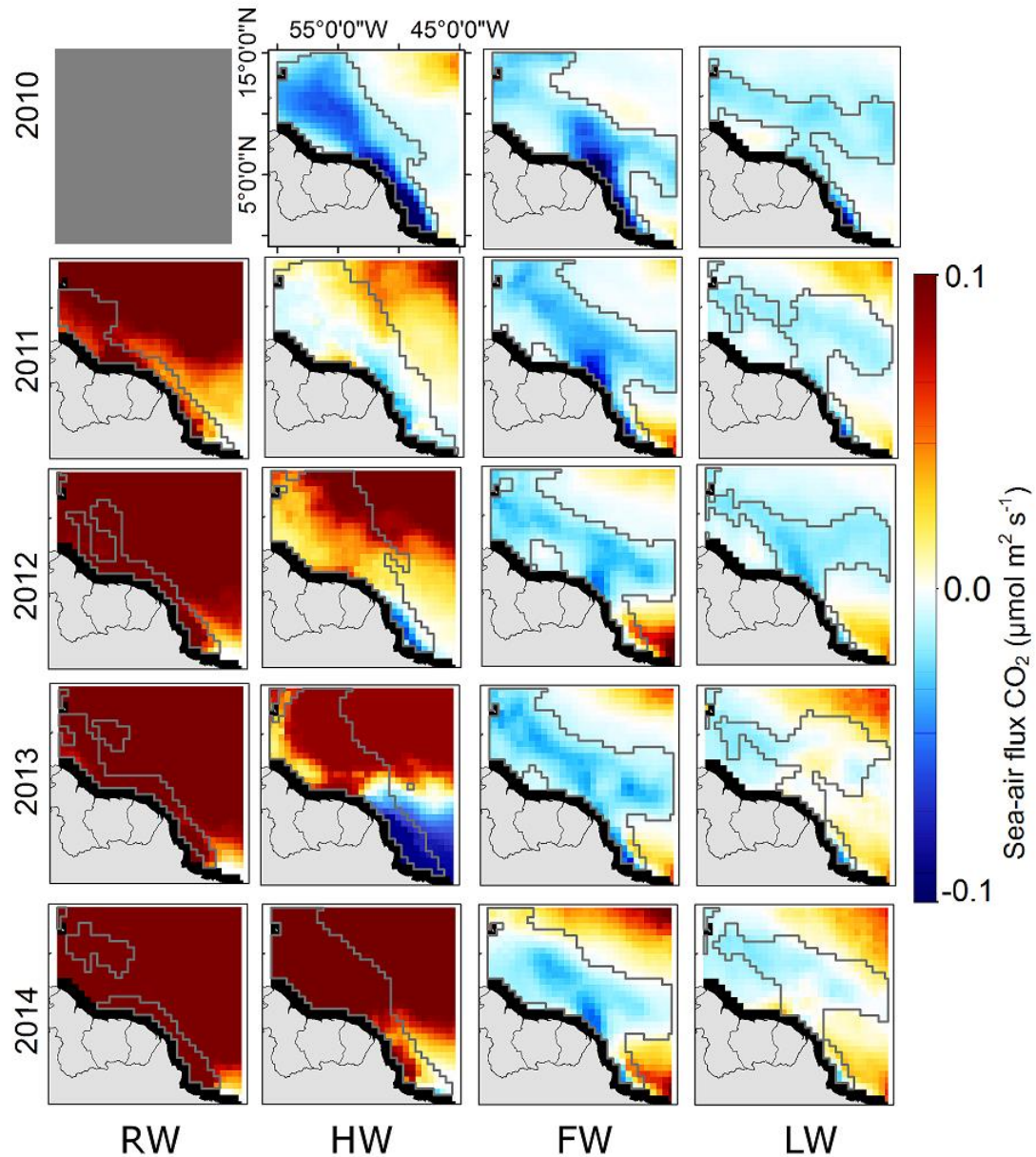
General statistics: minimum (Min), maximum (Max), Mean and standard deviation ( $\pm$ ).

Source: Author's production.

In general, during the RW season the ARP was a source of CO<sub>2</sub> to the atmosphere (red colour), likely due to the imprisonment of the CO<sub>2</sub>-rich Amazon River water that was trapped against the coast (Figure 7.7). During the rest of the seasons (except the year of 2010), even within the Amazon plume, patches acted as a source of CO<sub>2</sub>. It is interesting to note that during 2010 the ARP had the lowest values of  $F_{CO_2}^{sea}$ , acting as a bigger sink of atmospheric CO<sub>2</sub> (blue colour) compared to the other study years. The severe drought in 2010 and the lower river discharge can be clearly observed in the hydrograph (see chapter 3, section 3.4.2, Figure 3.6). The disconnection of the Amazon River from some streams and floodplains due to the unusually low river discharge (MARENGO et al., 2011) may explain lower inputs of CO<sub>2</sub> and organic matter.

The strongest CO<sub>2</sub> sink observed by Lefèvre et al. (2017) was derived from data acquired on cruises made during May and June, that are representative of the HW season. Although the FW season of the present study was representative of a CO<sub>2</sub> sink, this difference may be due to the average months used in this study against local measurements of Lefèvre et al. (2017) transect. For example, Lefèvre et al. (2017) sampled during May of 2010 and June of 2011 when the results from this study shows that the plume was acting strongly as a CO<sub>2</sub> sink. In their work, they did not consider other months representative of the HW season for comparison as considered in this study. Nevertheless, this peculiarity highlights that the variability of the plume cannot be considered universal for its whole extension.

Figure 7.7 - Sea-air CO<sub>2</sub> flux ( $\mu\text{mol m}^2 \text{s}^{-1}$ ) estimated for the Western Tropical North Atlantic area with SMOS products according to the discharge season for the years of 2010-2014.

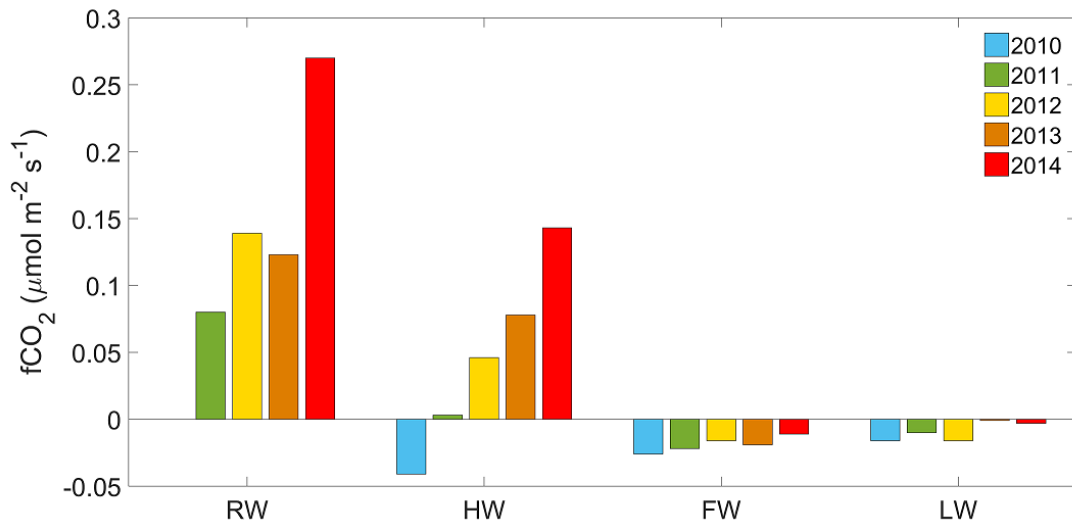


Rising water (RW), High water (HW), Falling water (FW) and Low water (LW). The gray line refers to the Amazon River Plume (SSS<35) and the black area refers to no-data (maximum distance of 100 km from the coast). The RW of 2010 was not represented in this spatial analysis because SMOS mission only began providing data in May of 2010.

Source: Author's production.

The year of 2014 showed the highest values of  $F_{CO_2}^{sea}$  (Figure 7.8). These two contrasting years (2010 and 2014) were marked by a severe drought (MARENGO et al., 2011) and a significant flood (MARENGO; ESPINOZA, 2016; ESPINOZA et al., 2014), respectively, illustrating the dependence of plume dynamics on large-scale hydrologic patterns.

Figure 7.8 - Average of all sea-air CO<sub>2</sub> flux for the Amazon River Plume area with SMOS resolution of 0.5° according to the discharge season for the years of 2010-2014.



Rising water (RW), High water (HW), Falling water (FW) and Low water (LW). The RW of 2010 was not represented in the spatial analysis because SMOS mission only began providing data in May of 2010.

Source: Author's production.

The years of 2012-2014 were marked by an unprecedented flood that started in 2012 associated with a La Niña event and continued due to SST anomalies in the Western Tropical Pacific and in the subtropical South Atlantic (MARENGO; ESPINOZA, 2016; ESPINOZA et al., 2014; SATYAMURTY et al., 2013). During the RW of 2014, the rainfall in the south-western Amazon was 80-100% above normal (ESPINOZA et al., 2014) and may be the responsible for leading the increase in water flux throughout the Amazon basin, flushing more terrestrial and floodplain material and leading to an increase in the input of organic matter and CO<sub>2</sub> from streams and floodplains into the mainstem.

For example, Neu et al. (2016) showed that dissolved organic and inorganic carbon fluxes from above ground flow paths (e.g. rainfall, throughfall, stemflow, and overland flow) and stream flow were greater in the Amazon forest during the first large rainfall event after a long dry period. Likewise, Ward et al. (2012) observed a similar phenomenon in streams of the temperate Pacific Northwest of the US, with dissolved organic carbon and vascular plant biomarker (i.e. lignin phenols) concentrations increasing linearly with river discharge during rain events following long dry periods. The increased rainfall that started in 2012 caused a record discharge of the Amazon River to the ocean with highly turbid waters, as observed in the discharge curve (see chapter 3, section 3.4.2, Figure 3.6).

The average annual flux of CO<sub>2</sub> for the entire plume during the study period was  $5.6 \pm 7.2 \text{ Tg C y}^{-1}$ , with strong inter and intra-annual variability (Table 7.9). The annual CO<sub>2</sub> flux from the ARP calculated here differs from Ibánhez et al. (2016) ( $-7.9 \pm 1.0 \text{ Tg C y}^{-1}$ ). This can be explained by: i) climatic events that intensified the rainfall at the basin during the study period, leading to a higher discharge of water into the ocean and; ii) this study has more sampling points comprising the entire plume, particularly in regions of the plume closer to the Amazon River mouth. Ibánhez et al. (2016) collected in situ samples to generate the model to estimate  $p\text{CO}_2$  in higher latitudes (14°N 5°N 52°W 41°W) (IBÁNHEZ et al., 2015) where the riverine water was more diluted by marine waters and supports phytoplankton blooms that leads to enhanced CO<sub>2</sub> sinking, resulting in an underestimation of the CO<sub>2</sub> fluxes for the whole plume. In this work, the average minimum carbon flux was  $-19 \text{ Tg C y}^{-1}$  during the five-year period (Table 7.9), which is lower than the estimations provided by Subramaniam et al. (2008), who estimated that the ARP was a net CO<sub>2</sub> sink of  $-27 \text{ Tg C y}^{-1}$ .

Table 7.9 - Statistics for the CO<sub>2</sub> flux (Tg C y<sup>-1</sup>) for the Amazon River Plume.

Year	Seasonal Discharge	Min	Max	Mean ± Std
2010	HW	-73.2	-1.9	-15.0 ± 11.5
	FW	-49.0	-0.6	-10.9 ± 8.8
	LW	-32.2	-1.4	-4.4 ± 2.9
	All year			-10.1 ± 7.7
2011	RW	-0.6	25.2	13.0 ± 5.0
	HW	-18.8	19.0	1.1 ± 5.8
	FW	-39.2	11.1	-9.6 ± 5.8
	LW	-15.9	3.1	-3.0 ± 1.8
	All year			0.4 ± 5.6
2012	RW	2.5	43.9	17.3 ± 6.1
	HW	-25.0	50.2	16.6 ± 13.9
	FW	-18.5	21.1	-6.3 ± 5.2
	LW	-8.3	2.6	-4.2 ± 1.4
	All year			5.9 ± 6.6
2013	RW	7.0	30.6	18.3 ± 4.4
	HW	-24.4	66.8	25.7 ± 17.9
	FW	-26.8	12.5	-8.0 ± 4.2
	LW	-11.6	6.0	-0.3 ± 2.7
	All year			8.9 ± 7.3
2014	RW	7.3	66.2	35.6 ± 9.4



HW	-8.7	85.4	$47.2 \pm 20.8$
FW	-23.2	24.7	$-4.7 \pm 6.7$
LW	-7.0	10.2	$-1.0 \pm 2.8$
All year			$19.3 \pm 9.9$
<hr/>			
Average 2010-2014	-19.2	25.0	$5.6 \pm 7.2$
<hr/>			

General statistics: minimum (Min), maximum (Max), Mean and standard deviation ( $\pm$ ).

Source: Author's production.

The inter-annual variability (2010:  $-10.1 \pm 7.7 \text{ Tg C y}^{-1}$ ; 2011:  $0.4 \pm 5.6 \text{ Tg C y}^{-1}$ ; 2012:  $5.9 \pm 6.7 \text{ Tg C y}^{-1}$ ; 2013:  $8.9 \pm 7.3 \text{ Tg C y}^{-1}$ ; 2014:  $19.3 \pm 9.9 \text{ Tg C y}^{-1}$ ) (Table 7.9) can largely be explained by the extreme climatic events. In early RW of 2010, a strong El Niño event occurred followed by a La Niña in the FW (MARENGO et al., 2011), along with an anomalous warming of the SST in the Northern Atlantic (ESPINOZA et al., 2011). The intra-annual variability was marked by a large carbon sink during the HW season of 2010 and high carbon emissions during the RW and HW seasons of 2014. Understanding the role of extreme climatic events is highly relevant to future projections of carbon cycling in the region and globally considering that climate change is expected to enhance flood/drought cycles (NOHARA et al., 2006). Therefore, the CO<sub>2</sub> flux difference among seasons through the years suggest that the CO<sub>2</sub> outgassing is driven by the discharge seasonality, climatic events and the ocean currents.

The CO<sub>2</sub> degassed in the plume is likely mostly derived from the decomposition of river dissolved organic matter by microbes in the river (WARD et al., 2013, 2016) or the very early stages of the plume (MEDEIROS et al., 2015; SEIDEL et al., 2015). Thus, the low outgassing flux during 2010 in the ARP was likely a consequence of the low discharge of the river to the ocean. Additionally, the reduced discharge likely resulted in a reduction of turbidity (i.e. lower suspended sediment concentrations), allowing more

light penetration that enhances the primary production and precedes an increase in CO<sub>2</sub> uptake. Smith and DeMaster (1996) showed that phytoplankton photosynthesis in waters influenced by the Amazon River is limited by low levels of available irradiance, particularly in the reaches of the plume closest to the river influence (MEDEIROS et al., 2015).

Medeiros et al. (2015) and Seidel et al. (2015) assessed the fate of organic matter along the Amazon River continuum and elucidated the processes and their spatial variability in the ARP. Near the mouth, where the water is more brackish with lower light penetration, the predominant process was bacterial remineralization, which releases CO<sub>2</sub> to the water. During 2012-2014 the annual flux of CO<sub>2</sub> was positive, suggesting that the greater load of turbid riverine water transported by the ARP interfered with the growth of phytoplankton, reducing primary production and therefore reducing the oceanic uptake of CO<sub>2</sub>.

Consideration of the inner plume CO<sub>2</sub> flux estimative significantly changes the respective impact of the net primary productivity on the overall the carbon balance of the ARP. Although primary production still plays an important role in the carbon budget of the plume, it may have been overestimated by previous studies that considered only the productive areas at the border of the plume.

### **7.3.5 Study limitations and future suggestions**

The algorithm presented here is based on data acquired by a microwave orbital sensor that has the advantage of weather independence, essentially, the presence of clouds that is a major issue for the studied area. Although it has a poor spatial resolution (0.5°) compared to other sensors operating in the visible part of the electromagnetic spectrum (< 4 km), the estimated *p*CO<sub>2</sub> average values showed a low coefficient of variation within each pixel. Despite this, the present algorithm had a weak relationship between the range of ~500-750 µatm. This interval speaks for only 3% of the total samples and it represents riverine water. Another drawback is that SMOS products do

not reach as close to the shoreline due to adjacency effects of land contamination. A limitation faced in this work is the poor performance of SMOS to retrieve lower values of salinity (<30 psu), as advancing into the river mouth the error of SSS increased. Additionally, part of the in situ salinity samples had to be discarded after an outlier analysis with the SMOS products.

As this study illustrates, the coastal region is crucial for understanding the turning point of the CO<sub>2</sub> flux along the ARP and including these waters will likely lead to higher estimates of degassing. To address this issue requires not only additional in situ measurements closer to the coastline for algorithm validation, but also the potential use of a visible sensor (e.g. Moderate Resolution Imaging Spectroradiometer - MODIS, Visible Infrared Imaging Radiometer Suite - VIIRS, Ocean and Land Colour Instrument - OLCI). This approach may allow both the coastline and river to be resolved in concert and allow for a more diverse combination of ocean color products to be related to  $p\text{CO}_2$  such as CDOM and chl $\alpha$ .

SSS was the most important proxy for  $p\text{CO}_2$  in the ARP and although visible sensors don't have a salinity product, it is possible to derive a synthetic salinity by the strong negative linear relationship between the absorption coefficients of coloured dissolved organic matter and salinity in river plume dominated coastal oceans (MOLLERI et al., 2010). However, to use optical data in the study area would require a very accurate atmospheric correction of satellite images, as well as effective cloud masking due to high turbidity normally observed in the region. High concentrations of suspended sediments have a high signal response which could be erroneously taken as clouds. Additionally, this is a significantly cloudy region that would limit the quality and/or quantity of imagery availability. Further, in situ sampling is required for validation of bio-optical properties, since the chl- $\alpha$  measured in very turbid water can be overestimated if an effective atmospheric correction and appropriated reflectance algorithm is not applied (VANHELLEMONT; RUDDICK, 2015; LOISEL et al. 2013; GITELSON et al., 2008).

## 7.4 Final considerations

This chapter estimated the concentration and net flux of CO<sub>2</sub> for the ARP by remote sensing based on an empirical relationship between in situ  $p\text{CO}_2$  and SMOS-derived SSS and SST. Intra-annual variability of the dissolved CO<sub>2</sub> input from the river to the ARP was a consequence of the rainy season and consequent hydrologic behavior, which influence the discharge of the Amazon River. The  $F_{\text{CO}_2}^{\text{sea}}$  responded to plume pathways, which is tied to the North Brazil Current, North Equatorial Counter Current and trade winds.

The RW season was characterized as a net source of CO<sub>2</sub> and was the most sensitive season according to sensitivity analysis performed. Therefore, it is suggested more in situ campaigns to better describe the region and improve the  $p\text{CO}_2$  model. During the HW season when the river discharges more dissolved CO<sub>2</sub> to the ocean, the plume takes up less or even emits and exports CO<sub>2</sub>. During the FW season, the river exported less CO<sub>2</sub> compared to the HW season. Moreover, the plume is deflected eastward by the North Equatorial Counter Current and as the extent of the plume gets bigger, the resultant retroflexion drives riverine nutrient export that enhances biological uptake. Thus, the FW season was ubiquitously a net sink of CO<sub>2</sub>.

Averaged throughout the study period, the plume generally acted as a source of CO<sub>2</sub> to the atmosphere even though it acted as a CO<sub>2</sub> sink during LW and FW periods. As was reflected in the behavior of the plume, the five-year study period provided contrasting conditions, with the drought of 2010 and the flood of 2012-2014. The Amazon River emitted less CO<sub>2</sub> during 2010 and more during 2014 and the ARP absorbed more CO<sub>2</sub> during 2010 and took up less during 2014.

Results from this study provide increased spatiotemporal coverage of CO<sub>2</sub> fluxes in the Amazon River plume from earlier studies, particularly in regions closer to the river. They show that the ARP acts less as carbon sink area than originally thought, and for the present study period, acted as a net source of CO<sub>2</sub>. This study hypothesize that the

ARP is an even larger source of CO<sub>2</sub> to the atmosphere than estimated here if the entire coastal extent, including the shore-side 100 km not covered by the SMOS sensor, if the plume is considered in future studies. Finally, this study highlights the importance of large-scale climate patterns on carbon cycling across the river to ocean continuum in the world's largest river system.



## 8 CONCLUDING REMARKS AND RECOMMENDATIONS

This research was a step forward on the use of water colour information to assess bio-optical properties on the Amazon River. A comprehensive assessment of the biogeochemical and bio-optical spatiotemporal variability of the Lower Amazon was performed and discussed according to the impact of regional environmental forcing. Moreover, the inclusion of the Amazon River Plume within this study, enriched the discussion considering an integrated water system and contributes to a better understanding of the biogeochemical dynamics of the water masses composing the Amazon River continuum.

The assessment of the bio-optical properties showed the challenge still represented by the measurements in the Lower Amazon of the absorption properties associated with the phytoplankton and non-algal particles ( $a_{\text{phy}}$  and  $a_{\text{nap}}$ , respectively) underlining the need to develop adapted methodological approaches.

A clear bio-optical distinction exists between the CW rivers where the absorption budget is dominated by CDOM and the Amazon mainstream waters where the relative contribution of CDOM and  $a_p$  is globally well-balanced. While a relatively low seasonality was observed in the bio-optical characteristics of the Amazonian waters, the situation observed during the RW season departs from the other discharges condition with a significant increase in SPM loads and thus in the relative importance of  $a_p$  in the overall water absorption. It is worthy to note that, although the RW season is usually assumed to correspond to the first trimester of the year, this temporal segmentation is subject to time-shifting due to extreme climatic events (e.g. El Niño and La Niña).

The optical characterization of the Amazon waters was assessed leading to the definition of four (4) optical classes. This optical typology is useful to synthetically follow the spatial distribution of the water masses of the Lower Amazon (CW vs

Amazon waters) but also, to monitor the temporal dynamics of these waters (taking into account for instance possible time-shifting in the Amazon waters characteristics).

The variability along the Lower Amazon transect underlines the dilution patterns related to the mixing of the Amazon waters with that corresponding to the CW tributaries. The decrease in CDOM from Óbidos to Macapá, and the associated increase in CDOM spectral slope in the UV ( $S_{275-295}$ , proxy for the DOM molecular weight) emphasized the importance of the bacterial degradation processes occurring along the course of the Amazon river. Small-scale processes, such as tidal effects, had a more limited impact on the Amazon water masses bio-optical variability.

In addition to an original description of the bio-optical variability of the Lower Amazon River, this study aimed to develop inversion algorithms allowing an estimation of major elements of the carbon cycle (DOC,  $p\text{CO}_2$ ) from water colour remote sensing information.

The heterogeneity in the DOM characteristics in CW and turbid waters, as well as sharp temporal variation in the nature of the DOM at regional scale, limit the use of a single relationship for estimating DOC content from CDOM optical properties ( $a_{\text{CDOM}}$  or  $S_{275-295}$ ).

Conversely,  $p\text{CO}_2$  was not susceptible to seasonal or optical variability and could be satisfactorily retrieved over the Amazon water continuum. In practice, two algorithms were developed: i) using single regional algorithm based on CDOM and water temperature for the Lower Amazon water, and ii) using salinity and water temperature for the Amazon River plume. The possible use of CDOM as a proxy for  $p\text{CO}_2$  in the Amazon plume still has to be further investigated.

Regional empirical algorithms for estimating CDOM absorption properties have been developed. Among the different formulations currently available in the literature, the multilinear model by Cao et al., 2018 and the nonlinear model by Vantrepotte et al.,



2015 adapted to the waters of the Lower Amazon waters were in practice selected for estimating  $a_{\text{CDOM}}(412)$  and  $S_{275-295}$ , respectively.

$a_{\text{CDOM}}(412)$ ,  $S_{275-295}$ , DOC and  $p\text{CO}_2$  models developed on this study were applied on MERIS seasonal composite images for the years of 2010 and 2011. The final maps allowed a description of the distribution of  $a_{\text{CDOM}}(412)$ ,  $S_{275-295}$ , DOC and  $p\text{CO}_2$  at the Amazon River's mouth, Tocantins River's mouth, as well as the transition area corresponding to the encounter of fresh and oceanic waters. For the assessed years (2010-2011), the seasonal variability of the Amazon water was more restricted contrasting with the clear waters of the Tocantins's River mouth, where a higher temporal variability was evidenced. Amazon River was a source of carbon during all seasons, with high values of  $a_{\text{CDOM}}(412)$ , DOC and  $p\text{CO}_2$  and less degraded DOM as indicated by low  $S_{275-295}$ . Conversely, Tocantins River's mouth was a source of  $\text{CO}_2$  during the RW and HW season, and a net  $\text{CO}_2$  sink during the FW and LW season. However, except for the LW season, Tocantins River's also exported a great load of DOC to the ocean. The DOC exported by the Tocantins River's to the ocean had lower molecular weight compared with the Amazon River. The intra-seasonal variability observed on MERIS images indicates a high variability in areas where the river and the ocean encounter, evidencing the need to better investigate these poorly described and highly dynamical waters.

The  $p\text{CO}_2$  and  $\text{CO}_2$  flux maps for the Amazon River plume emphasized the impact of the hydrological pattern on the inter and intra-annual variability. The ARP during the RW and HW seasons were characterized generally as a net source of  $\text{CO}_2$ . Conversely, during the FW and LW seasons, the ARP was a net sink of  $\text{CO}_2$ . Additionally, the assessed years for the ARP (2010-2014) was marked by extreme climate events that impact the  $\text{CO}_2$  flux through the seasons. Despite the gap between the Amazon River's mouth and the ARP, this study shows that the ARP acts less as a carbon sink area than previously thought (SUBRAMANIAM et al., 2008), and moreover, for the assessed period, acted also as a net source of  $\text{CO}_2$ . While additional studies are still needed to

better specify the carbon balance in the ARP, our results tend to suggest the neutral feature of this area.

The methodological developments performed in the frame of this study will support many future works. The present study has clearly underlined the interest of water colour based observations and underlining at the same time the need to consider regionally adapted methods for assessing the Amazon waters carbon content from remote sensing observation. The two approaches here developed for estimating  $p\text{CO}_2$  content provide first evidence of the possible monitoring of  $p\text{CO}_2$  over in the Amazon River's mouth (ARM) and Amazon River plume (ARP), completing the current gap between fresh and ocean waters. Future methodological approaches are however still required in order to properly combine the information here obtained regarding the  $p\text{CO}_2$  distribution in the ARM and the ARP and follow the carbon fluxes over the Amazon river continuum.

While, additional in situ studies are still needed to further validate the approaches proposed in the frame of this work, the application of the DOC and  $p\text{CO}_2$  inversion algorithms here developed on historical or more recent satellite water color archives will provide better insights into the understanding of the dynamics of major elements of the water carbon cycle at regional scale.

## REFERENCES

- ABRIL, G.; MARTINEZ, J.-M.; ARTIGAS, L. F.; MOREIRA-TURCQ, P.; BENEDETTI, M. F.; VIDAL, L.; MEZIANE, T.; KIM, J.-H.; BERNARDES, M. C.; SAVOYE, N.; DEBORDE, J.; SOUZA, E. L.; ALBÉRIC, P.; LANDIM DE SOUZA, M. F.; ROLAND, F. Amazon River carbon dioxide outgassing fueled by wetlands. **Nature**, v. 505, n. 7483, p. 395–398, 2014.
- ALBÉRIC, P.; PÉREZ, M. A. P.; MOREIRA-TURCQ, P.; BENEDETTI, M. F.; BOUILLON, S.; ABRIL, G. Variation of the isotopic composition of dissolved organic carbon during the runoff cycle in the Amazon River and the floodplains. **Comptes Rendus Geoscience**, n. February, 2017.
- ALCÂNTARA, E. H.; STECH, J. L.; LORENZZETTI, J. A.; BONNET, M. P.; CASAMITJANA, X.; ASSIREU, A. T.; NOVO, E. M. L. D. M.; HERENIO, E.; LUIZ, J.; ANTÔNIO, J.; PAULE, M.; TREVENZOLI, A.; MÁRCIA, E.; MORAES, L. DE. Remote sensing of water surface temperature and heat flux over a tropical hydroelectric reservoir. **Remote Sensing of Environment**, v. 114, n. 11, p. 2651–2665, 2010.
- ALCÂNTARA, E.; BERNARDO, N.; WATANABE, F.; RODRIGUES, T.; ROTTA, L.; CARMO, A.; SHIMABUKURO, M.; GONÇALVES, S.; IMAI, N. Estimating the CDOM absorption coefficient in tropical inland waters using OLI/Landsat-8 images. **Remote Sensing Letters**, v. 7, n. 7, p. 661–670, 2016.
- ALCÂNTARA, E.; NOVO, E. M.; BARBOSA, C. F.; BONNET, M.-P.; STECH, J.; OMETTO, J. P. Environmental factors associated with long-term changes in chlorophyll-a concentration in the Amazon floodplain. **Biogeosciences Discussions**, v. 8, n. 2, p. 3739–3770, 2011.
- ALLER, R. C.; BLAIR, N. E. Carbon remineralization in the Amazon–Guianas tropical mobile mudbelt: A sedimentary incinerator. **Continental Shelf Research**, v. 26, n. 17–18, p. 2241–2259, 2006.
- ARAÚJO, M.G.S. **Dinâmica do carbono no Baixo Tocantins**. Belém: Universidade Federal Rural da Amazônia, 2017.56p.
- AURIN, D. A.; DIERSEN, H. M.; AURIN, D. A.; DIERSEN, H. M. Advantages and limitations of ocean color remote sensing in CDOM-dominated, mineral-rich coastal and estuarine waters. **Remote Sensing of Environment**, v. 125, p. 181–197, 2012.
- BABIN, M.; STRAMSKI, D.; FERRARI, G. M.; CLAUSTRE, H.; BRICAUD, A.; OBOLENSKY, G.; HOEPPFNER, N. Variations in the light absorption coefficients of phytoplankton,

nonalgal particles, and dissolved organic matter in coastal waters around Europe. **Journal of Geophysical Research**, v. 108, n. C7, p. 3211, 2003.

BAI, Y.; CAI, W.-J.; HE, X.; ZHAI, W.; PAN, D.; DAI, M.; YU, P. A mechanistic semi-analytical method for remotely sensing sea surface pCO<sub>2</sub> in river-dominated coastal oceans: A case study from the East China Sea. **Journal of Geophysical Research: Oceans**, v. 120, p. 1–19, 2015.

BANKS, A. C.; MÉLIN, F. An assessment of cloud masking schemes for satellite ocean colour data of marine optical extremes. **International Journal of Remote Sensing**, v. 36, n. 3, p. 797–821, 2015.

BARBOSA, F.; MA, E.; BARBOSA, C. C. F.; MORAES NOVO, E. M. L.; MELACK, J. M.; GASTIL-BUHL, M.; FILHO, W. P. Geospatial analysis of spatiotemporal patterns of pH, total suspended sediment and chlorophyll-a on the Amazon floodplain. **Limnology**, v. 11, n. 2, p. 155–166, 2010.

BARNARD, A. H.; ZANEVELD, J. R. V.; PEGAU, W. S. In situ determination of the remotely sensed reflectance and the absorption coefficient: closure and inversion. **Applied optics**, v. 38, n. 24, p. 5108–17, 1999.

BATTIN, T. J.; KAPLAN, L. A.; FINDLAY, S.; HOPKINSON, C. S.; MARTI, E.; PACKMAN, A. I.; NEWBOLD, J. D.; SABATER, F. Biophysical controls on organic carbon fluxes in fluvial networks. **Nature Geoscience**, v. 2, n. 8, p. 595–595, 2008.

BERNARDES, M. C.; MARTINELLI, L. A.; KRUSCHE, A. V.; GUDEMAN, J.; MOREIRA, M.; VICTORIA, R. L.; OMETTO, J. P. H. B.; BALLESTER, M. V. R.; AUFDENKAMPE, A. K.; RICHEY, J. E.; HEDGES, J. I. Riverine organic matter composition as a function of land use changes, southwest amazon. **Ecological Applications**, v. 14, n. sp4, p. 263–279, 2004.

BILLEN, G.; LANCELOT, C.; MEYBECK, M. N, P, and Si retention along the aquatic continuum from land to ocean. **Ocean Margin Processes in Global Change**. 1991. n. 1764, p. 19–44.

BINDING, C. E.; JEROME, J. H.; BUKATA, R. P.; BOOTY, W. G. Spectral absorption properties of dissolved and particulate matter in Lake Erie. **Remote Sensing of Environment**, v. 112, n. 4, p. 1702–1711, 2008.

BIRKETT, C. M. Contribution of the TOPEX NASA Radar Altimeter to the global monitoring of large rivers and wetlands. **Water Resources Research**, v. 34, n. 5, p. 1223–1239, 1998.

BORGES, A. V.; RUDDICK, K.; LACROIX, G.; NECHAD, B.; ASTEROCA, R.; ROUSSEAU, V.; HARLAY, J. Estimating pCO<sub>2</sub> from Remote Sensing in the Belgian Coastal Zone. **Proceedings of the ESA Living Planet Symposium**, n. 1, p. 2–7, 2010.

BOWERS, D. G.; HARKER, G. E. L.; STEPHAN, B. Absorption spectra of inorganic particles in the Irish sea and their relevance to remote sensing of chlorophyll. **International Journal of Remote Sensing**, v. 17, n. 12, p. 2449–2460, 1996.

BRANDO, V. E.; DEKKER, A. G.; PARK, Y. J.; SCHROEDER, T. Adaptive semianalytical inversion of ocean color radiometry in optically complex waters. **Applied Optics**, v. 51, p. 2808, 2012.

BREZONIK, P. L.; OLMANSON, L. G.; FINLAY, J. C.; BAUER, M. E. Factors affecting the measurement of CDOM by remote sensing of optically complex inland waters. **Remote Sensing of Environment**, v. 157, p. 199–215, 2015.

BREZONIK, P.; MENKEN, K. D.; BAUER, M. Landsat-based remote Sensing of Lake Water Quality Characteristics, Including Chlorophyll and Colored Dissolved Organic Matter (CDOM). **Lake and Reservoir Management**, v. 21, n. 4, p. 373–382, 2005.

BRICAUD, A.; BABIN, M.; MOREL, A.; CLAUSTRE, H. Variability in the chlorophyll-specific absorption coefficients of natural phytoplankton: Analysis and parameterization. **Journal of Geophysical Research**, 1995.

BRICAUD, A.; CLAUSTRE, H.; RAS, J.; OUBELKHEIR, K. Natural variability of phytoplanktonic absorption in oceanic waters: Influence of the size structure of algal populations. **Journal of Geophysical Research**, v. 109, n. C11, p. C11010, 2004.

BRICAUD, A.; MOREL, A.; BABIN, M.; ALLALI, K.; CLAUSTRE, H. Variations of light absorption by suspended particles with chlorophyll a concentration in oceanic (case 1) waters: Analysis and implications for bio-optical models. **Journal of Geophysical Research**, v. 103, n. 13, p. 31,033–31,044, 1998.

BRICAUD, A.; MOREL, A.; PRIEUR, L. Absorption by Dissolved Organic Matter of the Sea (Yellow Substance) in the UV and Visible Domains. **Limnology and Oceanography**, v. 26, n. 1, p. 43–53, 1981.

BROWN, M. Transmission spectroscopy examinations of natural waters. **Estuar. Coast. Mar. Sci.**, v. 5, n. 1 1977, p. 309–317, 1977.

CAMPBELL, G.; PHINN, S. R. An assessment of the accuracy and precision of water quality parameters retrieved with the Matrix Inversion Method. **Limnology and Oceanography-Methods**, v. 8, p. 16–29, 2010.

CAO, F.; TZORTZIOU, M.; HU, C.; MANNINO, A.; FICHOT, C. G.; DEL VECCHIO, R.; NAJJAR, R. G.; NOVAK, M. Remote sensing retrievals of colored dissolved organic matter and dissolved organic carbon dynamics in North American estuaries and their margins. **Remote Sensing of Environment**, v. 205, p. 151–165, 2018.

CARDER, K. L.; CHEN, F. R.; CANNIZZARO, J. P.; CAMPBELL, J. W.; MITCHELL, B. G. Performance of the MODIS semi-analytical ocean color algorithm for chlorophyll-a. **Advances in Space Research**, v. 33, n. 7, p. 1152–1159, 2004.

CARDER, K. L.; CHEN, F. R.; LEE, Z. P.; HAWES, S. K.; KAMYKOWSKI, D. Semianalytic Moderate-Resolution Imaging Spectrometer algorithms for chlorophyll a and absorption with bio-optical domains based on nitrate-depletion temperatures. **Journal of Geophysical Research**, v. 104, n. 3, p. 5403–5421, 1999.

CARDER, K. L.; CHEN, F. R.; LEE, Z.; HAWES, S. K.; CANNIZZARO, J. P. MODIS Algorithm Theoretical Basis Document. **Ocean Science**, 2003.

CARDER, K. L.; HAWES, S. K.; BAKER, K. A.; SMITH, R. C.; STEWARD, R. G.; MITCHELL, B. G. Reflectance Model for Quantifying Chlorophyll a in the Presence of Productivity Degradation Products. **Journal of Geophysical Research**, v. 96, n. C11, p. 20599–20611, 1991.

CARDER, K. L.; STEWARD, R. G.; HARVEY, G. R.; ORTNER, P. B. Marine humic and fulvic acids: Their effects on remote sensing of ocean chlorophyll. **Limnology and Oceanography**, v. 34, n. 1, p. 68–81, 1989.

CARVALHO, L. A. S.; FARIA BARBOSA, C. C.; LEÃO DE MORAES NOVO, E. M.; DE MORAES RUDORFF, C. Implications of scatter corrections for absorption measurements on optical closure of Amazon floodplain lakes using the Spectral Absorption and Attenuation Meter (AC-S-WETLabs). **Remote Sensing of Environment**, v. 157, p. 123–137, 2015.

CAUWET, G. DOM in the Coastal Zone. **Biogeochemistry of Marine Dissolved Organic Matter**, n. 1988, p. 579–609, 2002.

CHASE, A.; BOSS, E.; ZANEVELD, R.; BRICAUD, A.; CLAUSTRE, H.; RAS, J.; DALL, G.; WESTBERRY, T. K. Decomposition of in situ particulate absorption spectra. **Methods in Oceanography**, v. 7, p. 110–124, 2013.

CHEN, Z.; LI, Y.; PAN, J. Distributions of colored dissolved organic matter and dissolved organic carbon in the Pearl River Estuary, China. **Continental Shelf Research**, v. 24, n. 16, p. 1845–1856, 2004.

CIOTTI, A. M.; BRICAUD, A. Retrievals of a size parameter for phytoplankton and spectral light absorption by colored detrital matter from water-leaving radiances at SeaWiFS channels in a continental shelf region off Brazil. **Limnology and Oceanography: Methods**, v. 4, n. 7, p. 237–253, 2006.

CLARK, C. D.; HISCOCK, W. T.; MILLERO, F. J.; HITCHCOCK, G.; BRAND, L.; MILLER, W. L.; ZIOLKOWSKI, L.; CHEN, R. F.; ZIKA, R. G. CDOM distribution and CO<sub>2</sub> production on the Southwest Florida Shelf. **Marine Chemistry**, v. 89, p. 145–167, 2004.

COLE, J. J.; PRAIRIE, Y. T.; CARACO, N. F.; MCDOWELL, W. H.; TRANVIK, L. J.; STRIEGL, R. G.; DUARTE, C. M.; KORTELAJINEN, P.; DOWNING, J. A.; MIDDELBURG, J. J.; MELACK, J. Plumbing the global carbon cycle: Integrating inland waters into the terrestrial carbon budget. **Ecosystems**, v. 10, n. 1, p. 171–184, 2007.

COLES, V. J.; BROOKS, M. T.; HOPKINS, J.; STUKEL, M. R.; YAGER, P. L.; HOOD, R. R. The pathways and properties of the Amazon river plume in the tropical North Atlantic Ocean. **Journal of Geophysical Research: Oceans**, v. 118, n. 12, p. 6894–6913, 2013.

COOK, S.; PEACOCK, M.; EVANS, C. D.; PAGE, S. E.; WHELAN, M. J.; GAUCI, V.; KHO, L. K. Quantifying tropical peatland dissolved organic carbon (DOC) using UV-visible spectroscopy. **Water Research**, v. 115, p. 229–235, 2017.

COOLEY, S. R.; COLES, V. J.; SUBRAMANIAM, A.; YAGER, P. L. Seasonal variations in the Amazon plume-related atmospheric carbon sink. **Global Biogeochemical Cycles**, v. 21, n. 3, p. 1–15, 2007.

CORREA, S. W.; DE PAIVA, R. C. D.; ESPINOZA, J. C.; COLLISCHONN, W. Multi-decadal Hydrological Retrospective: Case study of Amazon floods and droughts. **Journal of Hydrology**, 2017.

COSTA, M. P. F.; NOVO, E. M. L. M.; TELMER, K. H. Spatial and temporal variability of light attenuation in large rivers of the Amazon. **Hydrobiologia**, p. 171–190, 2013.

CUNHA, A. C.; STERNBERG, L. DA S. L. Using stable isotopes  $^{18}\text{O}$  and  $^2\text{H}$  of lake water and biogeochemical analysis to identify factors affecting water quality in four estuarine Amazonian shallow lakes. **Hydrological Processes**, 2018.

CURTARELLI, M. P.; OGASHAWARA, I.; DE ARAÚJO, C. A. S.; LORENZZETTI, J. A.; LEÃO, J. A. D.; ALCÂNTARA, E.; STECH, J. L. Carbon dioxide emissions from Tucuruí reservoir (Amazon biome): New findings based on three-dimensional ecological model simulations. **Science of the Total Environment**, v. 551–552, p. 676–694, 2016.

DAGG, M.; BENNER, R.; LOHRENZ, S.; LAWRENCE, D. Transformation of dissolved and particulate materials on continental shelves influenced by large rivers: plume processes. **Continental Shelf Research**, v. 24, n. 7–8, p. 833–858, 2004.

DALL'OLMO, G.; GITELSON, A. A. Effect of bio-optical parameter variability on the remote estimation of chlorophyll-a concentration in turbid productive waters: experimental results. **Applied Optics**, v. 44, n. 3, p. 412, 2005.

DALL'OLMO, G.; GITELSON, A. A.; RUNDQUIST, D. C.; LEAVITT, B.; BARROW, T.; HOLZ, J. C. Assessing the potential of SeaWiFS and MODIS for estimating chlorophyll concentration in turbid productive waters using red and near-infrared bands. **Remote Sensing of Environment**, v. 96, p. 176–187, 2005.

DANHIEZ, F. P.; VANTREPOTTE, V.; CAUVIN, A.; LEBOURG, E.; LOISEL, H. Optical properties of chromophoric dissolved organic matter during a phytoplankton bloom. Implication for DOC estimates from CDOM absorption. **Limnology and Oceanography**, 2017.

DEL CASTILLO, C. E.; MILLER, R. L. On the use of ocean color remote sensing to measure the transport of dissolved organic carbon by the Mississippi River Plume. **Remote Sensing of Environment**, v. 112, n. 3, p. 836–844, 2008.

DEMASTER, D. J.; KNAPP, G. B.; NITTROUER, C. A. Biological uptake and accumulation of silica on the Amazon continental shelf. **Geochimica et Cosmochimica Acta**, v. 47, n. 10, p. 1713–1723, 1983.

DEMASTER, D. J.; KUEHL, S. A.; NITTROUER, C. A. Effects of suspended sediments on geochemical processes near the mouth of the Amazon River: examination of biological silica uptake and the fate of particle-reactive elements. **Continental Shelf Research**, v. 6, n. 1–2, p. 107–125, 1986.



DOGLIOTTI, A. I. I.; RUDDICK, K. G. G.; NECHAD, B.; DOXARAN, D.; KNAEPS, E. A single algorithm to retrieve turbidity from remotely-sensed data in all coastal and estuarine waters. **Remote Sensing of Environment**, v. 156, p. 157–168, 2015.

DONG, Q.; SHANG, S.; LEE, Z. An algorithm to retrieve absorption coefficient of chromophoric dissolved organic matter from ocean color. **Remote Sensing of Environment**, v. 128, p. 259–267, 2013.

DÖRNHÖFER, K.; OPPELT, N. Remote sensing for lake research and monitoring - Recent advances. **Ecological Indicators**, v. 64, p. 105–122, 2016.

DOWNS, P. W.; SKINNER, K. S.; KONDOLF, G. M. Rivers and streams. **Handbook of Ecological Restoration**. 2002. v. 2, p. 267–296.

DOXARAN, D.; FROIDEFOND, J.-M.; CASTAING, P. Remote-sensing reflectance of turbid sediment-dominated waters. Reduction of sediment type variations and changing illumination conditions effects by use of reflectance ratios. **Applied optics**, v. 42, n. 15, p. 2623–34, 2003.

DUGDALE, S. J. A practitioner's guide to thermal infrared remote sensing of rivers and streams: recent advances, precautions and considerations. **Wiley Interdisciplinary Reviews: Water**, v. 3, n. 2, p. 251–268, 2016.

DUNNE, T.; MEADE, R. H.; RICHEY, J. E.; FORSBERG, B. R. Exchanges of sediment between the flood plain and channel of the Amazon River in Brazil. **Geological Society of America Bulletin**, v. 110, n. 4, p. 450–467, 1998.

ELEVELD, M.; RUESCAS, A.; HOMMERSOM, A.; MOORE, T.; PETERS, S.; BROCKMANN, C. An Optical Classification Tool for Global Lake Waters. **Remote Sensing**, v. 9, n. 5, p. 420, 2017.

ELLIS, E. E.; RICHEY, J. E.; AUFDENKAMPE, A. K.; KRUSCHE, A. V.; QUAY, P. D.; SALIMON, C.; BRANDÃO DA CUNHA, H. Factors controlling water-column respiration in rivers of the central and southwestern Amazon Basin. **Limnology and Oceanography**, v. 57, n. 2, p. 527–540, 2012.

ERTEL, J. R.; HEDGES, J. I.; DEVOL, A. H.; RICHEY, J. E.; DE NAZARE BEOES RIBEIRO, M. Dissolved humic substances of the Amazon River system. **Limnology and Oceanography**, v. 31, n. 4, p. 739–754, 1986.

ESPINOZA, J. C.; MARENGO, J. A.; RONCHAIL, J.; CARPIO, J. M.; FLORES, L. N.; GUYOT, J. L. The extreme 2014 flood in south-western Amazon basin: the role of tropical-

subtropical South Atlantic SST gradient. **Environmental Research Letters**, v. 9, n. 12, p. 124007, 2014.

ESTAPA, M. L.; BOSS, E.; MAYER, L. M.; ROESLER, C. S. Role of iron and organic carbon in mass-specific light absorption by particulate matter from Louisiana coastal waters. **Limnology and Oceanography**, v. 57, n. 1, p. 97–112, 2012.

FERRARI, G. M.; BO, F. G.; BABIN, M. Geo-chemical and optical characterizations of suspended matter in European coastal waters. **Estuarine, Coastal and Shelf Science**, v. 57, n. 1–2, p. 17–24, 2003.

FERRARI, G. M.; DOWELL, M. D.; GROSSI, S.; TARGA, C.; DOWEL, M. D. Relationship between the optical properties of chromophoric dissolved organic matter and total concentration of dissolved organic carbon in the southern Baltic Sea region. **Marine Chemistry**, v. 55, n. 3–4, p. 299–316, 1996.

FERRAZ, L. A. DE C. **Tidal and current prediction for the Amazon's north channel using a hydrodynamical-numerical model**. Monterey, California: Naval Postgraduate School, 1975. 176 p.

FFIELD, A. Amazon and Orinoco River Plumes and NBC Rings: Bystanders or Participants in Hurricane Events? **Journal of Climate**, v. 20, n. 2, p. 316–333, 2007.

FICEK, D.; ZAPADKA, T.; DERA, J. Remote sensing reflectance of Pomeranian lakes and the Baltic. **Oceanologia**, v. 53, n. 4, p. 959–970, 2011.

FICHOT, C. G.; BENNER, R. A novel method to estimate DOC concentrations from CDOM absorption coefficients in coastal waters. **Geophysical Research Letters**, v. 38, n. 3, p. 1–5, 2011.

FICHOT, C. G.; BENNER, R. The spectral slope coefficient of chromophoric dissolved organic matter (S<sub>275-295</sub>) as a tracer of terrigenous dissolved organic carbon in river-influenced ocean margins. **Limnology and Oceanography**, v. 57, n. 5, p. 1453–1466, 2012.

FILIZOLA, N.; GUYOT, J. L. Suspended sediment yields in the Amazon basin: an assessment using the Brazilian national data set. **Hydrological Processes**, v. 3215, n. August, p. 3207–3215, 2009.

FONTES, M.; MAROTTA, H.; MACINTYRE, S.; PETRUCIO, M. Inter- and intra-annual variations of pCO<sub>2</sub> and pO<sub>2</sub> in a freshwater subtropical coastal lake. **Inland Waters**, v. 5, n. 2, p. 107–116, 2015.

GAGNE-MAYNARD, W. C.; WARD, N. D.; KEIL, R. G.; SAWAKUCHI, H. O.; DA CUNHA, A. C.; NEU, V.; BRITO, D. C.; DA SILVA LESS, D. F.; DINIZ, J. E. M.; DE MATOS VALERIO, A.; KAMPEL, M.; KRUSCHE, A. V.; RICHEY, J. E. Evaluation of Primary Production in the Lower Amazon River Based on a Dissolved Oxygen Stable Isotopic Mass Balance. **Frontiers in Marine Science**, v. 4, p. 1–12, 2017.

GALLEGOS, C. L. Optical water quality of a blackwater river estuary: The Lower St. Johns River, Florida, USA. **Estuarine, Coastal and Shelf Science**, v. 63, n. 1–2, p. 57–72, 2005.

GARVER, S. A.; SIEGEL, D. A. Inherent optical property inversion of ocean color spectra and its biogeochemical interpretation 1. Time series from the Sargasso Sea. **Journal of Geophysical Research**, v. 102, n. C8, p. 18607–18625, 1997.

GITELSON, A. A.; DALL’OLMO, G.; MOSES, W.; RUNDQUIST, D. C.; BARROW, T.; FISHER, T. R.; GURLIN, D.; HOLZ, J. A simple semi-analytical model for remote estimation of chlorophyll-a in turbid waters: Validation. **Remote Sensing of Environment**, v. 112, n. 9, p. 3582–3593, 2008.

GOES, J. I.; GOMES, H. D. R.; CHEKALYUK, A. M.; CARPENTER, E. J.; MONTOYA, J. P.; COLES, V. J.; YAGER, P. L.; BERELSON, W. M.; CAPONE, D. G.; FOSTER, R. A.; STEINBERG, D. K.; SUBRAMANIAM, A.; HAFEZ, M. A. Influence of the Amazon River discharge on the biogeography of phytoplankton communities in the western tropical north Atlantic. **Progress in Oceanography**, v. 120, p. 29–40, 2014.

GORDON, R.; BROWN, O. B.; EVANS, H.; BROWN, W.; SMITH, C.; BAKER, K.; CLARK, D. K. A semianalytic Radiance Model of Ocean Color. **Journal of Geophysical Research**, v. 93, n. 8, p. 10.909-10.924, 1988.

GRIFFIN, C. G.; FREY, K. E.; ROGAN, J.; HOLMES, R. M. Spatial and interannual variability of dissolved organic matter in the Kolyma River, East Siberia, observed using satellite imagery. **Journal of Geophysical Research: Biogeosciences**, v. 116, n. 3, p. 1–12, 2011.

GRODSKY, S. A.; REUL, N.; LAGERLOEF, G.; REVERDIN, G.; CARTON, J. A.; CHAPRON, B.; QUILFEN, Y.; KUDRYAVTSEV, V. N.; KAO, H. Y. Haline hurricane wake in the Amazon/Orinoco plume: AQUARIUS/SACD and SMOS observations. **Geophysical Research Letters**, v. 39, n. 20, p. 4–11, 2012.

GRODSKY, S. A.; REVERDIN, G.; CARTON, J. A.; COLES, V. J. Year-to-year salinity changes in the Amazon plume: Contrasting 2011 and 2012 Aquarius/SACD and SMOS satellite data. **Remote Sensing of Environment**, v. 140, p. 14–22, 2014.

HALES, B.; STRUTTON, P. G.; SARACENO, M.; LETELIER, R.; TAKAHASHI, T.; FEELY, R.; SABINE, C.; CHAVEZ, F. Satellite-based prediction of pCO<sub>2</sub> in coastal waters of the eastern North Pacific. **Progress in Oceanography**, v. 103, p. 1–15, 2012.

HALES, B.; STRUTTON, P. G.; SARACENO, M.; LETELIER, R.; TAKAHASHI, T.; FEELY, R.; SABINE, C.; CHAVEZ, F. Satellite-based prediction of pCO<sub>2</sub> in coastal waters of the eastern North Pacific. **Progress in Oceanography**, v. 103, p. 1–15, 2012.

HAN, B.; LOISEL, H.; VANTREPOTTE, V.; MÉRIAUX, X.; BRYÈRE, P.; OUIILLON, S.; DESSAILLY, D.; XING, Q.; ZHU, J. Development of a Semi-Analytical Algorithm for the Retrieval of Suspended Particulate Matter from Remote Sensing over Clear to Very Turbid Waters. **Remote Sensing**, v. 8, n. 3, p. 211, 2016.

HANDCOCK, R. N.; TORGENSEN, C. E.; CHERKAUER, K. A.; GILLESPIE, A. R.; TOCKNER, K.; FAUX, R. N.; TAN, J. Thermal Infrared Remote Sensing of Water Temperature in Riverine Landscapes. **Fluvial Remote Sensing for Science and Management**, p. 85–113, 2012.

HANSEN, A. M.; KRAUS, T. E. C.; PELLERIN, B. A.; FLECK, J. A.; DOWNING, B. D.; BERGAMASCHI, B. A. Optical properties of dissolved organic matter (DOM): Effects of biological and photolytic degradation. **Limnology and Oceanography**, v. 61, n. 3, 2016.

HEDGES, J. I.; KEIL, R. G.; ARANSAS, P. What happens to terrestrial organic matter in the ocean? **Organic Geochemistry**, v. 27, n. 5, p. 195–212, 1997.

HELLWEGER, F. L.; GORDON, A. L. Tracing Amazon River water into the Caribbean Sea. **Journal of Marine Research**, v. 60, n. 4, p. 537–549, 2002.

HELMS, J. R.; MAO, J.; SCHMIDT-ROHR, K.; ABDULLA, H.; MOPPER, K. Photochemical flocculation of terrestrial dissolved organic matter and iron. **Geochimica et Cosmochimica Acta**, v. 121, p. 398–413, 2013.

HELMS, J. R.; STUBBINS, A.; RITCHIE, J. D.; MINOR, E. C.; KIEBER, D. J.; MOPPER, K. Absorption spectral slopes and slope ratios as indicators of molecular weight, source, and photobleaching of chromophoric dissolved organic matter. **Limnology and Oceanography**, v. 53, n. 3, p. 955–969, 2008.

HIERONYMUS, B.; GODOT, J. M.; BOULEGUE, J.; BARTAC, T.; NEGREL, P.; DUPRE, B. Chimie du fleuve Tocantins et des rivières côtières de l'Est du Para (Brésil). **Grands Bassins Fluviaux**, p. 357–374, 1995.

- HU, C.; MONTGOMERY, E. T.; SCHMITT, R. W.; MULLER-KARGER, F. E. The dispersal of the Amazon and Orinoco River water in the tropical Atlantic and Caribbean Sea: Observation from space and S-PALACE floats. **Deep Sea Research Part II: Topical Studies in Oceanography**, v. 51, n. 10–11, p. 1151–1171, 2004.
- IBÁÑHEZ, J. S. P.; ARAUJO, M.; LEFÈVRE, N. The overlooked tropical oceanic CO<sub>2</sub> sink. **Geophysical Research Letters**, v. 43, n. 8, p. 3804–3812, 2016.
- IBÁÑHEZ, J. S. P.; DIVERRE, D.; ARAUJO, M.; LEFÈVRE, N. Seasonal and interannual variability of sea-air CO<sub>2</sub> fluxes in the tropical Atlantic affected by the Amazon River plume. **Global Biogeochemical Cycles**, v. 28, n. 9, p. 1–16, 2015.
- JAEGER, J. M.; NITTROUER, C. A. Tidal controls on the formation of fine-scale sedimentary strata near the Amazon river mouth. **Water**, v. 125, p. 259–281, 1995.
- JAMET, C.; LOISEL, H.; DESSAILLY, D. Retrieval of the spectral diffuse attenuation coefficient  $K_d(\lambda)$  in open and coastal ocean waters using a neural network inversion. **Journal of Geophysical Research: Oceans**, v. 117, n. C10, p. n/a-n/a, 2012.
- JERLOV, N. G. **Marine Optics**. v. 14. 1976.
- JIANG, G.; MA, R.; LOISELLE, S. A.; DUAN, H. Optical approaches to examining the dynamics of dissolved organic carbon in optically complex inland waters. **Environmental Research Letters**, v. 7, n. 3, p. 034014, 2012.
- JIMÉNEZ-MUÑOZ, J. C.; MATTAR, C.; BARICHIVICH, J.; SANTAMARÍA-ARTIGAS, A.; TAKAHASHI, K.; MALHI, Y.; SOBRINO, J. A.; SCHRIER, G. VAN DER. Record-breaking warming and extreme drought in the Amazon rainforest during the course of El Niño 2015–2016. **Scientific Reports**, v. 6, n. May, p. 33130, 2016.
- JOHNS, E. M.; MUHLING, B. A.; PEREZ, R. C.; MELO, N.; SMITH, R. H.; LAMKIN, J. T.; GERARD, T. L.; MALCA, E.; SEA, C.; BRAZIL, N.; RING, C. Amazon River water in the northeastern Caribbean Sea and its effect on larval reef fish assemblages during April 2009. **Fisheries Oceanography**, v. 23, n. 2014, p. 472–494, 2014.
- JOHNSON, M. S.; LEHMANN, J.; COUTO, E. G.; FILHO, J. P. N.; RIHA, S. J. DOC and DIC in flowpaths of Amazonian headwater catchments with hydrologically contrasting soils. **Biogeochemistry**, v. 81, n. 1, p. 45–57, 2006a.
- JOHNSON, M. S.; LEHMANN, J.; SELVA, E. C.; ABDO, M.; RIHA, S.; COUTO, E. G. Organic carbon fluxes within and streamwater exports from headwater catchments in the southern Amazon. **Hydrological Processes**, v. 20, n. 12, p. 2599–2614, 2006b.

JORGE, D. S. F.; BARBOSA, C. C. F.; DE CARVALHO, L. A. S.; AFFONSO, A. G.; LOBO, F. D. L.; NOVO, E. M. L. D. M. SNR (Signal-To-Noise Ratio) Impact on Water Constituent Retrieval from Simulated Images of Optically Complex Amazon Lakes. **Remote Sensing**, v. 9, n. 7, p. 644, 2017.

JOSHI, I. D.; D'SA, E. J.; OSBURN, C. L.; BIANCHI, T. S.; KO, D. S.; OVIEDO-VARGAS, D.; ARELLANO, A. R.; WARD, N. D. Assessing chromophoric dissolved organic matter (CDOM) distribution, stocks, and fluxes in Apalachicola Bay using combined field, VIIRS ocean color, and model observations. **Remote Sensing of Environment**, v. 191, p. 359–372, 2017.

JOSHI, I.; D'SA, E. J. Seasonal variation of colored dissolved organic matter in Barataria bay, Louisiana, using combined Landsat and field data. **Remote Sensing**, v. 7, n. 9, p. 12478–12502, 2015.

JUNK, W. J.; BAYLEY, P. B.; SPARKS, R. E. The flood pulse concept in River-Floodplain Systems. **Can. Spec Publ. Fish. Aquat Sci**, v. 106, p. 110–127, 1989.

KAHRU, M.; MITCHELL, B. G. Seasonal and nonseasonal variability of satellite-derived chlorophyll and colored dissolved organic matter concentration in the California Current. **Journal of Geophysical Research**, v. 106, n. C2, p. 2517–2529, 2001.

KAISER, K.; ZECH, W. Competitive sorption of dissolved organic matter fractions to soils and related mineral phases. **Soil Science Society of America Journal**, v. 61, n. 1, p. 64–69, 1997.

KEITH, D.; LUNETTA, R.; SCHAEFFER, B. Optical Models for Remote Sensing of Colored Dissolved Organic Matter Absorption and Salinity in New England, Middle Atlantic and Gulf Coast Estuaries USA. **Remote Sensing**, v. 8, n. 4, p. 283, 2016.

KIRK, J. T. O. **Light and photosynthesis in aquatic ecosystems**. 3. ed. New York: Cambridge University Press, 2011.

KISHINO, M.; TANAKA, A.; ISHIZAKA, J. Retrieval of Chlorophyll a, suspended solids, and colored dissolved organic matter in Tokyo Bay using ASTER data. **Remote Sensing of Environment**, v. 99, n. 1–2, p. 66–74, 2005.

KLAVINS, M. Genesis, sources and sinks of aquatic humic substances. **Aquatic Humic Substances: Characterization, Structure and Genesis**, p. 105–123, 1997.

KNAEPS, E.; RUDDICK, K. G.; DOXARAN, D.; DOGLIOTTI, A. I.; NECHAD, B.; RAYMAEKERS, D.; STERCKX, S. A SWIR based algorithm to retrieve total suspended

matter in extremely turbid waters. **Remote Sensing of Environment**, v. 168, p. 66–79, 2015.

KOEHLER, B.; LANDELIUS, T.; WEYHENMEYER, G. A.; MACHIDA, N.; TRANVIK, L. J. Sunlight-induced carbon dioxide emissions from inland waters. **Global Biogeochemical Cycles**, v. 28, p. 696–711, 2014.

KÖHLER, S. J.; KOTHAWALA, D.; FUTTER, M. N.; LIUNGMAN, O.; TRANVIK, L. In-Lake Processes Offset Increased Terrestrial Inputs of Dissolved Organic Carbon and Color to Lakes. **PLoS ONE**, v. 8, n. 8, p. 1–12, 2013.

KOPONEN, S.; PULLIAINEN, J.; KALLIO, K.; HALLIKAINEN, M. Lake water quality classification with airborne hyperspectral spectrometer and simulated MERIS data. **Remote Sensing of Environment**, v. 79, n. 1, p. 51–59, 2002.

KOROSOV, A.; COUNILLON, F.; JOHANNESSEN, J. A. Monitoring the spreading of the Amazon freshwater plume by MODIS, SMOS, Aquarius, and TOPAZ. **Journal of Geophysical Research C: Oceans**, v. 120, n. 1, p. 268–283, 2015.

KOSTEN, S.; ROLAND, F.; DA MOTTA MARQUES, D. M. L.; VAN NES, E. H.; MAZZEO, N.; STERNBERG, L. D. S. L.; SCHEFFER, M.; COLE, J. J. Climate-dependent CO<sub>2</sub> emissions from lakes. **Global Biogeochemical Cycles**, v. 24, n. 2, p. 1–7, 2010.

KOSUTH, P.; CALL, J.; LARAQUE, A.; FILIZOLA, N.; GUYOT, J. L.; SEYLER, P.; FRITSCH, J. M.; GUIMAR, V. Sea-tide effects on flows in the lower reaches of the Amazon River. **Hydrological Processes**, v. 3150, n. September, p. 3141–3150, 2009.

KUTSER, T.; CASAL PASCUAL, G.; BARBOSA, C.; PAAVEL, B.; FERREIRA, R.; CARVALHO, L.; TOMING, K. Mapping inland water carbon content with Landsat 8 data. **International Journal of Remote Sensing**, v. 37, n. 13, p. 2950–2961, 2016.

KUTSER, T.; PIERSON, D. C.; KALLIO, K. Y.; REINART, A.; SOBEK, S. Mapping lake CDOM by satellite remote sensing. **Remote Sensing of Environment**, v. 94, n. 4, p. 535–540, 2005.

KUTSER, T.; VERPOORTER, C.; PAAVEL, B.; TRANVIK, L. J. Estimating lake carbon fractions from remote sensing data. **Remote Sensing of Environment**, v. 157, p. 138–146, 2015.

LANDSCHÜTZER, P.; GRUBER, N.; BAKKER, D. C. E.; SCHUSTER, U. Recent variability of the global ocean carbon sink. **Global and Planetary Change**, p. 927–949, 2014.

LAPIERRE, J. F.; DEL GIORGIO, P. A. Geographical and environmental drivers of regional differences in the lake pCO<sub>2</sub> versus DOC relationship across northern landscapes. **Journal of Geophysical Research: Biogeosciences**, v. 117, n. 3, p. 1–10, 2012.

LARSEN, S.; ANDERSEN, T.; HESSEN, D. O. The pCO<sub>2</sub> in boreal lakes: Organic carbon as a universal predictor? **Global Biogeochemical Cycles**, v. 25, n. 2, p. 1–8, 2011.

LAUERWALD, R.; LARUELLE, G.; HARTMANN, J.; CIAIS, P.; REGNIER, P. A. G. Spatial patterns in CO<sub>2</sub> evasion from the global river network. **Global Biogeochemical Cycles**, v. 29, p. 1–21, 2015.

LE, C.; HU, C. A hybrid approach to estimate chromophoric dissolved organic matter in turbid estuaries from satellite measurements: A case study for Tampa. **Optics Express**, v. 21, n. 16, p. 18849–18871, 2013.

LE, C.; HU, C.; CANNIZZARO, J.; ENGLISH, D.; MULLER-KARGER, F.; LEE, Z. Evaluation of chlorophyll-a remote sensing algorithms for an optically complex estuary. **Remote Sensing of Environment**, v. 129, p. 75–89, 2013.

LE, C.; LI, Y.; ZHA, Y.; SUN, D.; HUANG, C.; LU, H. A four-band semi-analytical model for estimating chlorophyll a in highly turbid lakes: The case of Taihu Lake, China. **Remote Sensing of Environment**, 2009.

LEE, Z. P.; CARDER, K. L.; ARNONE, R. A. Deriving inherent optical properties from water color: a multiband quasi-analytical algorithm for optically deep waters. **Applied optics**, v. 41, n. 27, p. 5755–72, 2002.

LEE, Z. P.; DARECKI, M.; CARDER, K. L.; DAVIS, C. O.; STRAMSKI, D.; RHEA, J. W. Diffuse attenuation coefficient of downwelling irradiance: An evaluation of remote sensing methods. **Journal of Geophysical Research C: Oceans**, v. 110, n. 2, p. 1–9, 2005.

LEE, Z. P.; DU, K. P. A model for the diffuse attenuation coefficient of downwelling irradiance. **Journal of Geophysical Research C: Oceans**, v. 110, n. 2, p. 1–10, 2005.

LEENHEER, J. A.; CROUÉ, J.-P. Characterizing dissolved aquatic organic matter. **Environmental Science & Technology**, v. 37, n. 1, p. 18A–26A, 2003.

LEFÉVRE, N.; DIVERRÉS, D.; GALLOIS, F. Origin of CO<sub>2</sub> undersaturation in the western tropical Atlantic. **Tellus, Series B: Chemical and Physical Meteorology**, v. 62, n. 5, p. 595–607, 2010.



- LEFÈVRE, N.; FLORES MONTES, M.; GASPAR, F. L.; ROCHA, C.; JIANG, S.; DE ARAÚJO, M. C.; IBÁÑHEZ, J. S. P. Net Heterotrophy in the Amazon Continental Shelf Changes Rapidly to a Sink of CO<sub>2</sub> in the Outer Amazon Plume. **Frontiers in Marine Science**, v. 4, n. September, 2017.
- LENTZ, S. J.; LIMBURNER, R. The Amazon River Plume during AMASSEDs: Subtidal current variability and the importance of wind forcing. **Journal of Geophysical Research**, v. 100, n. C2, p. 2355–2375, 1995.
- LI, F.; ZHANG, H.; ZHU, Y.; XIAO, Y.; CHEN, L. Effect of flow velocity on phytoplankton biomass and composition in a freshwater lake. **Science of the Total Environment**, v. 447, p. 64–71, 2013.
- LI, J.; YU, Q.; TIAN, Y. Q.; BECKER, B. L. Remote sensing estimation of colored dissolved organic matter (CDOM) in optically shallow waters. **ISPRS Journal of Photogrammetry and Remote Sensing**, v. 128, p. 98–110, 2017.
- LI, S.; ZHANG, J.; MU, G.; JU, H.; WANG, R.; LI, D.; SHABBIR, A. H. Spatiotemporal characterization of chromophoric dissolved organic matter (CDOM) and CDOM-DOC relationships for highly polluted rivers. **Water (Switzerland)**, v. 8, n. 9, 2016.
- LIBES, S. M. **Introduction to Marine Biogeochemistry**. Second ed. San Diego: Elsevier, 2009.
- LINS, R.; MARTINEZ, J.-M.; MOTTA MARQUES, D.; CIRILO, J.; FRAGOSO, C. Assessment of Chlorophyll-a Remote Sensing Algorithms in a Productive Tropical Estuarine-Lagoon System. **Remote Sensing**, v. 9, n. 6, p. 516, 2017.
- LISS, P. S. Processes of gas exchange across an air-water interface. **Deep-Sea Research**, v. 20, n. 1955, p. 221–238, 1973.
- LOBO, F. D. L.; NOVO, E. M. L. D. M.; BARBOSA, C. C. F.; GALVÃO, L. S. Reference spectra to classify Amazon water types. **International Journal of Remote Sensing**, v. 33, n. 11, p. 3422–3442, 2012.
- LOHRENTZ, S. E.; CAI, W. J.; CHAKRABORTY, S.; HUANG, W. J.; GUO, X.; HE, R.; XUE, Z.; FENNEL, K.; HOWDEN, S.; TIAN, H. Satellite estimation of coastal pCO<sub>2</sub> and air-sea flux of carbon dioxide in the northern Gulf of Mexico. **Remote Sensing of Environment**, v. 207, p. 71–83, 2018.

- LOHRENZ, S. E.; CAI, W.-J. Satellite ocean color assessment of air-sea fluxes of CO<sub>2</sub> in a river-dominated coastal margin. **Geophysical Research Letters**, v. 33, n. 1, p. L01601, 2006.
- LOISEL, H.; VANTREPOTTE, V.; DESSAILLY, D.; MÉRIAUX, X. Assessment of the colored dissolved organic matter in coastal waters from ocean color remote sensing. **Optics express**, v. 22, n. 11, p. 13109–24, 2014.
- LOISEL, H.; VANTREPOTTE, V.; JAMET, C.; DAT, D. N. Challenges and New Advances in Ocean Color Remote Sensing of Coastal Waters. **Oceanography Research**, p. 1–38, 2013.
- LOISEL, H.; VANTREPOTTE, V.; OUIILLON, S.; NGOC, D. D.; HERRMANN, M.; TRAN, V.; MÉRIAUX, X.; DESSAILLY, D.; JAMET, C.; DUHAUT, T.; NGUYEN, H. H.; VAN NGUYEN, T. Assessment and analysis of the chlorophyll-a concentration variability over the Vietnamese coastal waters from the MERIS ocean color sensor (2002–2012). **Remote Sensing of Environment**, v. 190, 2017.
- LOISELLE, S. A.; AZZA, N.; GICHUKI, J.; BRACCHINI, L.; TOGNAZZI, A.; DATTILO, A. M.; ROSSI, C.; COZAR, A. Spatial dynamics of chromophoric dissolved organic matter in nearshore waters of Lake Victoria. **Aquatic Ecosystem Health & Management**, v. 13, n. 2, p. 185–195, 2010.
- LUBAC, B.; LOISEL, H. Variability and classification of remote sensing reflectance spectra in the eastern English Channel and southern North Sea. **Remote Sensing of Environment**, v. 110, n. 1, p. 45–58, 2007.
- MANNINO, A.; NOVAK, M. G.; HOOKER, S. B.; HYDE, K.; AURIN, D. Algorithm development and validation of CDOM properties for estuarine and continental shelf waters along the northeastern U.S. coast. **Remote Sensing of Environment**, v. 152, p. 576–602, 2014.
- MANNINO, A.; RUSS, M. E.; HOOKER, S. B. Algorithm development and validation for satellite-derived distributions of DOC and CDOM in the U.S. Middle Atlantic Bight. **Journal of Geophysical Research**, v. 113, n. C7, p. C07051, 2008.
- MARENGO, J. A.; ESPINOZA, J. C. Extreme seasonal droughts and floods in Amazonia: Causes, trends and impacts. **International Journal of Climatology**, v. 36, n. 3, p. 1033–1050, 2016.

MARENGO, J. A.; TOMASELLA, J.; ALVES, L. M.; SOARES, W. R.; RODRIGUEZ, D. A. The drought of 2010 in the context of historical droughts in the Amazon region. **Geophysical Research Letters**, v. 38, n. 12, p. 1–5, 2011.

MARITORENA, S.; SIEGEL, D. A.; PETERSON, A. R. Optimization of a semianalytical ocean color model for global-scale applications. **Applied optics**, v. 41, n. 15, p. 2705–14, 2002.

MAROTTA, H.; DUARTE, C. M.; PINHO, L.; ENRICH-PRAST, A. Rainfall leads to increased pCO<sub>2</sub> in Brazilian coastal lakes. **Biogeosciences**, v. 7, n. 5, p. 1607–1614, 2010.

MAROTTA, H.; DUARTE, C. M.; SOBEK, S.; ENRICH-PRAST, A. Large CO<sub>2</sub> disequilibria in tropical lakes. **Global Biogeochemical Cycles**, v. 23, n. 4, p. 13–16, 2009.

MAROTTA, H.; PAIVA, L. T.; PETRUCIO, M. M. Changes in thermal and oxygen stratification pattern coupled to CO<sub>2</sub> outgassing persistence in two oligotrophic shallow lakes of the Atlantic Tropical Forest, Southeast Brazil. **Limnology**, v. 10, n. 3, p. 195–202, 2009.

MARTINEZ, J. M.; BOURGOIN, L. M. M.; KOSUTH, P.; SEYLER, F.; GUYOT, J. L. L. Analysis of multitemporal MODIS and Landsat 7 images acquired over Amazonian floodplains lakes for suspended sediment concentrations retrieval. **IGARSS 2003. 2003 IEEE International Geoscience and Remote Sensing Symposium**. Proceedings (IEEE Cat. No.03CH37477), v. 00, n. C, p. 2122–2124, 2003.

MARTINEZ, J.; ESPINOZA-VILLAR, R.; ARMIJOS, E.; SILVA MOREIRA, L. The optical properties of river and floodplain waters in the Amazon River Basin: Implications for satellite-based measurements of suspended particulate matter. **Journal of Geophysical Research: Earth Surface**, p. 1–14, 2015.

MARTINS, V. S.; BARBOSA, C. C. F.; DE CARVALHO, L. A. S.; JORGE, D. S. F.; LOBO, F. DE L.; DE MORAES NOVO, E. M. L. Assessment of atmospheric correction methods for sentinel-2 MSI images applied to Amazon floodplain lakes. **Remote Sensing**, v. 9, n. 4, 2017.

MASSICOTTE, P.; ASMALA, E.; STEDMON, C.; MARKAGER, S. Global distribution of dissolved organic matter along the aquatic continuum: Across rivers, lakes and oceans. **Science of the Total Environment**, v. 609, p. 180–191, 2017.

MATSUOKA, A.; BRICAUD, A.; BENNER, R.; PARA, J.; SEMPÉRÉ, R.; PRIEUR, L.; BÉLANGER, S.; BABIN, M. Tracing the transport of colored dissolved organic matter in

water masses of the Southern Beaufort Sea: relationship with hydrographic characteristics. **Biogeosciences**, v. 9, n. 3, p. 925–940, 2012.

MATSUOKA, A.; BABIN, M.; DOXARAN, D.; HOOKER, S. B.; MITCHELL, B. G.; BÉLANGER, S.; BRICAUD, A. A synthesis of light absorption properties of the Arctic Ocean: Application to semianalytical estimates of dissolved organic carbon concentrations from space. **Biogeosciences**, v. 11, n. 12, 2014.

MATSUOKA, A.; HOOKER, S. B.; BRICAUD, A.; GENTILI, B.; BABIN, M. Estimating absorption coefficients of colored dissolved organic matter (CDOM) using a semi-analytical algorithm for southern Beaufort Sea waters: application to deriving concentrations of dissolved organic carbon from space. **Biogeosciences**, v. 10, n. 2, p. 917–927, 2013.

MATTHEWS, M. W. A current review of empirical procedures of remote sensing in inland and near-coastal transitional waters. **International Journal of Remote Sensing**, v. 32, n. 21, p. 6855–6899, 2011.

MAYORGA, E.; SEITZINGER, S. P.; HARRISON, J. A.; DUMONT, E.; BEUSEN, A. H. W.; BOUWMAN, A. F.; FEKETE, B. M.; KROEZE, C.; VAN DRECHT, G. Global Nutrient Export from WaterSheds 2 (NEWS 2): Model development and implementation. **Environmental Modelling and Software**, v. 25, n. 7, p. 837–853, 2010.

MECKLENBURG, S.; DRUSCH, M.; KERR, Y. H.; FONT, J.; MARTIN-NEIRA, M.; DELWART, S.; BUENADICHA, G.; REUL, N.; DAGANZO-EUSEBIO, E.; OLIVA, R.; CRAPOLICCHIO, R. ESA's soil moisture and ocean salinity mission: Mission performance and operations. **IEEE Transactions on Geoscience and Remote Sensing**, v. 50, n. 5 PART 1, p. 1354–1366, 2012.

MEDEIROS, P. M.; SEIDEL, M.; NIGGEMANN, J.; SPENCER, R. G. M.; HERNES, P. J.; YAGER, P. L.; MILLER, W. L.; DITTMAR, T.; HANSELL, D. A. A Novel Molecular Approach for Tracing Terrigenous Dissolved Organic Matter into the Deep Ocean. **Global Biogeochemical Cycles**, v. 50, p. 1–11, 2016.

MEDEIROS, P. M.; SEIDEL, M.; WARD, N. D.; CARPENTER, E. J.; GOMES, H. R.; NIGGEMANN, J.; KRUSCHE, A. V.; RICHEY, J. E.; YAGER, P. L.; DITTMAR, T. Fate of the Amazon River dissolved organic matter in the tropical Atlantic Ocean. **Global Biogeochemical Cycles**, v. 29, p. 1–14, 2015.

MÉLIN, F.; VANTREPOTTE, V. How optically diverse is the coastal ocean? **Remote Sensing of Environment**, v. 160, p. 235–251, 2015.

MÉLIN, F.; VANTREPOTTE, V.; CLERICI, M.; D'ALIMONTE, D.; ZIBORDI, G.; BERTHON, J. F.; CANUTI, E. Multi-sensor satellite time series of optical properties and chlorophyll-a concentration in the Adriatic Sea. **Progress in Oceanography**, v. 91, n. 3, p. 229–244, 2011.

MERTES, L. A. K.; MAGADZIRE, T. T. Large Rivers from Space. **Large Rivers: Geomorphology and Management**. 2008. p. 535–552.

MITCHELL, B. G.; KAHRU, M.; WIELAND, J.; STRAMSKA, M.; MUELLER, J. L. Determination of spectral absorption coefficients of particles, dissolved material and phytoplankton for discrete water samples. **Ocean optics protocols for satellite ocean color sensor validation**, Revision, v. 3, n. 2, p. 231, 2002.

MOBLEY, C. D. Estimation of the remote-sensing reflectance from above-surface measurements. **Applied Optics**, v. 38, n. 36, p. 7442–55, 1999.

MOBLEY, C. D.; SUNDMAN, L. K.; DAVIS, C. O.; BOWLES, J. H.; DOWNES, T. V.; LEATHERS, R. A.; MONTES, M. J.; BISSETT, W. P.; KOHLER, D. D. R.; REID, R. P.; LOUCHARD, E. M.; GLEASON, A. Interpretation of hyperspectral remote-sensing imagery by spectrum matching and look-up tables. **Applied Optics**, v. 44, n. 17, p. 3576–92, 2005.

MOLLERI, G. S. F.; NOVO, E. M. L. D. M.; KAMPEL, M. Space-time variability of the Amazon River plume based on satellite ocean color. **Continental Shelf Research**, v. 30, n. 3–4, p. 342–352, 2010.

MONTANHER, O. C.; NOVO, E. M. L. M.; BARBOSA, C. C. F.; RENNÓ, C. D.; SILVA, T. S. F. International Journal of Applied Earth Observation and Geoinformation Empirical models for estimating the suspended sediment concentration in Amazonian whitewater rivers using Landsat 5 / TM. **International Journal of Applied Earth Observations and Geoinformation**, v. 29, p. 67–77, 2014.

MOORE, T. S.; DOWELL, M. D.; BRADT, S.; RUIZ VERDU, A. An optical water type framework for selecting and blending retrievals from bio-optical algorithms in lakes and coastal waters. **Remote Sensing of Environment**, v. 143, p. 97–111, 2014.

MOORE, W. S. The Effect of Submarine Groundwater Discharge on the Ocean. **Annual Review of Marine Science**, v. 2, n. 1, p. 59–88, 2010.

MOREIRA-TURCQ, P.; BONNET, M. P.; AMORIM, M.; BERNARDES, M.; LAGANE, C.; MAURICE, L.; PEREZ, M.; SEYLER, P. Seasonal variability in concentration, composition,

age, and fluxes of particulate organic carbon exchanged between the floodplain and Amazon River. **Global Biogeochemical Cycles**, v. 27, n. 1, p. 119–130, 2013.

MOREIRA-TURCQ, P.; SEYLER, P.; GUYOT, J. L.; ETCHEBER, H. Exportation of organic carbon from the Amazon River and its main tributaries. **Hydrological Processes**, v. 17, n. 7, p. 1329–1344, 2003.

MOREL, A. A.; PRIEUR, L. Analysis of variations in ocean color. **Limnology and Oceanography**, v. 22, n. 4, p. 709–722, 1977.

MOREL, A. Y.; GORDON, H. R. Report of the working group on water color. **Boundary-Layer Meteorology**, 1980

MOREL, A.; GENTILI, B. A simple band ratio technique to quantify the colored dissolved and detrital organic material from ocean color remotely sensed data. **Remote Sensing of Environment**, v. 113, n. 5, p. 998–1011, 2009.

MOREL, A.; MARITORENA, S. Bio-optical properties of oceanic waters: A reappraisal. **Journal of Geophysical Research**, v. 106, n. C4, p. 7163–7180, 2001.

MOUW, C. B.; GREB, S.; AURIN, D.; DIGIACOMO, P. M.; LEE, Z.; TWARDOWSKI, M.; BINDING, C.; HU, C.; MA, R.; MOORE, T.; MOSES, W.; CRAIG, S. E. Aquatic color radiometry remote sensing of coastal and inland waters: Challenges and recommendations for future satellite missions. **Remote Sensing of Environment**, v. 160, p. 15–30, 2015.

MULHOLLAND, P. J. 6 - Large-Scale Patterns in Dissolved Organic Carbon Concentration, Flux, and Sources. **Aquatic Ecosystems**. 2003. p. 139–159.

NECHAD, B.; RUDDICK, K. G.; PARK, Y. Calibration and validation of a generic multisensor algorithm for mapping of total suspended matter in turbid waters. **Remote Sensing of Environment**, v. 114, n. 4, p. 854–866, 2010.

NELSON, N. B.; SIEGEL, D. A. The global distribution and dynamics of chromophoric dissolved organic matter. **Annual Review of Marine Science**, v. 5, p. 447–76, 2013.

NELSON, N. B.; SIEGEL, D. A.; MICHAELS, A. F. Seasonal dynamics of colored dissolved material in the Sargasso Sea. **Deep Sea Research Part I: Oceanographic Research Papers**, v. 45, n. 6, p. 931–957, 1998.

NEU, V.; NEILL, C.; KRUSCHE, A. V. Gaseous and fluvial carbon export from an Amazon forest watershed. **Biogeochemistry**, v. 105, n. 1, p. 133–147, 2011.

NEU, V.; WARD, N. D.; KRUSCHE, A. V.; NEILL, C. Dissolved Organic and Inorganic Carbon Flow Paths in an Amazonian Transitional Forest. **Frontiers in Marine Science**, v. 3, 2016.

NIKIEMA, O.; DEVENON, J.; BAKLOUTI, M. Numerical modeling of the Amazon River plume. **Continental Shelf Research**, v. 27, n. 7, p. 873–899, 2007.

NOHARA, D.; KITOH, A.; HOSAKA, M.; OKI, T. Impact of Climate Change on River Discharge Projected by Multimodel Ensemble. **Journal of Hydrometeorology**, v. 7, n. 5, p. 1076–1089, 2006.

NOVO, E. M. L. D. M.; BARBOSA, C. C. F.; FREITAS, R. M.; SHIMABUKURO, Y. E.; MELACK, J. M.; PEREIRA, W. Seasonal changes in chlorophyll distributions in Amazon floodplain lakes derived from MODIS images. **Limnology**, v. 7, n. 3, p. 153–161, 2006.

ODERMATT, D.; GITELSON, A.; BRANDO, V. E.; SCHAEPMAN, M. Review of constituent retrieval in optically deep and complex waters from satellite imagery. **Remote Sensing of Environment**, v. 118, p. 116–126, 2012.

PALMER, S. C. J.; KUTSER, T.; HUNTER, P. D. Remote sensing of inland waters: Challenges, progress and future directions. **Remote Sensing of Environment**, v. 157, p. 1–8, 2015.

PARK, E.; LATRUBESSE, E. M. Modeling suspended sediment distribution patterns of the Amazon River using MODIS data. **Remote Sensing of Environment**, v. 147, p. 232–242, 2014.

PARK, E.; LATRUBESSE, E. M. Surface water types and sediment distribution patterns at the confluence of mega rivers: The Solimões-Amazon and Negro Rivers junction. **Water Resources Research**, v. 51, n. 5, p. n/a-n/a, 2015.

PEREIRA, R.; ISABELLA BOVOLO, C.; SPENCER, R. G. M.; HERNES, P. J.; TIPPING, E.; VIETH-HILLEBRAND, A.; PEDENTCHOUK, N.; CHAPPELL, N. A.; PARKIN, G.; WAGNER, T. Mobilization of optically invisible dissolved organic matter in response to rainstorm events in a tropical forest headwater river. **Geophysical Research Letters**, v. 41, n. 4, p. 1202–1208, 2014.

PINET, S.; MARTINEZ, J.-M.; OUILLON, S.; LARTIGES, B.; VILLAR, R. E. Variability of apparent and inherent optical properties of sediment-laden waters in large river basins – lessons from in situ measurements and bio-optical modeling. **Optics Express**, v. 25, n. 8, p. A283, 2017.

PINHO, L.; DUARTE, C. M.; MAROTTA, H.; ENRICH-PRAST, A. Temperature-dependence of the relationship between pCO<sub>2</sub> and dissolved organic carbon in lakes. **Biogeosciences Discussions**, v. 12, n. 3, p. 2787–2808, 2015.

PREISENDORFER, R. W. **Hydrological optics**, vol. 1. VI, US Dept. of Commerce, 1976.

PRIEUR, L.; SATHYENDRANATH, S. An optical classification of coastal and oceanic waters based on the specific spectral absorption curves of phytoplankton pigments, dissolved organic matter, and other particulate materials. **Limnology and Oceanography**, v. 26, n. 4, p. 671–689, 1981.

RASERA, M. DE F. F. L.; KRUSCHE, A. V.; RICHEY, J. E.; BALLESTER, M. V. R.; VICTÓRIA, R. L. Spatial and temporal variability of pCO<sub>2</sub> and CO<sub>2</sub> efflux in seven Amazonian Rivers. **Biogeochemistry**, v. 116, n. 1–3, p. 241–259, 2013.

RAYMOND, P. A.; HARTMANN, J.; LAUERWALD, R.; SOBEK, S.; MCDONALD, C. P.; HOOVER, M.; BUTMAN, D.; STRIEGL, R.; MAYORGA, E.; HUMBORG, C.; KORTELAINE, P.; DURR, H.; MEYBECK, M.; CIAIS, P.; GUTH, P. Global carbon dioxide emissions from inland waters. **Nature**, v. 503, n. 7476, p. 355–359, 2013.

RAYMOND, P. A.; SAIERS, J. E.; SOBCZAK, W. V. Hydrological and biogeochemical controls on watershed dissolved organic matter transport: Pulse- shunt concept. **Ecology**, v. 97, n. 1, p. 5–16, 2016.

RAYMOND, P. A.; SPENCER, R. G. M. Riverine DOM. In: HANSELL, D. A.; CARLSON, C. A. (Org.). **Biogeochemistry of Marine Dissolved Organic Matter**. Burlington: Academic Press, 2015. n. 2nd, p. 509–535.

REUL, N.; TENERELLI, J.; BOUTIN, J.; CHAPRON, B.; PAUL, F.; BRION, E.; GAILLARD, F.; ARCHER, O. Overview of the first SMOS sea surface salinity products. Part I: Quality assessment for the second half of 2010. **IEEE Transactions on Geoscience and Remote Sensing**, v. 50, n. 5 PART 1, p. 1636–1647, 2012.

RICHEY, J. E.; HEDGES, J. I.; DEVOL, A. H.; QUAY, P. D.; VICTORIA, R.; MARTINELLI, L.; FORSBERG, B. R. Biogeochemistry of carbon in the Amazon River. **Limnology and Oceanography**, v. 35, n. 2, p. 352–371, 1990.

RICHEY, J. E.; KRUSCHE, A. V.; JOHNSON, M. S.; DA CUNHA, H. B.; BALLESTER, M. V. The Role of Rivers in the Regional Carbon Balance. **Amazonia and Global Change**. 2013. p. 489–504.



RICHEY, J. E.; MEADE, R. H.; SALATI, E.; DEVOL, A. H.; NORDIN, C. F.; SANTOS, U. Water discharge and suspended sediment concentrations in the Amazon River: 1982-1984. **Water Resources Research**, v. 22, n. 5, p. 756–764, 1986.

RICHEY, J. E.; MELACK, J. M.; AUFDENKAMPE, A. K.; BALLESTER, V. M.; HESS, L. L. Outgassing from Amazonian rivers and wetlands as a large tropical source of atmospheric CO<sub>2</sub>. **Nature**, v. 416, n. 1991, p. 617–620, 2002.

RIDDICK, C. A. L.; HUNTER, P. D.; TYLER, A. N.; MARTINEZ-VICENTE, V.; HORVÁTH, H.; KOVÁCS, A. W.; VÖRÖS, L.; PRESTON, T.; PRÉSING, M. Spatial variability of absorption coefficients over a biogeochemical gradient in a large and optically complex shallow lake. **Journal of Geophysical Research: Oceans**, 2015.

RÖDENBECK, C.; BAKKER, D. C. E.; GRUBER, N.; IIDA, Y.; JACOBSON, A. R.; JONES, S.; LANDSCHÜTZER, P.; METZL, N.; NAKAOKA, S.; OLSEN, A.; PARK, G. H.; PEYLIN, P.; RODGERS, K. B.; SASSE, T. P.; SCHUSTER, U.; SHUTLER, J. D.; VALSALA, V.; WANNINKHOF, R.; ZENG, J. Data-based estimates of the ocean carbon sink variability - First results of the Surface Ocean pCO<sub>2</sub> Mapping intercomparison (SOCOM). **Biogeosciences**, v. 12, n. 23, p. 7251–7278, 2015.

RODRÍGUEZ-ZÚÑIGA, U. F.; MILORI, D. M. B. P.; DA SILVA, W. T. L.; MARTIN-NETO, L.; OLIVEIRA, L. C.; ROCHA, J. C. Changes in Optical Properties Caused by UV-Irradiation of Aquatic Humic Substances from the Amazon River Basin: Seasonal Variability Evaluation. **Environmental Science & Technology**, v. 42, n. 6, p. 1948–1953, 2008.

ROUSSEEUW, P. J. Silhouettes: A graphical aid to the interpretation and validation of cluster analysis. **Journal of Computational and Applied Mathematics**, v. 20, n. C, p. 53–65, 1987.

RUDDICK, K. G.; CAUWER, V. DE; PARK, Y.; MOORE, G. Seaborne measurements of near infrared water-leaving reflectance: The similarity spectrum for turbid waters. **Limnol. Oceanogr.**, v. 51, n. 2, p. 1167–1179, 2006.

RUDDICK, K. G.; OVIDIO, F.; RIJKEBOER, M. Atmospheric correction of SeaWiFS imagery for turbid coastal and inland waters. **Applied Optics**, v. 39, n. 6, p. 897–912, 2000.

RUDDICK, K.; CAUWER, V. DE; MOL, B. VAN. Use of the near infrared similarity reflectance spectrum for the quality control of remote sensing data. **Remote Sensing of the Coastal Oceanic Environment**, v. 5885, p.588501-12, 2005.

RUDORFF, C. M.; MELACK, J. M.; MACINTYRE, S.; BARBOSA, C. C. F.; NOVO, E. M. L. M. Seasonal and spatial variability of CO<sub>2</sub> emission from a large floodplain lake in the lower Amazon. *Journal of Geophysical Research: Biogeosciences*, v. 116, n. 4, p. 1–12, 2011.

RUDORFF, N.; RUDORFF, C. M.; KAMPEL, M.; ORTIZ, G. Remote sensing monitoring of the impact of a major mining wastewater disaster on the turbidity of the Doce River plume off the eastern Brazilian coast. *ISPRS Journal of Photogrammetry and Remote Sensing*, 2018.

SA, E. J. D.; MILLER, R. L.; CASTILLO, C. DEL. Bio-optical properties and ocean color algorithms for coastal waters influenced by the Mississippi River during a cold front. *Applied Optics*, v. 45, n. 28, p. 7410–28, 2006.

SACHSE, A.; HENRION, R.; GELBRECHT, J.; STEINBERG, C. E. W. Classification of dissolved organic carbon (DOC) in river systems: Influence of catchment characteristics and autochthonous processes. *Organic Geochemistry*, v. 36, n. 6, p. 923–935, 2005.

SANTOS, A. L. M. R. DOS; MARTINEZ, J. M.; FILIZOLA, N. P.; ARMIJOS, E.; ALVES, L. G. S. Purus River suspended sediment variability and contributions to the Amazon River from satellite data (2000–2015). *Comptes Rendus - Geoscience*, v. 350, n. 1–2, p. 13–19, 2018.

SARMA, V. V. S. S.; SAINO, T.; SASAOKA, K.; NOJIRI, Y.; ONO, T.; ISHII, M.; INOUE, H. Y.; MATSUMOTO, K. Basin-scale pCO<sub>2</sub> distribution using satellite sea surface temperature, Chla, and climatological salinity in the North Pacific in spring and summer. *Global Biogeochemical Cycles*, v. 20, n. 3, 2006.

SATHYENDRANATH, S. **Reports of the International Ocean-Colour Coordinating Group**. IOCCG, Dartmouth, Canada, v. 3, p. 140, 2000

SATYAMURTY, P.; DA COSTA, C. P. W.; MANZI, A. O.; CANDIDO, L. A. A quick look at the 2012 record flood in the Amazon Basin. *Geophysical Research Letters*, v. 40, n. 7, p. 1396–1401, 2013.

SAWAKUCHI, H. O.; NEU, V.; WARD, N. D.; BARROS, M. D. L. C.; VALERIO, A.; GAGNE-MAYNARD, W.; CUNHA, A. C.; FERNANDA, D.; DINIZ, J. E.; BRITO, D. C.; KRUSCHE, A. V.; RICHEY, J. E. Carbon dioxide emissions along the lower Amazon River. *Frontiers in Marine Science*, v. 4, p. 1–12, 2017.

SCHAEFFER, B. A.; CONMY, R. N.; DUFFY, A. E.; AUKAMP, J.; YATES, D. F.; CRAVEN, G. Northern Gulf of Mexico estuarine coloured dissolved organic matter derived from MODIS data. **International Journal of Remote Sensing**, v. 36, n. 8, p. 2219–2237, 2015.

SCHILLER, H.; DOERFFER, R. Neural network for emulation of an inverse model operational derivation of Case II water properties from MERIS data. **International Journal of Remote Sensing**, v. 20, n. 9, p. 1735–1746, 1999.

SEDELL, J. The river continuum concept: a basis for the expected ecosystem behavior of very large rivers. In: Proceedings of the International Large River Symposium. **Can. Spec. Publ. Aquat. Sci.**, 1989. p. 49–55

SEIDEL, M.; DITTMAR, T.; WARD, N. D.; KRUSCHE, A. V.; RICHEY, J. E.; YAGER, P. L.; MEDEIROS, P. M. Seasonal and spatial variability of dissolved organic matter composition in the lower Amazon River. **Biogeochemistry**, v. 131, n. 3, p. 281–302, 2016.

SEIDEL, M.; YAGER, P. L.; WARD, N. D.; CARPENTER, E. J.; GOMES, H. R.; KRUSCHE, A. V.; RICHEY, J. E.; DITTMAR, T.; MEDEIROS, P. M. Molecular-level changes of dissolved organic matter along the Amazon River-to-ocean continuum. **Marine Chemistry**, v. 177, p. 218–231, 2015.

SELLERS, T.; BUKAVECKAS, P. A. Phytoplankton production in a large, regulated river: A modeling and mass balance assessment. **Limnol. Oceanogr.**, v. 48, n. 4, p. 1476–1487, 2003.

SHANMUGAM, P. CAAS: An atmospheric correction algorithm for the remote sensing of complex waters. **Annales Geophysicae**, v. 30, p. 203–220, 2012.

SHEN, Q.; LI, J.; ZHANG, F.; SUN, X.; LI, J.; LI, W.; ZHANG, B. Classification of several optically complex waters in China using in situ remote sensing reflectance. **Remote Sensing**, v. 7, n. 11, p. 14731–14756, 2015.

SHI, K.; LI, Y.; ZHANG, Y.; LI, L.; LV, H.; SONG, K. Classification of inland waters based on bio-optical properties. **IEEE Journal of Selected Topics in Applied Earth Observations and Remote Sensing**, v. 7, n. 2, p. 543–561, 2014.

SHI, W.; WANG, M. An assessment of the black ocean pixel assumption for MODIS SWIR bands. **Remote Sensing of Environment**, v. 113, n. 8, p. 1587–1597, 2009.

SHI, W.; WANG, M. Detection of turbid waters and absorbing aerosols for the MODIS ocean color data processing. **Remote Sensing of Environment**, v. 110, p. 149–161, 2007.

SHOAF, W. T.; LIUM, B. W. Improved extraction of chlorophyll a and b from algae using dimethyl sulfoxide. **Limnology and Oceanography**, v. 21, n. 6, p. 926–928, 1976.

SIOLI, H. **The Amazon. Limnology and landscape ecology of a mighty tropical river and its basin**. v. 56. 1984.

SISWANTO, E.; TANG, J.; YAMAGUCHI, H.; AHN, Y. H.; ISHIZAKA, J.; YOO, S.; KIM, S. W.; KIYOMOTO, Y.; YAMADA, K.; CHIANG, C.; KAWAMURA, H. Empirical ocean-color algorithms to retrieve chlorophyll-a, total suspended matter, and colored dissolved organic matter absorption coefficient in the Yellow and East China Seas. **Journal of Oceanography**, v. 67, n. 5, p. 627–650, 2011.

SLONECKER, E. T.; JONES, D. K.; PELLERIN, B. A. The new Landsat 8 potential for remote sensing of colored dissolved organic matter (CDOM). **Marine Pollution Bulletin**, v. 107, n. 2, p. 518–527, 2016.

SMITH, J.; SMITH, P. **Environmental modelling: an introduction**. Oxford University Press, 2007.

SMITH, W. O.; DEMASTER, D. J. Phytoplankton biomass and productivity in the Amazon River plume: correlation with seasonal river discharge. **Continental Shelf Research**, v. 16, n. 3, p. 291–319, 1996.

SOBEK, S.; TRANVIK, L. J.; COLE, J. J. Temperature independence of carbon dioxide supersaturation in global lakes. **Global Biogeochemical Cycles**, v. 19, n. 2, p. 1–10, 2005.

SONG, X.; BAI, Y.; CAI, W. J.; ARTHUR CHEN, C. T.; PAN, D.; HE, X.; ZHU, Q. Remote sensing of sea surface pCO<sub>2</sub> in the Bering sea in summer based on a mechanistic semi-analytical algorithm (MeSAA). **Remote Sensing**, v. 8, n. 7, p. 1–25, 2016.

SPENCER, R. G. M.; BUTLER, K. D.; AIKEN, G. R. Dissolved organic carbon and chromophoric dissolved organic matter properties of rivers in the USA. **Journal of Geophysical Research: Biogeosciences**, v. 117, n. 3, 2012.

SPENCER, R. G. M.; STUBBINS, A.; HERNES, P. J.; BAKER, A.; MOPPER, K.; AUFDENKAMPE, A. K.; DYDA, R. Y.; MWAMBA, V. L.; MANGANGU, A. M.; WABAKANGHANZI, J. N.; SIX, J. Photochemical degradation of dissolved organic matter

and dissolved lignin phenols from the Congo River. **Journal of Geophysical Research**, v. 114, n. G3, p. G03010, 2009.

SPYRAKOS, E.; O'DONNELL, R.; HUNTER, P. D.; MILLER, C.; SCOTT, M.; SIMIS, S. G. H.; NEIL, C.; BARBOSA, C. C. F.; BINDING, C. E.; BRADT, S.; BRESCIANI, M.; DALL'OLMO, G.; GIARDINO, C.; GITELSON, A. A.; KUTSER, T.; LI, L.; MATSUSHITA, B.; MARTINEZ-VICENTE, V.; MATTHEWS, M. W. et al. Optical types of inland and coastal waters. **Limnology and Oceanography**, 2017.

STEINMETZ, F.; DESCHAMPS, P.-Y.; RAMON, D. (POLYMER)Atmospheric correction in presence of sun glint: application to MERIS. **Optics Express**, v. 19, n. 10, p. 9783–9800, 2011.

STEVENSON, F. J. Humus Chemistry: Genesis, Composition, Reactions. **Nature**, v. 303, n. 30, p. 835–836, 1983.

SUBRAMANIAM, A.; YAGER, P. L.; CARPENTER, E. J.; MAHAFFEY, C.; BJÖRKMAN, K.; COOLEY, S.; KUSTKA, A. B.; MONTOYA, J. P.; SAÑUDO-WILHELMY, S. A.; SHIPE, R.; CAPONE, D. G. Amazon River enhances diazotrophy and carbon sequestration in the tropical North Atlantic Ocean. **Proceedings of the National Academy of Sciences of the United States of America**, v. 105, n. 30, p. 10460–5, 2008.

SUESS, E. Interaction of organic compounds with calcium carbonate-I. Association phenomena and geochemical implications. **Geochimica et Cosmochimica Acta**, v. 34, n. 2, p. 157–168, 1970.

SUN, D.; HU, C.; QIU, Z.; CANNIZZARO, J. P.; BARNES, B. B. Influence of a red band-based water classification approach on chlorophyll algorithms for optically complex estuaries. **Remote Sensing of Environment**, v. 155, p. 289–302, 2014.

TAKAHASHI, T.; SUTHERLAND, S. C.; WANNINKHOF, R.; SWEENEY, C.; FEELY, R. A.; CHIPMAN, D. W.; HALES, B.; FRIEDERICH, G.; CHAVEZ, F.; SABINE, C.; WATSON, A.; BAKKER, D. C. E.; SCHUSTER, U.; METZL, N.; YOSHIKAWA-INOUE, H.; ISHII, M.; MIDORIKAWA, T.; NOJIRI, Y.; K?RTZINGER, A. et al. Climatological mean and decadal change in surface ocean pCO<sub>2</sub>, and net sea-air CO<sub>2</sub> flux over the global oceans. **Deep-Sea Research Part II: Topical Studies in Oceanography**, v. 56, n. 8–10, p. 554–577, 2009.

TALONE, M.; CAMPS, A.; MOURRE, B.; SABIA, R.; VALL-LLOSSERA, M.; GABARRÓ, C.; FONT, J. The impact of combining SMOS and ARGO data on the SMOS level 2 and 3 products and effect of the vicinity of the coast. In: **Microwave Radiometry and**

**Remote Sensing of the Environment** - 10th Specialist Meeting, Proceedings, MICRORAD, 2008.

TASSAN, S. Local algorithms using SeaWiFS data for the retrieval of phytoplankton, pigments, suspended sediment, and yellow substance in coastal waters. **Applied Optics**, v. 33, n. 12, p. 2369–78, 1994.

TASSAN, S.; FERRARI, G. An alternative approach to absorption measurements of aquatic particles retained on filters. **Limnol. Oceanogr.**, v. 40, n. 8, p. 1358–1368, 1995.

TASSAN, S.; FERRARI, G. M. A sensitivity analysis of the “Transmittance – Reflectance” method for measuring light absorption by aquatic particles. **J. Plankton Res.**, v. 24, n. 8, p. 757–774, 2002.

TEHRANI, N. C.; D’SA, E. J.; OSBURN, C. L.; BIANCHI, T. S.; SCHAEFFER, B. A. Chromophoric dissolved organic matter and dissolved organic carbon from sea-viewing wide field-of-view sensor (seawifs), moderate resolution imaging spectroradiometer (modis) and meris sensors: Case study for the Northern Gulf of Mexico. **Remote Sensing**, v. 5, n. 3, p. 1439–1464, 2013.

TELSZEWSKI, M.; CHAZOTTES, A.; SCHUSTER, U.; WATSON, A. J.; MOULIN, C.; BAKKER, D. C. E.; GONZ, M. Estimating the monthly pCO<sub>2</sub> distribution in the North Atlantic using a self-organizing neural network. **Biogeosciences**, v. 6, p. 1405–1421, 2009.

TERNON, J. F.; OUDOT, C.; DESSIER, A.; DIVERRÉS, D. A seasonal tropical sink for atmospheric CO<sub>2</sub> in the Atlantic Ocean: the role of the Amazon River discharge. **Marine Chemistry**, v. 68, p. 183–201, 2000.

TIWARI, S. P.; SHANMUGAM, P. An optical model for the remote sensing of coloured dissolved organic matter in coastal/ocean waters. **Estuarine, Coastal and Shelf Science**, v. 93, n. 4, p. 396–402, 2011.

TRANVIK, L. J.; DOWNING, J. A.; COTNER, J. B.; LOISELLE, S. A.; STRIEGL, R. G.; BALLATORE, T. J.; DILLON, P.; FINLAY, K.; FORTINO, K.; KNOLL, L. B. Lakes and reservoirs as regulators of carbon cycling and climate. **Limnology and Oceanography**, v. 54, n. 6, part 2, p. 2298–2314, 2009.

TWARDOWSKI, M. S.; BOSS, E.; SULLIVAN, J. M.; DONAGHAY, P. L. Modeling the spectral shape of absorption by chromophoric dissolved organic matter. **Marine Chemistry**, v. 89, n. 1–4, p. 69–88, 2004.

TYLER, A. N.; HUNTER, P. D.; SPYRAKOS, E.; GROOM, S.; CONSTANTINESCU, A. M.; KITCHEN, J. Developments in Earth observation for the assessment and monitoring of inland, transitional, coastal and shelf-sea waters. **Science of the Total Environment**, v. 572, p. 1307–1321, 2016.

TZORTZIOU, M.; SUBRAMANIAM, A.; HERMAN, J.; GALLEGOS, C.; NEALE, P.; HARDINGJR, L. Remote sensing reflectance and inherent optical properties in the mid Chesapeake Bay. **Estuarine, Coastal and Shelf Science**, v. 72, n. 1–2, p. 16–32, 2007.

ULLOA, O.; SATHYENDRANATH, S.; PLATT, T. Effect of the particle-size distribution on the backscattering ratio in seawater. **Applied Optics**, v. 33, n. 30, p. 7070–7077, 1994.

UNCLES, R. J.; STEPHENS, J. A.; SMITH, R. E. The dependence of estuarine turbidity on tidal intrusion length, tidal range and residence time. **Continental Shelf Research**, v. 22, n. 11–13, p. 1835–1856, 2002.

VAN DER LINDE, D. W. Protocol for determination of total suspended matter in oceans and coastal zones. **JRC Technical Note I**, v. 98, p. 182, 1998.

VANHELLEMONT, Q.; RUDDICK, K. Advantages of high quality SWIR bands for ocean colour processing: Examples from Landsat-8. **Remote Sensing of Environment**, v. 161, p. 89–106, 2015.

VANNOTE, R. L.; MINSHALL, G. W.; CUMMINS, K. W.; SEDELL, J. R.; CUSHING, C. E. The River Continuum Concept. **Canadian Journal of Fisheries and Aquatic Sciences**, v. 37, n. 1, p. 130–137, 1980.

VANTREPOTTE, V. Seasonal and inter-annual (2002–2010) variability of the suspended particulate matter as retrieved from satellite ocean color sensor over the French Guiana coastal waters. **Journal of Coastal Research**, v. 64, p. 1750–1754, 2011.

VANTREPOTTE, V.; BRUNET, C.; MÉRIAUX, X.; LÉCUYER, E.; VELLUCCI, V.; SANTER, R. Bio-optical properties of coastal waters in the Eastern English Channel. **Estuarine, Coastal and Shelf Science**, v. 72, n. 1–2, p. 201–212, 2007.

VANTREPOTTE, V.; DANHIEZ, F.; LOISEL, H.; MÉRIAUX, X.; CAUVIN, A.; DESSAILLY, D. CDOM-DOC relationship in contrasted coastal waters: implication for DOC retrieval from ocean color remote sensing observation. **Optics Express**, v. 23, n. 1, p. 578–590, 2015.

VANTREPOTTE, V.; LOISEL, H.; DESSAILLY, D.; MÉRIAUX, X. Optical classification of contrasted coastal waters. **Remote Sensing of Environment**, v. 123, p. 306–323, 2012.

VECCHIO, R. DEL; BLOUGH, N. V.; DEL VECCHIO, R. Photobleaching of chromophoric dissolved organic matter in natural waters: kinetics and modeling. **Marine Chemistry**, v. 78, n. 4, p. 231–253, 2002.

VIHERMAA, L. E.; WALDRON, S.; DOMINGUES, T.; GRACE, J.; COSIO, E. G.; LIMONCHI, F.; HOPKINSON, C.; DA ROCHA, H. R.; GLOOR, E. Fluvial carbon export from a lowland Amazonian rainforest in relation to atmospheric fluxes. **Journal of Geophysical Research: Biogeosciences**, 2016.

VILLAR, R. E.; MARTINEZ, J. M.; LE TEXIER, M.; GUYOT, J. L.; FRAIZY, P.; MENESES, P. R.; OLIVEIRA, E. DE. A study of sediment transport in the Madeira River, Brazil, using MODIS remote-sensing images. **Journal of South American Earth Sciences**, v. 44, p. 45–54, 2013.

VODACEK, A.; BLOUGH, N. V.; DEGRANDPRE, M. D.; PELTZER, E. T.; NELSON, R. K. Seasonal variation of CDOM and DOC in the Middle Atlantic Bight: Terrestrial inputs and photooxidation. **Limnology and Oceanography**, v. 42, n. 4, p. 674–686, 1997.

WANG, M.; SHI, W. The NIR-SWIR combined atmospheric correction approach for MODIS ocean color data processing. **Optics Express**, v. 15, n. 24, p. 15722–15733, 2007.

WANG, M.; SHI, W.; JIANG, L. Atmospheric correction using near-infrared bands for satellite ocean color data processing in the turbid western Pacific region. **Optics Express**, v. 20, n. 2, p. 741, 2012.

WANG, Y.; SHEN, F.; SOKOLETSKY, L.; SUN, X. Validation and calibration of QAA algorithm for CDOM absorption retrieval in the Changjiang (Yangtze) estuarine and coastal waters. **Remote Sensing**, v. 9, n. 11, p. 1–20, 2017.

WANNINKHOF, R. Relationship between wind speed and gas exchange over the ocean revisited. **Limnology and Oceanography: Methods**, v. 12, p. 351–362, 2014.

WANNINKHOF, R. Relationship Between Wind Speed and Gas Exchange. **Journal of Geophysical Research**, v. 97, n. 92, p. 7373–7382, 1992.

WARD, N. D.; BIANCHI, T. S.; MEDEIROS, P. M.; SEIDEL, M.; RICHEY, J. E.; KEIL, R. G.; SAWAKUCHI, H. O. Where Carbon Goes When Water Flows: Carbon Cycling across the Aquatic Continuum. **Frontiers in Marine Science**, v. 4, 2017.

WARD, N. D.; BIANCHI, T. S.; SAWAKUCHI, H. O.; GAGNE-MAYNARD, W.; CUNHA, A. C.; BRITO, D. C.; NEU, V.; DE MATOS VALERIO, A.; DA SILVA, R.; KRUSCHE, A. V.; RICHEY, J.



E.; KEIL, R. G. The reactivity of plant-derived organic matter and the potential importance of priming effects along the lower Amazon River. **Journal of Geophysical Research: Biogeosciences**, p. 1–18, 2016.

WARD, N. D.; KEIL, R. G.; MEDEIROS, P. M.; BRITO, D. C.; CUNHA, A. C.; DITTMAR, T.; YAGER, P. L.; KRUSCHE, A. V.; RICHEY, J. E. Degradation of terrestrially derived macromolecules in the Amazon River. **Nature Geoscience**, v. 6, n. 7, p. 530–533, 2013.

WARD, N. D.; KRUSCHE, A. V.; SAWAKUCHI, H. O.; BRITO, D. C.; CUNHA, A. C.; MOURA, J. M. S.; DA SILVA, R.; YAGER, P. L.; KEIL, R. G.; RICHEY, J. E. The compositional evolution of dissolved and particulate organic matter along the lower Amazon River-Óbidos to the ocean. **Marine Chemistry**, v. 177, p. 244–256, 2015.

WARD, N. D.; RICHEY, J. E.; KEIL, R. G. Temporal variation in river nutrient and dissolved lignin phenol concentrations and the impact of storm events on nutrient loading to Hood Canal, Washington, USA. **Biogeochemistry**, v. 111, n. 1–3, p. 629–645, 2012.

WARD, N. D.; SAWAKUCHI, H. O.; NEU, V.; LESS, D. F. S.; VALERIO, A. M.; CUNHA, A. C.; KAMPEL, M.; BIANCHI, T. S.; KRUSCHE, A. V.; RICHEY, J. E.; KEIL, R. G. Velocity-amplified microbial respiration rates in the lower Amazon River. **Limnology and Oceanography Letters**, 2018.

WATANABE, F. S. Y.; ALCÂNTARA, E.; RODRIGUES, T. W. P.; IMAI, N. N.; BARBOSA, C. C. F.; ROTTA, L. H. DA S. Estimation of chlorophyll-a concentration and the trophic state of the Barra Bonita hydroelectric reservoir using OLI/landsat-8 images. **International Journal of Environmental Research and Public Health**, v. 12, n. 9, p. 10391–10417, 2015.

WATANABE, F.; ALCÂNTARA, E.; CURTARELLI, M.; KAMPEL, M.; STECH, J. Landsat-based remote sensing of the colored dissolved organic matter absorption coefficient in a tropical oligotrophic reservoir. **Remote Sensing Applications: Society and Environment**, v. 9, n. January 2017, p. 82–90, 2018.

WEBER, S. C.; CARPENTER, E. J.; COLES, V. J.; YAGER, P. L.; GOES, J.; MONTOYA, J. P. Amazon River influence on nitrogen fixation and export production in the western tropical North Atlantic. **Limnology and Oceanography**, v. 62, n. 2, p. 618–631, 2017.

WEISS, R. F. Carbon dioxide in water and seawater: the solubility of a non-ideal gas. **Marine Chemistry**, v. 2, n. 3, p. 203–215, 1974.

WERDELL, P. J.; MCKINNA, L. I. W.; BOSS, E.; ACKLESON, S. G.; CRAIG, S. E.; GREGG, W. W.; LEE, Z.; MARITORENA, S.; ROESLER, C. S.; ROUSSEAU, C. S.; STRAMSKI, D.; SULLIVAN, J. M.; TWARDOWSKI, M. S.; TZORTZIOU, M.; ZHANG, X. An overview of approaches and challenges for retrieving marine inherent optical properties from ocean color remote sensing. **Progress in Oceanography**, v. 160, p. 186–212, 2018.

WETZEL, R. G.; LIKENS, G. E. **Limnological Analyses**. 3. ed. 2000.

WILKS, D. S. **Statistical methods in the atmospheric sciences**. Second Edition. California, USA: Academic Press, 2006.

WRIGHT, L. D.; NITTROUER, C. A. Dispersal of River Sediments in Coastal Seas: Six Contrasting Cases. **Estuaries**, v. 18, n. 3, p. 494, 1995.

WU, N.; SCHMALZ, B.; FOHRER, N. Distribution of phytoplankton in a German lowland river in relation to environmental factors. **Journal of Plankton Research**, v. 33, n. 5, p. 807–820, 2011.

XENOPOULOS, M. A.; DOWNING, J. A.; KUMAR, M. D.; MENDEN-DEUER, S.; VOSS, M. Headwaters to oceans: Ecological and biogeochemical contrasts across the aquatic continuum. **Limnology and Oceanography**, v. 62, p. S3–S14, 2017.

XI, H.; LAROUCHE, P.; TANG, S.; MICHEL, C. Seasonal variability of light absorption properties and water optical constituents in Hudson Bay, Canada. **Journal of Geophysical Research: Oceans**, v. 118, n. 6, p. 3087–3102, 2013.

XIAO, Y.-H.; HOIKKALA, L.; KASURINEN, V.; TIROLA, M.; KORTELAINE, P.; VÄHÄTALO, A. V. Iron affects the biodegradation of natural dissolved organic matter. **Journal of Geophysical Research: Biogeosciences**, p. 1–18, 2016.

XIAO, Y.-H.; SARA-AHO, T.; HARTIKAINEN, H.; VÄHÄTALO, A. V. Contribution of ferric iron to light absorption by chromophoric dissolved organic matter. **Limnology and Oceanography**, v. 58, n. 2, p. 653–662, 2013.

XU, S.; CHEN, L.; CHEN, H.; LI, J.; LIN, W.; QI, D. Sea-air CO<sub>2</sub> fluxes in the Southern Ocean for the late spring and early summer in 2009. **Remote Sensing of Environment**, v. 175, p. 158–166, 2016.

XUE, Z.; HE, R.; FENNEL, K.; CAI, W. J.; LOHRENTZ, S.; HUANG, W. J.; TIAN, H.; REN, W.; ZANG, Z. Modeling pCO<sub>2</sub> variability in the Gulf of Mexico. **Biogeosciences**, v. 13, n. 15, p. 4359–4377, 2016.

- YEPEZ, S.; LARAQUE, A.; MARTINEZ, J. M.; DE SA, J.; CARRERA, J. M.; CASTELLANOS, B.; GALLAY, M.; LOPEZ, J. L. Retrieval of suspended sediment concentrations using Landsat-8 OLI satellite images in the Orinoco River (Venezuela). **Comptes Rendus - Geoscience**, v. 350, n. 1–2, p. 20–30, 2018.
- YEUNG, L. Y.; BERELSON, W. M.; YOUNG, E. D.; PROKOPENKO, M. G.; ROLLINS, N.; COLES, V. J.; MONTOYA, J. P.; CARPENTER, E. J.; STEINBERG, D. K.; FOSTER, R. A.; CAPONE, D. G.; YAGER, P. L. Impact of diatom-diazotroph associations on carbon export in the Amazon River plume. **Geophysical Research Letters**, v. 39, n. 18, p. L18609, 2012.
- ZHANG, X.; HUOT, Y.; BRICAUD, A.; SOSIK, H. M. Inversion of spectral absorption coefficients to infer phytoplankton size classes, chlorophyll concentration, and detrital matter. **Applied Optics**, v. 54, n. 18, p. 5805, 2015.
- ZHOU, W.; GAO, J.; LIAO, J.; SHI, R.; LI, T.; GUO, Y.; LONG, A. Characteristics of phytoplankton biomass, primary production and community structure in the Modaomen channel, pearl river estuary, with special reference to the influence of saltwater intrusion during neap and spring tides. **PLoS ONE**, v. 11, n. 12, 2016.
- ZHU, W.; TIAN, Y. Q.; YU, Q.; BECKER, B. L. Using Hyperion imagery to monitor the spatial and temporal distribution of colored dissolved organic matter in estuarine and coastal regions. **Remote Sensing of Environment**, v. 134, p. 342–354, 2013.
- ZHU, W.; YU, Q. Inversion of Chromophoric Dissolved Organic Matter From EO-1 Hyperion Imagery for Turbid Estuarine and Coastal Waters. **Geoscience and Remote Sensing, IEEE Transactions**, v. 51, n. 6, p. 3286–3298, 2013.
- ZHU, W.; YU, Q.; TIAN, Y. Q.; BECKER, B. L.; ZHENG, T.; CARRICK, H. J. An assessment of remote sensing algorithms for colored dissolved organic matter in complex freshwater environments. **Remote Sensing of Environment**, v. 140, p. 766–778, 2014.
- ZHU, W.; YU, Q.; TIAN, Y. Q.; CHEN, R. F.; GARDNER, G. B. Estimation of chromophoric dissolved organic matter in the Mississippi and Atchafalaya river plume regions using above-surface hyperspectral remote sensing. **Journal of Geophysical Research**, v. 116, n. C2, p. C02011, 2011.
- ZHU, Y.; SHANG, S.; ZHAI, W.; DAI, M. Satellite-derived surface water pCO<sub>2</sub> and air-sea CO<sub>2</sub> fluxes in the northern South China Sea in summer. **Progress in Natural Science**, v. 19, n. 6, p. 775–779, 2009.

ZREDA, M. Environmental Isotopes in Hydrogeology. **Eos, Transactions American Geophysical Union**, v. 80, n. 19, p. 217, 1999.

## Appendix A

### A.1 SPM regional algorithm

For deriving SPM in the Lower Amazon, several nonlinear relationships of SPM- $R_{rs}$  were assessed using selected wavelengths in the green-NIR domain. The selected wavelengths from in situ measured  $R_{rs}$  were representative of the following water colour sensors' central bands: Medium Resolution Imaging Spectrometer (MERIS), Moderate Resolution Imaging Spectroradiometer (MODIS), Visible Infrared Imaging Radiometer Suite (VIIRS), Ocean and Land Colour Instrument (OLCI) and Operational Land Imager (OLI). Additionally, two nonlinear models developed for turbid water were tested using the Lower Amazon dataset: Nechad et al. (2010) herein called N10 and Martinez et al. (2015) herein called M15.

Nechad et al. (2010) developed an algorithm for turbid coastal waters of the North Sea:

$$SPM = \frac{A \cdot \rho_w}{1 - \rho_w/C} + B \quad (A.1)$$

where  $\rho_w$  corresponds to the water leaving reflectance ( $\rho = R_{rs} \cdot \pi$ ) in certain wavelength. The coefficients A, B and C are dependent of the chosen wavelength. Considering the OLCI sensor, it was chosen  $\rho(761)$  as the central band wavelength so that the coefficient adjusted to the N10 algorithm were as follows: A = 403.49; B = 1.04; C = 17.75.

Martinez et al. (2015) developed an algorithm to estimate SPM in Amazon white and black rivers: Madeira, Solimões and Negro, using  $R_{rs}$  at the NIR spectrum:

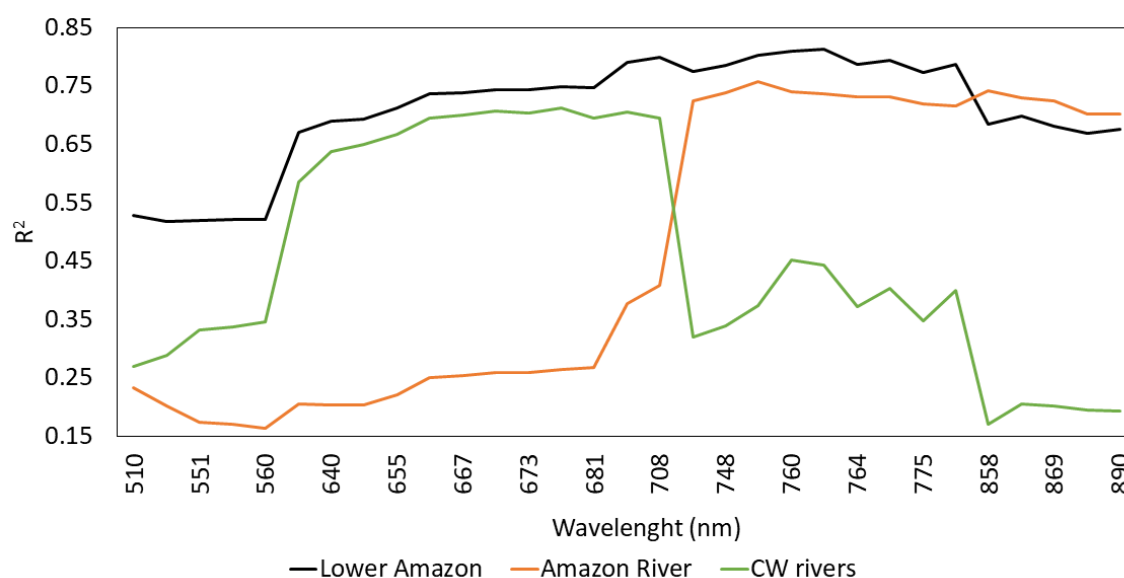
$$SPM = A(R_{rs}(860))^B \quad (A.2)$$

where A = 20.41 and B = 1.173.

### A.2 Results and Discussion

SPM showed a high variability in both Amazon River (124%) and CW (53%) (see Chapter 4, section 4.3.1.1 Table 4.2). Concentration values are within the range described by other authors working in Amazon white waters ( $\sim 5.5 - 1138 \text{ mg L}^{-1}$ ) (CARVALHO et al., 2015; MARTINEZ et al. 2015; BARBOSA et al., 2010). To assess SPM by remote sensing in turbid waters, many authors proposed simple algorithms based on red and/or NIR reflectance (PARK; LATRUBESSE, 2015; 2014; VILLAR et al., 2013; NECHAD et al., 2010; VANTREPOTTE et al., 2011; DOXARAN et al., 2003). A non-linear relationship between SPM and selected in situ  $R_{rs}$  corresponding to the central bands of different ocean colour orbital sensors - MERIS, MODIS, VIIRS, OLCI and OLI, shows that the  $R_{rs}$  interval 655-778 nm is the most suitable for deriving SPM in the Lower Amazon region ( $R^2 > 0.70$ ,  $p < 0.05$ ) when all dataset is considered (Figure A.1). The option to use a non-linear relationship based on a single  $R_{rs}$  wavelength relies on the algorithm proposed by Nechad et al. (2010) calibrated for turbid waters. As already reported in previous studies for very turbid waters, the correlation improves as the wavelengths increases, from the green to the NIR spectrum domain (NECHAD et al., 2010; DOXARAN et al., 2003). In this study, the best SPM inversion performance is obtained when considering the 705-708 nm and 753-767 nm  $R_{rs}$  intervals ( $R^2 \sim 0.80$ ,  $p < 0.05$ ). These intervals can be related to wavelengths available for MERIS (705 and 760 nm) and OLCI (708, 753-767 nm) sensors. Nevertheless, when the data is partitioned into Amazon River and CW samples, a clear difference is observed. The relationship  $R_{rs} \times \text{SPM}$  for CW rivers have a better performance in the red spectrum (667-678 nm) ( $R^2 \sim 0.71$ ,  $p < 0.05$ ), while for the Amazon River NIR (746-890 nm)  $R_{rs}$  are undoubtedly providing stronger correlation with SPM loads ( $R^2 \sim 0.73$ ,  $p < 0.05$ ). Therefore, considering the partition of the OWT into CW and Amazon River, the OCR sensors MODIS (667, 678, 748, 858 and 869 nm), VIIRS (672, 746, 865 nm) and OLI (865 nm) are also suitable to assess SPM, accordingly.

Figure A.1 - Coefficients of determination for the nonlinear relationship between selected wavelengths from in situ  $R_{rs}$  and SPM.



Source: Author's production.

This result suggests that the general relationship is not homogenous across the study area; SPM probably has different composition where, comparatively, CW has more organic particles and Amazon River has a larger part of fine inorganic sediments (where DOM are adsorbed). The SPM composition difference was also discussed by Martinez et al. (2015). Assessing distinct OWT from the Amazon region, they documented that SPM in white rivers (Madeira and Solimões) are composed of mineral particles at high concentrations, while in black river and floodplains, SPM are composed by a larger organic fraction (living and nonliving). As reported by Martinez et al. (2015),  $R_{rs}$  fluctuate more according to the proportion of organic and inorganic particles at low SPM concentrations ( $< 20 \text{ mg L}^{-1}$ ), which is the average value found in this study for CW rivers (see Chapter 4, section 4.3.1.1 Table 4.2).

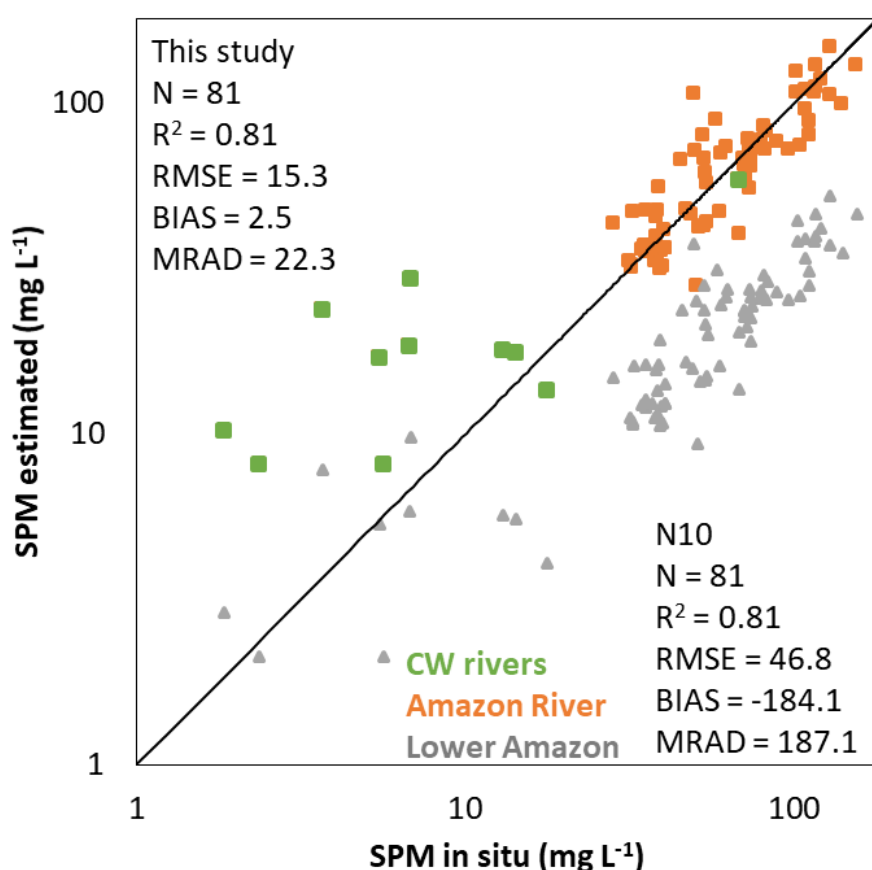
Although band ratio algorithms are also widely used to estimate SPM in turbid waters (HAN et al., 2016; VILLAR et al., 2013; DOXARAN et al., 2003), when tested in this study (672/555; 764/555; 865/555; 858/645 nm) it was not possible to improve the relationships already obtained. Therefore, it was decided not to show these results

here. Other authors have also reported that band ratio algorithms adjusted for other rivers at the Amazon basin didn't enhance globally the relationship between SPM and  $R_{rs}$  (YEPEZ et al., 2018; MARTINEZ et al., 2015). Recent studies used the short-wave infrared (SWIR) band to retrieve SPM concentrations from extremely turbid waters ( $> 100 \text{ mg L}^{-1}$ ) (KNAEPS et al., 2015), with concentration values close to those obtained for some samples from the Amazon River during the RW season. Nevertheless, the use of SWIR is recommended when  $R_{rs}(865)$  is higher than  $0.09 \text{ sr}^{-1}$ , and this threshold was not exceeded in the samples obtained for this study.

Similar results indicating positive relationship for  $R_{rs}$  at red and/or NIR spectrum and SPM in rivers from the Amazon basin were presented by other authors, using linear and nonlinear regressions (MARTINEZ et al. 2015; PARK; LATRUBESSE, 2014; VILLAR et al., 2013). The relationship between  $\rho_w(761)$  and SPM using the N10 nonlinear algorithm is shown in Figure A.2 for the entire dataset of this study, where Amazon and CW rivers are shown in different colours (orange and green, respectively). The coefficients were calibrated for the study area were:  $A = 1100$ ,  $B = 5.121$  and  $C = 30650$  ( $R^2 = 0.81$ ,  $\text{RMSE} = 15.3 \text{ mg L}^{-1}$ ,  $\text{BIAS} = 2.5$ ,  $\text{MRAD} = 22.3$ ). The coefficients documented by Nechad et al. (2010) were estimated using in situ data from coastal waters of the North Sea (SPM range: 1.24 to 110.27  $\text{mg L}^{-1}$ , SPM average: 26.16  $\text{mg L}^{-1}$ ). When the same coefficients are applied in the Lower Amazon, the estimated SPM are overall underestimated despite that some samples from the CW rivers are in line with the N10 model. When applying the coefficients here calibrated for the Lower Amazon, gathering together Amazon and CW rivers samples, the result is improved but SPM from CW are overestimated. The overestimation of SPM at CW rivers might be related to the use of a NIR band instead of a red band, that could have a better performance for clearwater samples (Figure A.1).



Figure A.2 - Estimated suspended particle matter as a function of  $\rho_w(761)$  for Amazon and clearwater rivers using Lower Amazon coefficients and Nechad et al. (2010) – N10 coefficients.



Lower Amazon coefficients (N = 81,  $R^2 = 0.81$ ,  $p < 0.005$ , RMSE = 15.3 mg L<sup>-1</sup>, BIAS = 2.5, MRAD = 22.3); Nechad et al. (2010) – N10 coefficients (N = 81,  $R^2 = 0.81$ ,  $p < 0.005$ , RMSE = 46.8 mg L<sup>-1</sup>, BIAS = -184.1, MRAD = 187.1).

Source: Author's production.

The performance of M15 applied to in situ  $R_{rs}(860)$  calibrated for the Lower Amazon data is relatively lower than that obtained when using of Lower Amazon calibrated N10. Despite the good coefficient of determination ( $R^2 = 0.77$ ) obtained with the M15 algorithm, the computed SPM was underestimated in comparison to in situ values. This underestimation might be related to the range of SPM concentration on which M15 was developed (2-621 mg L<sup>-1</sup>, average = 141 mg L<sup>-1</sup>), which is much higher than that found in the present study area (see Chapter 4, section 4.3.1.1, Table 4.2). Also,

the correlation of  $R_{rs}(860)$  with SPM has a decay when all the dataset is used, as well as evident lower values when only CW samples are considered (Figure A.1). One can also consider the occurrence of some noise in the reflectance measurements obtained at wavelengths  $> 800$  nm as a potential source of error or cause for observed differences. When M15 is applied using the coefficients calibrated for the Lower Amazon ( $A = 2797.6$ ,  $B = 0.8651$ ) the outcome has a lower performance ( $N = 81$ ,  $R^2 = 0.77$ ,  $p < 0.005$ ,  $RMSE = 17.4 \text{ mg L}^{-1}$ ,  $BIAS = -9.9$ ,  $MRAD = 28.8$ ) than N10.

### **A.3 Final considerations**

The best  $R_{rs}$  to estimate SPM was 761 nm when all the Lower Amazon dataset is considered. The algorithm proposed by Nechad et al. (2010) worked well when calibrated for the study area. The  $R_{rs}$  divergence found at CW and Amazon River suggests a different particle composition for both OWT. One approach to achieve a better fit considering the intrinsic characteristic of SPM from CW and Amazon River could be the development of an algorithm based on different weight for selected  $R_{rs}$  as the one proposed by Dogliotti et al. (2015) to assess the turbidity in optically complex waters. This method can switch according to the composition, size distribution and refractive index of SPM. Another suggestion for a future work is to use the classification scheme presented in Chapter 4 and develop a specific algorithm to each optical type.